Testing the Standard Cosmological Model

SAWANGWIT, UTANE

Testing the Standard Cosmological Model

by Utane Sawangwit

PhD Thesis, July 2011

Abstract

This thesis exploits the wealth of information contained in the existing cosmological surveys, and demonstrates how the use of tools such as two-point statistics permit the extraction of such information. In particular, the wide-field imaging survey – the Sloan Digital Sky Survey (SDSS) in conjunction with Luminous Red Galaxy (LRG) spectroscopic surveys carried out by the Two-degree-Field (2dF) and AAOmega instruments on the Anglo-Australian telescope (AAT) are utilised here. This also includes the observations of the Cosmic Microwave Background (CMB) radiation from the *Wilkinson Microwave Anisotropy Probe* (*WMAP*) experiment.

Combining the imaging and spectroscopic surveys, we extract three photometric LRG samples at redshift ≈ 0.35, 0.55 and 0.7 which cover ≈ 7600 deg^2 of the sky, probing a total cosmic volume of $\approx 5.5\ h^{-3}\,\mathrm{Gpc}^3$. We find very little clustering evolution in these massive early-type galaxies out to $z \simeq 0.8$ or nearly half the age of the Universe. The shape of the large-scale correlation functions is consistent with a simple 'high-peaks' bias and linear theory framework of the standard ΛCDM model. The new $\bar{z} \approx 0.7$ LRG sample is then used in the CMB-LSS cross-correlation analysis to look for the the Integrated Sachs-Wolfe (ISW) effect as a dynamical evidence for the accelerated expansion of the Universe. The measured zero CMB-LRG correlation is inconsistent with the ΛCDM model expectation at 2.2σ significance level. Furthermore, our rotation tests show that the previous detections of the ISW effect may not be as significant as previously claimed.

We make independent estimates of the *WMAP* CMB temperature power spectra and show explicitly how sensitive they are to the instrumental beams. We propose an alternative method for determining the beam profiles by stacking radio point sources and demonstrate its robustness via Monte Carlo simulations plus realistic point source detection algorithm. Using this technique, we find significantly wider *W*-band beam profiles than the *WMAP* Jupiter beam analysis. We also find a tentative evidence for a non-linearity in the *WMAP* radio source fluxes when compared with the ground-based measurements. Finally, we investigate if the recently claimed timing offset in the *WMAP* time-ordered data can explain the observed wider than expected beam profile.

Testing the Standard Cosmological Model

by

Utane Sawangwit

A thesis submitted to the University of Durham
in accordance with the regulations for admission to the
Degree of Doctor of Philosophy.

Extragalactic & Cosmology Group

Department of Physics

2011

Preface | *Declaration*

The work described in this thesis was undertaken between 2006 and 2011 while the author was a research student under the supervision of Prof. Tom Shanks in the Department of Physics at Durham University. This work has not been submitted for any other degree at Durham University or at any other University.

Portions of this work have appeared in the following papers:

- Sawangwit, U., Shanks, T., Abdalla, F., Cannon, R. D., Croom, S. M., Edge, A., Ross, N. P. & Wake, D. A. 2011, MNRAS, 416, 3033, **Angular correlation function of 1.5 million luminous red galaxies: clustering evolution and a search for baryon acoustic oscillations** (chapters 2)
- Sawangwit, U., Shanks, T., Cannon, R. D., Croom, S. M., Ross, N. P. & Wake, D. A. 2010, MNRAS, 402, 2228, **Cross-correlating WMAP5 with 1.5 million LRGs: a new test for the ISW effect** (chapter 3)
- Sawangwit, U. & Shanks, T. 2010, MNRAS, 407, L16, **Beam profile sensitivity of the *WMAP* CMB power spectrum** (chapter 4)

The major part of the work presented in this thesis is the author's own work except where specifically noted in the text, as summarised below

- The computer code used in inferring 3D clustering from an angular correlation function (Chapter 2) is the improvement made by the thesis author on the original Limber equation code provided by Prof. Tom Shanks.
- The computer code for estimating dark matter halo mass from a galaxy linear bias factor (Chapter 2) was adapted from the code originally written by Dr. Scott Croom.
- The halo model software featured in Chapter 2 is adapted from the code provided by Dr. David Wake.

Contents

List of Figures

List of Tables

Acknowledgements

I am grateful first and foremost to my supervisor, Prof. Tom Shanks, for his support, time and guidance. This thesis would not have been possible without his supervision, enthusiasm and vast knowledge of cosmology and general astronomy. I also thank his wife Kath for her hospitality and kindness.

Thank you also to my other collaborators, Dr. David Wake, Dr. Scott Croom, Dr. Russell Cannon, Dr. Alastair Edge, Dr. Filipe Abdalla, Dr. Nigel Metcalfe and Dr. Nicholas Ross in particular, for providing data, help and advice during the early time of my PhD. Alan Lotts deserves special credit for his work constantly keeping the network up and running and for taking care of all sort of computer matters.

I would like to thank all fellow postgrads and postdocs with whom I shared an office, a discussion on the days headlines/recent astro-ph postings or a pint, Dr. Nicholas Ross, Dr. Rich Bielby, Dr. Michael Hill, Joe Whitbourn, Nok Pimpunyawat Tummuangpak, Nikolaos Nikoloudakis, Dr. Stephen Fine, Monsit Tanasittikosol and many others who have made the years pass faster and full of interesting memories. Special thanks also go to my college tutors Dr. Nui Rataporn Deesomsak and Dr. Frankie Chau whose advices have been very helpful, especially during my early time in Durham. Another big "thank you" to Joe for (proof-) reading my thesis.

I thank the SDSS and *WMAP* collaborations for making their data and supplementary materials publicly available where most of the works presented in this thesis have benefited from. I also thank all the present and former staff of the Anglo–Australian Observatory for their work in building and operating the 2dF and AAOmega facility. I am also grateful for the financial support from the Institute for the Promotion of Teaching Science and Technology (IPST) of The Royal Thai Government during most of my academic career in the UK.

Finally, my special gratitude goes to the person who deserves the most thanks of all. I am grateful for her support, her friendship and her love. She is the person without whom I could never have accomplished this thesis, and therefore the person to whom it is dedicated.

To my wife,

于馨

Chapter 1 | *Introduction*

1.1 The Cosmological Principle

Much of modern cosmology is built upon two fundamental assumptions called the 'Cosmological Principle'. The principle asserts that the Universe is homogeneous and isotropic on sufficiently large scales. The latter has been proved to be very precise in the observations of the Cosmic Microwave Background (CMB) radiation, i.e. to about one part in 10^5 (once our motion relative to the CMB field has been taken into account, see below). The observed near-perfect isotropy does not immediately imply the homogeneity without invoking the 'Copernican Principle' which states that we do not occupy a unique position in the Universe. Nonetheless, the galaxy (and the inferred underlying matter) distribution has been shown to satisfy the homogeneity and isotropy assumption of the Cosmological Principle on scales larger than $\sim 100\ h^{-1}\,\mathrm{Mpc}$ (e.g. Wu, Lahav, and Rees 1999; Sarkar et al. 2009). However, note that arguments against the claimed homogeneity also exist (e.g. Sylos Labini, 2011; Maartens, 2011).

The Cosmological Principle then leads to a non-static Universe, either expanding or contracting (e.g. Weinberg, 2008). This can be derived independently from the Einstein field equations of General Relativity (GR). In fact, the expanding Universe could have been predicted as early as the 17th century using Newtonian physics in conjunction with the Cosmological Principle if not for the philosophical/religious background at the time (Coles and Lucchin, 2002). The long-held belief of the unchanging nature of the Cosmos lingered on until the observational result of Edwin Hubble (1929). Hubble finally demonstrated to the astronomical community that the Universe is in fact expanding by showing that the speed at which Extra-Galactic Nebulae, now known to be galaxies like our own, are receding is directly proportional to their distances away from us.

This then implies that all the matter in the Universe was once ($\sim$ 14 billion years ago) very close together in a hot dense state of the so called 'Big Bang' theory, a term coined by Sir Fred Hoyle. The Big Bang theory was originally proposed by Lemaître (1931) in his 'hypothesis of the primeval atom'. Using nuclear physics, the Big-Bang Nucleosynthesis

(BBN) framework can be used to predict the abundance of light elements (nuclei), e.g. Deuterium, Helium and Lithium, created during the first few minutes after the Big Bang (Gamow, 1946). The structures we see today, e.g. galaxies, clusters of galaxy etc., were formed via gravitational instability seeded by quantum mechanical fluctuations which were amplified by a period of rapid expansion of the Universe called 'Inflation'[1] (Guth, 1981). However, there existed a competing model called 'Steady State' theory, proposed by F. Hoyle (1948), H. Bondi and T. Gold (1948), where new matter is continuously created as the Universe expands in order to maintain its *Perfect Cosmological Principle*, i.e. the Universe which is homogeneous and isotropic in both space and time, therefore removing the need for a singularity beginning. The Steady State theory was largely refuted once the relic thermal radiation predicted by the Big Bang model was discovered in 1965. Consequently, the Big Bang theory is now the framework of the mainstream cosmological model.

For the rest of this chapter, we outline the modern cosmological paradigm, and the techniques employed to study it. We also take this opportunity to establish the notations and conventions which will appear later in the thesis.

1.2 Dynamics of the expanding Universe

During the 1920s and 1930s, what is now known as 'Friedmann-Robertson-Walker' (FRW) metric[2] was being developed independently by the cosmologist, physicist and mathematician named A. Friedmann (1922), H. P. Robertson (1935) and A. G. Walker (1936), respectively. The FRW metric is a pillar of modern cosmology. Although it is an exact solution of Einstein's field equations, its form can also be derived using Newtonian physics and the Cosmological Principle (e.g. Weinberg, 2008). The Einstein field equations are only needed to solve for the scale factor, $a(t)$ (also known as Robertson-Walker scale factor). In the FRW metric, the line element is given by

$$ds^2 = c^2dt^2 + a(t)^2\left[\frac{dr^2}{1-\frac{Kr^2}{R_u^2}} + r^2(d\theta^2 + \sin^2\theta d\phi^2)\right], \tag{1.1}$$

where c is the speed of light, t is the proper time, r, θ and ϕ are comoving spherical coordinates. R_u is the 'radius of curvature' defined as a constant with dimensions of length.

[1] This was originally proposed as a solution to the flatness and horizon problems (see later).

[2] This is sometimes known as Friedmann-Lemaître-Robertson-Walker (FLRW) metric, as the solutions originally derived by A. Friedmann was independently discovered five years later by G. Lemaître (1927).

The curvature parameter K is a constant related to the spatial geometry of the Universe and can take values

$$K = \begin{cases} -1 & \text{Open (Hyperbolic)} \\ 0 & \text{Flat (Euclidean)} \\ 1 & \text{Closed (Spherical)} \end{cases} \tag{1.2}$$

The proper distance, d_p, derived from the above metric by setting $dt = 0$ is $d_p = a(t)\chi$, where χ is a comoving distance and $\chi = \sinh^{-1}(r)$, r and $\sin^{-1}(r)$ for $K = -1$, 0 and 1, respectively.

To proceed further one is required to solve for the scale factor $a(t)$ using the Einstein equations which relate the energy-matter content to the space-time geometry of the Universe. The problem can be greatly simplified if one assumes a homogeneous and isotropic, i.e. Cosmological Principle, perfect fluid with equation of state $p = w\rho c^2$, where p is the pressure, ρc^2 is the energy density and w is defined by the nature of that particular fluid. The solutions are known as the Friedmann equations,

$$H^2 \equiv \left(\frac{\dot{a}}{a}\right)^2 = \frac{8\pi G}{3}\rho - \frac{Kc^2}{R_u^2 a^2}, \tag{1.3}$$

and

$$\frac{\ddot{a}}{a} = -\frac{4\pi G}{3}\left(\rho + \frac{3p}{c^2}\right), \tag{1.4}$$

where the dot denotes a derivative with respect to proper time t, G is the gravitational constant and H is the Hubble parameter. The second equation is sometimes called the 'Acceleration equation'. From Eq. 1.4 we see that the Universe is in the state of accelerated expansion if the w is lower than $-1/3$, we shall return to discuss this below. Using the first equation, the second equation can be re-written as

$$\dot{\rho} = -3H\left(\rho + \frac{p}{c^2}\right), \tag{1.5}$$

which describes the adiabatic expansion of the Universe (e.g. Coles and Lucchin, 2002).

In the Friedmann equations, the fluid can be made up of more than one component, i.e. matter, radiation. The (energy) density is then given by the total (energy) density of all the constituents of the Universe, $\rho = \sum_i \rho_i$. If the fluid components are non-interacting then Eq. 1.5 can be applied to each component individually and its evolution is given by

$$\rho = \rho_0\, a^{-3(1+w)}, \tag{1.6}$$

where $\rho_0 = \rho(t_0)$[3] is the density at the present time and w is assumed to be time-independent in this case. In a universe which contains radiation ($w = 1/3$), matter/dust ($w = 0$), and some exotic form of energy, says positive 'Cosmological Constant'[4] (Λ) or sometimes called vacuum energy ($w = -1$), the density evolution becomes

$$\rho = \rho_{\gamma,0}\, a^{-4} + \rho_{m,0}\, a^{-3} + \rho_{\Lambda}, \tag{1.7}$$

where $\rho_{m,0}$ and $\rho_{\gamma,0}$ are matter and radiation density at present epoch, and $\rho_\Lambda \equiv \Lambda c^2/8\pi G$. At early times ($a \ll 1$), the Universe is radiation-dominated which is then followed by the matter-dominated and eventually Λ-dominated eras as the Universe expands. The expression for $\rho(a)$ can be substituted into Eq. 1.3 and the time evolution of the scale factor can be solved directly.

1.2.1 Observables

The Hubble parameter $H(t) \equiv \dot{a}/a$ (Eq. 1.3) measures the expansion rate at any given time t. And the Hubble Law states that two points which are separated by a proper distance d_p are moving away from each other at a speed

$$v_r = \frac{\dot{a}}{a} \times d_p \tag{1.8}$$

The Hubble parameter at present time, H_0, is called Hubble's constant. The Hubble constant is usually estimated by measuring redshift z of a distant galaxy and then obtaining the distance to that galaxy using 'Standard Candles' such as Cepheid variables (e.g. Tanvir, Ferguson, and Shanks, 1999) and/or type Ia supernovae (SNIa) (e.g. Freedman et al., 2001). The latest measurement from over 600 Cepheid variables in the nearby SNIa host galaxies observed with the Hubble Space Telescope (HST) gives the best estimate of $H_0 = 73.8 \pm 2.4$ km s^{-1} Mpc^{-1} (Riess et al., 2011). Throughout this thesis, we parametrise the Hubble constant such that $H_0 = 100h$ km s^{-1} Mpc^{-1}, where h is a dimensionless constant to be determined.

Observationally, the effect of the expanding Universe is seen as the light from distant luminous objects, usually galaxies, being stretched to higher wavelengths. The amount of change is usually refer to as 'redshift z' and by definition is quantified by

[3] Throughout this chapter, subscript 0 denotes the value of that parameter today

[4] Originally introduced by Einstein (1917) as an extra constant term in order to make the solutions to his field equations static.

$$z = \frac{\lambda_0}{\lambda_e} - 1, \tag{1.9}$$

where λ_e is the emitted wavelength of the radiation in the object's rest-frame and λ_0 is the observed wavelength by us at present time. For a nearby galaxy, redshift can be thought of as a result of a Doppler shift as the galaxy is moving away at speed $v = cz$ and the proper distance can be estimated by $d_p \approx cz/H_0$. At higher redshift, especially at $z \geq 1$, this does not lead to a violation of Special Relativity as the receding speed is due to the expansion of space-time itself and not the galaxy's motion. Alternatively, redshift can be viewed as the stretching of the wavelength embedded in an expanding space-time continuum. Using the FRW metric, one can derive that $a/\lambda_e = a_0/\lambda_0$ and therefore

$$a = \frac{a_0}{1+z}. \tag{1.10}$$

This provides a way to relate the scale factor a to the more directly observable parameter z. Note that throughout this thesis we set $a_0 = a(t_0)$ to 1.

Another useful quantity for comparing different cosmological models is the density parameter Ω defined as $\rho/\rho_{\rm crit}$ where $\rho_{\rm crit}$ is the density at which the Universe is spatially flat, i.e. $K = 0$. Setting $K = 0$ in Eq. 1.3 gives

$$\rho_{\rm crit} = \frac{3H^2}{8\pi G} \tag{1.11}$$

Substituting Eqs. 1.7, 1.10 and 1.11, Eq. 1.3 can be re-written as a function of density parameter and redshift z,

$$H^2(z) = H_0^2 \left\{ \Omega_{\gamma,0}(1+z)^4 + \Omega_{m,0}(1+z)^3 + \Omega_{X,0}(1+z)^{3(1+w_X)} + \Omega_{K,0}(1+z)^2 \right\}, \tag{1.12}$$

where Λ is replaced by an unknown fluid X with equation of state w_X and $\Omega_{K,0} \equiv -Kc^2/R_u^2H_0^2$ is the curvature density parameter. More commonly, Ω_K is written as $\Omega_K = 1 - \Omega_{\rm tot}$, where $\Omega_{\rm tot} = \sum_i \Omega_i$. Therefore, the Universe is said to be spatially flat if $\Omega_{\rm tot} = 1$ or open if $\Omega_{\rm tot} < 1$ or closed if $\Omega_{\rm tot} > 1$.

The expansion history of the Universe as governed by $H(z)$ has been the main subject of modern cosmology for the past decade or so, as this allows us to constrain the matter-energy components of the Universe and therefore build up a picture of the Cosmos. Techniques which have been widely employed include the use of distance scales estimated using Standard Candles as in the case of SNIa (e.g. Perlmutter et al., 1999;

Riess et al., 1998, 2007) or Standard Ruler from the Baryon Acoustic Oscillation (BAO) scales in the galaxy distributions (e.g. Blake and Glazebrook, 2003; Eisenstein et al., 2005; Percival et al., 2010) and the Acoustic Peak scales in the CMB fluctuations (e.g. Spergel et al., 2003, 2007; Komatsu et al., 2011). These techniques involve measuring the $H(z)$ in the form of either 'Angular Diameter Distance' (D_A) or 'Luminosity Distance' (D_L) as a function of redshift,

$$D_A(z) = \frac{D_L(z)}{(1+z)^2} = \frac{r}{1+z} = \frac{c}{(1+z)H_0\sqrt{|\,\Omega_K|}}\, f_K\left[H_0\sqrt{|\,\Omega_K|}\int_0^z \frac{dz'}{H(z')}\right] \qquad (1.13)$$

where $f_K(x) = \sin(x)$, x, or $\sinh(x)$ for closed, flat, and open models, respectively.

1.3 The Cosmic Microwave Background

The Cosmic Microwave Background (CMB) was discovered serendipitously by A. Penzias and R. Wilson in 1964. The static background signal they found was first thought to be caused by instrumental noise which they could not get rid of nor explain its origin. The background 'noise' was estimated to have antenna temperature of 3.5 ± 1.0 K at 7.3-cm wavelength. At the time, they were not aware of the prediction of residual cosmic radiation made a decade and a half earlier by Alpher and Herman (1948). Based on nucleosynthesis, Alpher and Herman estimated the present temperature of this residual radiation to be about 5 K. Penzias and Wilson later shared their finding with Dicke, Peebles, Roll, and Wilkinson (1965) who were building radio antenna to look for the CMB signal predicted by their theory. The two groups published the result with its interpretation being the relic cosmic radiation from the Big Bang as provided by the latter group.

The first successful attempt to make precise measurement of the full-sky CMB map is the NASA's *COsmic Background Explorer* (*COBE*; Boggess et al., 1992) mission launched in November 1989. The Far-Infrared Absolute Spectrophotometer (FIRAS) instrument on the *COBE* satellite measured the CMB spectrum between 60-600 GHz and showed that it has a near-perfect blackbody spectrum (Mather et al., 1994; Fixsen et al., 1996). Fig. 1.1 shows the CMB spectrum measured by the *COBE* mission and various other experiments made at lower wavelengths (Credit: Smoot, 1997). This provides compelling evidence that the CMB is indeed the remnant thermal afterglow from a hot, dense, early Universe which has been travelling towards us since the epoch of recombination[5]. The best-estimate of

[5]As the Universe expands, the temperature drops until it is cool enough, $T \sim 4000$ K at $z_* \sim 1000$,

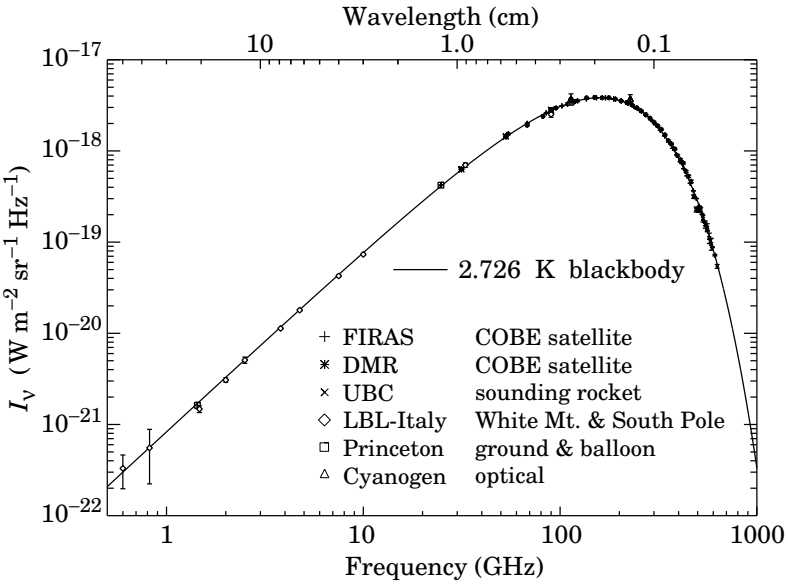

Figure 1.1: The CMB spectrum measurements made by *COBE* and various other experiments (Smoot, 1997, and references therein). The spectrum is well described by a blackbody spectrum with thermal temperature $T = 2.726$ K. Figure credit: G. Smoot (1997).

the CMB temperature made with the four-year *COBE* data is $T_0 = 2.725 \pm 0.002$ K (95 per cent CL) (Mather et al., 1999).

The Differential Microwave Radiometer (DMR) aboard the *COBE* satellite was designed to study the CMB fluctuation on scales larger than about 7° (Smoot et al., 1990). The CMB temperature map was found to be remarkably uniform once the dipole contribution due to our motion relative to the CMB field (or sometimes called cosmological rest-frame) has been subtracted (see Fig. 1.2). The lack of fluctuations for regions separated by more than a few degrees which should have never been in causal contact in the history of the Universe was very puzzling at the time, i.e. the horizon problem. However, *COBE* DMR finally detected $\simeq 10^{-5}$ fluctuations in the temperature field, i.e. rms fluctuations on 10° scales $\simeq 30$ μK. The fluctuations are consistent with a Gaussian distribution and the Harrison-Zel'dovich scale-invariant spectrum, i.e. $n = 1$ (see later), predicted by inflationary models (Smoot et al., 1992). The discovery of the CMB near-isotropy or rather the small anisotropy has been regarded as the important milestone in modern cos-

the hydrogen and helium atoms begin to form and the number of charged particles drastically reduced leading to a decoupling of the photon-baryon fluid (Peebles, 1968; Zel'Dovich et al., 1969; Seager et al., 2000)

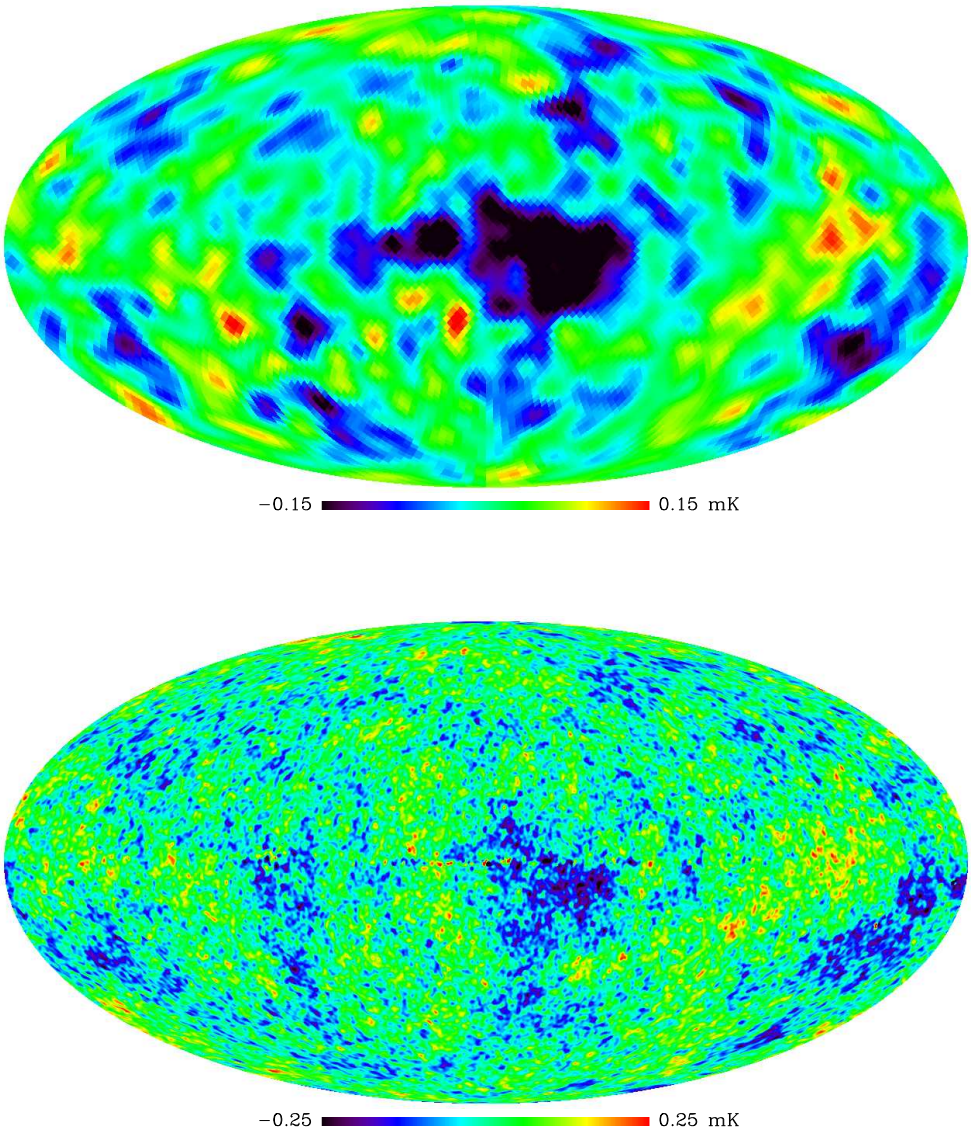

Figure 1.2: The full-sky CMB temperature fluctuation maps constructed from the four-year *COBE* DMR (Bennett et al., 1996) (top) and seven-year *WMAP* (Jarosik et al., 2011) (bottom) observations. Each map has been appropriately smoothed according to the survey angular resolution. Both maps are foreground-reduced using linear combination technique (Bennett et al., 1992; Gold et al., 2011). The foreground-reduced data used in making the plots are publicly available at `http://lambda.gsfc.nasa.gov`.

mology since the discovery of the CMB itself. The importance of CMB anisotropy lies in the fact that these features (see Hu and Dodelson, 2002, for a pedagogical review of CMB anisotropy) are associated with the density perturbation believed to give rise to the structures we see today and are still free from nonlinear evolution (see below). Therefore by studying the CMB fluctuations we can learn about the origin, evolution and nature of the density perturbation and hence improve our understanding of cosmology.

The CMB anisotropy has since become the main arena for 'precision cosmology'. Although there were some ground-based and balloon-borne experiments, e.g. BOOMERanG (Mauskopf et al., 2000), MAXIMA (Hanany et al., 2000), it had taken almost another decade until another space-based mission with an improved sensitivity and angular resolution was launched. The *Wilkinson Microwave Anisotropy Probe* (*WMAP*; Bennett et al., 2003a) has measured the full-sky CMB temperature maps (Fig. 1.2) with 33 times the angular resolution and 45 times the sensitivity of the *COBE* DMR experiment. The $\simeq 10^{-5}$ fluctuations in the CMB temperature field has been confirmed over a wide range of angular scales (e.g. Bennett et al., 2003b; Jarosik et al., 2011).

1.3.1 The CMB angular power spectrum

To exploit the full potential of the current CMB data such as the *WMAP*, a full-sky temperature map typically contains in excess of a million pixels. Thus it is much more efficient to study the CMB anisotropy using statistical tool such as the temperature two-point function. For the fluctuations which are believed to possess a Gaussian distribution[6] due to its primordial quantum mechanical origin, all the informations can be extracted using the two-point function. Most CMB analyses use the angular power spectrum, C_ℓ, as a tool to study the CMB anisotropy which can be directly (once all the observational effects, e.g. beam, mask etc., have been taken into consideration) compared with theoretical expectations. The theoretical models can be computed effectively using well-tested publicly-available codes such as CMBFAST (Seljak and Zaldarriaga, 1996) and CAMB (Lewis et al., 2000).

The temperature fluctuations, $\delta_T(\hat{\mathbf{n}})$, on the sky can be written as a spherical harmonic expansion,

$$\delta_T(\hat{\mathbf{n}}) \equiv \frac{\Delta T(\hat{\mathbf{n}})}{T_0} = \sum_{\ell=2}^{\infty} \sum_{m=-\ell}^{m=+\ell} a_{\ell m} Y_{\ell m}(\hat{\mathbf{n}}), \tag{1.14}$$

[6]This has been shown to be accurate to the 0.1 per cent level by Komatsu et al. (2009)

where $a_{\ell m}$ is a complex coefficient for each spherical harmonic $Y_{\ell m}(\hat{\mathbf{n}})$ mode. The monopole moment ($\ell = 0$) of the temperature field corresponds to the mean temperature of the CMB, T_0, which has been determined to a great accuracy by the *COBE* FIRAS mission (see above). It is, however, not measured by differential experiments such as the *COBE* DMR and *WMAP* missions and in terms of the fluctuations the monopole corresponds to a zero-point of the temperature map. It is therefore omitted in the anisotropy study and the above equation. The dipole moment ($\ell = 1$) is the most dominant component in the anisotropy field with amplitude 3.355 ± 0.008 mK measured using the seven-year *WMAP* observations (Jarosik et al., 2011). This is caused by the Doppler shift arising from our motion relative to the near-isotropic CMB field towards $(l,\ b)$=(263.°99$\pm$0.°14, 48.°26$\pm$0.°03). The dipole is usually not included in the anisotropy study due to its non-cosmological origin and its contribution is subtracted from the temperature fluctuations field.

The angular power spectrum is then given by

$$C_\ell = \frac{1}{2\ell + 1} \sum_m |a_{\ell m}|^2 \tag{1.15}$$

The number of modes available for averaging each multipole moment ℓ is $2\ell + 1$. This leads to a sampling uncertainty at low ℓ known as 'cosmic variance'. And at small scales, large ℓ, the measurements is limited by the instrument noise which starts to dominate at the survey resolution. If the noise is Gaussian and its spectrum is known, the statistical uncertainty in measuring C_ℓ can be given by

$$\Delta C_\ell = \sqrt{\frac{2}{f_{\rm sky}(2\ell + 1)}} \left(C_\ell^{\rm CMB} + C_\ell^{\rm noise}\right), \tag{1.16}$$

where $f_{\rm sky}$ accounts for an incomplete sky which results from an exclusion of regions with Galactic and extra-galactic contaminations. The incomplete sky also causes different ℓ modes to become correlated and the estimated C_ℓ will need to be corrected (e.g. Hinshaw et al., 2003b; Chon et al., 2004).

In practice, the $a_{\ell m}$ coefficients are evaluated using fast spherical transforms. The $\widetilde{C}_\ell$ is then estimated from the sum given in Eq. 1.15. This method is referred to as a 'pseudo-C_ℓ' estimator (Peebles, 1974; Hivon et al., 2002). A more elaborate method called 'maximum-likelihood' estimator (Hamilton, 1997; Tegmark, 1997; Bond, Jaffe, and Knox, 1998) is regarded as more optimal, i.e. more accurate, than the former (see Efstathiou, 2004, for a review on the estimation of power spectra). As the name suggests, the method estimates a power spectrum by maximising the likelihood function given the data. This

generally requires $\mathcal{O}(N_d^3)$ operations for N_d data points and for $N_d \sim 10^6 - 10^7$ the method becomes computationally impractical. Efstathiou (2004) proposed a 'hybrid estimator' where a maximum-likelihood method is employed for small ℓ's while at large ℓ's a pseudo-C_ℓ can be used. The author argued that the combination leads to a computationally fast, and yet accurate and nearly optimal estimator over the full range of multipoles. In fact this is the method utilised by the *WMAP* team to analyse their data (e.g. Hinshaw et al., 2007; Nolta et al., 2009).

1.3.2 Measurements and cosmological implication

One of the main features in the CMB angular power spectrum is a series of 'Acoustic peaks'. The coupling between the photon and the baryon (plasma) fluid (Peebles and Yu, 1970) prior to the recombination leads to acoustic waves which appear as a spatial inhomogeneity in the CMB we see today. The oscillations are caused by the gravitational collapse of the baryons due to the initial perturbations while the radiation pressure acts as a restoring force. The temperature fluctuations correspond to the hotter or cooler regions where the coupled fluid are compressed or rarefied. At the recombination, the oscillating pattern are frozen and modes which are at maxima or minima are imprinted in the CMB as a harmonic series of peaks in its angular power spectrum.

The peak spacing is set by $\ell_a = \pi D_A(z_*)/s_*$, where s_* is the sound horizon, the distance sound can travel before recombination. Since the sound horizon can be confidently determined (e.g. Hu and Dodelson, 2002), the acoustic peaks scales can be used as a set of standard rulers to constrain cosmological parameters. The position of the first peak, in particular, is sensitive to spatial curvature of the Universe via a geometrical projection. The measurement, however, suffers from degeneracy with the Hubble constant H_0 and requires H_0 to be measured from other experiments (see Fig. 1.3). The relative amplitudes of the peaks also depend on the background cosmology, for example by increasing baryon density the odd peaks are enhanced relative to even ones. This is because the odd peaks correspond to the maximally compressed mode at the recombination whereas the opposite is true for the latter and the 'rebound' has to work against the baryon inertia.

The measurements from high resolution CMB experiments such as BOOMERanG, MAXIMA and *WMAP* have detected the acoustic peaks in the angular power spectra out to $\ell \sim 800$. The position of the first peak has been detected at $\ell \simeq 200$ which is consistent with a spatially flat Universe (e.g. de Bernardis et al., 2000; Jaffe et al., 2001; Spergel et al., 2003; Larson et al., 2011). As mentioned above the curvature measure-

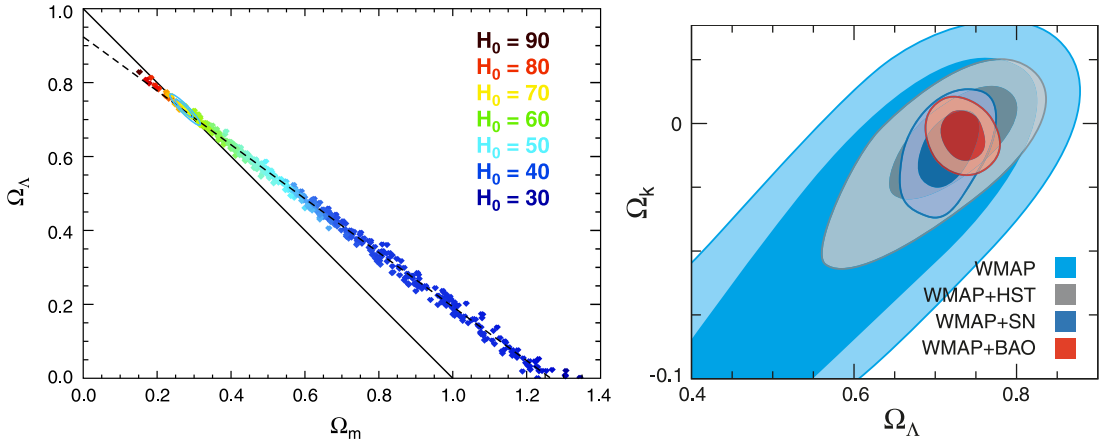

Figure 1.3: (left) Constraints on the cosmological parameters from *WMAP* data alone. The closed model, i.e. $\Omega_K < 0$, cannot be ruled out if the low H_0 values are allowed, due to geometric degeneracy. However, when combining with other observations the Universe is very close to being spatially flat (small error ellipse on $\Omega_{\rm tot} = 1$ line). Figure credit: Larson et al. (2011). (right) The constraints on cosmological parameters from combining the latest *WMAP*, HST, BAO and SNIa data. Figure adapted from Komatsu et al. (2009)

ment has a degeneracy with H_0. This is demonstrated by the left panel of Fig. 1.3 for the seven-year *WMAP* observations (Larson et al., 2011). If a flat prior on the curvature parameter is set, the best-fit is $H_0 = 53^{+13}_{-15}$ km s^{-1} Mpc^{-1}. However, when combined with other dataset, H_0, BAO and SNIa, the constraint on $\Omega_{\rm tot}$ becomes much stronger and closer to 1. The best-fit baryon density, $\omega_b \equiv \Omega_b h^2$, is $\simeq 0.022$ in good agreement with the observations of light element abundances (Copi et al., 1995) and the Big-Bang nucleosynthesis (although see Steigman 2006 and Fields and Sarkar 2010 for a more recent review).

The measurements from large-scale structure (LSS) (e.g. Tegmark et al., 2004; Cole et al., 2005; Eisenstein et al., 2005) are consistent with matter density $\Omega_{m,0} \simeq 0.27$ where ~ 80 per cent of the matter is non-baryonic dark matter called 'Cold Dark Matter' (CDM). These provide a compelling argument for the existence of some unknown form of energy termed 'Dark Energy' (DE) with $\Omega_{\rm DE,0} \simeq 0.73$ required to obtain the critical density. The SNIa measurements (e.g. Riess et al., 1998; Perlmutter et al., 1999) have provide geometrically inferred evidence that the Universe is currently in the accelerated expansion phase. This then suggest that the DE equation of state w has to be lower than -1/3. In fact, most observations suggest that $w_{\rm DE} \simeq -1$ and so far no time-dependence has been detected (e.g. Filippenko, 2004; Riess et al., 2007; Percival et al., 2010; Komatsu et al., 2011), i.e.

consistent with cosmological constant Λ. This emerging 'Standard Cosmological Model' is also known as the flat ΛCDM model. Although the model has been remarkably successful in explaining many independent observations, it also contains several fundamental and astrophysical problems (e.g. Weinberg, 1989; Carroll, 2001; Shanks, 2005). This is discussed in more detail below.

1.3.3 The Integrated Sachs-Wolfe effect

The secondary anisotropy which arises from the interaction between the CMB photons with the intervening gravitational potential is called the 'Integrated Sachs-Wolfe' (ISW) effect (Sachs and Wolfe, 1967). As the CMB photons traverse through the time-varying gravitational potential, the associated temperature perturbation is given by

$$\delta_T^{\rm ISW}(\hat{\mathbf{n}}) \equiv \frac{\Delta_T^{\rm ISW}(\hat{\mathbf{n}})}{T_0} = -2\int_0^{z_*} dz\ \frac{1}{c^2}\frac{\partial\Phi}{\partial z}(\hat{\mathbf{n}}, z) \tag{1.17}$$

where Φ is the gravitational potential which is related to the matter density fluctuation, $\delta \equiv \delta\rho/\bar{\rho}$, via Poisson equation,

$$\nabla^2\Phi(\hat{\mathbf{n}}, z) = 4\pi G a^2 \rho_m(z)\, \delta(\hat{\mathbf{n}}, z) \tag{1.18}$$

The ISW temperature anisotropy in the direction $\hat{\mathbf{n}}$ on the sky is the sum of all temperature changes $\propto \partial\left[\delta(\hat{\mathbf{n}}, z)/a\right]/\partial z$ along the line of sight from the surface of last scattering. In the linear regime ($\delta \ll 1$), the perturbations grow independently of their comoving spatial scale (e.g. Peebles, 1980), i.e. $\delta(\hat{\mathbf{n}}, z) = D(z)\delta(\hat{\mathbf{n}}, 0)$ where $D(z)$ is the linear growth factor (see later) and therefore

$$\delta_T^{\rm ISW}(z) \propto \frac{d}{dz}\left[\frac{D(z)}{a}\right] \tag{1.19}$$

For a spatially flat Universe with $\Omega_m = 1$, $D(z)$ is equal to $a(z)$ hence the temperature anisotropy due to the ISW effect is expected to be zero. This is because the Universe expands as fast as the perturbations grow and the energy gained by a CMB photon when entering the gravitational well is exactly cancelled by the work done in climbing out at later time. However, in a Universe which is dominated by Λ, the accelerated expansion means that the potential decays much faster than the structure growth and the photon end up with a temperature boost as it leaves the potential well. The detection of the ISW effect would provide a direct dynamical evidence for the accelerated expansion of the Universe unlike the geometrical inference of the SNIa measurements. Unfortunately,

the ISW contribution is only $\lesssim 10$ per cent of the primary anisotropy for $\ell \gtrsim 10$ due to the projection effect (Hu and Dodelson, 2002) and the C_ℓ measurements suffer from cosmic variance at low ℓ's (Eq. 1.16). Crittenden and Turok (1996) proposed that the ISW effect can be studied by cross-correlating the CMB to the foreground large-scale structure tracer instead. Previous attempts to detect the ISW effect are discussed in Chapter 3 as well as the detailed theoretical prediction for a CMB-LSS cross-correlation analysis.

1.4 Large-Scale Structures

Unlike the CMB, the local large-scale structures (LSS), e.g. galaxies, groups and clusters of galaxies, are observed to be very clumpy (see Fig. 1.4). This stark contrast can be reconciled in the framework of 'gravitational instability' where the density fluctuations can grow in time provided that the stabilising pressure caused by the collapse is negligible (e.g. Silk, 1968; Peebles and Yu, 1970). The condition can easily be satisfied once the matter becomes dominant ($z_{\rm eq} \simeq 3200$) and especially after the epoch of recombination ($z_* \simeq 1100$). The initial perturbations responsible for the CMB temperature fluctuations are the overdense seeds needed for the formation of self-gravitating regions which further accrete more matter and thus becoming even denser. This then results in the instability which lead to a gravitational collapse of an initially perturbed region to a gravitationally bound objects.

The Cold Dark Matter (CDM) is now believed to be the key ingredient for structure formation. The argument for the existence of the CDM which dominates the matter content needed to grow the inhomogeneity in the LSS observed today was made by a number of authors, e.g. Blumenthal et al. (1982); Peebles (1982). As the BBN predicts the baryon density to be far too low to grow the density fluctuation over $\sim 10^4$ (as given by the upper limits on CMB fluctuations at the time) from the end of recombination to now. The presence of dark matter was originally postulated by Zwicky (1937) to explain the 'missing mass' problem in the rotation curve of galaxies in clusters if Newtonian gravity theory is assumed to hold on such scales. The emerging 'standard' CDM (SCDM) model (Davis et al., 1985; White et al., 1987) assumes a flat Universe with $\Omega_{m,0} = 1$ and $h = 0.5$. In the early 1990s, the measurements of galaxy clustering (e.g. Maddox et al., 1990; Efstathiou et al., 1990a) found that the model under-predicts large-scale amplitudes. The attempts to 'resuscitate' the SCDM model ranging from lowering the primordial spectral index and the Hubble constant to $n \simeq 0.8 - 0.9$ and $h \simeq 0.4 - 0.45$

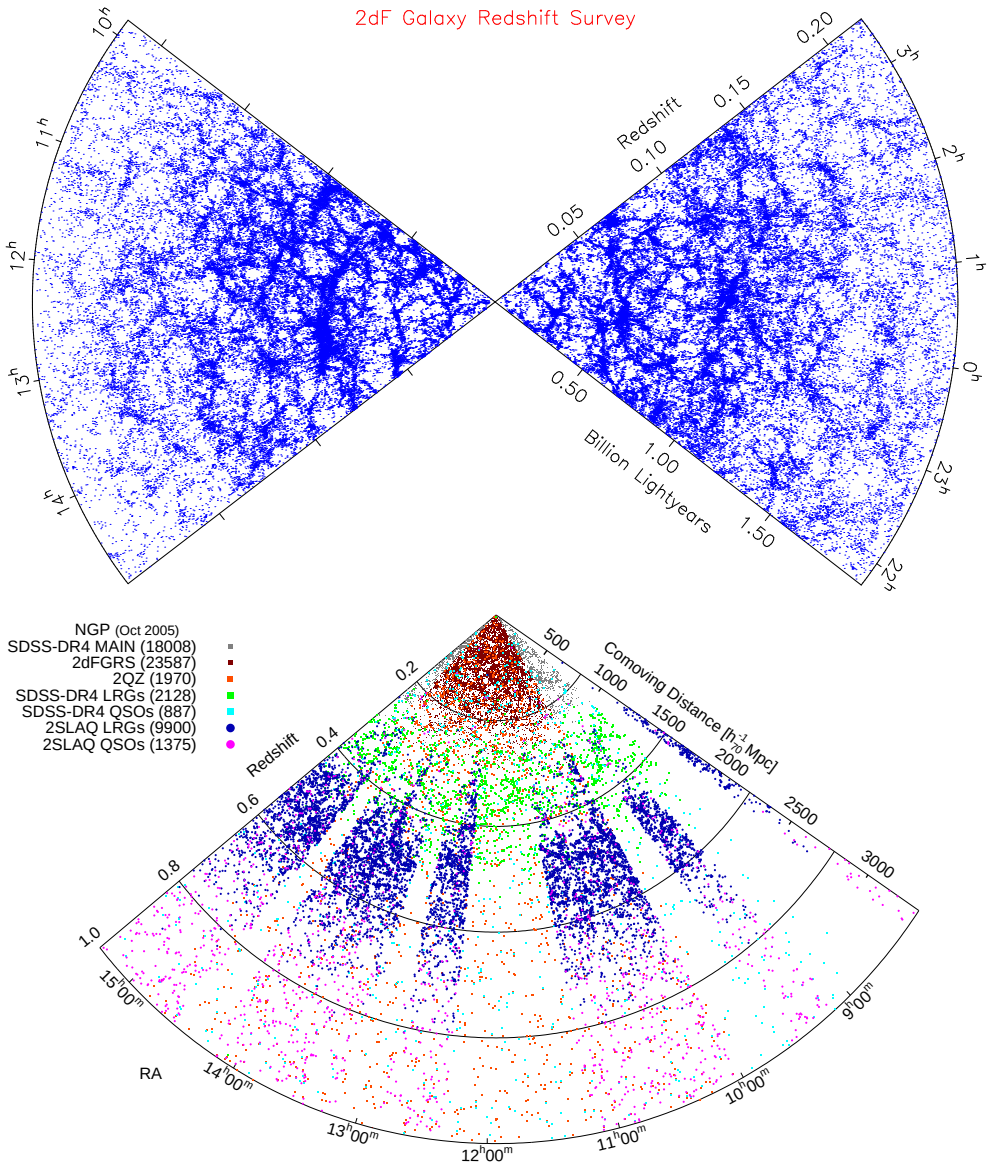

Figure 1.4: The galaxies distribution from various redshift surveys, illustrating the large-scale structure of the Universe. (top) the 2dFGRS targetting galaxies brighter than $b_J = 19.45$. Credit: the 2dFGRS collaboration (Colless et al., 2001). (bottom) Compilation of various redshift surveys targeting different classes of objects, galaxies, LRGs and QSOs, out to $z = 1$ in the Northern Galactic Cap. Credit: Peter Weilbacher for the 2SLAQ collaboration.

(White et al., 1995) to reducing the matter density $\Omega_{m,0} \simeq 0.3$, i.e. shape parameter $\Gamma \simeq 0.2$, and are thus called the 'open' CDM (OCDM) model. Given our historical hindsight, the solution proposed by Efstathiou et al. (1990b) who argued that the spatial geometry of the Universe should remain flat by having extra energy density in the form of cosmological constant with $\Omega_\Lambda \simeq 0.7$ closely corresponds to the modern cosmological paradigm, i.e. the ΛCDM model.

In the standard ΛCDM model, the initial perturbations are assumed to follow a Gaussian random field which originated from quantum mechanical fluctuations in the hot, dense, early Universe. The period of rapid expansion called 'Inflation' (Guth, 1981) amplifies these primordial infinitesimal fluctuations to physical scales. Most inflation models predict the fluctuations to have a scale-invariant Harrison-Zel'dovich spectrum, i.e. $P(k) \propto k^n$ with spectral index[7] $n = 1$ and $k = 2\pi/r$ is the comoving wavenumber. At later time, the primordial power spectrum is modified by the growth of structures. In the Linear Theory framework, the power spectrum at present epoch is given by

$$P(k, z = 0) = Ak^n T^2(k), \tag{1.20}$$

where $T(k)$ is the transfer function which can be determined for the different components of the cosmic fluid using fitting formulae or solving Einstein-Boltzmann equation (e.g. Seljak and Zaldarriaga, 1996; Eisenstein and Hu, 1998; Lewis et al., 2000). The amplitude A is a normalisation factor conventionally determined by setting the rms density fluctuation within a sphere of radius 8 h^{-1} Mpc, σ_8, to the value constrained by observations,

$$\sigma_8^2 = \frac{1}{2\pi^2} \int_0^\infty k^2 P(k) w(kr)^2 dk, \tag{1.21}$$

where $w(kr)$ is the window function, given by (e.g. Peebles, 1980)

$$w(kr) = 3\frac{\sin(kr) - kr\cos(kr)}{(kr)^3}, \tag{1.22}$$

for a spherical top-hat function and $r = 8\ h^{-1}$ Mpc. The linear power spectrum at any intermediate redshift z is given by $P(k, z) = D^2(z)P(k, 0)$, where $D(z)$ is the linear growth factor which can be computed from an approximation formula given by Carroll et al. (1992).

[7] Current constraint from CMB observations on the spectral index is $n \simeq 0.95 - 0.96$ (e.g. Larson et al., 2011).

The density fluctuations grow linearly, $\delta(z) = D(z)\delta_0$, until $\delta \gtrsim 1$, i.e. non-linear regime, the self-gravitating regions (see above) then collapse once the fluctuation reach the critical overdensity ($\delta_c \equiv 1.686$ for spherical collapse). The collapse continues until it reaches virial equilibrium. The virialised structures are called 'haloes' of dark matter and their distribution function is generally described by Press-Schechter theory (Press and Schechter, 1974). These haloes provide potential wells for gas (baryon) to form stars and galaxies. The haloes then grow hierarchically via merging (e.g. Lacey and Cole, 1993). The galaxies residing in the merged haloes are also expected to merge with one another and thus building up more massive galaxies as the time past. However, the real situation may be more complicated than this simple picture (see later). Therefore one can learn about the matter distribution by using galaxies as a biased tracer of LSS via galaxy clustering. Their clustering evolution is also used as a tool to study galaxy evolutionary models in conjunction with other tools such as the galaxy Luminosity Function (LF; Schechter 1976).

1.4.1 Galaxy clustering

The commonly used statistical tool for studying galaxy clustering is the two-point function. In the Gaussian random field, the second moment, i.e. variance, contains all the information of that fluctuation field. This is of course the same argument made in §1.3.1 for the CMB angular power spectrum. Unlike the CMB observation where one only looks at the surface of last scattering, the galaxy distributions can be obtained in three-dimension (see Fig. 1.4). Their distances away from us are usually determined by a redshift survey, where one either targets certain classes of objects, e.g. Luminous Red Galaxy (LRG; Eisenstein et al. 2001; Cannon et al. 2006; Ross et al. 2008b), Quasi-Stellar Object (QSO; Shanks et al. 2000; Croom et al. 2009), Emission-Line Galaxy (ELG; Drinkwater et al. 2010), Lyman-Break Galaxy (LBG; Bielby et al. 2011), or all the galaxy populations with apparent magnitude brighter than certain limit (York et al., 2000; Colless et al., 2001).

The power spectrum, $P(k)$, has been mentioned above to explain the growth of density perturbation without giving the definition. Here, it is given in terms of the density fluctuations observed in the galaxy distributions. The galaxies are not exact tracers of large-scale structure. This is indicated by the luminosity dependence (e.g. Norberg et al., 2002b; Zehavi et al., 2005b) and different clustering for different types of galaxies. In fact, galaxies are said to be a 'bias' tracer of the matter distribution. In the linear regime, i.e. large scales and $\delta \ll 1$, the bias factor is approximately scale-independent and one

can relate the observed galaxy number density, $\delta_g \equiv n_g/\bar{n}_g - 1$, to the underlying matter fluctuations as

$$\delta_g(\mathbf{x}) = b\,\delta_m(\mathbf{x}), \tag{1.23}$$

where b is the linear bias factor and $\mathbf{x}$ is the comoving coordinate in the density field. It is sometimes more convenient to compare the measurements made in Fourier space to the linear theory prediction. The spatial density fluctuations can be Fourier transformed,

$$\delta(\mathbf{k}) = \int \delta(\mathbf{x})\,\exp(i\mathbf{k}\cdot\mathbf{x})\,d^3x, \tag{1.24}$$

where $\mathbf{k}$ is the comoving wavevector of a given Fourier mode. The power spectrum is then given by

$$\langle\delta(\mathbf{k})\,\delta(\mathbf{k}')\rangle \equiv (2\pi)^3\,\delta_{\rm Dirac}(\mathbf{k}-\mathbf{k}')\,P(k), \tag{1.25}$$

where $\delta_{\rm Dirac}$ is the Dirac-δ function and $k = |\mathbf{k}|$. The correlation function $\xi(r)$ is also widely used to study the clustering in configuration space and is defined such that

$$\xi(r) \equiv \langle\delta(\mathbf{x})\delta(\mathbf{x}+\mathbf{r})\rangle \tag{1.26}$$

where $r = |\mathbf{r}|$ is a comoving separation between any two regions in the density field. In other words, power spectrum and correlation function are Fourier transforms of each other,

$$\xi(r) = \frac{1}{(2\pi)^3}\int P(k)\exp(-i\mathbf{k}\cdot\mathbf{r})\,d^3k, \tag{1.27}$$

and r is related to the wavenumber k by $r = 2\pi/k$. For a homogeneous and isotropic density field the equation can be reduced to (e.g. Lahav and Suto, 2004)

$$\xi(r) = \frac{1}{2\pi^2}\int P(k)k^2\frac{\sin kr}{kr}\,dk. \tag{1.28}$$

In practice, the correlation function is estimated by counting the numbers of galaxy pairs separated by a given distance relative to a set of uniformly distributed random samples. The random sample or 'random catalogue' is constructed such that its spatial selection function mimics the real data except the clustering information. Various estimators have been proposed including a commonly used 'minimum-variance' estimator proposed by Landy and Szalay (1993). In Chapter 2, the choice of estimators is discussed

in more detail. If redshift information for individual galaxy is not available, the angular correlation function, $w(\theta)$, can be measured instead. The $\xi(r)$ can be inferred if the redshift distribution of the galaxy sample is known (see Chapter 2).

The galaxy correlation function is related to the matter correlation via the linear bias factor such that $\xi_g(r) = b^2\,\xi_m(r)$. Measurements of galaxy $\xi(r)$ have found that for $0.1 \lesssim r \lesssim 10\ h^{-1}\,\mathrm{Mpc}$ the real-space[8] correlation function can be described by a power-law $\xi(r) = (r/r_0)^{-\gamma}$ where $r_0 \simeq 5 - 6\ h^{-1}\,\mathrm{Mpc}$ is the correlation length of galaxy clustering and $\gamma \simeq 1.7 - 1.8$ (e.g. Shanks et al., 1989; Zehavi et al., 2002; Hawkins et al., 2003). Beyond $r \simeq 10 - 15\ h^{-1}\,\mathrm{Mpc}$ the correlation function has a much steeper slope and quickly goes to zero. The scale-independent linear bias is a good approximation down to $r \sim 3\ h^{-1}\,\mathrm{Mpc}$, i.e. the $\xi_g(r)$ appears to have the same shape as $\xi_m(r)$. However at small scales, the naive linear bias assumption is not sufficient to explain the relation between $\xi_g(r)$ and $\xi_m(r)$ as the galaxies are more likely to trace the clustering of dark matter haloes at the quasi-linear regime. In the non-linear regime, N-body simulations have been used to calibrate a formula to compute non-linear power spectra from linear $P(k)$ given a background cosmology (Smith et al., 2003).

Another approach for describing the galaxy bias at quasi- and non-linear scales is through the 'Halo Occupation Distribution' (HOD) model (see Cooray and Sheth, 2002, for a review). Recently, the formalism became very popular and is now almost a standard way of analysing galaxy correlation function. The measurements are normally fitted to a HOD model with certain ways of parametrising the numbers of galaxies a dark matter halo can host as a function of its mass. The galaxies within a halo are usually distinguished into central and satellite galaxies. The satellite galaxies are distributed in a halo according to the halo profile. The correlation function at small scales is dominated by the galaxy pairs within the same halo whereas at large scales it corresponds to galaxy pairs in two separate haloes. The HOD parameters that best describe the $\xi(r)$ measurements can be used to make predictions (either via N-body simulations or analytic approach) which can be compared to, for example, the clustering of similar type of objects at a later time and therefore provides an insight into the galaxy evolution (e.g. White et al., 2007; Seo et al., 2008; Wake et al., 2008).

[8] As opposed to the redshift-space correlation function $\xi(s)$ where the slope at small scales is flattened due to random peculiar motion and large-scale clustering amplitude is boosted due to the structure coherent infall (e.g. Hawkins et al., 2003; Ross et al., 2007).

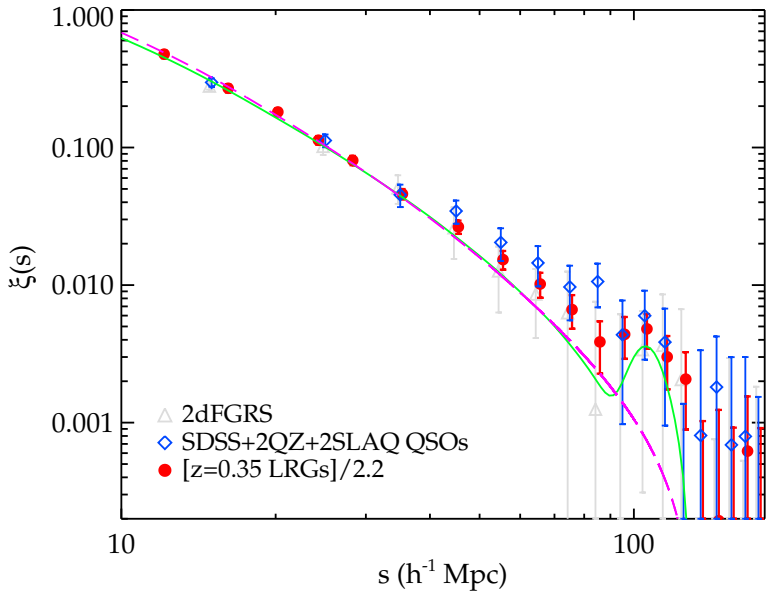

Figure 1.5: The correlation function $\xi(s)$ measured from the 2dFGRS galaxy catalogue (Colless et al., 2001), $\bar{z} \simeq 0.35$ LRG (Eisenstein et al., 2005) and the combined QSO sample at $\bar{z} \simeq 1.5$ (Sawangwit et al., 2011b). The amplitude of the $\bar{z} \simeq 0.35$ LRG measurement is lowered by a factor of 2.2 to match the linear theory prediction for the combined QSO sample at the intermediate scales. The solid line is the standard ΛCDM model with $(\Omega_m, \Omega_\Lambda)$=(0.27,0.73), $h = 0.7$, $f_{\rm baryon} = 0.167$ and $n = 0.95$. The dashed line is the 'no-wiggle' version of the model (Eisenstein and Hu, 1998).

1.4.2 Baryon Acoustic Oscillations

One of the most interesting features in the large-scale distribution of LSS is the 'Baryon Acoustic Oscillations' (BAO). The same physics that gives rise to the acoustic peaks in the CMB power spectrum is also responsible for the BAO in the matter distribution. In a correlation function the series of peaks appear as a single BAO *bump* at the sound horizon scale, $\simeq 105\ h^{-1}$ Mpc, due to the excess clustering caused by the perturbation ripples (solid line in Fig. 1.5). However, the level of the BAO bump in the background matter density field is expected to be very small in the LSS. This is because after the photon-baryon decoupling the baryons can freely follow the dark matter perturbations which are very smooth on large scales so the BAO ripples are smeared by the dominant dark matter field (e.g. Eisenstein and Hu, 1998).

The BAO scales can be used as a standard ruler to measure the matter-energy content of the Universe as well as the dark energy equation of state (e.g. Blake and Glazebrook,

2003). The first clear detection of the BAO bump was made by Eisenstein et al. (2005) by measuring the correlation function of $\bar{z} \simeq 0.35$ LRG (Fig. 1.5) observed by the Sloan Digital Sky Survey (SDSS) survey. And it has been confirmed by different groups of authors using later SDSS dataset. Current measurements are in good agreement with a low matter density Universe, $\Omega_{m,0} \approx 0.27$ and only $\approx 15 - 20$ per cent of which is in the form of ordinary matter (e.g. Eisenstein et al., 2005; Percival et al., 2010). An example of cosmological parameter constraints from combining BAO measurement with the *WMAP* observations is given in the right panel of Fig. 1.3.

1.5 Problems with the ΛCDM paradigm

The impressive apparent agreement of many cosmological observations (as outlined above) leads to the so-called 'concordance model'. Dictated by the terms given to its dominant constituents, the model is called 'flat ΛCDM model'. The model can be minimally described by six parameters, namely physical dark matter density ($\Omega_c h^2$), physical baryon density ($\Omega_b h^2$), dark energy density (Ω_Λ), scalar spectral index (n_s), curvature fluctuation amplitude (Δ^2_R) and reionization optical depth (τ) (e.g. Spergel et al., 2003; Komatsu et al., 2011).

However, the model has several fundamental and astrophysical problems (e.g. Shanks, 2005, and references therein). Firstly, the model heavily relies on two pieces of undiscovered physics, i.e. the Λ and the CDM. The latter is sometimes viewed as an extension of the standard model of particle physics however the weakly interacting massive particle candidates are yet to be directly detected in the laboratory or elsewhere (Aprile et al., 2010). The problem with cosmological constant is twofold; a) the *fine-tuning* problem where its extreme smallness requires that the observed ρ_Λ is 1 part in 10^{120} of the vacuum energy expected from quantum zero-point energy and yet non-zero (e.g. Weinberg, 1989; Copeland et al., 2006) and b) the *cosmic coincidence* problem, i.e. why this astonishingly small vacuum energy starts to dominate at almost the same time we happen to be observing. The explanation for these problems often resorts to the anthropic principle (e.g. Efstathiou, 1995; Susskind, 2003; Peacock, 2007), even then the counter arguments can often be made against such an approach (e.g. Tegmark and Rees, 1998; Starkman and Trotta, 2006; Mersini-Houghton and Adams, 2008). To many cosmologists, the anthropic reasoning is scientifically unsatisfactory. Other solutions proposed to solve the late-time accelerated expansion problem ranges from a hypothetical time-dependent

and spatially inhomogeneous energy field called 'Quintessence' (e.g. Caldwell, Dave, and Steinhardt, 1998) to models based on a large-distance modification of gravity whether it be a braneworld model (e.g. DGP model; Dvali, Gabadadze, and Porrati, 2000) or an $f(R)$ gravity model (e.g. Carroll et al., 2004), and the possibility of a 'backreaction' of the cosmological perturbation due to the homogeneity assumption in the FRW metric (e.g. Kolb et al., 2006). Apparently, none of these proposed models is as successful as the flat ΛCDM model.

There are also several astrophysical problems faced by the model which are mostly related to the hierarchical galaxy formation in the CDM framework. For example, the predicted CDM profile is too cuspy to explain the rotation curves of the dark matter dominated galaxies, i.e. low surface brightness galaxies (Moore et al., 1999b). The well-known 'missing satellites problem' is another example where the model (via high resolution N-body simulation; e.g. Moore et al. 1999a; Springel et al. 2008) produces too many dark matter substructures in galactic sized haloes as well as too high maximum circular velocities than the observations expected in the Local Group (e.g. Klypin et al., 1999; Martin et al., 2008; Watkins et al., 2009). These first two problems may in fact be related through the true nature of dark matter. Recently, it has been suggested by Lovell et al. (2011) that if the dark matter is warm rather than cold then these problems can be alleviated as the power at high wavenumbers is significantly reduced due to free streaming. The bright end of galaxy luminosity function shows a sharp 'knee' feature and a flat slope at faint end (e.g. Blanton et al., 2001; Norberg et al., 2002a) whereas hierarchical galaxy formation predicts a near power-law mass function (Benson et al., 2003). To reconcile with the observations, 'feedback' processes (supernova feedback for faint end and AGN feedback for bright end) needed to suppress star formation are introduced in the semi-analytic model (e.g. Bower et al., 2006). However, the real question is whether the amount of energy needed in these feedback processes can be realistically met. Another example worth mentioning is the galaxy 'downsizing problem' where the CDM model predicts that the most massive systems form last, i.e. the most massive galaxies are expected to grow rapidly via mergers after $z \approx 1$ (e.g. De Lucia et al., 2006). However, observationally, the most massive galaxies appear old and the bulk of recent star formation have taken place only in the intermediate mass galaxies (e.g. Cowie et al., 1996; Kodama et al., 2004). To reconcile with observations, the massive galaxies have to accumulate their masses via 'dry' merging of gas-poor systems where no new significant star formation is allowed to happen in order for them to appear old. Furthermore, the AGN feedback is still needed

to prevent further gas cooling and star formation in these massive haloes as mentioned above.

There are also observational results which are at odds with the current cosmological paradigm. For example, the strong lensing of the background faint QSOs in the 2dF QSO redshift survey (2QZ) by foreground galaxies, groups and clusters of galaxies implied a high $\Omega_{\rm m}$ and/or strong anti-bias than the ΛCDM model suggests (Croom and Shanks 1999; Myers et al. 2003, 2005; Guimarães et al. 2005; Mountrichas and Shanks 2007). The similar strong lensing signal has also been observed in an independent spectroscopic bright QSO sample, the Hamburg-ESO Survey, by Nollenberg and Williams (2005). However, note that an analysis of a photometric QSO sample from the SDSS by Scranton et al. (2005) has suggested that the lensing result may be compatible with the standard ΛCDM prediction when analysed in conjunction with the HOD framework. More examples of the observational evidence which indicate that Ω_m may be higher than 0.3 are reviewed by Shanks (2005).

It may be fair to say that most of the astrophysics problems discussed above arise from our incomplete understanding of complex gas physics in galaxy formations. By tackling these issues we would develop a more complete picture of the subject and it is likely that some of the issues can be addressed by a more complicated galaxy formations model (see Baugh, 2006, for a review). However, the fundamental problems highlighted earlier are the most serious and one should balance the successes of the standard cosmological model against these problems. It is therefore scientifically prudent that we continue to confront the standard model with new observations and re-tests of the old ones.

1.6 This thesis

In this thesis, we present results from using observational tools commonly employed in studying cosmology and galaxy evolution. These are, as outlined above, the galaxy clustering as a biased tracer of the LSS, the CMB temperature power spectrum and the CMB-LSS cross-correlation. In Chapter 2, we perform a clustering analysis of photometrically selected samples of Luminous Red Galaxy (LRG) at three different average redshifts. The sample selection functions are calibrated by spectroscopic redshift surveys where their redshift distributions are then used to infer the 3D clustering information. The samples at different redshifts where each one covers a large area and contains a large number of objects provide a unique opportunity for studying clustering evolution

of massive early-type galaxies and to search for the BAO signal. The latter can be used to inform the ongoing or upcoming photometric surveys such as the Panoramic Survey Telescope & Rapid Response System (Pan-STARRS; Chambers 2009), the Large Synoptic Survey Telescope (LSST; Ivezic et al. 2008) projects where the photometric-redshift or colour-magnitude selected LRG sample can be used as a biased tracer for the LSS and BAO studies.

In Chapter 3, we review previous claims of the detections of the ISW effect and present a new measurement using the LRG sample at $\bar{z} \sim 0.7$, the redshift where one expects the ISW signal-to-noise to be maximised (Douspis et al., 2008). The sample is also located at the redshift close to where the transition from a decelerated to an accelerated expansion is believed to occur and thus should present an interesting opportunity for a new test of the ISW effect. We then perform a robustness test on the new results as well as the previously claimed ISW detections which, as mentioned above, is very important as the direct dynamical evidence for dark energy.

In Chapter 4, we make independent estimates of the CMB temperature power spectra using publicly available data from the *WMAP* collaboration. We investigate the angular power spectrum sensitivity to the instrumental beam profiles. We then make an independent beam profile measurements using radio point sources detected by the *WMAP* team as well as the sources detected at other frequency bands made by ground-based telescopes. The robustness tests of the technique used is also presented. And the initial impact on the final *WMAP* power spectrum is then briefly investigated.

In Chapter 5, we review the effect of the *WMAP* beam asymmetry and investigate the claim of the existence of timing offset in the *WMAP* time-ordered data to see if it can produce a wider beam profile observed in Chapter 4. We construct the on-sky beam maps from the *WMAP* scan strategy and the Jupiter beam maps. To test the hypothesis, the induced timing offset is left uncorrected in the map-making process and the results are tested against the 2D stacked temperature maps around the radio point sources. Finally, Chapter 6 presents the conclusions and summarise our findings as well as the future prospects of using LSS and CMB to study and further our understanding of the Universe.

Chapter 2

LRG angular correlation functions

2.1 Introduction

The galaxy two-point function whether in its correlation function or power spectrum form has long been recognised as a powerful statistical tool for studying Large-Scale Structure (LSS) of the Universe (Peebles, 1980). In an isotropic and homogeneous Universe, if the density fluctuation arises from a Gaussian random process, the two-point correlation function, $\xi(r)$, and its Fourier transform, $P(k)$, contains a complete description of such fluctuations. It has been used to measure the clustering strength of galaxies in numerous galaxy surveys (see e.g. Groth and Peebles 1977; Shanks et al. 1989; Baugh and Efstathiou 1993; Ratcliffe et al. 1998a) and the observed $\xi(r)$ is reasonably well represented by a power-law of the form $\xi(r) = (r/r_0)^{-1.8}$ over a large range of scales, $\approx 100\ h^{-1}\,\mathrm{kpc}$ – $10\ h^{-1}\,\mathrm{Mpc}$, where r_0 is approximately $5\ h^{-1}\,\mathrm{Mpc}$.

More recently, large galaxy redshift surveys have become available (SDSS:York et al. 2000, 2dFGRS:Colless et al. 2001) and these surveys provide a perfect opportunity to exploit the two-point function as a tool to constrain cosmological parameters (Hawkins et al., 2003; Cole et al., 2005; Eisenstein et al., 2005; Tegmark et al., 2006; Percival et al., 2007) which in turn provides an excellent test for our current understanding of the Universe and the processes by which the LSS were formed.

In the past, when galaxy redshift surveys were less available, the angular correlation function, $w(\theta)$, was heavily utilised in the analysis of imaging galaxy samples. The spatial correlation function, $\xi(r)$, can be related to $w(\theta)$ via Limber's equation (Limber, 1953), alternatively $w(\theta)$ can be inverted to $\xi(r)$ using Lucy's iterative technique (Lucy 1974), both approaches providing a means to recover the 3–D clustering information numerically. Even today, galaxy imaging surveys still tend to cover a bigger area of the sky and occupy a larger volume than redshift surveys and therefore could offer a route to a more accurate

estimation of the correlation function and power spectrum (see e.g. Baugh and Efstathiou 1993). One of the disadvantages of using $w(\theta)$ is the dilution of the clustering signal from projection and hence any small-scale/sharp feature which might exist in the 3–D clustering may not be observable in $w(\theta)$.

As mentioned above, the correlation function at small to intermediate scales can be approximately described by a single power-law which also results in a power-law $w(\theta)$ but with a slope of $1 - \gamma$. However with larger sample sizes, recent analyses of galaxy distributions start to show a deviation from a simple power-law (Zehavi et al. 2005b; Phleps et al. 2006; Ross et al. 2007; Blake et al. 2008, see also Shanks et al. 1983). This poses a challenge for a physical explanation and understanding of non-linear evolution of structure formation. Several authors attempted to fit such correlation function using a halo model framework (e.g. Cooray and Sheth, 2002) invoking a transition between 1– and 2– halo terms which occurs at $\approx 1\ h^{-1}\,\mathrm{Mpc}$ where the feature is observed. This distance scale could potentially be used as a 'standard ruler' in tracking the expansion history of the Universe, provided that its physical origin is well understood and the scale can be accurately calibrated.

Another feature in the correlation function predicted by the standard ΛCDM model is the 'Baryon Acoustic Oscillations' (BAO). BAO arise from sound waves that propagated in the hot plasma of tightly coupled photons and baryons in the early Universe. As the Universe expands and temperature drops below 3000 K, photons decouple from the baryons at the so called 'epoch of recombination'. The sound speed drops dramatically and the oscillatory pattern is imprinted on the baryon distribution as well as the temperature distribution of the photons which approximately 13 billions years after the Big Bang is revealed as the acoustic oscillations in the temperature anisotropies of the CMB. The equivalent but attenuated feature exists in the clustering of matter, as baryons fall into dark matter potential wells after the recombination. In recent years, the acoustic peak scale in the LSS has been proposed as a potential 'standard ruler' (e.g. Blake and Glazebrook, 2003; Glazebrook et al., 2007; McDonald and Eisenstein, 2007) for constraining the Dark Energy equation of state ($w = p/\rho c^2$) and its evolution.

For the BAO approach to the study of Dark Energy to yield a competitive result, a large survey of several million galaxies is generally required (Blake and Glazebrook 2003; Seo and Eisenstein 2003; Parkinson et al. 2007; Angulo et al. 2008). A galaxy spectroscopic redshift survey would requires a substantial amount of time and resources. An alternative route which will enable a quicker and larger area covered is through the use

photometric redshift (photo–z hereafter) at the expense of the ability to probe the radial component directly. The photo–z errors are worse than spectroscopic redshift errors, but this can be compensated by a larger survey and deeper imaging.

The potential of the distribution of Luminous Red Galaxies (LRGs) as a powerful cosmological probe has long been appreciated (Gladders and Yee 2000; Eisenstein et al. 2001). Their intrinsically high luminosities provide us with at least two advantages, one being the ability to observe such a population out to a greater distance whilst the other is the possibility of detecting the small overdensity of the BAO in matter distribution at $\approx 100\ h^{-1}\,\mathrm{Mpc}$ owing to their high linear bias[1]. In addition, their typically uniform Spectral Energy Distributions (SEDs) allow a homogeneous sample to be selected over the volume of interest. Moreover, the strong 4000 Å break in their SEDs make them an ideal candidate for the photometric redshift route or even a colour-magnitude cut as demonstrated by the success of the target selection algorithm of three LRG spectroscopic follow-ups using SDSS imaging. In fact, the first clear detection of the BAO in the galaxy distribution came from the analysis of LRG clustering at low redshift (Eisenstein et al., 2005).

Here we shall present new measurements of the angular correlation functions determined from colour selected LRG samples. We shall show that this route provides redshift distribution, $n(z)$, widths that are close to the current photo–z accuracy, with none of the associated systematic problems. Indeed, one of our aims is to assess the efficiency of this route to BAO measurement compared to a full 3–D redshift correlation function. This possibility arises because the $n(z)$ width that we obtain is comparable to the $\approx 100\ h^{-1}\,\mathrm{Mpc}$ scale of the expected acoustic peak. It is important therefore to assess how much this 'colour-cut' route can compete with spectroscopic redshifts and indeed photometric redshifts in terms of the BAO detection efficiency.

A similar clustering analysis measuring $w(\theta)$ of LRGs with photo–z's has been carried out by Blake et al. (2008). Equipped with a higher-redshift LRG selection algorithm whose effectiveness has been tested with the new LRG spectroscopic redshift survey, VST-AAΩ *ATLAS* pilot run (Ross et al., 2008b), our approach is an improvement over Blake et al. (2008) as it probes an almost four times larger cosmic volume and we extend the analysis to large scales to search for the BAO peak.

[1]This is the well known luminosity dependant bias as shown observationally by e.g. Norberg et al. (2002b); Zehavi et al. (2005b) and is expected in hierarchical clustering cold dark matter universe (Benson et al., 2001).

Table 2.1: Summary of the properties of LRG samples used in this study.

Sample	$\bar{z}$	Number	Density ($\deg^{-2}$)	Magnitude (AB)
SDSS	0.35	106 699	$\approx$13	$17.5 \leq r_{\rm petro} < 19.5$
2SLAQ	0.55	655 775	$\approx$85	$17.5 < i_{\rm deV} < 19.8$
AAΩ	0.68	800 346	$\approx$105	$19.8 < i_{\rm deV} \leq 20.5$

The layout of this chapter is as follows. An overview of the galaxy samples used here is given in §2.2. §2.3 describes the techniques for estimating the angular correlation functions and their statistical uncertainties. We then present the correlation results in §2.4. In §2.5, the clustering evolution of these LRGs are discussed. We then investigate a possibility of the acoustic peak detection in the $w(\theta)$ from the combined sample in §2.6. We then discuss the future wide-field photo–z LRG surveys designed to study BAO in §2.6. Finally, summary and conclusions of our study are presented in §2.7.

2.2 Data

The galaxy samples used in this study were selected photometrically from SDSS DR5 (Adelman-McCarthy et al., 2007) imaging data based on three LRG spectroscopic redshift surveys with $\bar{z} \approx 0.35, 0.55$ and 0.7 (Eisenstein et al., 2001; Cannon et al., 2006; Ross et al., 2008b). In summary, these surveys utilised a crude but effective determination of photometric redshift as the strong 4000 Å feature of a typical LRG spectral energy distribution (SED) moves through SDSS $u, g, r, i,$ and z bandpasses (Fukugita et al., 1996; Smith et al., 2002). In each survey, a two-colour system (either $g-r$ versus $r-i$ or $r-i$ versus $i-z$) suitable for the desired redshift range was used in conjunction with r or i-band magnitude to select luminous intrinsically red galaxies. The method employed by these surveys has been proven to be highly effective in selecting LRGs in the target redshift range. The full selection criteria will not be repeated here but a summary of the algorithms and any additional criteria will be highlighted below (see Eisenstein et al. 2001; Cannon et al. 2006; Ross et al. 2008b for further details). Redshift distributions, $n(z)$, of the LRGs from the spectroscopic surveys utilised in this work are shown in Fig. 2.1. The LRG samples corresponding to the above $n(z)$ have been carefully selected to match our selection criteria hence these $n(z)$ will be assumed in determining the 3–D correlation

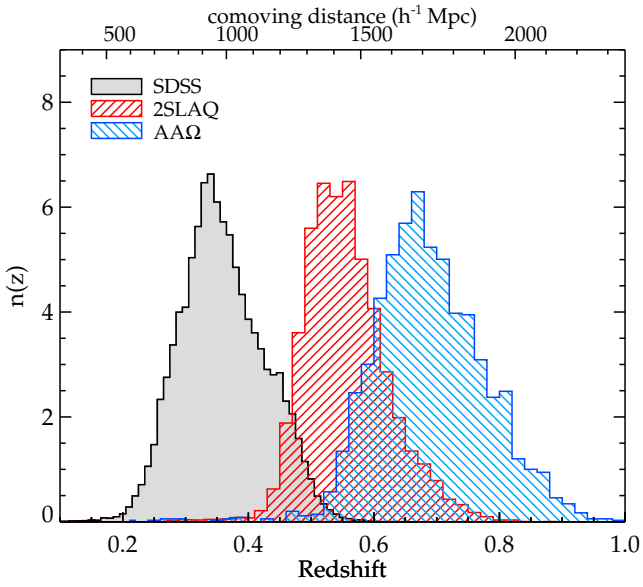

Figure 2.1: Normalised redshift distributions, $n(z)$, of the three LRG spectroscopic surveys used as the basis for selection criteria in this study. The word 'normalised' above and hereafter refers to the fact that the area under the curve $n(z)$ has been set to one.

functions, $\xi(r)$, from their projected counterparts, $w(\theta)$, via the Limber (1953) equation.

All magnitudes and colours are given in SDSS *AB* system and are corrected for extinction using the Galactic dust map of Schlegel, Finkbeiner, and Davis (1998). In our analysis, we shall only use the galaxy samples in the most contiguous part of the survey, i.e. the northern Galactic cap (NGC). All colours described below refer to the differences in 'model' magnitudes (see Lupton et al., 2001, for a review on model magnitudes) unless otherwise stated.

Hereafter we shall refer to the photometrically selected sample (not to be confused with the spectroscopic sample from which they are associated) at average redshift of 0.35, 0.55 and 0.7 as the 'SDSS LRG', '2SLAQ LRG' and 'AAΩ LRG', respectively.

2.2.1 SDSS LRG

The sample used here is similar to the target sample of the recently completed SDSS-LRG spectroscopic survey which contains $\approx 100\,000$ spectra and cover over 1 $h^{-3}\,\mathrm{Gpc}^3$. These objects are classified as LRGs on the basis of their colours and magnitudes following Eisenstein et al. (2001, E01 hereafter). The sample is approximately volume-limited up to $z \approx 0.38$ and spans out to $z \approx 0.5$. The selection is done using $(g-r)$ and $(r-i)$ colours coupled with r-band Petrosian (1976) magnitude system. The algorithm is designed to

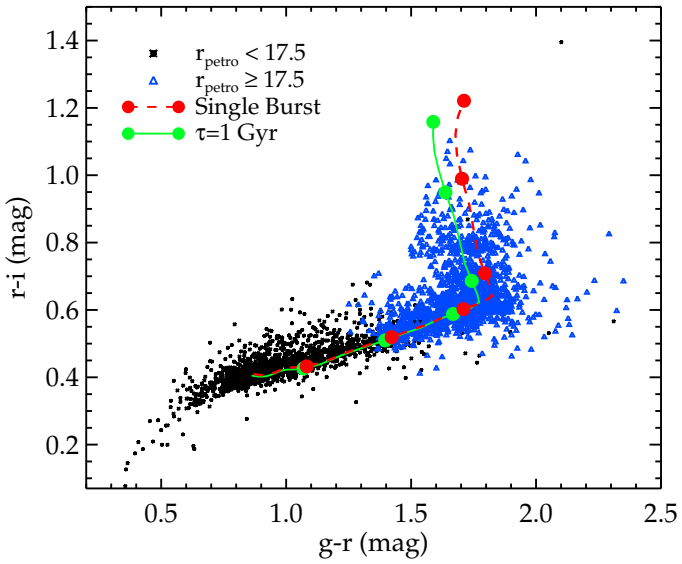

Figure 2.2: The colour-colour plot of SDSS LRG *cut I* and *II* showing their positions on the *gri* colour plane compared to the predicted colour-colour locus (observer frame) of typical early-type galaxies as a function of redshift (see text for more details). Each solid circle denotes the redshift evolution of the colour-colour tracks at the interval of 0.1 beginning with $z = 0.1$ (bottom left).

extract LRGs in two different (but slightly overlapped) regions of the *gri* colour space and hence using two selection criteria (*Cut I* and *Cut II* in E01) as naturally suggested by the locus of early-type galaxy on this colour plane (see Fig. 2.2). The tracks shown in Fig. 2.2 were constructed using a spectral evolution model of stellar populations (Bruzual and Charlot, 2003) with output spectra mimicking a typical SED of the LRGs. The stellar populations were formed at $z \approx 10$ and then evolve with two different scenarios, namely a) passive evolution of an instantaneous star formation (single burst), and b) exponentially decayed star formation rate (SFR) with *e-folding* time of 1 Gyr. Solar metallicity and Salpeter (1955) Initial Mass Function (IMF) were assumed in both evolutionary models.

We used the same colour-magnitude selection as that described by E01 but with additional restriction on the r-band apparent magnitudes of the objects, i.e. $r_{\rm petro} \geqslant 17.5$. This is due mainly to two reasons, a) to separate out the objects with $z < 0.2$ because *Cut I* is too permissive and allows under-luminous objects to enter the sample below redshift 0.2 as also emphasised by E01, and b) to tighten the redshift distribution of our sample while maintaining the number of objects and its average redshift (see Fig. 2.3).

The selection criteria mentioned above also has another star-galaxy separation algo-

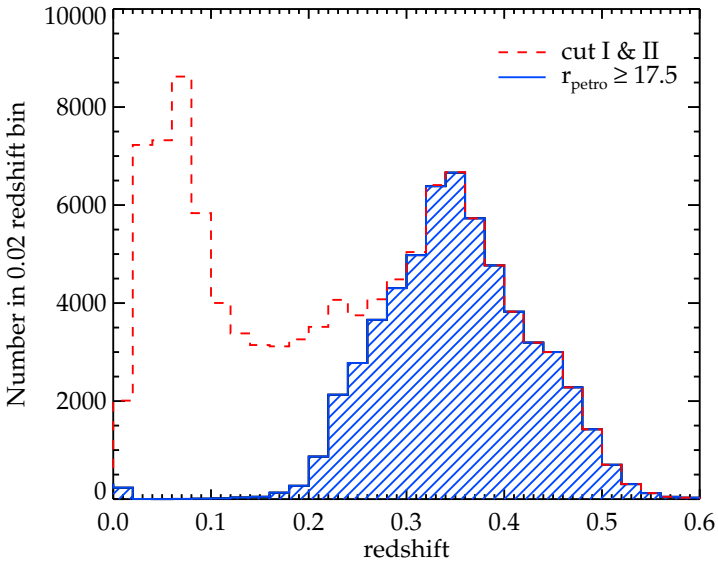

Figure 2.3: The number of objects as a function of redshift from SDSS LRG spectroscopic redshift survey also shown is the subset of *Cut I* and *II* with additional magnitude cut, $\mathrm{r_{petro}} \geqslant 17.5$, applied.

rithm apart from the pipeline PHOTO classification (Lupton et al., 2001). This was done by setting a lower limit on the differences in r-band point-spread function (PSF) magnitudes and model magnitudes as most galaxies populate the upper part of $r_{\mathrm{PSF}} - r_{\mathrm{model}}$ space compared to the foreground star of similar apparent magnitude. The algorithm has been proven to be quite effective (less than 1 per cent stellar contamination) for this range of redshift and magnitude although *Cut II* needs a more restrictive threshold, $r_{\mathrm{PSF}} - r_{\mathrm{model}} > 0.5$ as compared to 0.3 for *Cut I*.

In practice, the LRG sample described here can be extracted from the SDSS DR5 imaging database using the SQL query by setting the flag PRIMTARGET to GALAXY_RED. This yields a catalogue of approximately 200 000 objects which after applying the additional magnitude cut mentioned above, becomes 106 699 objects and results in the sky surface density of about 13 objects per square degree.

2.2.2 2SLAQ LRG

The 2dF-SDSS LRG and Quasar Survey (2SLAQ) is the spectroscopic follow-up of intermediate to high redshift ($z > 0.4$) LRGs from photometric data of SDSS DR4 (Adelman-McCarthy et al., 2006) using the two-degree Field (2dF) instrument on the Anglo-Australian Telescope (AAT). This survey is now completed and contains approximately 13 000 *bona*

fide LRGs in two narrow equatorial strips covering 180 square degrees with over 90 per cent having redshift $0.45 < z < 0.8$. The primary sample of the survey (*Sample 8*, Cannon et al. 2006;C06 hereafter) was selected using $(g-r)$ versus $(r-i)$ colours and 'de Vaucouleurs' i-band magnitude ($17.5 < i_{\rm deV} < 19.8$). The colour selection of *Sample 8* is similar to that of *Cut II* which utilises the upturn of the early-type galaxy locus in gri colour plane and hence is immune against the confusion with the late-type galaxy locus at higher redshift (see Fig. 2 in E01) but the scattering up in colour of interlopers from lower redshift and contamination of M-stars can also affect the accuracy of the selection. The latter could be prevented by using a similar method for star-galaxy separation as described in the last section but in this case we used the i-band magnitude rather than the r-band. Following C06, two criteria were used,

$$i_{\rm psf} - i_{\rm model} > 0.2(21 - i_{\rm deV}) \tag{2.1}$$

and

$$\mathrm{radius}_{\rm deV(i)} > 0.2, \tag{2.2}$$

where $\mathrm{radius}_{\rm deV(i)}$ is de Vaucouleurs radius fit of the i-band photometry. As reported by C06, approximately 5 per cent of the cool dwarf M-star is still present in their sample and we shall assume this value when correcting for the dilution of the correlation signal due to the uncorrelated nature of foreground stars and the LRGs. In this work, we only use *Sample 8* as this provides us with a narrower $n(z)$ and higher average redshift than the whole 2SLAQ sample.

A sample of 655 775 photometrically selected LRG candidates ($\approx$ 5 per cent stellar contamination) is returned by the SDSS DR5 'Best Imaging' database when the *Sample 8* selection criteria is used in the SQL query from table GALAXY. Objects with BRIGHT or SATURATED or BLENDED but not DEBLENDED flags are not included in our sample.

2.2.3 AAΩ LRG

The AAΩ-AAT LRG Pilot observing run was carried out in March 2006 by Ross et al. (2008b, and reference therein) as a 'Proof of Concept' for a large spectroscopic redshift survey, VST-AAΩ *ATLAS*, using the new AAOmega instrument on the AAT. The survey was designed to target photometrically selected LRGs out to $z \approx 1.0$ with the average redshift of 0.7. The target sample was observed in three 2-degree fields including the COSMOS field (Scoville et al., 2007), the COMBO-17 S11 field (Wolf et al., 2001), and

2SLAQ d05 field (Cannon et al., 2006).

We follow the survey main selection criteria, $19.8 < i_{\rm deV} \leq 20.5$ together with the riz colour cuts as described by Ross et al. (2008b). In summary, the cut utilises the upturn of the early-type galaxy colour-colour locus similar to that used by 2SLAQ and SDSS LRG surveys. The turning point of the track on the riz colour plane occurs at $z = 0.6 - 0.7$ as the 4000 Å feature moves from the SDSS r to i band whilst this happens at $z \approx 0.4$ in the gri case. The selection technique has been proven to work reasonably well by the observed redshift distribution. This is further confirmed by the ongoing AAT–AAΩ LRG project, the down-sized version of the VST–AAΩ *ATLAS* survey, designed to observed several thousands of LRG redshifts for photo–z calibration and a clustering evolution study. The $n(z)$ (Fig. 2.1) used in inferring the 3–D clustering information also includes $\approx$ 2000 AAΩ LRG redshifts taken during the run in June 2008.

As emphasised by Ross et al. (2008b), the stellar contamination in the sample can be readily reduced to $\approx$ 16 per cent by imposing star-galaxy separation in the z-band without any significant loss of the genuine galaxies. Although the level of contamination could be further reduced by using near-infrared photometry, we do not attempt it here as there is no infrared survey that covers the entire SDSS DR5 NGC sky with similar depth. Therefore we shall use the quoted contamination fraction when correcting the measured $w(\theta)$ for the same reason mentioned in §2.2.2. Since no expression for star-galaxy separation is given in Ross et al. (2008b), here such a procedure is performed using an equation defining the dashed line in their Fig. 3,

$$z_{\rm psf} - z_{\rm model} > 0.53 + 0.53(19.0 - z_{\rm model}) \tag{2.3}$$

Applying the above selection rules on the 'Best Imaging' data of the SDSS DR5 yields a photometric sample of 800 346 high-redshift LRG candidates with the sky surface density of approximately 110 objects per square degree. As with the 2SLAQ LRG sample, objects with BRIGHT or SATURATED or BLENDED but not DEBLENDED flags are discarded from our sample.

2.3 Estimating $w(\theta)$ and its error

2.3.1 Optimal estimator and techniques

The two-point correlation function, $\xi(r)$, measures the excess probability of finding a pair of objects separated by distance r relative to that expected from a randomly distributed

process. The joint probability of finding two objects of interest (in this case the LRGs) in the volume elements δV_1 and δV_2 separated by a distance r is given by

$$\delta P(r) = n^2 \left[1 + \xi(r)\right] \delta V_1 \delta V_2 \tag{2.4}$$

where n is the number space density of the sample. In practice, redshift of individual object is required to estimate the separation between a given pair. However if such redshift information is not available as in this study, the sky projected version, $w(\theta)$, can be used to analyse the clustering property of the sample instead. The 2D equivalent of Eq. 2.4 is

$$\delta P(\theta) = \aleph^2 \left[1 + w(\theta)\right] \delta\Omega_1 \delta\Omega_2 \tag{2.5}$$

where $\aleph$ is the surface density of the objects and $\delta P(\theta)$ is now the joint probability of finding two objects in solid angle $\delta\Omega_1$ and $\delta\Omega_2$ separated by angle θ.

Two possible routes for estimating $w(\theta)$ are the pixelisation of galaxy number over-density, $\delta_g = \delta_n/\bar{n}$ and pair counting. The pixelisation approach usually requires less computation time but its smallest scale probed is limited by the pixel size. We choose to follow the latter. To calculate $w(\theta)$ using the pair counting method, one usually generates a random catalogue whose angular selection function is described by the survey. The number of random points are generally required to be 10 times the number of objects or more. This is necessary to reduce the shot noise. Our random catalogue for each sample has $\approx$ 20 times the number of LRGs in SDSS and 10 times for 2SLAQ and AAΩ-pilot (see next section for details on how this was achieved).

We compute $w(\theta)$ using the minimum variance estimator of Landy and Szalay (1993). It is also an unbiased estimator (Martínez and Saar, 2002) for 2PCF as it can be reduced to the exact theoretical definition of 2PCF, i.e. a variance of density fluctuation in Gaussian field, $\xi(r) = \langle \delta(\mathbf{x}) \delta(\mathbf{x} + \mathbf{r}) \rangle$. The form of this estimator is

$$w_{\rm LS}(\theta) = 1 + \left(\frac{N_{rd}}{N}\right)^2 \frac{DD(\theta)}{RR(\theta)} - 2\left(\frac{N_{rd}}{N}\right) \frac{DR(\theta)}{RR(\theta)} \tag{2.6}$$

where $DD(\theta)$ is the number of LRG-LRG pairs with angular separation within the angular bin centres at θ. $DR(\theta)$ and $RR(\theta)$ are the numbers of LRG-random and random-random pairs, respectively. N_{rd}/N ratio is required for normalisation. N_{rd} is the total number of random points and N is the total number of LRGs. We use a logarithmic bin width of $\Delta \log(\theta/\mathrm{arcmin}) = 0.176$ for $\theta = 0.1'$ to $50'$ and a linear bin width of $20'$ at scales larger than $50'$.

The uncertainty in the number density of the sample could lead to a bias in the estimation of $w(\theta)$ when using Landy-Szalay estimator especially at large scale where the amplitude is small and hence we also utilise the Hamilton (1993) estimator, given by

$$w_{\rm HM}(\theta) = \frac{DD(\theta) \cdot RR(\theta)}{DR(\theta)^2} - 1 \tag{2.7}$$

which requires no normalisation. We used the Hamilton estimator to cross-check our $w_{\rm LS}$ for each sample and found the difference given by the two estimators to be negligible in all three samples.

For the purpose of determining statistical uncertainty in our measurement, three methods of estimating the errors are considered. The first method is the simple Poisson error given by

$$\sigma_{\rm Poi}(\theta) = \frac{1 + w(\theta)}{\sqrt{DD(\theta)}} \tag{2.8}$$

For the second method, *field-to-field* error, we split the sample into 24 subfields of approximately equal size. These subfields are large enough for estimating the correlation function up to the scale of interest. This is simply a standard deviation of the measurement in each subfield from the best estimate and is calculated using

$$\sigma^2_{\rm FtF}(\theta) = \frac{1}{N-1} \sum_{i=1}^{N} \frac{DR_i(\theta)}{DR(\theta)} [w_i(\theta) - w(\theta)]^2 \tag{2.9}$$

where N is the total number of subfields, $w_i(\theta)$ is a measurement from the ith subfield and $w(\theta)$ is measured using the whole sample. The deviation of the angular correlation function computed in each subfield is weighted by $DR_i(\theta)/DR(\theta)$ to account for their relative sizes.

The third method is the *jackknife* resampling. This is a method of preference in a number of correlation studies (see e.g. Scranton et al., 2002; Zehavi et al., 2005a; Ross et al., 2007). The jackknife errors is computed using the deviation of $w(\theta)$ measured from the combined 23 subfields out of the 24 subfields. The subfields are the same as used for the estimation of *field-to-field* error above. $w(\theta)$ is calculated repeatedly, each time leaving out a different subfield and hence results in a total of 24 measurements. The jackknife error is then

$$\sigma^2_{\rm JK}(\theta) = \sum_{i'=1}^{N} \frac{DR_{i'}(\theta)}{DR(\theta)} [w_{i'}(\theta) - w(\theta)]^2 \tag{2.10}$$

where $w_{i'}(\theta)$ is now an angular correlation function estimated using the whole sample except the ith subfield and $DR_{i'}(\theta)/DR(\theta)$ is approximately 23/24 with slight variation depending on the size of resampling field.

The $w(\theta)$ measured from a restricted area are known to suffer from a negative offset called 'integral constraint', ic, which tends to force the fluctuation on the scales of the survey to zero (Groth and Peebles, 1977), i.e. $w_{\rm est}(\theta) = w(\theta) - ic$. The integral constraint can be estimated from the random pair counts drawn from the same angular selection function (§2.3.2) as the data (see e.g. Roche and Eales, 1999);

$$ic = \frac{\Sigma RR(\theta) w_{\rm model}(\theta)}{\Sigma RR(\theta)}, \tag{2.11}$$

where we assume our fiducial ΛCDM model (see §2.4.2) for $w_{\rm model}$. The ic for the SDSS, 2SLAQ and AAΩ-LRG samples are 4×10^{-4}, 1.5×10^{-4} and 8×10^{-5}, respectively. These are much smaller than the $w(\theta)$'s amplitudes in the angular ranges being considered in this paper, as expected given the large sky coverage of the SDSS data.

It is well known that the correlation function bins are correlated which could affect the confidence limit on the parameter estimation performed under the assumption that each data point is independent. Comparison of the estimated error using the field-to-field and jackknife techniques to the simple Poisson error can give a rough estimate of the deviation from the independent point assumption. This is plotted in Fig. 2.4 which shows that the assumption is valid on small scales where Poisson error is a fair estimate of the statistical uncertainty. However the same cannot be said on large scales where the data points are correlated and the independent point assumption no longer holds. At these scales, such statistical uncertainty is likely to be dominated by edge-effects and cosmic variance.

Fig. 2.4 also shows that the errors estimated using field-to-field and jackknife method are in good agreement at all angular scales except for 2SLAQ and AAΩ samples where the jackknife errors are slightly smaller towards the large scales but still agree within 10 per cent. The errors quoted in later sections are estimated using the jackknife resampling method.

The covariance matrix allows the correlation between each bin to be quantified and can be used in the fitting procedure to de-correlate the separation bins. We calculate the covariance matrix from the jackknife resampling using

$$\mathbf{C}_{ij} = (N-1)\langle [w(\theta_i) - \overline{w(\theta_i)}] \cdot [w(\theta_j) - \overline{w(\theta_j)}] \rangle \tag{2.12}$$

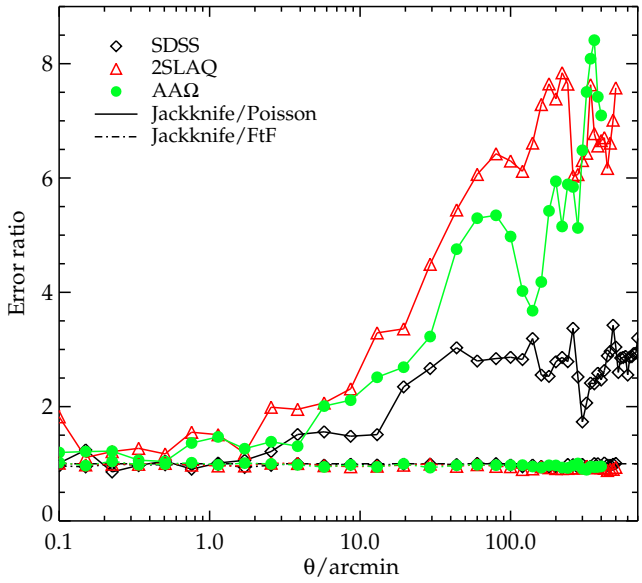

Figure 2.4: The ratio of jackknife to Poisson and field-to-field errors on the measurements of $w(\theta)$. The open diamonds, triangles and solid circles give the error ratios of $w(\theta)$ estimated from SDSS, 2SLAQ, and AAΩ LRG, respectively.

where $\overline{w(\theta_j)}$ is the mean angular correlation function of all the jackknife subsamples in the jth bin. The measured variance, σ^2, is the diagonal element of the covariance matrix, $\mathbf{C}_{ii}$. Note that the difference between $\overline{w(\theta_j)}$ and $w(\theta)$ estimated using the whole sample is negligible. We then proceed to compute the 'correlation coefficient', $\mathbf{r}_{ij}$, defined by

$$\mathbf{r}_{ij} = \frac{\mathbf{C}_{ij}}{\sqrt{\mathbf{C}_{ii} \cdot \mathbf{C}_{jj}}} \tag{2.13}$$

Fig. 2.5 shows the correlation coefficients for the three samples which are strongly correlated at the largest scale considered and less at small scales confirming the simple correlation test using Poisson errors. Note that for the purpose of model fitting in the large-scale sections (§2.4.2, 2.4.3 and 2.6) where a more stable covariance matrix is required, we increase the number of resampling fields to 96 sub-regions with approximately equal area. The size of these sub-regions are also big enough for the largest scale being considered in this paper. The correlation coefficients constructed from these 96 JK resampling are shown in Fig. A.1 for the three LRG samples.

We use the kd-trees code (Moore et al., 2001) to minimise the computation time required in the pair counting procedure. The angular correlation function is estimated using the method described above and then corrected for stellar contamination which would have reduced the amplitude by a factor $(1 - f)^2$, where f is the contamination

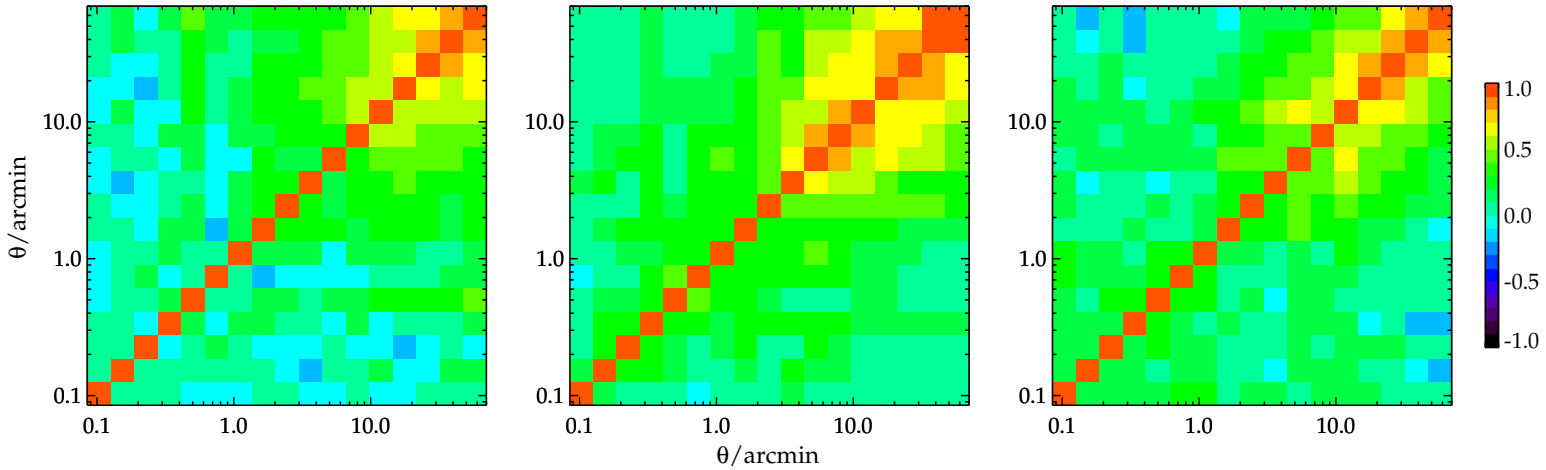

Figure 2.5: The correlation coefficients, $\mathbf{r}_{ij}$, showing the level of correlation between each angular separation bin for SDSS, 2SLAQ, and AAΩ LRG (left to right). Note that for each sample we only show $\mathbf{r}_{ij}$ up to the angular separation corresponds to $\approx 20\ h^{-1}$ Mpc where later we shall attempt to fit power-law forms to the measured $w(\theta)$'s.

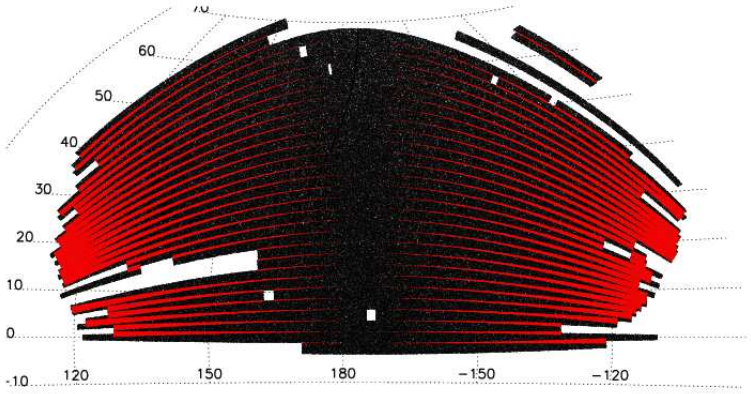

Figure 2.6: An equal area Aitoff projection of a random catalogue described in §2.3.2. The red/grey highlighted regions indicate the areas where adjacent stripes are overlapped. Note that the shading is purely diagrammatic to show the overlap regions and is unrelated to galaxy density.

fraction for each sample given in §2.2.

2.3.2 Constructing random catalogues

In order to calculate the angular correlation function accurately, a random catalogue is required. This catalogue consists of randomly distributed points with the total number at least 10 times that of the data. Each random point is assigned a position in Right Ascension (RA) and Declination (DEC). Since our sample spans a wide range in DEC (see Fig. 2.6 for the SDSS DR5 sky coverage), care must be taken to keep the surface number density constant assuming the survey completeness is constant and uniform throughout. Only the random points that satisfy the angular selection function of the survey as defined by the mask are selected.

The mask is constructed from 'BEST' DR5 imaging sky coverage given[2] in the survey coordinate (λ, η) and stripe number. The sky is drift scanned in a strip parallel to η and two strips are required to fill a stripe (York et al., 2000). Each stripe is 2.5° wide and their centres are separated by 2.5°. In addition to the 'BEST' sky coverage mask, we also exclude regions in the quality 'holes' and regions defined as 'BLEEDING', 'BRIGHT_STAR', 'TRAIL' and 'HOLE' in the 'mask' table given by the SDSS database. The final mask is applied to both our data and random catalogues.

[2] `http://www.sdss.org/dr5`

Note that further away from the survey equator ($RA_{2000} = 185°$), the adjacent stripes become overlapped which account for almost 20 per cent of the sky coverage. The 'BEST' imaging database only keep the best photometry of the objects which have been detected more than once in the overlap regions. At the faint magnitude limit of our sample, this could lead to a higher completeness in the overlap region and introduces bias in the estimated correlation function. This issue has also been addressed by Blake et al. (2007). They compared the measurement from the sample which omits the overlap region against their best estimate and found no significant difference. We follow their approach by excluding the overlap regions and re-calculating the angular correlation function of our faintest apparent magnitude sample, AAΩ-LRG, where the issue is expected to be the most severe. We found no significant change compared to our best estimate using the whole sample.

2.3.3 Inferring 3–D clustering

The angular correlation function estimated from the same population with the same clustering strength will have a different amplitude at a given angular scale if they are at different depths (redshifts) or have different redshift selection functions, $\phi(z)$. Therefore in order to accurately compare the clustering strengths of different samples inferred from $w(\theta)$, one needs to know the sample $\phi(z)$. Even if the redshifts of individual galaxies are not available, their 3–D clustering information can be recovered if the sample redshift distribution, $n(z)$, is known. The equation that relates the spatial coherence length, r_0, to the amplitude of $w(\theta)$ is usually referred to as Limber's equation.

Recently, the accuracy of Limber's equation has been called into question. This is due to the assumption made for Limber's approximation that the selection function, $\phi(z)$, varies much more slowly than $\xi(r)$ in addition to the flat–sky (small angle) approximation. It was shown by Simon (2007) that such an assumption would lead to $w(\theta)$ being overestimated at large angle where the breakdown scale becomes smaller for narrower $\phi(z)$ (see Fig. 2.7). Here, we shall use the relativistic generalisation of Limber's equation suggested by Phillipps et al. (1978) but without the approximation mentioned above. Following Phillipps et al. (1978) for the comoving case,

$$w(\theta) = \frac{\int_0^\infty dz_1 f(z_1) \int_0^\infty dz_2 f(z_2) \xi(r)}{\left[\int_0^\infty dz f(z)\right]^2} \tag{2.14}$$

The source's radial distribution, $f(z)$, is simply given by the galaxy selection function,

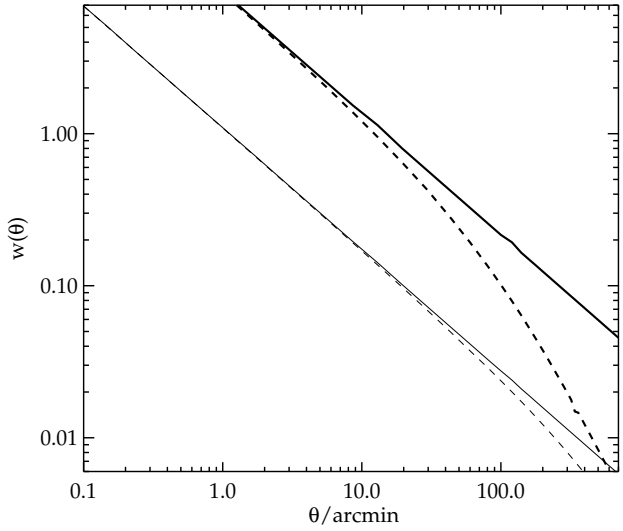

Figure 2.7: The angular correlation function computed using the exact (dashed-lines) and Limber approximation (solid-lines), derived using a power-law, $\xi(r) = (r/r_0)^{-\gamma}$ where $r_0 = 10\ h^{-1}\,\mathrm{Mpc}$ and $\gamma = 1.8$ with the SDSS LRG $n(z)$ for the thin lines and much narrower $n(z)$ (± 0.01 centred at $z = 0.35$) for the thick lines.

$\phi(z)$, as

$$f(z) \equiv \chi^2(z)\frac{d\chi(z)}{dz} n_c(z)\phi(z) \tag{2.15}$$

where χ is the radial comoving distance, $n_c(z)$ is the comoving number density of the sources and $r = r(\theta, z_1, z_2)$ is a comoving separation of the galaxy pair. We shall assume a spatially flat cosmology (see §2.4.2) hence

$$r \equiv \sqrt{\chi^2(z_1) + \chi^2(z_2) - 2\chi(z_1)\chi(z_2)\cos\theta} \tag{2.16}$$

Note that Eq. 2.14 can also be used to relate a non-power-law spatial correlation function to $w(\theta)$ unlike the conventional power-law approximation of Limber's equation (Phillipps et al., 1978).

Fig. 2.7 shows $w(\theta)$ computed using Eq. 2.14 (dashed lines) compared to the conventional Limber's approximation (solid lines) for a power-law $\xi(r)$ with clustering length $10\ h^{-1}\,\mathrm{Mpc}$ and $\gamma = 1.8$. The effect of a much narrower redshift distribution (thick lines) is also shown where the break scale becomes smaller and the power-law slope of $w(\theta)$ asymptotically approaches that of $\xi(r)$, agreeing with the finding of Simon (2007). We shall use Eq. 2.14 together with the known $n(z)$ to infer the 3–D spatial clustering of the

LRGs.

2.4 Results

2.4.1 Power-law fits

We first look at the angular correlation function measured from the LRG sample at scales less than 1° corresponding to approximately 20 h^{-1} Mpc where previous studies suggested that the spatial 2PCF can be described by a single power-law of the form $\xi(r) = (r/r_0)^{-\gamma}$ (typically $\gamma = 1.8$) and a single power-law $w(\theta)$ with slope $1 - \gamma$ is expected (see Fig. 2.7). However in this study, we find a deviation from a single power-law with a break in the slope at $\approx 1\ h^{-1}$ Mpc in all three samples (less significant for the SDSS LRG). The measurement has a steeper slope at small scales ($< 1\ h^{-1}$ Mpc) and is slightly flatter on scales up to $\approx 20\ h^{-1}$ Mpc where it begins to drop sharply (see Fig. 2.8 and Fig. 2.9). The inflexion feature at $\approx 1\ h^{-1}$ Mpc has also been reported in the spatial and semi-projected, $w_p(\sigma)$, correlation function by many authors (e.g. Zehavi et al., 2005a; Phleps et al., 2006; Ross et al., 2007; Blake et al., 2008) and detections go back as far as Shanks et al. (1983). We shall return to discuss these features in the halo model framework (§2.4.3).

If we first consider $w(\theta)$ at scales smaller and larger than the break point separately, each can be approximately described by a power-law with a slope of ≈ -1.15 ($\gamma = 2.15$), and ≈ -0.83 ($\gamma = 1.83$), respectively. A more detailed analysis is performed by fitting a set of models to the measured $w(\theta)$ using a chi-squared minimisation method with the full covariance matrix constructed from the jackknife resampling (see §2.3.1). This allows us to quantify the significance of the deviation from the single power-law by comparing its *goodness of fit* to a double power-law. We proceed by calculating

$$\chi^2 = \sum_{i,j=1}^{N} \Delta w(\theta_i) \mathbf{C}_{ij}^{-1} \Delta w(\theta_j) \tag{2.17}$$

where N is the number of angular bins, $\Delta w(\theta_i)$ is the difference between the measured angular correlation function and the model for the ith bin, and $\mathbf{C}_{ij}^{-1}$ is the inverse of covariance matrix.

The single power-law fit is of the form $w(\theta) = (\theta/\theta_0)^{(1-\gamma)}$. We also recover the spatial clustering length, r_0, and its slope through the fitting via Eq. 2.14. For a double power-law, the fitting procedure is performed separately at the scales smaller and larger than θ_b, corresponding to $\approx 1\ h^{-1}$ Mpc for all three samples (see Fig. 2.9). The largest scale

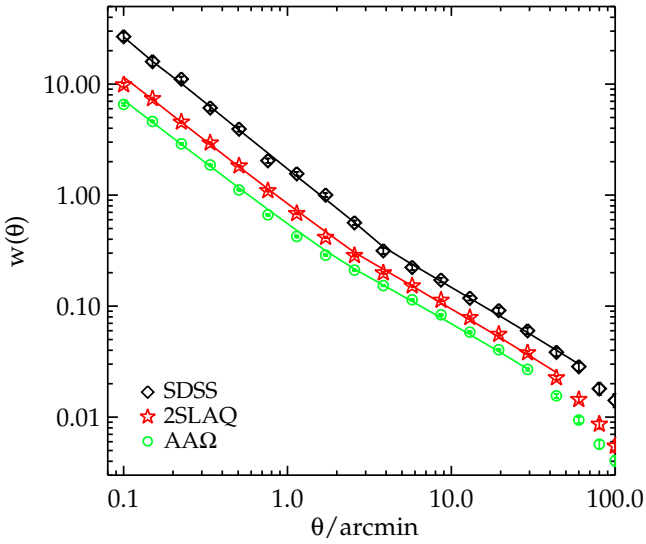

Figure 2.8: The angular correlation function measured from the three LRG samples. The solid lines are the projection of best-fit double power-law $\xi(r)$ with r_0 and γ given in Table 2.2 for each sample. The break scales occur at approximately a few arcminutes depending on the average redshift of the sample. This corresponds to a comoving separation of $\approx 1\ h^{-1}\,\mathrm{Mpc}$ (see Fig. 2.9).

considered in the fitting for all cases is $\approx 20\ h^{-1}\,\mathrm{Mpc}$ where a steeper drop-off of $w(\theta)$ is observed.

In Fig. 2.9, the best-fit power-laws for all three samples are shown. The summary of the best-fit parameters are given in Table 2.2. Eq. 2.14 and 2.17 are then used to find the spatial clustering lengths and slopes that best describe our $w(\theta)$ results. The best-fit clustering slopes from r_0-γ analysis using Limber's equation are in good agreement with that from θ_0-γ and hence we only report the latter in Table 2.2. If we require a continuity in the double power-law $\xi(r)$ at the break scale, such a scale can be constrained by the pair of best-fit r_0-γ's for each sample. From Table 2.2, the double power-law break for the SDSS, 2SLAQ and AAΩ samples are then at 2.2, 1.9 and 1.3 $h^{-1}\,\mathrm{Mpc}$, respectively (see §2.5.2 for further discussion of the possible small-scale evolution of $\xi(r)$). By assuming the 1 $h^{-1}\,\mathrm{Mpc}$ break instead of aforementioned values, the $w(\theta)$ is underestimated by ≈ 10 per cent for the SDSS case (less for the other two samples) which is only localised to around θ_b. The clustering length (single power-law), r_0, ranges from 7.5 to 8.7 $h^{-1}\,\mathrm{Mpc}$, consistent with highly biased luminous galaxies. Single power-law fits to the data can be ruled out at high statistical significances. While the double power-law give better fits to

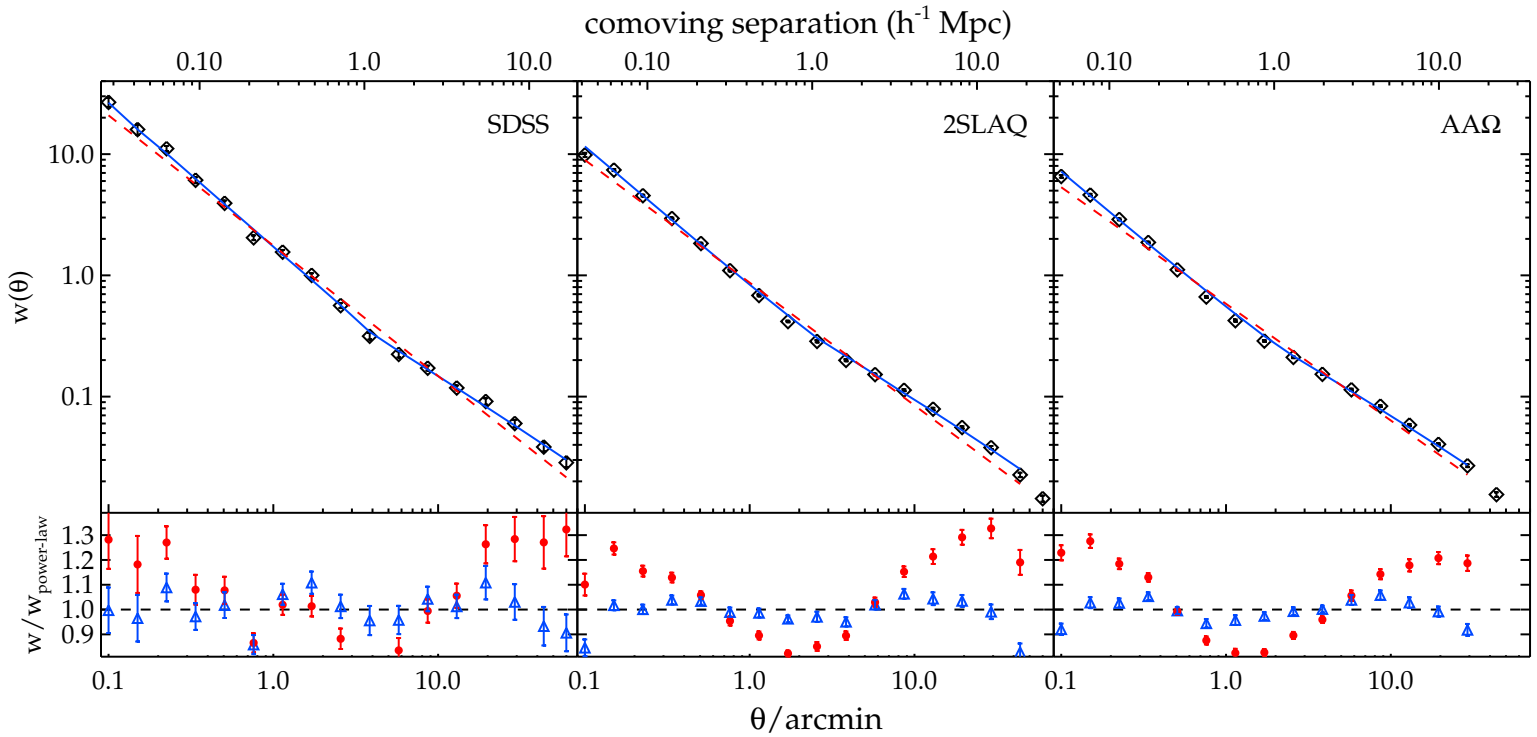

Figure 2.9: The angular correlation function with the best-fit single (red dashed line) and double (blue solid line) power-law for the SDSS, 2SLAQ and AAΩ LRGs. Lower panels show the fitting residuals for the single (circles) and double (triangles) power-law.

Table 2.2: Parameters for the power-law fits to the angular correlation function derived from three LRG samples. The best-fit parameters given are defined such that $w(\theta) = (\theta/\theta_0)^{1-\gamma}$ and $\xi(r) = (r/r_0)^{-\gamma}$. The parameters for the best-fit double power-law are given in two rows where the $\theta < \theta_b$ result is given in the top row. Also given are the corresponding 1σ error for each parameter.

Sample	$\bar{z}$	$n_{\rm g}$	Single power-law				Double power-law			
		$(h^3\ {\rm Mpc}^{-3})$	$\theta_0(')$	γ	$r_0(h^{-1}\,{\rm Mpc})$	$\chi^2_{\rm red}$	$\theta_0(')$	γ	$r_0(h^{-1}\,{\rm Mpc})$	$\chi^2_{\rm red}$
SDSS	0.35	1.1×10^{-4}	1.69 ± 0.03	2.07 ± 0.01	8.70 ± 0.09	16.2	1.57 ± 0.05	2.19 ± 0.03	7.35 ± 0.08	2.2
							1.05 ± 0.09	1.85 ± 0.04	9.15 ± 0.16	
2SLAQ	0.55	3.2×10^{-4}	0.87 ± 0.01	2.01 ± 0.01	7.50 ± 0.04	57.5	0.83 ± 0.01	2.16 ± 0.01	6.32 ± 0.03	3.9
							0.60 ± 0.03	1.84 ± 0.02	7.78 ± 0.05	
AAΩ	0.68	2.7×10^{-4}	0.57 ± 0.01	1.96 ± 0.01	7.56 ± 0.03	42.8	0.56 ± 0.01	2.14 ± 0.01	5.96 ± 0.03	3.4
							0.38 ± 0.02	1.81 ± 0.02	7.84 ± 0.04	

the data than the single power-law, their $\chi^2_{\rm red}$ values indicate that such a model is still not a good fit to the data, given the small statistical errors. Nevertheless, to first order, the double power-law fits provide a good way of quantifying the spatial clustering strength of the samples via the use of Limber's equation.

The best-fit slopes at small scales show a slight decrease with increasing redshift, similar to that found by Wake et al. (2008). The SDSS LRG sample is more strongly clustered than the rest as expected. This is simply because the SDSS LRG sample is intrinsically more luminous than the 2SLAQ and AAΩ LRG samples and is not an indication of evolution.

The galaxy number density (see Table 2.2) are calculated from the unnormalised $n(z)$, assuming the redshift distribution from the spectroscopic surveys as described in §2.2. This is galaxy pair-weighted by $n^2(z)$ (see e.g. Ross and Brunner, 2009)

$$n_{\rm g} = \int {\rm d}z \, \frac{H(z) n(z)}{\Omega_{\rm obs} c \chi^2(z)} \times n^2(z) \Big/ \int {\rm d}z \, n^2(z) \tag{2.18}$$

where $\Omega_{\rm obs}$ is the observed area of the sky, $\chi(z)$ is the comoving distance to redshift z and c is the speed of light. The samples' pair-weighted average redshifts determined in the similar manner as $n_{\rm g}$ are consistent with their median redshifts and are given in Table 2.2.

To this end, we cut back the faint magnitude limit of 2SLAQ and AAΩ LRG's to $i_{\rm deV} < 19.32$ and 20.25, respectively. These cuts are imposed in order to select the samples of galaxies whose comoving number densities are approximately matched to that of the SDSS LRG. The $K + e$ corrected i-band absolute magnitudes of these samples are presented in Fig. 2.10. We see that their absolute magnitudes are also approximately matched. This would then allow us to roughly constrain the evolution of LRG clustering up to $z \approx 0.68$ (see §2.5). A summary of the properties of these samples and the best-fit parameters are given in Table 2.3. The measured $w(\theta)$'s are shown in Fig. 2.11a.

As expected, the amplitudes of the brighter cut 2SLAQ and AAΩ samples (denoted by 2SLAQ* and AAΩ* hereafter) are higher than the original sample. In its raw form, $w(\theta)$ measured from 2SLAQ* increases relative to 2SLAQ more than AAΩ relative to AAΩ*, due to the narrower redshift distribution of the 2SLAQ* sample. However, if we perform a double power-law fit to these results, the large-scale, $\gtrsim 1 \; h^{-1}\,{\rm Mpc}$, clustering lengths are very similar and agree within $\approx 1\sigma$ statistical error. To first order these large-scale clustering lengths are also consistent with that of the SDSS LRG's. We shall investigate the clustering evolution of these LRG samples further in §2.5.

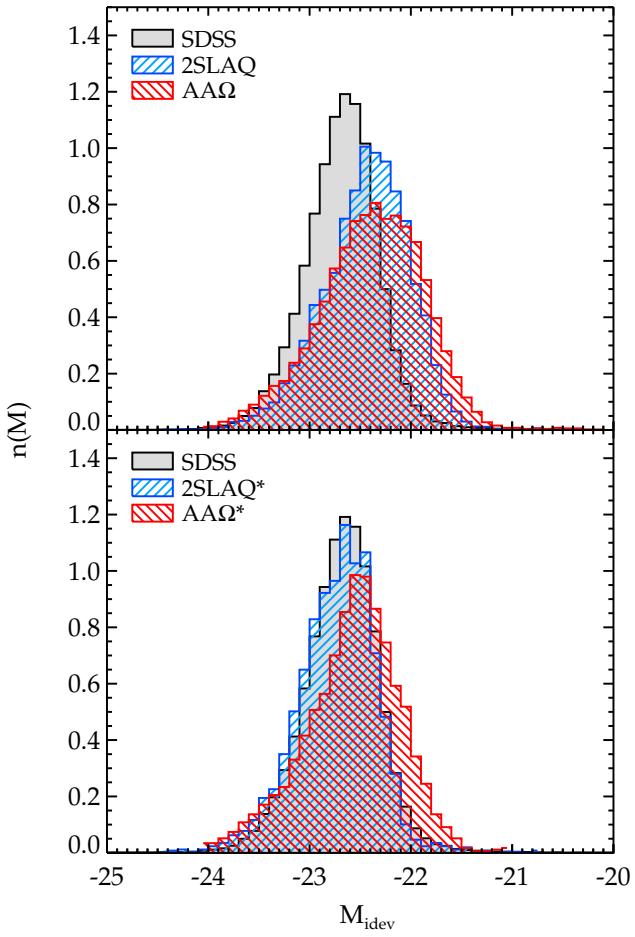

Figure 2.10: *Top:* The i-band absolute magnitude distribution of the spectroscopic LRG catalogues. All photometry is galactic-extinction corrected using dust map of Schlegel, Finkbeiner, and Davis (1998) and $K + e$ corrected to $z = 0$ using the Early-type galaxy templates from Bruzual and Charlot (2003). *Bottom:* The distribution of the absolute magnitude after applying a faint limit cut to 2SLAQ and AAΩ LRG in order to match the comoving number density of the SDSS LRG.

Table 2.3: Properties and the best-fit parameters for double power-law of $w(\theta)$ measured from the SDSS-density matched samples.

Sample	number	magnitude	$\bar{z}$	$n_{\rm g}$	Double power-law		
				$(h^3\ {\rm Mpc}^{-3})$	γ	$r_0(h^{-1}\ {\rm Mpc})$	$\chi^2_{\rm red}$
2SLAQ*	182 841	$17.5 < i_{\rm deV} < 19.32$	0.53	1.2×10^{-4}	2.25 ± 0.02	6.33 ± 0.04	2.1
					1.80 ± 0.02	8.88 ± 0.08	
AAΩ*	374 198	$19.8 < i_{\rm deV} < 20.25$	0.67	1.1×10^{-4}	2.20 ± 0.02	6.25 ± 0.03	1.7
					1.76 ± 0.03	9.08 ± 0.06	

2.4.2 Comparison of the clustering form to the standard ΛCDM model

We shall compare our $w(\theta)$ measurements to the predictions of the standard ΛCDM model in the linear perturbation theory of structure growth framework along with the non-linear correction. For the theoretical models, we first generate matter power spectra, using the 'CAMB' software (Lewis, Challinor, and Lasenby, 2000). In the case of non-linear correction, the software has the 'HALOFIT' routine (Smith et al., 2003) implemented. Such matter power spectra, $P_{\rm m}(k,z)$, are then output at the average redshift of each sample. The matter correlation function, $\xi_{\rm m}(r)$, is then obtained by Fourier transforming these matter power spectra using

$$\xi_{\rm m}(r) = \frac{1}{2\pi^2}\int_0^\infty P_m(k)k^2\frac{\sin kr}{kr}dk \tag{2.19}$$

Under the assumption that galaxies trace dark matter haloes, the galaxy correlation function, $\xi_{\rm g}(r)$, is related to the underlying dark matter by the bias factor, $b_{\rm g}$, via

$$b_{\rm g}^2 = \frac{\xi_{\rm g}(r)}{\xi_{\rm m}(r)} \tag{2.20}$$

Therefore the bias factor is expected to be a function of scale unless galaxies cluster in exactly the same manner as the dark matter does at all scales. However, at large scales, i.e. the linear regime, the bias factor is approximately scale–independent over almost a decade of scales (Verde et al., 2002; Ross et al., 2008a).

Although we found the clustering lengths and hence the amplitude of $\xi(r)$ to be very similar for the SDSS, 2SLAQ* and AAΩ^* samples, the evolution in the dark matter clustering means that the linear bias could be a strong function of redshift as we shall see in the next section where we investigate the clustering evolution in more detail. The evolution of structures in linear theory framework is described by the linear growth factor, $D(z)$, (e.g. Peebles 1984; Carroll et al. 1992) such that

$$\delta(r,z) = D(z)\delta(r,z=0), \tag{2.21}$$

recall that $\xi(r) = \langle\delta(\mathbf{r_1})\,\delta(\mathbf{r_2})\rangle$, where $r = |\mathbf{r_1} - \mathbf{r_2}|$, then

$$\xi_m(r,z) = D^2(z)\xi_m(r,0) \tag{2.22}$$

The linear growth factor is unity at the present epoch, by definition, and decreases as a function of redshift. The $\xi_m(r,z)$ therefore decreases as the redshift increases hence given that the number-density/luminosity matched samples have similar $\xi_g(r)$ amplitudes, suggesting that the bias increases as a function of redshift.

We proceed by projecting the predicted $\xi_{\rm m}(r)$ using Eq. 2.14. Our fiducial models assume a ΛCDM Universe with $\Omega_\Lambda = 0.73$, $\Omega_{\rm m} = 0.27$, $f_{\rm baryon} = 0.167$, $\sigma_8 = 0.8$, $h = 0.7$ and $n_s = 0.95$. The linear bias factor is then estimated by fitting the matter $w(\theta)$ to our measurements for the comoving separation of $\approx$ 6–60 h^{-1} Mpc, using the full covariance matrices. Although the lower limit of 6 h^{-1} Mpc may appear low for the linear regime, the non-linear correction at these scales is still very small and to first order the shape of linear theory prediction is consistent with the data[3]. The best-fit linear bias ($\chi^2_{\rm red}$) for SDSS, 2SLAQ*, AAΩ*, 2SLAQ and AAΩ samples are 2.09 ± 0.05 (1.2), 2.20 ± 0.04 (0.65), 2.33 ± 0.03 (0.66), 1.98 ± 0.03 (0.53) and 2.07 ± 0.02 (1.2), respectively. The measured biases are consistent with the results from other authors. For example, Tegmark et al. (2006) analysed $P(k)$ of SDSS LRG and found $b(z = 0.35) = 2.25 \pm 0.08$ for the best-fit $\sigma_8 = 0.756 \pm 0.035$ and for our fiducial σ_8 this becomes $b = 2.12 \pm 0.12$. Ross et al. (2007) found 2SLAQ LRG $b = 1.66 \pm 0.35$ using redshift-space distortion analysis. Padmanabhan et al. (2007) , using $C(\ell)$ of SDSS+2SLAQ photo-z sample, found that $b(z = 0.376) = 1.94 \pm 0.06$ and $b(z = 0.55) = 1.8 \pm 0.04$ (assumed $\sigma_8 = 0.9$), for our fiducial σ_8 these are $b = 2.18 \pm 0.07$ and $b = 2.02 \pm 0.05$, respectively.

Fig. 2.11b shows the full scaling of of the $w(\theta)$'s, accounting for their survey differences. First, the $w(\theta)$ of the SDSS, and 2SLAQ* samples scaled in the angular direction according to their average redshifts and relative to the AAΩ* sample. The amplitudes are then scaled to obtain a fair comparison for samples with different redshift distributions. This is done by taking the relative amplitudes of the projections of a power-law $\xi(r)$ of the same clustering strength but projected through different $n(z)$ widths. Since the observed large-scale clustering lengths are very similar, ≈ 9 h^{-1} Mpc, the scaled $w(\theta)$'s in these ranges agree reasonably well. The figure also shows the best-fit biased non-linear model for the AAΩ* sample. Our $w(\theta)$ shapes in the ranges $6 \lesssim r \lesssim 60$ h^{-1} Mpc can be described very well by linear perturbation theory in the standard flat ΛCDM Universe (see the $\chi^2_{\rm red}$ for the best-fit bias factor given above). However, at smaller scales the theory underestimates the clustering amplitude, as expected for early-type galaxies. As we shall see in §2.4.3 that the reason for this may lie in the details of how the LRGs populate their dark matter halo hosts.

[3]Note that changing the lower limit of the fitting to 10 h^{-1} Mpc does not significantly change the best-fit bias nor the reduced χ^2.

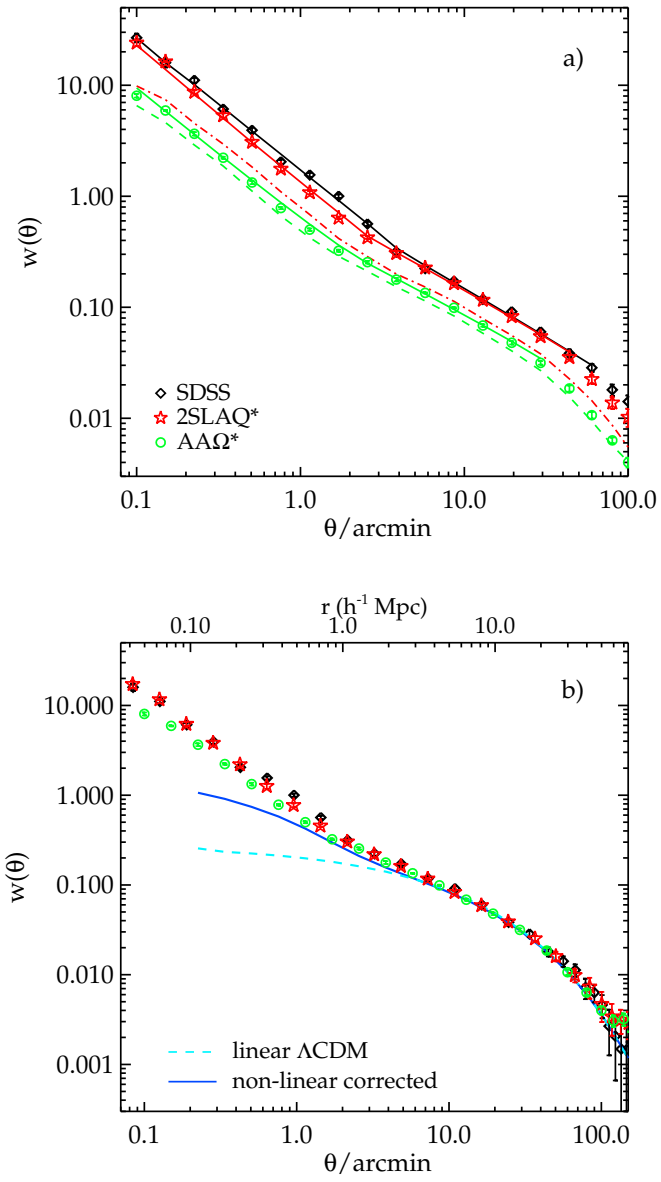

Figure 2.11: (a): The angular correlation function measured from the SDSS LRG and the brighter magnitude limit samples drawn from 2SLAQ and AAΩ sample (symbols). The solid lines are the projection of the best-fit double power-law $\xi(r)$ with the parameters shown in Table 2.3. For comparison, the dot-dashed and dashed lines are $w(\theta)$ measured from the whole 2SLAQ and AAΩ samples, respectively. (b): Same as (a) but now scaled to AAΩ depth and taking into account the relative amplitude due to the different $n(z)$ widths (see text for more details).

2.4.3 Halo model fits

We fit the halo model (e.g. Peacock and Smith, 2000; Berlind and Weinberg, 2002; Cooray and Sheth, 2002) to our angular correlation function results. One of the key ingredients of the halo model is the Halo Occupation Distribution (HOD) which tells us how the galaxies populate dark matter haloes as a function of halo mass. Recently, the model has been used to fit various datasets as a means to physically interpret the galaxy correlation function and gain insight into their evolution (e.g. White et al., 2007; Blake et al., 2008; Wake et al., 2008; Brown et al., 2008; Ross and Brunner, 2009; Zheng et al., 2009)

Here, we use a three-parameter model (e.g. Seo et al., 2008; Wake et al., 2008) which distinguishes between the central and satellite galaxies in a halo (Kravtsov et al., 2004). The mean number of galaxies residing in a halo of mass M is

$$\langle N(M)\rangle = \langle N_{\rm c}(M)\rangle \times (1 + \langle N_{\rm s}(M)\rangle) \tag{2.23}$$

where the number of central galaxy is either zero or one with the mean given by

$$\langle N_{\rm c}(M)\rangle = \exp\left(\frac{-M_{\rm min}}{M}\right) \tag{2.24}$$

We assume that only haloes with a central galaxy are allowed to host satellite galaxies. In such a halo, the satellite galaxies are distributed following an NFW profile (Navarro et al., 1997) around a central galaxy at the centre of the halo. We also assume that their numbers follow a Poisson distribution (Kravtsov et al., 2004) with a mean

$$\langle N_{\rm s}(M)\rangle = \left(\frac{M}{M_1}\right)^{\alpha} \tag{2.25}$$

The NFW profile is parametrised by the concentration parameter $c \equiv r_{\rm vir}/r_{\rm s}$ where $r_{\rm vir}$ is the virial radius and $r_{\rm s}$ is the characteristic scale radius. We assume the Bullock et al. (2001) parametrisation of the halo concentration as a function of mass and redshift,

$$c(M,z) \approx \frac{9}{(1+z)}\left(\frac{M}{M_*}\right)^{-0.13}, \tag{2.26}$$

where M_* is the typical collapsing mass and is determined by solving Eq. 2.42 with $\sigma(M_*) = \delta_c(0)$.

The galaxy number density predicted by a given HOD is then

$$n_{\rm g} = \int {\rm d}M\, n(M)\, \langle N(M)\rangle \tag{2.27}$$

where $n(M)$ is the halo mass function, here we use the model given by Sheth and Lemson (1999). The effective galaxy linear bias can be determined from the HOD;

$$b_{\rm lin} = \frac{1}{n_{\rm g}} \int {\rm d}M\, n(M) b(M) \left\langle N(M) \right\rangle , \tag{2.28}$$

where $b(M)$ is the halo bias as a function of mass, for which we use the model of Sheth, Mo, and Tormen (2001) plus the improved parameters of Tinker et al. (2005) (see §2.5.1, Eq. 2.41). The average mass of haloes hosting such galaxy population is then

$$M_{\rm eff} = \frac{1}{n_{\rm g}} \int {\rm d}M\, n(M) M \left\langle N(M) \right\rangle \tag{2.29}$$

And the satellite fraction of the galaxy population is given by

$$F_{\rm sat} = \frac{1}{n_{\rm g}} \int {\rm d}M\, n(M) \left\langle N_{\rm c}(M) \right\rangle \left\langle N_{\rm s}(M) \right\rangle \tag{2.30}$$

The galaxy power spectrum/correlation function can then be modelled as having the contribution at small scales arises from galaxy pairs in the same dark matter halo (1-halo term). On the other hand, the galaxy pairs in two separate haloes (2-halo term) dominates at larger scales,

$$P(k) = P_{\rm 1h} + P_{\rm 2h} \tag{2.31}$$

The 1-halo term can be distinguished into central-satellite, $P_{\rm cs}(k)$, and satellite-satellite, $P_{\rm ss}(k)$, contributions (see e.g. Skibba and Sheth, 2009);

$$P_{\rm cs}(k) = \frac{1}{n_{\rm g}^2} \int {\rm d}M\, n(M) 2 \left\langle N_{\rm c}(M) \right\rangle \left\langle N_{\rm s}(M) \right\rangle u(k, M), \tag{2.32}$$

and

$$P_{\rm ss}(k) = \frac{1}{n_{\rm g}^2} \int {\rm d}M\, n(M) \left\langle N_{\rm c}(M) \right\rangle \left\langle N_{\rm s}(M) \right\rangle^2 u(k, M)^2, \tag{2.33}$$

where $u(k, M)$ is the Fourier transform of the NFW profile and we have simplified the number of satellite-satellite pairs $\langle N_{\rm s}(N_{\rm s} - 1) \rangle$ to $\langle N_{\rm s}(M) \rangle^2$, i.e. Poisson distribution.

For 2-halo term, we implement the halo exclusion, '$n_{\rm g}'$-matched', and scale-dependent halo bias, $b(M, r)$, of Tinker et al. (2005);

$$P_{2\mathrm{h}}(k,r) = P_{\mathrm{m}}(k) \times \frac{1}{n_{\mathrm{g}}'^2} \times \left[\int_0^{M_{\mathrm{lim}}(r)} \mathrm{d}M\, n(M) b(M,r) \langle N(M)\rangle\, u(k,M)\right]^2, \quad (2.34)$$

where $P_{\mathrm{m}}(k)$ is a non-linear matter power spectrum (see §2.4.2), $M_{\mathrm{lim}}(r)$ is the mass limit at separation r due to halo exclusion and n_{g}' is the restricted galaxy number density (Eq. B13 of Tinker et al., 2005). The scale-dependent halo bias is given by (Tinker et al., 2005)

$$b^2(M,r) = b^2(M) \frac{[1+1.17\xi_{\mathrm{m}}(r)]^{1.49}}{[1+0.69\xi_{\mathrm{m}}(r)]^{2.09}}, \quad (2.35)$$

where ξ_{m} is the non-linear correlation function (see §2.4.2).

The galaxy correlation function is then the Fourier transform of the power spectrum which can be calculated separately for 1- and 2-halo terms. For the 2-halo term, we need to correct the galaxy pairs from the restricted galaxy density to the entire galaxy population. This is done by

$$1+\xi_{2\mathrm{h}}(r) = \left(\frac{n_{\mathrm{g}}'}{n_{\mathrm{g}}}\right)^2 \left[1+\xi_{2\mathrm{h}}'(r)\right], \quad (2.36)$$

where $\xi_{2\mathrm{h}}'(r)$ is the Fourier transform of Eq. 2.34.

We then project the predicted galaxy correlation function to $w(\theta)$ using Eq. 2.14 for a range of HOD parameters. The best-fit model for each of our sample is then determined from chi-square minimisation using the full covariance matrix. Note that we exclude angular bins corresponding to scales smaller than 0.1 h^{-1} Mpc because of any uncertainty in the $\xi(r)$ model at the very small scales, $r \lesssim 0.01\ h^{-1}$ Mpc, can have a strong effect on $w(\theta)$ even at these scales due to the projection. The best-fit M_{min}, M_1 and α and the associated values for n_{g}, M_{eff}, F_{sat} and b_{lin} are given in Table 2.4. The 1σ uncertainties on the best-fit M_{min}, M_1 and α are determined from the parameter space where $\Delta\chi^2 \leq 1$. For n_{g}, M_{eff}, F_{sat} and b_{lin} which depend on the three main HOD parameters, this becomes $\Delta\chi^2 \leq 3.53$. Fig. 2.12 shows the best-fit HOD for each sample, the coloured solid lines are the mean number of LRGs per halo with the central and satellite contributions shown separately as the dashed and dotted lines, respectively.

As expected, the LRGs populate rather massive dark matter haloes with the masses $\approx 10^{13} - 10^{14} h^{-1} M_{\odot}$. At approximately the same redshift, the more luminous samples, 2SLAQ* and AAΩ*, are hosted by more massive haloes than the fainter samples. Most

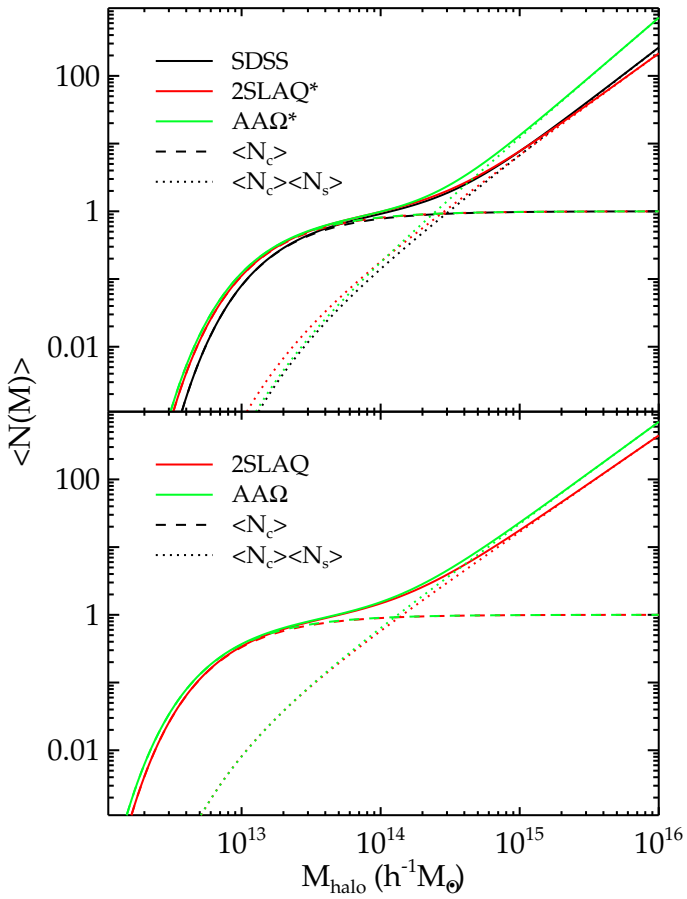

Figure 2.12: The mean number of LRGs per halo as a function of mass (solid lines) from the best-fit HOD for the SDSS, 2SLAQ*, AAΩ* samples (top) and 2SLAQ, AAΩ samples (bottom). The central and satellite contributions for each sample are shown as the dashed and dotted lines.

Table 2.4: Best-fit HOD parameters.

Sample	$\bar{z}$	$M_{\rm min}$	M_1	α	$n_{\rm g}$	$M_{\rm eff}$	$F_{\rm sat}$	$b_{\rm lin}$	$\chi^2_{\rm red}$
		$(10^{13}h^{-1}M_\odot)$	$(10^{13}h^{-1}M_\odot)$		$(10^{-4}h^3\ {\rm Mpc}^{-3})$	$(10^{13}h^{-1}M_\odot)$	(per cent)		
SDSS	0.35	2.5 ± 0.2	29.5 ± 2.5	1.58 ± 0.04	1.3 ± 0.4	6.4 ± 0.5	8.1 ± 1.8	2.08 ± 0.05	3.1
2SLAQ*	0.53	2.2 ± 0.1	27.3 ± 2.0	1.49 ± 0.03	1.3 ± 0.3	4.7 ± 0.2	7.0 ± 0.8	2.21 ± 0.04	7.7
AAΩ*	0.67	2.1 ± 0.1	23.8 ± 2.0	1.76 ± 0.04	1.2 ± 0.2	4.3 ± 0.2	5.7 ± 0.7	2.36 ± 0.04	10.1
2SLAQ	0.55	1.10 ± 0.07	13.6 ± 1.1	1.42 ± 0.02	3.2 ± 0.5	3.4 ± 0.2	10.0 ± 1.1	1.97 ± 0.03	14.2
AAΩ	0.68	1.02 ± 0.03	12.6 ± 1.0	1.50 ± 0.03	3.1 ± 0.4	3.0 ± 0.1	9.0 ± 0.09	2.08 ± 0.03	13.6

of the LRGs, > 90 per cent, are central galaxies in their dark matter haloes, the satellite fractions is only 10 per cent or less with an increasing trend towards low redshift. This can be explained in the framework of halo mergers at lower redshift (see §2.5.2). The best-fit linear bias factors for all samples are in excellent agreement with the values derived in §2.4.2. Also the galaxy number density from the best-fit halo model is consistent with that derived from Eq. 2.18 (see Tables 2.2 and 2.3).

Note that, to first order, our best-fit HODs are compatible with the measurements from other authors although a direct comparison with samples selected differently may not be simple. For example, our SDSS sample has similar space density (although at higher redshift, $z = 0.35$ versus 0.3) as the sample studied by Seo et al. (2008). Our $M_1/M_{\rm min}$ and satellite fraction are in excellent agreement with their model 11 (their best-fit N-body evolved HOD). But their α is somewhat lower which is caused by the higher $\sigma_8 = 0.9$ value (Wake et al., 2008) and the lower average redshift. Their M_1 and $M_{\rm min}$ are also somewhat higher than our best-fit values for the same reason as for α. Another example, our best-fit M_1, $M_{\rm min}$, b_{lin} and $F_{\rm sat}$ for 2SLAQ* sample are in good agreement with Wake et al. (2008) $z = 0.55$ 2SLAQ selection, although our values are somewhat higher which may be due to our lower galaxy number density, implying that our sample contains rarer and more biased objects.

The best-fit models for $w(\theta)$ are shown in Fig. 2.13, comparing to the data. Both the models and data are scaled to account for the projection effect (see §2.4.2) and are plotted at the depth of AAΩ*/AAΩ sample. We immediately see that while the fits at the large scales ($r \gtrsim 3\ h^{-1}\,$Mpc) are good, the fits at the small scales and at $r \approx 1 - 2\ h^{-1}\,$Mpc are rather poor especially for the higher redshift samples. This is evident in the high best-fit reduced chi-square values in Table 2.4. Given our small error bars, this may indicate that a more complicated halo model may be needed, e.g. five/six parameters HOD, an improved halo-exclusion model (see Fig. 11 of Tinker et al., 2005), or different halo concentration parametrisation. Another important point to note is that the HOD formalism assumes a volume-limited sample, which we do not have here. This means that our observed galaxy number density corresponds to a cut-off which evolves with redshift rather than a cut-off in halo mass or LRG luminosity. Nevertheless, to first order the HOD fits generally describe the shape and amplitude of our measured $w(\theta)$ and we believe that the derived $b_{\rm lin}$ and $M_{\rm eff}$ are reasonably robust despite the statistically poor fits.

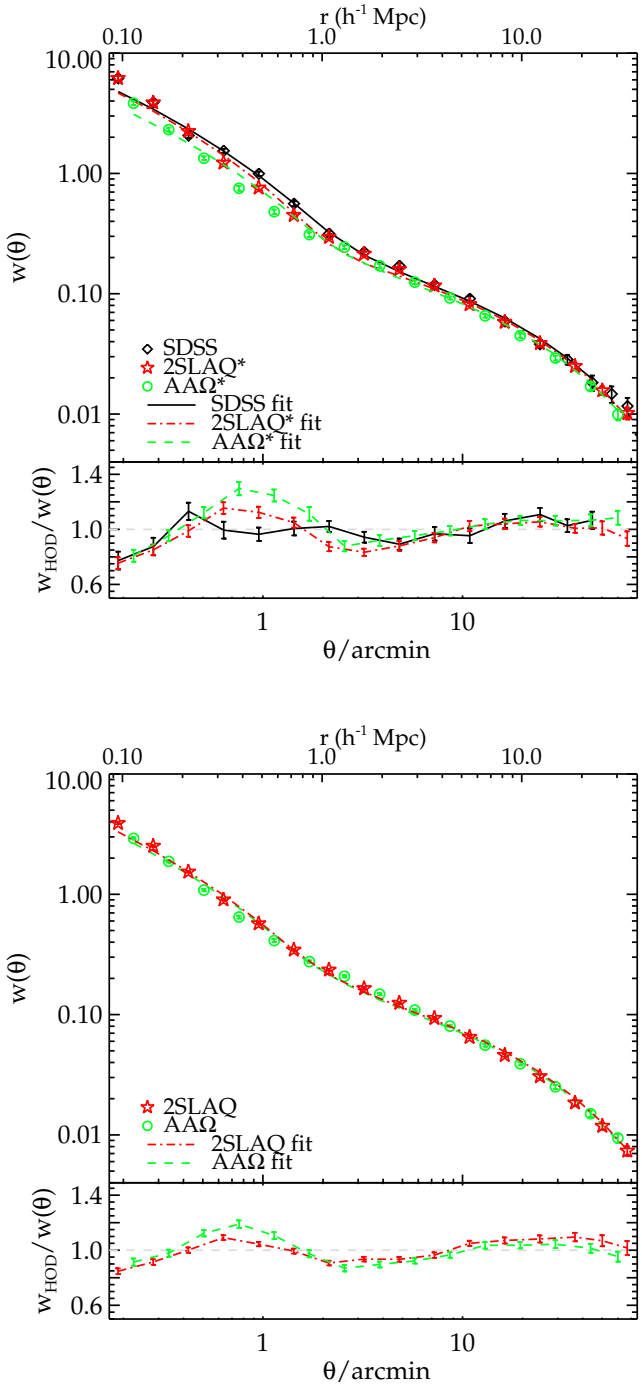

Figure 2.13: The best-fit HOD models for the SDSS, 2SLAQ*, AAΩ* samples (left) and 2SLAQ, AAΩ samples (right). These are scaled to the AAΩ*/AAΩ depth similar to that shown in Fig. 2.11b. The bottom panels show the ratios between the best-fit HOD models and the measured correlation functions.

2.5 Evolution of LRG clustering and dark matter halo masses

2.5.1 Intermediate scales

We study the LRGs clustering and dark matter halo mass evolution by employing the methods used by Croom et al. (2005) and da Ângela et al. (2008) to analyse their QSO samples. We then proceed by considering the small-scale clustering evolution in the framework of the halo model.

Clustering evolution

In this section, we make an attempt to quantify the clustering evolution of the LRGs via the use of the $w(\theta)$'s measured from the number-density (roughly luminosity) matched samples as presented in the last section. We shall first compare the result at the intermediate scales, $1 \lesssim r \lesssim 20\ h^{-1}\,\mathrm{Mpc}$, to the simple long–lived model of Fry (1996). The model assumes that galaxies are formed at a particular time in the past and their clustering evolution is determined by the influence of gravitational potential where no galaxies are destroyed/merged or new population created, hence preserving the comoving number density. In such a model the galaxy linear bias is given by

$$b(z) = 1 + \frac{b(0) - 1}{D(z)} \tag{2.37}$$

and as we saw in §2.4.2 that $\xi_m(r, z) = D^2(z)\xi_m(r, 0)$, the clustering evolution is such that

$$\xi_g(r, z) = \left[\frac{b(0) + D(z) - 1}{b(0)}\right]^2 \xi_g(r, 0) \tag{2.38}$$

We shall also compare the data directly to the linear theory prediction for dark matter evolution in the ΛCDM model, $\xi(r, z) \propto D^2(z)$. In addition, we shall also check the stable clustering and no–evolution (comoving) clustering models of Phillipps et al. (1978). The stable model refers to clustering that is virialised and therefore stable in proper coordinates. For a $\xi(r)$ with r measured in comoving coordinates, the stable model has evolution $\xi(r) \propto (1 + z)^{\gamma-3}$ and the no-evolution model has $\xi(r)$ independent of redshift. At these intermediate scales, the clustering is unlikely to be virialised so the stable model is shown mainly as a reference point. From Eq. 2.38, the no–evolution model represents the high bias limit of the long–lived model of Fry (1996). The stable and comoving models are similar to the long–lived model in that they both assume that the comoving galaxy density remains constant with redshift.

In order to quantify the clustering amplitude of each sample, we shall use the integrated correlation function in a 20 h^{-1} Mpc sphere as also utilised by several authors (e.g. Croom et al., 2005; Ross et al., 2008b; da Ângela et al., 2008). The volume normalisation of this quantity is then given by

$$\xi_{20} = \frac{3}{20^3} \int_0^{20} \xi(r) r^2 dr \tag{2.39}$$

The 20 h^{-1} Mpc radius is chosen to ensure a large enough scale for linear theory to be valid and in our case the power-law with $\gamma \approx 1.8$ remains a good approximation up to $\approx 20\ h^{-1}$ Mpc. Furthermore, the non-linearity at small scales does not significantly affect the clustering measurements, when averaged over this range of scales.

The integrated correlation function, ξ_{20}, approach also provides another means of measuring the linear bias of the sample. For this, we again assume scale-independent bias which is a reasonable assumption in the linear regime. The bias measured in this way is given by

$$b_g(z) = \sqrt{\frac{\xi_{20,g}}{\xi_{20,m}}} \tag{2.40}$$

The mass integrated correlation functions are again computed assuming our fiducial cosmological model using the matter power spectra output from CAMB. The values for $\xi_{20,m}$ used here are 0.153, 0.126 and 0.112 for $z = 0.35$, 0.55 and 0.68, respectively.

The $\xi_{20,g}$ is calculated using the best-fit double power-law parameters for each sample. The results are plotted in Fig. 2.14a along with the best-fit linear theory evolution (long–dashed line), stable clustering (dotted line), long-lived (dashed line) and no-evolution models (dot-dot-dashed line). The linear bias factors measured using the ξ_{20} approach are given in Table 2.5 and also presented in Fig. 2.14b. The bias factors determined here are in good agreement with the large-scale ΛCDM (§2.4.2) and HOD (§2.4.3) best-fit models.

To extend the redshift range, we shall compare our results to the clustering of early-type galaxies in 2dFGRS studied by Norberg et al. (2002b) that roughly match the absolute magnitude of our samples after the $K + e$ correction. These are the samples with $-21.0 > M_{b_j} - 5\log_{10} h > -22.0$ and $-20.5 > M_{b_j} - 5\log_{10} h > -21.5$, being compared to the SDSS/2SLAQ*/AAΩ* and 2SLAQ/AAΩ data and denoted N02E1 and N02E2 in Table 2.5, respectively. We proceed in a similar fashion to the procedure described above and use the author's best-fit power-law to estimate the $\xi_{20,g}$'s and hence the bias values

Table 2.5: Summary of the estimated LRG and 2dFGRS early-type galaxy bias factor and $M_{\rm DMH}$ as a function of redshift and luminosity.

Sample	$\overline{z}$	$\overline{M_i}$ $-5\log_{10}h$	b	$M_{\rm DMH}$ $(10^{13}h^{-1}M_\odot)$
SDSS	0.35	-22.67	2.02 ± 0.04	4.1 ± 0.3
2SLAQ*	0.53	-22.69	2.16 ± 0.04	3.3 ± 0.2
AAΩ*	0.67	-22.60	2.33 ± 0.03	3.1 ± 0.1
2SLAQ	0.55	-22.40	1.91 ± 0.03	2.1 ± 0.1
AAΩ	0.68	-22.37	2.04 ± 0.02	1.9 ± 0.1
N02E1	≈ 0.1	-22.68	1.90 ± 0.23	6.2 ± 2.2
N02E2	≈ 0.1	-22.40	1.66 ± 0.20	3.9 ± 1.5

(see Table 2.5).

Both luminosity bins can be reasonably fitted by the long–lived model. The best-fit models for the $M_i - 5\log_{10}h = -22.7$ and -22.4 samples have $b(0) = 1.93 \pm 0.02$ and 1.74 ± 0.02 with $\chi^2 = 7.34$ (3 d.o.f) and 4.11 (2 d.o.f) respectively, i.e. $1.5-1.9\sigma$ deviation. This is interesting given the lack of number density evolution seen in the LRG luminosity function by Wake et al. (2006). Nevertheless, it is intriguing that such a simple model gets so close to fitting data over the wide redshift range analysed here.

The stable model and the linear theory (with constant bias) model rise too quickly as the redshift decreases, excluded at $> 99.99\%$ confidence. However, the comoving model also gives a good fit to the SDSS/2SLAQ*/AAΩ* data in Fig. 2.14a, as expected from the lack of evolution shown in Fig. 2.11b. For this model to be exactly correct it would suggest that there was an inconsistency in these results with the underlying ΛCDM halo mass function. More certainly, we conclude that the evolution of the LRG clustering seems very slow. This general conclusion agrees with previous work (White et al., 2007; Wake et al., 2008). The latter author also only found a marginal rejection of the long-lived model from the large-scale clustering signal (1.8σ) compared to 1.9σ here. They found a much stronger rejection of a 'passive' evolution model from the small-scale LRG clustering and we shall return to this issue in §2.5.2.

LRG dark matter halo masses

The large-scale galaxy bias is roughly the same as that of the dark matter haloes which is a known function of mass threshold. Thus by measuring the clustering of the LRGs one can infer the typical mass of the haloes they reside in. The procedure employed here is similar to that used by Croom et al. (2005) and da Ângela et al. (2008) to estimate the dark matter halo masses of QSOs.

An ellipsoidal collapse model relating a halo bias factor to its mass was developed by Sheth et al. (2001) as an improvement over an earlier spherical collapse model of Mo and White (1996). In this analysis, we shall use the expression given in Sheth et al. (2001) and the revised parameters of Tinker et al. (2005) which were calibrated to give better fits to a wide range of σ_8 values for variants of ΛCDM model;

$$b(M_{\rm DMH},z) = 1+\frac{1}{\sqrt{a}\delta_c(z)}\Bigg[\sqrt{a}(a\nu^2)+\sqrt{a}b(a\nu^2)^{1-c} - \frac{(a\nu^2)^c}{(a\nu^2)^c+b(1-c)(1-c/2)}\Bigg], \quad (2.41)$$

where $a=0.707$, $b=0.35$ and $c=0.80$. ν is defined as $\nu=\delta_c(z)/\sigma(M_{\rm DMH},z)$. δ_c is the critical density for collapse, and is given by $\delta_c=0.15(12\pi)^{2/3}\Omega_m(z)^{0.0055}$ (Navarro et al., 1997). The rms fluctuation of the density field as a function of mass $M_{\rm DMH}$ at redshift z is $\sigma(M_{\rm DMH},z)=\sigma(M_{\rm DMH})D(z)$ where $\sigma(M_{\rm DMH})$ is given by

$$\sigma(M_{\rm DMH})^2=\frac{1}{2\pi^2}\int_0^\infty k^2P(k)w(kr)^2dk \quad (2.42)$$

$P(k)$ is the linear power spectrum of density perturbations and $w(kr)$ is the window function, given by (Peebles, 1980)

$$w(kr)=3\frac{\sin(kr)-kr\cos(kr)}{(kr)^3}, \quad (2.43)$$

for a spherical top-hat function. The radius r can be related to mass via

$$r=\left(\frac{3M_{\rm DMH}}{4\pi\rho_0}\right)^{1/3}, \quad (2.44)$$

where $\rho_0=\Omega_m^0\rho_{crit}^0$ is the present mean density of the Universe, given by $\rho_0=2.78\times10^{11}\Omega_m^0h^2M_\odot$ Mpc^{-3}. Here, we use the transfer function, $T(k)$, fitting formula given by Eisenstein and Hu (1998) to construct $P(k)$, assuming our fiducial cosmology (see §2.4.2).

The estimated dark matter halo masses of the LRG samples are given in Table 2.5 and plotted in Fig. 2.14c. Note that the formalism of estimating dark matter halo masses

from the galaxy biases used here assumes one galaxy per halo and can overestimate the threshold mass for a given value of bias (Zheng et al., 2007). This is particularly true when we consider the mass estimated from Eq. 2.41 as the threshold mass, minimum mass required for a halo to host at least one galaxy and compare the results derived here to $M_{\rm min}$ from the best-fit HOD (§2.4.3). However, if it is used as an estimate for the average mass of the host halo then it is under-estimated by ≈40 per cent compared to the value given by the HOD due to the one galaxy per halo assumption.

Next, we attempt to fit the derived dark matter halo masses of these LRGs to the halo merger framework in hierarchical models of galaxy formation. We use the formalism discussed by Lacey and Cole (1993) to predict the median $M_{\rm DMH}$ of the descendants of virialised haloes at $z = 1$ for a given halo mass and fit this to our data. In essence, the model gives the probability distribution of the haloes with mass M_1 at time t_1 evolving into a halo of mass M_2 at time t_2 via merging. Fig. 2.14c shows the best-fit models for the $M_{\rm DMH}$ evolution estimated in this way. These models appear to be good fits to both luminosity bins with the best-fit $M_{\rm DMH}(z = 1) = 2.32 \pm 0.07 \times 10^{13}\ h^{-1}\,M_{\odot}$ and $1.47 \pm 0.05 \times 10^{13}\ h^{-1}\,M_{\odot}$ for the $\ell \gtrsim 3L^*$ and $\gtrsim 2L^*$ samples, respectively.

The most massive haloes hosting these luminous early-type galaxies appear to have tripled their masses over the past 7 Gyr (i.e. half cosmic time) in stark contrast to the little evolution observed in the LRG stellar masses over the same period (see e.g. Wake et al., 2006; Cool et al., 2008). This lack of evolution contradicts the predictions in the standard hierarchical models of galaxy formation where one expects the most massive galaxies to form late via 'dry' merging of many less massive galaxies. However, this comes with a caveat that the $M_{\rm DMH}$ at $z \sim 0$ is an extrapolation (assuming Lacey and Cole (1993) halo merging model) of the $z = 0.35 - 0.7$ measurements and the constraint on the $M_{\rm DMH}(z = 0.1)$ is much weaker than the higher redshift results.

2.5.2 Small-scale clustering evolution

Finally, we discuss the evolution of the correlation function at scales corresponding to $r < 1\ h^{-1}\,$Mpc. We concentrate on comparing the number density matched AAΩ* and 2SLAQ* samples to the SDSS sample. As can be seen in Fig. 2.11b, while at larger scales the $w(\theta)$ show amplitudes that are remarkably independent of redshift, at smaller scales the high redshift AAΩ* sample appears to have a lower amplitude than the lower redshift surveys. Here, we compare the clustering in non-linear regime to two clustering models.

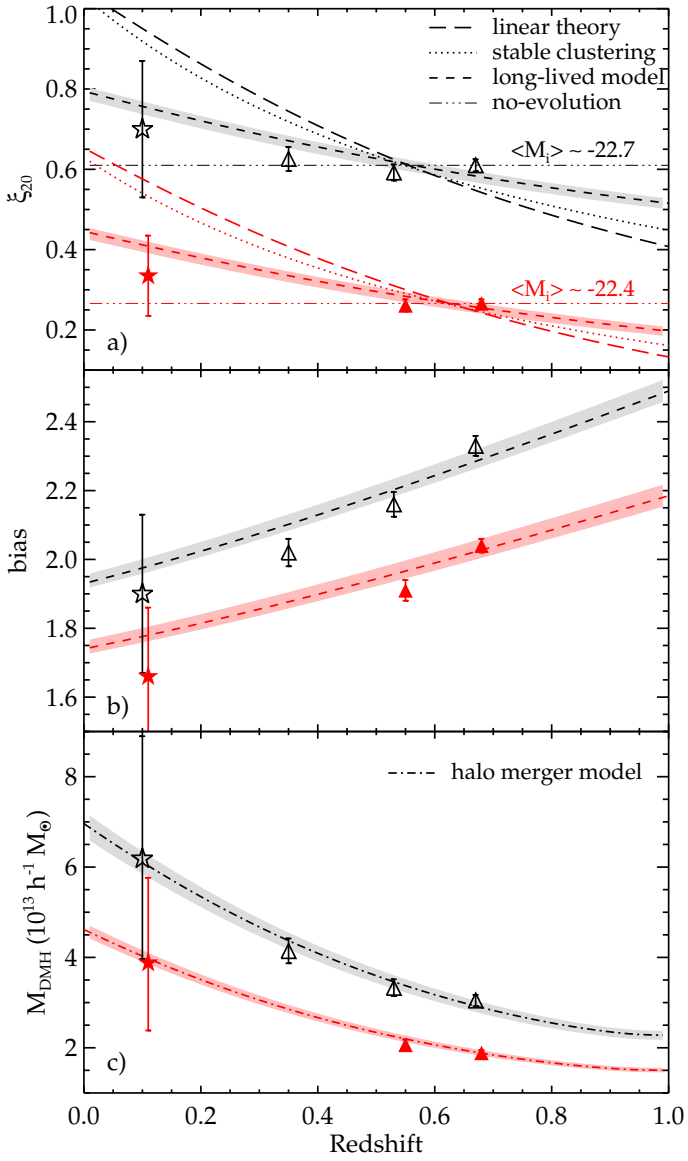

Figure 2.14: (a): The LRG ξ_{20} measurements as a function of redshift and luminosity. The data at $z \approx 0.1$ (stars) are taken from the correlation functions of early-type galaxies in 2dFGRS (Norberg et al., 2002b). Open and solid symbols correspond to the samples with median absolute magnitude, $M_i - 5\log_{10} h = -22.7$ (SDSS/2SLAQ*/AAΩ*) and -22.4 (2SLAQ/AAΩ). The best fits for various models are also shown (see text for more details). The lower luminosity data have been lowered by 0.2 for clarity. (b): The LRG linear biases as a function of redshift and luminosity, comparing to the best–fit long–lived model. (c): The typical mass of dark matter haloes occupied by the LRGs as estimated from the halo bias function. The dot-dashed lines are the best-fit evolution model of dark matter halo mass via the merger framework (Lacey and Cole, 1993).

Stable clustering model

The stable model describes the clustering in the virialised regime and hence stable (unchanged) in proper coordinates (e.g. Phillipps et al., 1978). Therefore, assuming this model one expects the spatial correlation function to evolve as $\xi(r) \propto (1+z)^{\gamma-3}$, where r is measured in comoving coordinates and γ is the power-law slope of the correlation function. Fig. 2.15 shows the small-scale, $r \lesssim 1\ h^{-1}\,\mathrm{Mpc}$, $w(\theta)$ of the SDSS sample plus its best-fit double power-law model, comparing to the evolved $w(\theta)$ from the $z1 = 0.53$ and 0.67 best-fit models. Their ratios to the $z = 0.35$ best-fit model are shown in the bottom panel with the shaded regions representing 1σ uncertainties in the best-fit models. We see that the stable model evolved from $z1 = 0.67$ under-predicts the $z = 0.35$ $w(\theta)$ somewhat but otherwise is within the 1σ regions of each other. The agreement between the evolved $z1 = 0.53$ and the $z = 0.35$ is better given that the redshift difference is smaller. Note that the stable clustering model over-predicts the clustering amplitude at $r \gtrsim 1\ h^{-1}\,\mathrm{Mpc}$ which is also observed in Fig. 2.14a as expected.

The physical picture that is suggested is that the inflexion in the correlation function may represent the boundary between a virialised regime at small scales and a comoving or passively evolving biased regime at larger scales. As noted by Hamilton et al. (1991) and Peacock and Dodds (1996), the small scale, non-linear, DM clustering is clearly expected from N-body simulations to follow the evolution of the virialised clustering model. However, for galaxies in an ΛCDM context, the picture may be more complicated.

For example, by comparing the 2SLAQ and SDSS LRG redshift surveys using the semi-projected correlation function, Wake et al. (2008) have suggested that a passively evolving model is rejected, weakly from the large scale evolution but more strongly from the evolution at small scales. Wake et al. (2008) interpret the clustering evolution using a HOD description based on the ΛCDM halo mass function. Their 'passive' model predicts a far faster evolution at small scales than is given by our stable clustering (see Fig. 2.16). Our stable model is certainly passive in that it is based on the idea that the comoving number density of galaxies is independent of redshift. However, the passive HOD model of Wake et al. (2008) requires only 7.5 per cent of LRGs to merge between z=0.55 and z=0.19 to reconcile the slow LRG density and clustering evolution in the ΛCDM model. We shall see in the the next section if this model can also accommodate our z=0.68 clustering result while maintaining such a low merger rate.

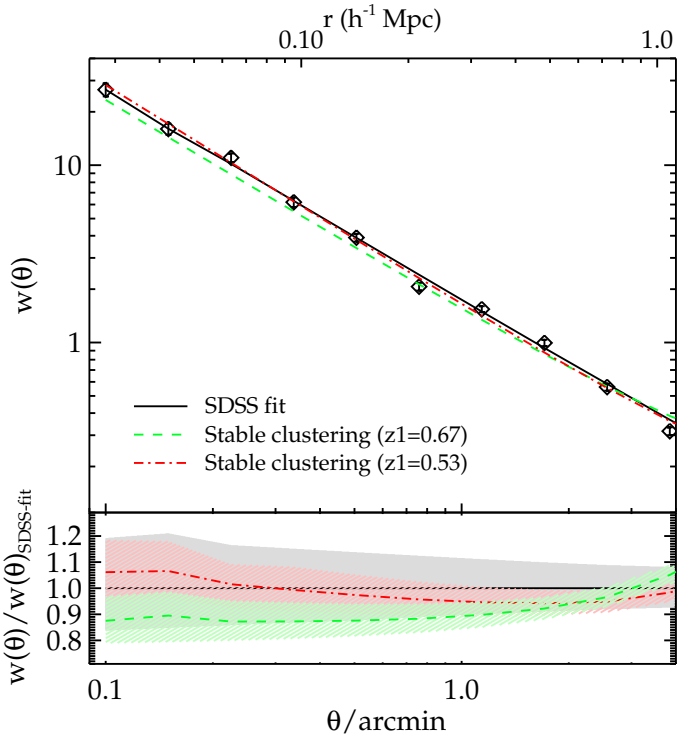

Figure 2.15: The small-scale $w(\theta)$ at $z = 0.35$ evolved from the best-fit double power-law of AAΩ* (green dashed line) and 2SLAQ* (red dot-dashed line) samples, assuming stable clustering model. The ratios of the evolved $w(\theta)$'s to the best-fit double power-law of SDSS sample are shown in the bottom panel. The shaded regions signify 1σ uncertainties in the best-fit models.

HOD evolution

In §2.5.1, we found using the large-scale linear bias that the long-lived model (Fry, 1996) is only marginally rejected at 1.5-1.9σ. This is in good agreement with the similar analysis of Wake et al. (2008). However, they argued that if the small-scale clustering signal was also taken into consideration, the long-lived model can be ruled out at much higher significance (>99.9 per cent).

Recall that our goodness-of-fit (based on the minimum χ^2) for the halo models is rather poor (see table 2.4). This may be an indication that a more complicated model may be needed, e.g. five-parameters HOD and/or a better two halo-exclusion prescription etc., given our small error bars. Nevertheless, the HOD fit generally describe the shape and amplitude of our measured $w(\theta)$ between 0.1-40 h^{-1} Mpc. Therefore, at the risk of over-interpreting these HOD fits, we make a further test of the long-lived model by evolving the best-fit HODs of the higher redshift samples to the SDSS LRG average

redshift.

Following the methods described in (Wake et al., 2008, and references therein), the mean number of galaxies hosted by haloes of mass M at later time, $z0$, is related to the mean number of galaxies in haloes of mass m, $\langle N(m)\rangle$, at earlier time, $z1$, via

$$\begin{aligned}\langle N(M)\rangle &= \int_0^M \mathrm{d}m\, N(m,M)\,\langle N(m)\rangle \\ &= \int_0^M \mathrm{d}m\, N(m,M)\,\langle N_\mathrm{c}(m)\rangle\,[1+\langle N_\mathrm{s}(m)\rangle] \\ &= C(M)+S(M), \end{aligned} \tag{2.45}$$

where $N(m,M)$ is the conditional halo mass function of Sheth and Tormen (2002) which is the generalisation of Lacey and Cole (1993) results, $C(M)$ and $S(M)$ are the number of objects which used to be central and satellite galaxies.

We then model the central galaxy counts in the low-redshift haloes assuming that the progenitor counts in these haloes is 'sub-Poisson' (Sheth and Lemson, 1999; Seo et al., 2008; Wake et al., 2008) such that

$$\langle N_\mathrm{c}(M)\rangle = 1-\left[1-\frac{C(M)}{N_\mathrm{max}}\right]^{N_\mathrm{max}}, \tag{2.46}$$

where $N_\mathrm{max}=\mathrm{int}(M/M_\mathrm{min})$. This model is favoured by the Wake et al. (2008) analysis and is also seen in the numerical models of Seo et al. (2008). The mean number of satellite galaxies in the low-redshift haloes is then given by

$$\langle N_\mathrm{c}(M)\rangle\,\langle N_\mathrm{s}(M)\rangle = S(M)+f_\mathrm{no-merge}\,[C(M)-\langle N_\mathrm{c}(M)\rangle]\,, \tag{2.47}$$

where $f_\mathrm{no-merge}$ is the fraction of un-merged low-z satellite galaxies which were high-z central galaxies. This model is called 'central-central mergers' in Wake et al. (2008), where the more massive high-z central galaxies are more likely to merge with one another or the new central galaxy rather than satellite-satellite mergers.

For the long-lived model, we set $f_\mathrm{no-merge}=1$. The results of passively evolving the best-fit HODs from $z1=0.67$ (AAΩ*) and $z1=0.53$ (2SLAQ*) to $z0=0.35$ are shown in Fig. 2.16 along with the SDSS best-fit model. At large scales ($r\geq 5\ h^{-1}\,\mathrm{Mpc}$), the long-lived model can only be marginally rejected at no more than 2σ for the AAΩ* case and is consistent within 1σ in the case of 2SLAQ*. However, if we now consider the small-scale, $r<1\ h^{-1}\,\mathrm{Mpc}$, clustering signal we see from the bottom panel of Fig. 2.16 that the long-lived model becomes increasingly inconsistent with the best-fit model at

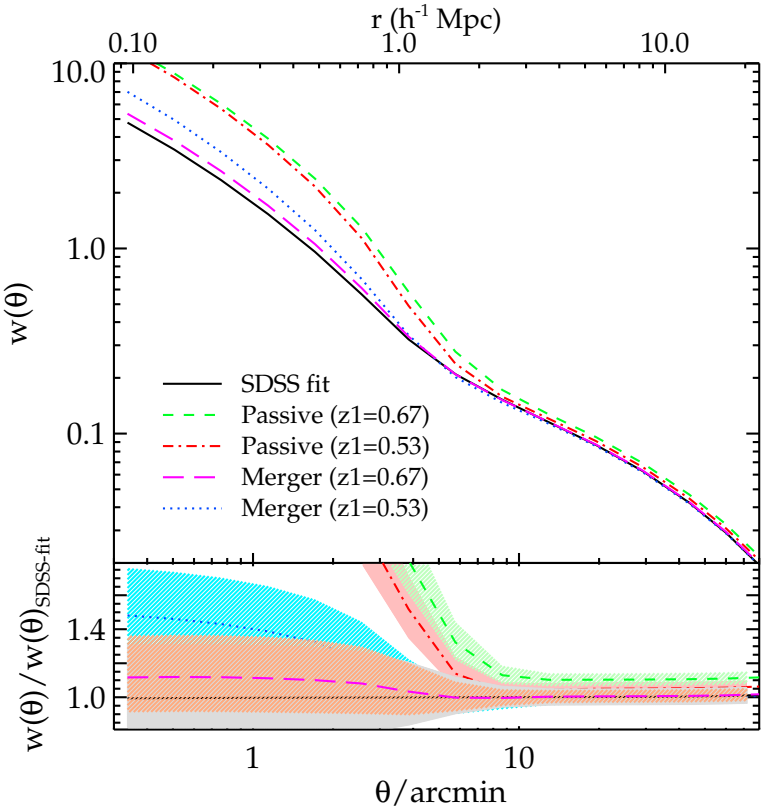

Figure 2.16: The predicted SDSS LRG $w(\theta)$ from passively ($f_{\rm no-merge} = 1$) evolving the best-fit HODs of 2SLAQ* ($z1 = 0.53$, red dot-dashed line) and AAΩ* ($z1 = 0.67$, green dashed line) samples. The results when central galaxies from high redshift samples are allowed to merge (see text for more detail) are also shown, blue dotted and magenta long-dashed lines. The bottom panel shows the ratios of the evolved $w(\theta)$'s to the SDSS best-fit, the shaded regions signify the 1σ uncertainties.

$z = 0.35$. If we take the fiducial scales at 0.5 h^{-1} Mpc as we did in the last section, the long-lived model can be rejected at 98.2 and 99.9 per cent significance using the evolved 2SLAQ* and AAΩ* HODs, respectively. The much higher clustering signal at small scales is caused by far too many satellite galaxies in the low-redshift haloes being predicted by the long-lived model. This also results in the higher satellite fractions than observed; both evolved 2SLAQ* and AAΩ* give $F_{\rm sat} = 18 \pm 1$ per cent at $z = 0.35$ compared to 8.1 ± 1.8 seen in the SDSS best-fit.

Next, if we assume the central-central mergers model (Wake et al., 2008) and attempt to match the large-scale clustering signal of the evolved to the $z = 0.35$ best-fit model. As argued by Wake et al. (2008) and here that this is more likely to happen than the satellite-satellite merging case. The $f_{\rm no-merge}$ parameters in Eq. 2.47 required to give the best matches to the large-scale clustering amplitude of the SDSS best-fit is 0.2 and 0.1 for the 2SLAQ* and AAΩ* case, respectively. The new $w(\theta)$'s determined from these models are plotted in Fig. 2.16 as the blue dotted and magenta long-dashed lines. We can see that the $z1 = 0.67$ evolved $w(\theta)$ at small scales is in excellent agreement with the SDSS best-fit model. The predicted satellite fraction, $F_{\rm sat} = 7.8 \pm 0.9$, is also consistent with the SDSS best-fit value. For the $z1 = 0.53$ case, the small-scale clustering signal is still somewhat stronger that the SDSS best-fit model but otherwise are within 1σ confidence regions of each other, and the predicted $F_{\rm sat} = 10.5 \pm 1.3$ is also somewhat higher than the best-fit value. The galaxy number density is reduced due to these central-central merger by ≈6 and 11 per cent for the $z1 = 0.53$ and 0.67, respectively. However, note that this is 2–3 times smaller than the fractional errors of our best-fit $n_{\rm g}$, ≈ 20 per cent.

In order to get a handle on the merger rates which can then be compared to the previous results of White et al. (2007) and Wake et al. (2008), we follow their method of adjusting the galaxy number density. This is because for this type of analysis the galaxy samples at different redshifts are usually designed to have the same space density. Whereas merging means that the space density of the low-z sample must be reduced unless there are new galaxies created via merging of the fainter objects which fail to be in the high-z sample but become bright enough to be in the low-z sample. To account for such an effect by physically removing galaxies in a sample is rather difficult to do in practice as argued by Wake et al. (2008). White et al. (2007) and Wake et al. (2008) adjusted the mass-scale of the low-z HOD fit by several per cents which reduce the space density and increase the clustering signal and hence require lower amount of merging of the high-z population needed to match the low-z measurement. Increasing the $f_{\rm no-merge}$ factor

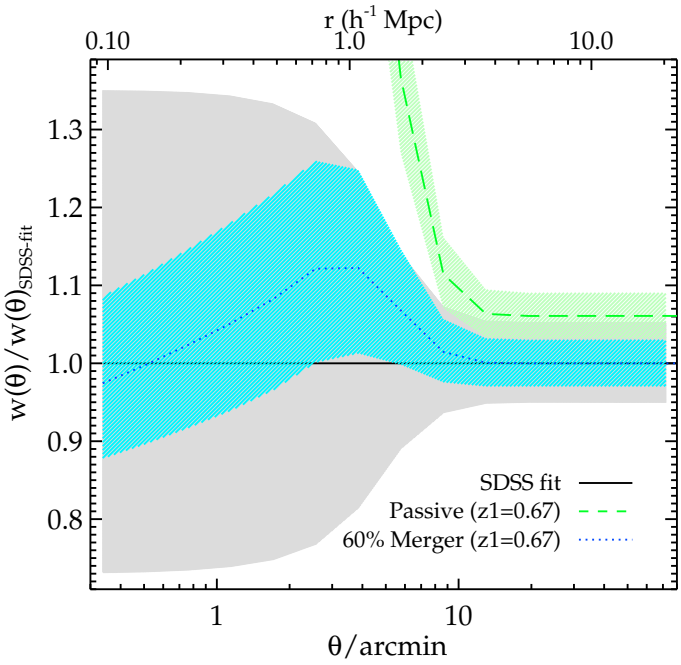

Figure 2.17: The ratio of the evolved $w(\theta)$ to the SDSS best-fit model with the HOD mass-scale increased by 12 per cent.

in Eq. 2.47 results in a higher galaxy number density and clustering signal. Therefore the opposing effect of adjusting mass-scaling and merging fraction on the galaxy number density ensures that a unique solution which simultaneously satisfy the galaxy number density and the clustering signal (at large scales) of the low-z sample can be reached.

For the $z1 = 0.67$ (0.53), we increase the mass-scale of $z = 0.35$ HOD fit by 12 (7) per cent and allow 60 (50) per cent of the high-z central galaxies to merge in order to get the matched large-scale bias of 2.12 (2.10) and $n_{\rm g} = 1.12$ (1.19) $\times 10^{-4} h^3\,{\rm Mpc}^{-3}$. This yields the merger rate between $z = 0.67$ (0.53) and $z = 0.35$ of ≈ 6.6 (5) per cent, i.e. ≈ 2.8 (3.4) per cent Gyr^{-1}. The evolved $w(\theta)$ divided by the model at $z = 0.35$ with increased mass-scaled HOD fit is shown in Fig. 2.17. As noted earlier that the reduction in the galaxy number density is small compared to its best-fit fractional error which means that our constraints on these merger rates are rather weak. However, to first order the merger rates derived here appear to be consistent with the value of 2.4 ± 0.7 and 3.4 per cent Gyr^{-1} found by Wake et al. (2008) and White et al. (2007), respectively.

In summary, the combination of stable clustering and passive evolution model is very close to explaining the clustering evolution of the LRGs at small and large scales. These models are much simpler than the HOD framework which require an understanding of how galaxies populate dark matter haloes and how they and their host haloes merge.

And yet the HOD model only requires $\approx 2-3$ per cent/Gyr of these LRGs to merge in order to explain their slow number density and clustering evolution. On the contrary, the stable model requires the comoving number density to be constant with redshift. This suggests that the simple virialised model may only provide a phenomenological fit to the small-scale clustering evolution in the context of the ΛCDM model.

2.6 Searching for the BAO peak

Next, we inspect the correlation functions at larger scales to make a search for the BAO feature. We first present the raw correlation functions in Fig. 2.18a. Each correlation shows a feature at large scales, the most significant detection comes from the AAΩ sample where the clustering signal at $120' < \theta < 500'$ is detected at more than 4σ significance, $P(< \chi^2) = 1 \times 10^{-6}$ (with covariance matrix) and 3.5σ significance for $200' < \theta < 500'$.

The question is are they real or simply due to systematic error? (see §2.6.1 for a series of systematic tests). Here, we perform a classic scaling test to see if any feature is reproduced at the different depths of the three LRG samples. Given that the samples have intrinsically different r_0 (see Table 2.2), we choose simply to scale in the angular direction only. The SDSS and 2SLAQ LRG correlation functions are scaled in the angular direction to the AAΩ's depth using the average radial comoving distance of each sample. In Fig. 2.18b, we see that the scaling agreement of the large scale, $\theta \approx 300'$, features is poor. Although SDSS shows a moderately strong peak feature, this is not reproduced at the same comoving physical scale in the other two datasets.

Despite this failure of the scaling test, we now attempt to increase the signal to noise ratio by combining the measurements from the three samples using inverse quadrature error weighting. Firstly, the SDSS and 2SLAQ $w(\theta)$'s are scaled in the angular direction to the depth of the AAΩ LRGs (radial comoving distance, $\chi \approx 1737\ h^{-1}$ Mpc as opposed to $\approx 1451\ h^{-1}$ Mpc for 2SLAQ and $\approx 970\ h^{-1}$ Mpc for SDSS) where their amplitudes and errors are then interpolated to the AAΩ's angular bins (i.e. Fig. 2.18b). The amplitudes of the scaled SDSS and 2SLAQ $w(\theta)$'s are then normalised to that of the AAΩ sample's at $10'$. This involves lowering SDSS and 2SLAQ amplitudes by 25 and 15 per cent, respectively. The resulting correlation function is presented in Fig. 2.19 with the arrow showing the expected position of the BAO peak. Note that due to the relatively small statistical errors of the AAΩ LRG compared to other samples, the $w(\theta)$ result is dominated by the AAΩ sample, therefore the possible SDSS peak at $\approx 100\ h^{-1}$ Mpc is

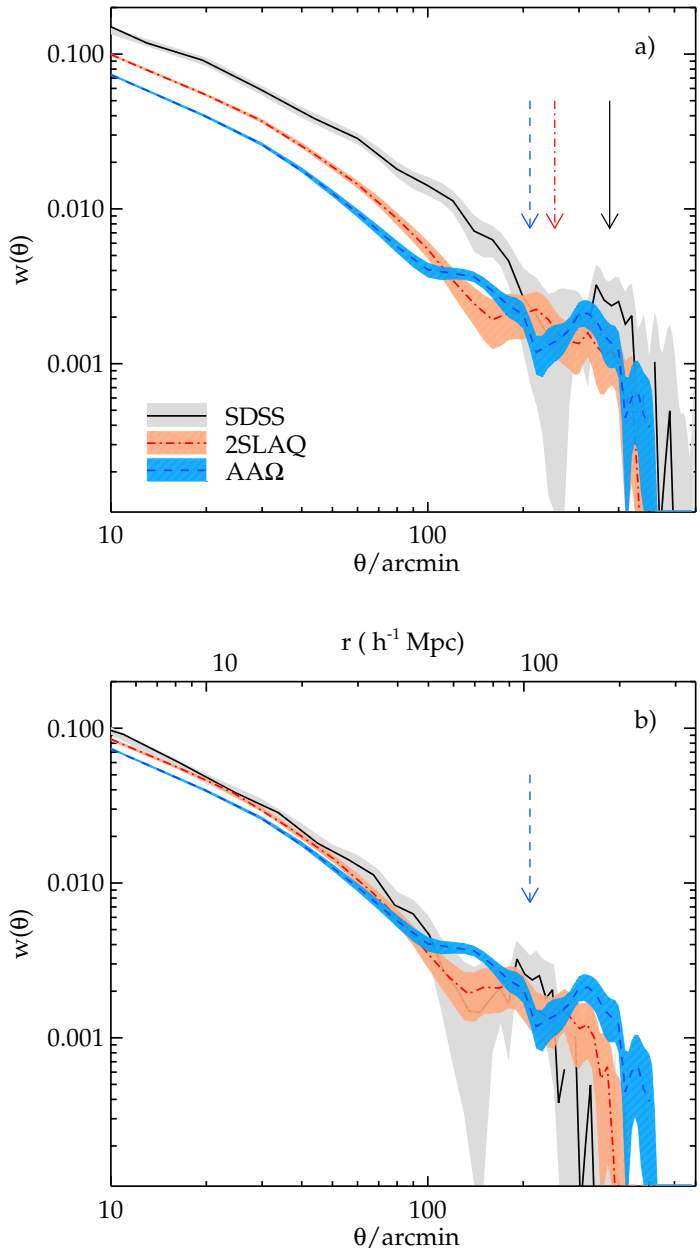

Figure 2.18: (a): The angular correlation function of the three LRG samples at large scales. The shaded regions are 1σ JK errors. The arrow indicates the expected BAO angular separation in each sample, assuming our fiducial cosmology. (b): Same as (a) but now scaled in the angular direction to the depth of the AAΩ LRG sample. Note that the errors in the angular correlation functions are correlated, see Fig. A.1 for the relevant scales.

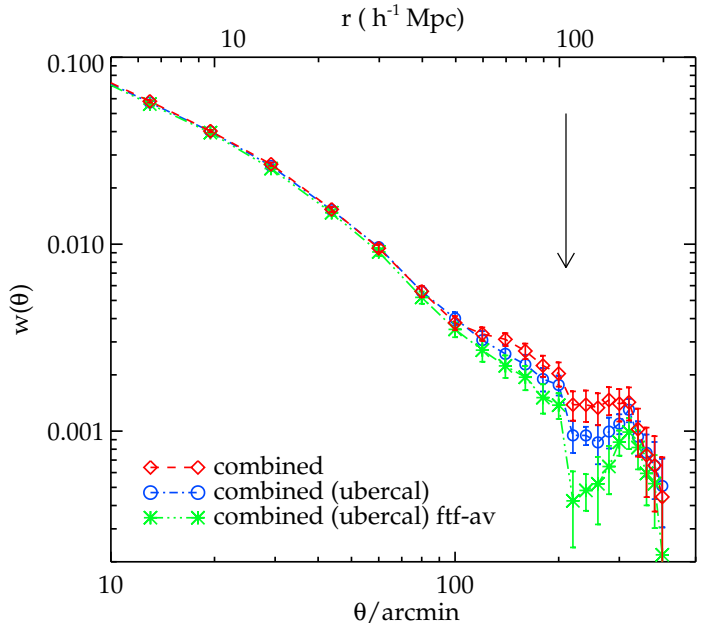

Figure 2.19: The combined angular correlation function of the three LRG samples scaled to the AAΩ depth, comparing the results when the SDSS standard (diamonds) and uber- (circles) calibration are used. Also shown is the average field-to-field $w(\theta)$ (asterisks) which represents an attempt to filter out any large scale gradients in the SDSS data.

not evident in the combined sample. There also seems to be an indication of an excess out to possibly 200 h^{-1} Mpc, see §2.6.1 for robustness test of this excess clustering signal.

Using the 'ubercalibration'[4] (Padmanabhan et al., 2008) instead of the standard calibration, we find similar results at small and intermediate scales but somewhat lower amplitude at $\approx$ 100 h^{-1} Mpc although the results agree within the 1σ error (see Fig. 2.19). This means the correlation functions at small and intermediate scales including the parameters derived (e.g. power-law fits, linear biases, dark matter halo masses) in the earlier parts are not affected by which calibration we use. The biggest difference, although less than 1.5σ, is observed at scales larger than 120 h^{-1} Mpc and up to 150 h^{-1} Mpc where the correlation signal is small and hence more prone to possible systematics. The weak dependence of $w(\theta)$ at very large scales on the different calibrations may be an indication that this apparent extra peak at $\theta \approx 300'$ could indeed be a systematics effect. We shall return to this in §2.6.1.

We also tested whether the 200 h^{-1} Mpc excess can be eliminated by taking the

[4]This is the improved photometric calibration of the SDSS imaging data which have been simultaneously solved for the calibration parameters and relative stellar fluxes using overlapping observations.

average $w(\theta)$ from the 15×20 deg^2 subfields used for the jackknife errors. The result, after integral constraint correction, is shown in Fig. 2.19. The 200 h^{-1} Mpc excess persists even though there is some change at smaller scales. Given the model dependence introduced by the integral constraint correction, hereafter, we shall use the correlation function of the ubercal sample measured using our normal method.

2.6.1 Testing for systematic effects

We have performed a series of tests to check our results against possible systematic effects. The tests include exclusions of high dust extinction and 'poor' astronomical seeing regions, an improved star-galaxy separation for the AAΩ sample and effects of possible contamination by clustered stars.

First, we exclude the regions where the i-band extinction is greater than 0.1 mag which discards ≈ 20 per cent of the data. The results are shown in the top row of Fig. 2.20. For 2SLAQ and AAΩ samples, the results appear to be lower than the main measurements but otherwise remain within 1σ statistical errors of each other. Although the amplitudes at $\theta \geq 220'$ are somewhat lower than the default AAΩ result, the excess at $\theta \gtrsim 300'$ still persists. We then investigate the effect of excluding the regions with 'poor' astronomical seeing, the limit of $1''.7$ is used following the SDSS 'poor' seeing definition which discards ≈ 30 per cent of the data. The results here are in good agreement with the main results with the exception of a few angular bins around $320'$ of the 2SLAQ sample where they are somewhat (non-significantly) lower than the default measurements.

Next, we attempt to reduce the stellar contamination fraction in the AAΩ sample. As a reminder, our default (optimised) star–galaxy separation algorithm (see §2.2) leaves ≈ 16 per cent stellar contamination in the sample while losing genuine LRGs only at a sub-per cent level. Here, we impose a more aggressive star–galaxy separation cut which reduces the contamination level to $\approx$9 per cent at the expense of nearly halving the number of genuine AAΩ LRGs. The cut is a combination of the fitted 'de Vaucouleurs' radius as a function of $z_{\rm deV}$ magnitude and the correlation between the 'de Vaucouleurs' and fiber magnitudes in z-band. The $w(\theta)$ measurement for this new AAΩ sample after correction by a factor of $1/(1-f)^2$, where $f = 0.09$ is shown in the top-right panel of Fig. 2.20. This is in good agreement with the main results.

We test our earlier assumption (§2.3, see also Blake et al. 2008) that the effect of the stellar contamination is simply a dilution of $\delta_{\rm g}$ by $(1-f)$ and hence the amplitude of galaxy–galaxy correlation function by $(1-f)^2$, where f is the contamination fraction. We

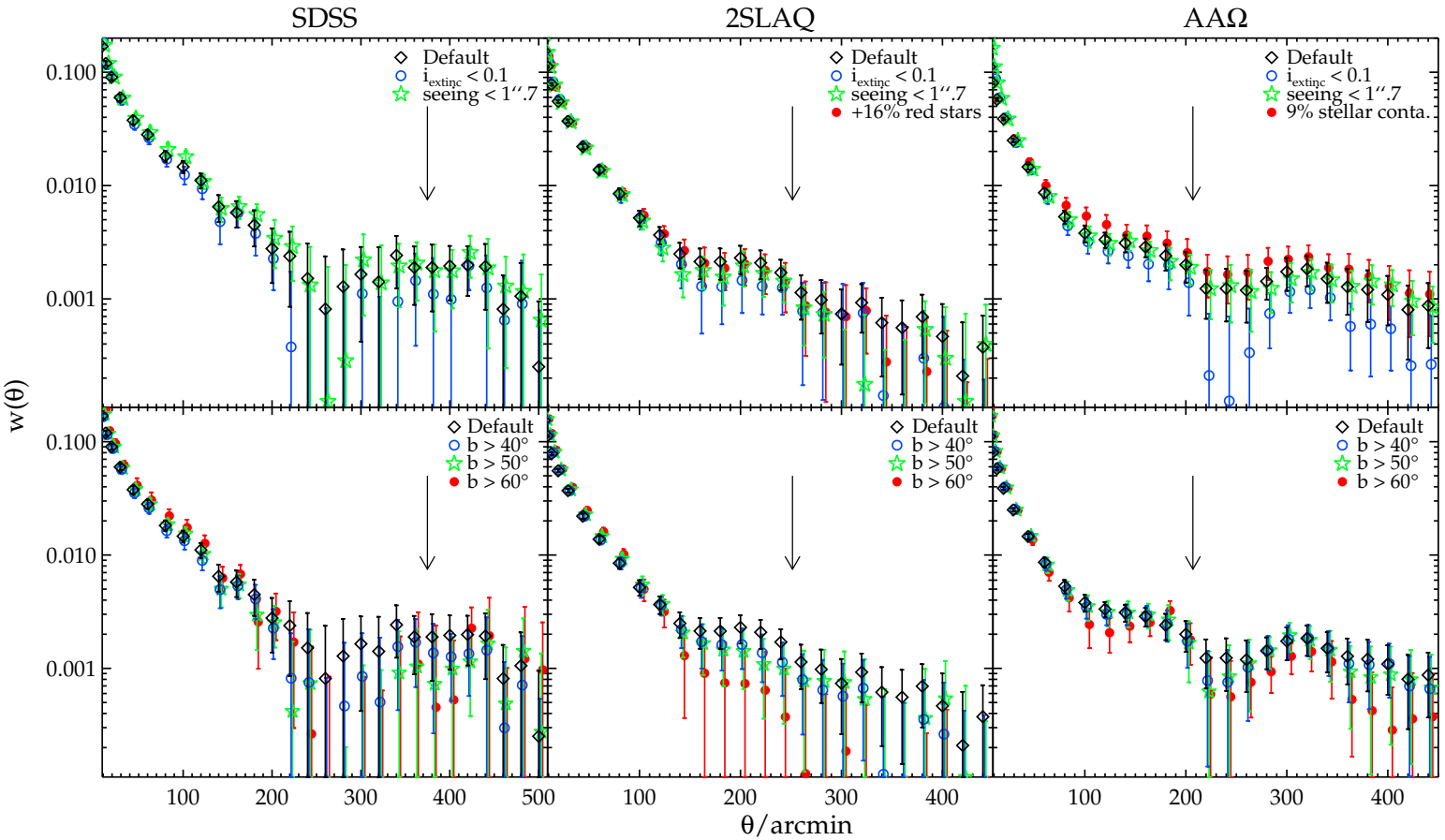

Figure 2.20: The angular correlation functions for SDSS, 2SLAQ and AAΩ samples (left to right), measured with varying dust extinction limit, astronomical seeing and different star-galaxy separation (top row), compared to our 'Default' results. Also shown is the effect of low galactic latitude region exclusion for each sample (bottom row). Note that for the $b > 60°$, the sample size is reduced by 60 per cent. In each case, an arrow indicates the expected position of the BAO peak assuming our fiducial cosmology.

add a sample of red stars to the 2SLAQ sample at the 16 per cent level, similar to what we expect in the AAΩ sample. The stars are selected from SDSS photometric objects which are classified as 'star'. The colour selections have been matched to that of the AAΩ-LRG sample. The sample is then randomly selected to have the number of objects at 16 per cent of the 2SLAQ sample. They therefore follow the stellar distribution with galactic latitude. The $w(\theta)$ result after correction by $1/(1-f)^2$ is shown in the top-middle panel of Fig. 2.20 and is found to be in excellent agreement with the main 2SLAQ result. We do not see any evidence of a slope change which may arise from a possible clustering of the stellar contaminants at large scales, at least for the contamination level expected in our sample.

We apply various minimum galactic latitude cuts on the data in order to test for any systematic error. Such systematics (if they exist) could be due to the gradient caused by galactic dust extinction and/or different stellar contamination fractions which one might expect to be worse in the lower galactic latitude regions. Note that in our default datasets ≈ 95 per cent of the data are at $b \geq 30^\circ$. The results of applying the galactic latitude cuts of $b \geq 40^\circ$, 50° and 60° are shown in the bottom row of Fig. 2.20. Note that with the $b \geq 60^\circ$ limit, ≈ 60 per cent of the data are discarded. The 2SLAQ results appear to be marginally dependent on the galactic latitude limits. In the AAΩ sample the results are in good agreement with the main measurement although the $b \geq 60^\circ$ limit appears to be $\approx 1\sigma$ lower in some angular bins.

Finally, we cross-correlate the SDSS and AAΩ samples. The redshift distributions of the two samples are well separated with only slight overlap (see Fig.2.1). Therefore any residual signal in their cross-correlation function, CCF, at large scales can be used as an evidence for systematic errors. The CCF is shown in Fig. 2.21, comparing to the auto correlation functions of the SDSS and AAΩ samples in the top and bottom panels, respectively. The CCF has much lower signal than the ACF at $\theta < 120'$ and is consistent with zero, $P(< \chi^2) = 0.997$, between $120' < \theta < 500'$ whereas the AAΩ $w(\theta)$ signal is detected at more than 4σ significance (see above) in the same angular ranges.

We note that Ross et al. (2011) have suggested that there is a systematic effect associated with the area effectively masked by foreground stars which may be important in terms of a systematic that may produce excess clustering at large scales. However, such an effect would predict a decrease in galaxy density at low galactic latitudes and this is not seen in our samples (see Fig. 9 of Sawangwit et al., 2010, also Fig. 3.8). If anything, the opposite effect is seen in our data with an increase in density towards lower

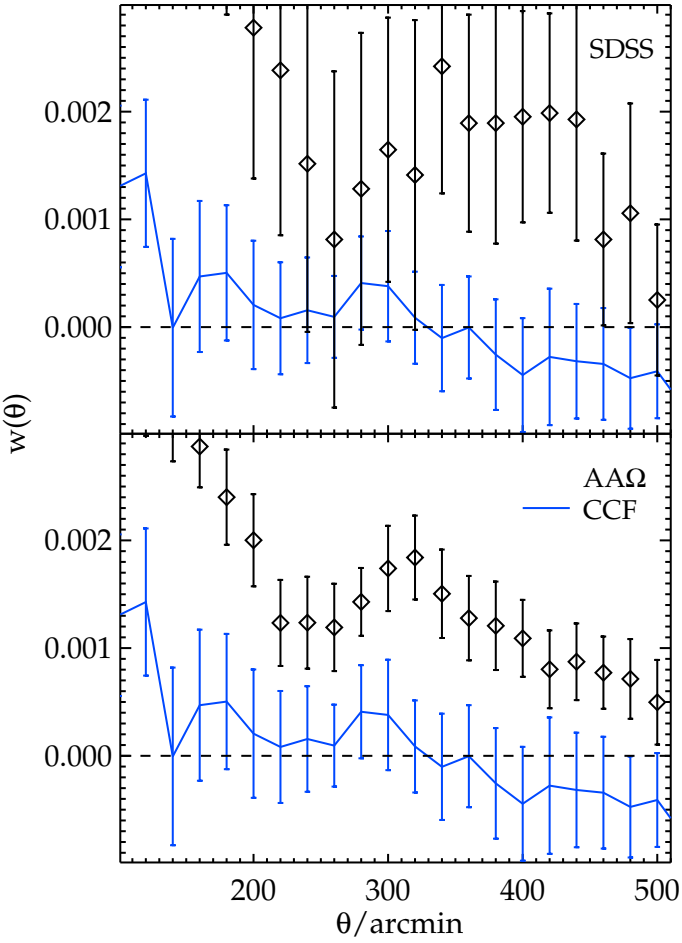

Figure 2.21: The auto correlation functions for SDSS (top panel) and AAΩ (bottom panel) samples, comparing to the CCF between the two samples (blue solid lines).

galactic latitude which may be caused by stellar contamination. Here, we have tested our $w(\theta)$ measurements by successively cutting out data at low galactic latitudes. Although the 2SLAQ results may show some marginal dependence on the galactic latitude cut, the AAΩ results seem reasonably unaffected (see Fig. 2.20(f)). This may be due to the higher stellar contamination fraction in AAΩ sample which means that the effect seen by Ross et al. (2011) may not be directly applicable to the AAΩ sample.

We conclude that the apparent clustering excess at $\approx 300'$ in the AAΩ sample appears to be reasonably robust against most of the systematic tests we performed here. However, one might argue that the weakening of the excess signal when $i_{\rm extinc} > 0.1$ regions (≈20 per cent) are excluded and the marginal dependence on the galactic latitude cuts of the 2SLAQ results may be taken as some evidence for systematic effects. On the other hand, the SDSS-AAΩ cross-correlation test also tends to limit the size of possible systematic

errors.

2.6.2 Model comparisons

Standard ΛCDM model

First, we compare the measured angular correlation function to the perturbation theory prediction in the standard ΛCDM Universe. To compute the theoretical prediction, we proceed in the same manner as described in §2.4.2, calculating $w(\theta)$ by projecting $\xi(r)$ which is a Fourier transform of a non-linear $P(k)$. However, here we assume the best-fit cosmological parameters from Eisenstein et al. (2005), a flat ΛCDM model with $\Omega_m h^2 = 0.13$, $\Omega_b h^2 = 0.024$, $h = 0.7$ and $n = 0.98$. And unlike in §2.4.2, the non-linear modelling of the BAO peak using only HALOFIT is not adequate. The BAO peak in the correlation function can also be broadened (and perhaps slightly shifted) by the non-linear gravity suppression of the higher harmonics in the power spectrum via mode coupling (Meiksin et al., 1999). To model such an effect, we follow Eisenstein et al. (2005) and smoothly interpolate between the linear power spectrum and the 'no-wiggle' spectrum with the same overall shape but with the acoustic oscillations erased. This is done mathematically by

$$P(k) = P_{\rm lin}\left[x + \frac{T_{\rm nw}(k) \times (1-x)}{T_{\rm lin}(k)}\right]^2, \tag{2.48}$$

where $P_{\rm lin}$ is linear matter power spectrum, $T_{\rm nw}(k)$ and $T_{\rm lin}(k)$ are 'no-wiggle' and linear transfer functions computed from Eisenstein and Hu (1998) and $x = \exp(-k^2a^2)$ with $a = 7\ h^{-1}\,{\rm Mpc}$ chosen to fit the BAO suppression seen in their N-body simulations.

The $P(k)$ is then corrected for non-linear gravitational collapse using the HALOFIT software. The final $P(k)$ is then transformed to $\xi(r)$ using Eq. 2.19. Although the scale-dependent redshift-distortion and halo bias correction is weak at these scales, we follow Eisenstein et al. (2005) and multiply the correlation function by the square of $1 + 0.06/[1 + (0.06r)^6]$ (solid line in their Fig. 5), again chosen to fit what is seen in the N-body simulations. Such a correction is small at the BAO scale, only sub-percent at $r \gtrsim 25\ h^{-1}\,{\rm Mpc}$ and increases to $\approx 10\%$ at $10\ h^{-1}\,{\rm Mpc}$. We then correct for the linear redshift-space distortion, the $\xi(s)$ amplitude is enhanced relative to the real-space correlation function, $\xi(r)$, such that (Kaiser, 1987)

$$\xi(s) = \left(1 + \frac{2\beta}{3} + \frac{\beta^2}{5}\right)\xi(r). \tag{2.49}$$

Here, we assume $\beta = 0.45$ for these LRG samples (see Ross et al. 2007). The final $\xi(s)$ model prediction with galaxy bias $b = 2.09$ for SDSS-LRG (see §2.4.2) is shown (cyan solid line) in the inset of Fig. 2.22. Eisenstein et al. (2005) find this model to be a good fit to their $\xi(s)$ data with the best-fit $\chi^2 = 16.1$ on 17 degrees of freedom for a particular set of cosmological parameters given above. We then computed $w(\theta)$ from the $\xi(r)$ derived above via Eq. 2.14. Although the model (cyan solid line in Fig. 2.22) was found to be consistent with the LRG $\xi(s)$, it is inconsistent with our $w(\theta)$ measurement, especially at $r \gtrsim 60\ h^{-1}\,\mathrm{Mpc}$ or $\theta \gtrsim 120'$. The uber-cal AAΩ $w(\theta)$ between $40' - 400'$ (corresponding to $20 \lesssim r \lesssim 200\ h^{-1}\,\mathrm{Mpc}$) are incompatible with the model at 99.8 per cent level (χ^2=39.3 over 18-1 d.o.f with covariance matrix). We note that this rejection may be associated with the apparent clustering excess at $\theta \gtrsim 200'$, which still could be subject to systematics.

Next, we compare our $w(\theta)$ to the best estimate of $\xi(s)$ at the BAO scale as measured by Eisenstein et al. (2005). Although these measurements may have been superseded by DR7 spectrosopic LRG clustering analyses based on larger samples, these more recent estimates are usually in reasonable agreement with the results of Eisenstein et al. (2005), whether they are in correlation function (Martínez et al., 2009; Kazin et al., 2010) or power spectrum (Percival et al., 2010) form. For our comparison, we thus simply make a polynomial fit to the best estimate $\xi(s)$ of Eisenstein et al. (2005) (blue dashed line in the inset of Fig. 2.22). The polynomial-fit $\xi(s)$ is Kaiser de-boosted (Eq. 2.49) to give $\xi(r)$ by assuming $\beta = 0.45$. The $\xi(r)$ is then corrected for the linear growth between $z = 0.35$ and $z = 0.68$ which reduces the amplitude by $\approx 30\%$. The resulting model has similar amplitude with the expected AAΩ-LRG $\xi(r)$ because the SDSS and AAΩ-LRG linear biases are coincidentally the same (see §2.4.2). The model is then projected to $w(\theta)$ using Eq. 2.14 and is shown as a blue dashed line in Fig. 2.22. Our result appears to be in good agreement with the model up to $\approx 120\ h^{-1}\,\mathrm{Mpc}$ given statistical uncertainties in our measurement and the $\xi(s)$ data. Beyond $\approx 120\ h^{-1}\,\mathrm{Mpc}$, our $w(\theta)$ shows a higher clustering amplitude as noted above.

Summarising, the w_{com} result appears consistent with the $w(\theta)$ prediction based on the Eisenstein et al. (2005) best estimate of $\xi(s)$ (at least out to $\approx 120\ h^{-1}\,\mathrm{Mpc}$) but not with the prediction based on the flat ΛCDM model due to the apparent large-scale clustering excess in the $w(\theta)$. This means that given the size of error bars of the Eisenstein et al. (2005) result, the ΛCDM model is quite compatible with the $\xi(s)$ data but given the much smaller statistical error on $w(\theta)$, in this case our measurements are inconsistent with the ΛCDM model. While the feature observed at $\approx 300'$ persists in most of the

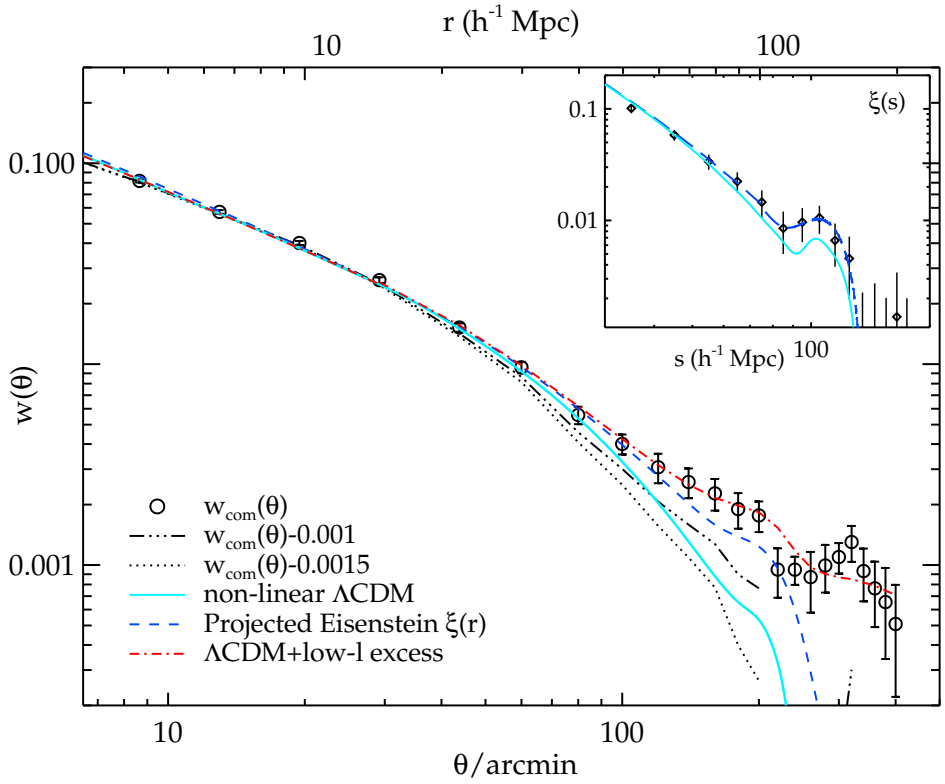

Figure 2.22: The combined $w(\theta)$ (open circles) compared to the projections of non-linear ΛCDM model plus mode coupling, scale-dependent redshift-space distortion and halo bias correction (cyan solid line) and the Eisenstein et al. (2005) $\xi(s)$ (blue dashed line). The red dot-dashed line is the ΛCDM model plus low-ℓ power excess (see below). The dash-dot-dotted and dotted line shows the effect of subtracting the data by 0.001 and 0.0015, respectively. The $\xi(r)$ models used in the $w(\theta)$ projection are given as an inset together with the Eisenstein et al. (2005) measurement (diamonds). Here, the same symbols are used for the Eisenstein et al. (2005) and non-linear ΛCDM $\xi(s)$ models as for the $w(\theta)$ models above. Note that the errors in the angular correlation functions are correlated, see Fig. A.1 for the relevant scales.

systematic tests we performed on the AAΩ samples (§2.6.1), a few of these tests, e.g. dust extinction, indicate there is still the possibility that systematic errors are affecting the $w(\theta)$. Therefore, if we now assume that the excess signal at $\approx 150\ h^{-1}\,\mathrm{Mpc}$ is an indication of a systematic and subtract 0.001 to 0.0015, the level of the excess amplitude at this point in $w_{\rm com}$ (see Fig. 2.22), we obtain the $w(\theta)$ results as shown by the dash-dot-dotted and dotted lines. These two lines now bracket the flat ΛCDM result. Thus the issue of the disagreement between the $w(\theta)$ result and the ΛCDM model seems to rest on the reality of the apparent clustering excess at large scales.

low-ℓ power excess?

Recently, Thomas et al. (2010) (see also Padmanabhan et al., 2007; Blake et al., 2007; Thomas et al., 2011) has also found a significant excess in their angular power spectrum, C_ℓ, at the low multipoles relative to the best-fit ΛCDM models. They used photometric-redshift catalogues of the LRGs at $z \approx 0.5$ similar to our 2SLAQ sample. The most significant ($\approx 4\sigma$) low-ℓ power excess is observed in the highest redshift bin while the three lower-z samples show similar power excesses at 2-2.5σ significance in each bin. The author carried out various systematic checks and found no indication of such an effect. Their reconstruction of the matter distribution implied by the low-ℓ data also found no preferred region of the observed sky where the signal could be coming from. While the clustering excess only affects C_ℓ at multipoles smaller than the acoustic oscillations in Fourier space, unfortunately in configuration space the effect is expected on a wider range of scales and could affect our $w(\theta)$ BAO measurement.

To estimate the effect of this low ℓ excess on the angular correlation function, we assume the extra power at $\ell \lesssim 30$ as observed by Thomas et al. (2010) (see Fig. 2.23). The excess power is modelled as a power-law at $\ell \lesssim 30$ and is truncated at $\ell \leq 5$ (blue dot-dashed line in Fig.2.23). Thomas et al. (2010) best-fit ΛCDM (blue solid line) and the power-law low-ℓ excess models are then used to predict the expected C_ℓ for the AAΩ-LRG $n(z)$ (red dot-dashed and dashed lines in Fig.2.23), using the formalism described in §3.3 (see also Padmanabhan et al. 2007; Thomas et al. 2011) but without the small-angle approximation (Limber, 1953). The predicted $w(\theta)$ is then

$$w(\theta) = \sum_{\ell=0}^{\infty} \frac{2\ell+1}{4\pi} P_\ell(\cos\theta) C_\ell, \tag{2.50}$$

where $P_\ell(x)$ is the Legendre polynomial of order ℓ.

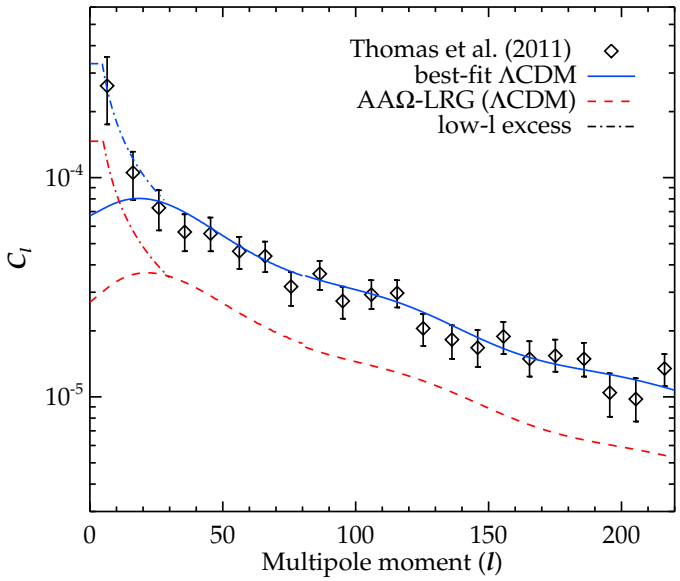

Figure 2.23: The angular power spectrum of the $0.6 < z < 0.65$ MegaZ-DR7 LRG (Thomas et al., 2011) with significant power excess at low multipoles (diamonds). The low-ℓ power excess plus the best-fit ΛCDM model of the $0.6 < z < 0.65$ C_ℓ (blue dot-dashed and solid lines) is extrapolated to the AAΩ redshift range (red dot-dashed and dashed lines).

The resulting $w(\theta)$ model with the amplitude normalised to fit the data at $\theta = 40' - 400'$ ($r \approx 20 - 200\ h^{-1}\,\mathrm{Mpc}$) is shown as the red dot-dashed line in Fig. 2.22. The model appears to be consistent with our $w_{\rm com}$. Using uber-cal AAΩ-LRG result and its covariance matrix at $\theta = 40' - 400'$, the model is acceptable at 13 per cent level ($\chi^2 = 23.6$ over $18 - 1$ d.o.f) when the amplitude of the $w(\theta)$ model is allowed to vary. On the contrary, the best-fit ΛCDM model without the low-ℓ excess (red dashed line in Fig. 2.23) is significantly rejected at 99.6 per cent ($\approx 3\sigma$) level by the same χ^2 analysis. This is consistent with the result derived in §2.6.2. The fact that the excess power in the C_ℓ taken the form of an $\ell \approx 10$ spike, suggests that this excess in $w(\theta)$ is due to something other than acoustic oscillations in the power spectrum. Note that changing the truncation scale of the low-ℓ power-law excess to $\ell \leq 1$ ($\ell \leq 10$) decreases (increases) χ^2 to 23.5 (24.6) and does not alter our main conclusion here.

We note that evidence for a large-scale ($> 150\ h^{-1}\,\mathrm{Mpc}$) correlation function excess has also been detected in the NVSS radio source survey by Blake and Wall (2002) and Xia et al. (2010). We have compared our results with theirs and find that our correlation function

shows a similar shape but a factor of 2-3× lower amplitude. If the excess clustering signal observed here is real then it could be evidence for non-Gaussianity (Xia et al., 2010) or for the gauge dependence[5] of the matter power spectrum on the largest scales (Lin, 2001; Yoo et al., 2009). But until this feature is detected in an independent galaxy dataset, there will always be the possibility that it is caused by some unknown systematics. Certainly, if the ΛCDM model were correct then we would have to conclude that this excess was caused by systematics at the level of $\Delta w \approx 0.001 - 0.0015$ in the photometric AAΩ-LRG sample. Thus the question of whether we have detected the BAO scale in $w(\theta)$ is therefore not straightforward to answer. If the excess clustering signal is real which may have enhanced $w(\theta)$ amplitude at the BAO scale then we may have, given the agreement between our result and the projected Eisenstein et al. $\xi(s)$ and the ΛCDM model plus low-ℓ power excess. But if it is an artefact then systematics are dominant and the BAO peak is at too low an amplitude to be detected in our dataset.

2.6.3 Future improvement

Finally, we shall investigate the effects the redshift distribution width has on the detectability of the BAO peak in angular correlation functions. For this purpose, we compute $w(\theta)$ by projecting the real-space correlation function using Eq. 2.14 with various galaxy redshift distributions. We use the observed $\xi(s)$ form of Eisenstein et al. (2005) rather than the ΛCDM prediction from CAMB or CMBfast. For the observed $\xi(r)$, we use a fit of the de-boosted Eisenstein et al. (2005) LRG $\xi(s)$ assuming Kaiser factor, $\beta = 0.4$ in the linear regime, $r \geq 15\ h^{-1}\,\mathrm{Mpc}$, and a power-law with $r_0 = 10.5\ h^{-1}\,\mathrm{Mpc}$ and $\gamma = 1.9$ for $r < 15\ h^{-1}\,\mathrm{Mpc}$ (Zehavi et al., 2005a). This model is shown as a dashed line in the inset of Fig. 2.22. To compare our $w(\theta)$ measurement to the predicted photo–z result with redshift error, σ_z, we model the $n(z)$ as a Gaussian with width σ_z and average $z = 0.68$. We calculate the expected $w(\theta)$'s assuming the AAΩ LRG $n(z)$, $\sigma_z = 0.01, 0.03$ and 0.05.

The results are shown in Fig. 2.24. The narrower $n(z)$ gives a higher $w(\theta)$ amplitude and steeper power-law slope as expected. This is because there are fewer galaxy pairs separated by different spatial scales in different redshift slices that project on to the sky at similar angular separation to dilute the spatial clustering signal. With a sufficiently

[5] At around and beyond horizon scales, the matter power spectrum in the conformal Newtonian and synchronous gauges can differ significantly. And it may not be trivial to relate the fluctuation variables to observable quantities in a gauge-invariant way (see e.g. Yoo et al., 2009)

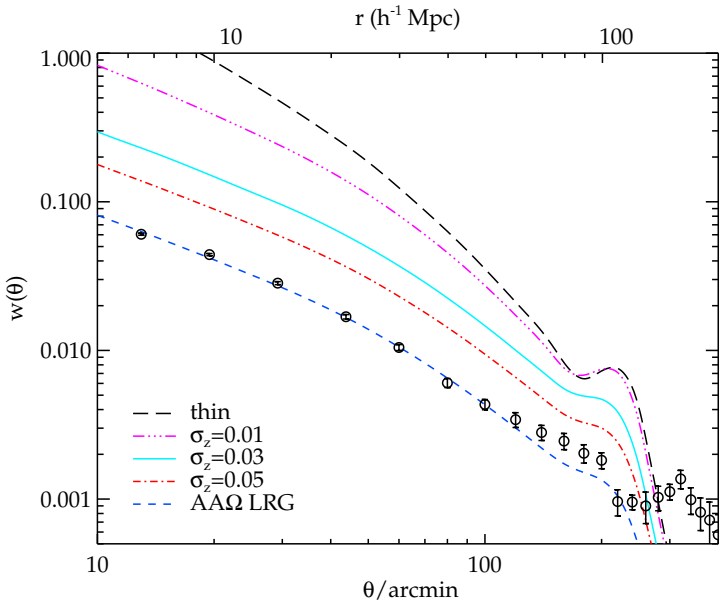

Figure 2.24: The angular correlation functions from the projected LRG $\xi(r)$ of Eisenstein et al. (2005) assuming different $n(z)$ widths. Our $w(\theta)$ measurement is also shown (diamonds) along with its expectation.

small $n(z)$, $w(\theta)$ converges to the spatial correlation function as shown in Fig. 2.24 for the thin-layer approximation.

The thin-layer model is calculated by using an infinitesimally thin galaxy selection function, in this case a delta function, $\delta(z-0.68)$, centred at the same redshift as the mean of the Gaussian $n(z)$. The result is an angular rescaling, corresponding to the radial comoving distance out to $z=0.68$, i.e. $w(\theta)=\xi(\chi\theta)$. This is shown as a long-dashed line in Fig. 2.24. The BAO peak appears at $w\approx 0.01$, the same amplitude as the input $\xi(r)$ shown in the inset to Fig. 2.22. Clearly it would not make sense to pursue the angular correlation function route when the photo-z accuracy becomes much smaller than the BAO scale because at that point it will start to be advantageous to include the BAO signal from the radial direction as well as the angular direction by using either the 3-D correlation function, $\xi(s)$, or the semi-projected correlation function, $w(r_p)$. Thus for the approach we have followed here, the results in Fig. 2.24 corresponding to $\sigma_z\approx 0.03-0.05$ (i.e. $\Delta r\approx 60-100\ h^{-1}\,\mathrm{Mpc}$) are the best the 2-D correlation functions can do. However, such a factor of $2\times$ improvement in the photo-z or colour-cut accuracy would be useful for the increased signal with respect to the systematic noise shown by the SDSS data in Fig. 2.24. Also with $\sigma_z=0.03-0.05$ the signal to noise ratio is within a factor 1.5-2 of its best value in a spectroscopic survey in our redshift range (see Fig. 2.24).

The AAΩ LRG $n(z)$ can be narrowed down by the use of photo–z as opposed to using the simple colour-magnitude cut considered in this study. The current best photo–z accuracy for $z \approx 0.5$ LRGs using the SDSS photometry with the Neural Networks algorithm gives $\sigma_z \approx 0.05 - 0.06$ (Collister et al., 2007; Abdalla et al., 2008), a modest improvement over what we currently achieve. But by combining with near-infrared photometry and a spectroscopic redshift training set of a few thousands, the photo–z accuracy of the AAΩ LRGs could be further improved, possibly to achieve the $\sigma_z = 0.03$ limit for the usefulness of the 2-D correlation function technique. The southern VST ATLAS and VISTA VHS surveys will double the area with optical-NIR photometry to search for BAO. The inclusion of NIR data from VISTA VHS survey is also expected to improve the photo–z accuracy (Banerji et al., 2008) of the proposed Dark Energy Survey (DES). The deeper grizy photometry of the Panoramic Survey Telescope and Rapid Response System (Pan-STARRS, Chambers 2009) 3π survey combined with the JHK photometry from the the UKIRT Infrared Deep Sky Survey (UKIDSS, Lawrence et al. 2007) Large Area Survey (LAS) should also give a photo-z accuracy of $\sigma_z(z = 0.7) \gtrsim 0.03$ (Cai et al., 2009). These improved photometric redshifts and the application of the full Limber's formula used here should also reduce any systematics in estimating the BAO scale (see Simpson et al., 2009) from this new generation of 2-D cosmological surveys.

2.7 Summary and Conclusions

We have presented here a new and detailed analysis of the angular correlation function of the Luminous Red Galaxies extracted from the SDSS DR5 photometric catalogue. All the necessary information for inferring the spatial clustering is obtained and calibrated through redshift surveys of sample subsets. Our conclusions are as follows;

(i) We measured the angular correlation function of the LRGs at three different redshifts, namely 0.35, 0.55 and 0.68 and found the results to be well approximated by power-laws at small and intermediate scales.

(ii) With the large samples in terms of the numbers of objects and volume cover by the data, we see the deviation from the canonical single power-law at high significance.

(iii) The data are better fitted by a double power-law where the large-scale ($\gtrsim 1 - 2\ h^{-1}\,\mathrm{Mpc}$) slope is equal to that of the conventional single power-law, i.e. $\gamma \approx 1.8$.

(iv) The form of the angular correlation functions at large scales are consistent with the expectation of the linear perturbation theory in the flat standard ΛCDM Universe.

(v) The LRG linear bias is high, $b_g \approx 2.0$, as expected for massive luminous early-type galaxies and the clustering strength is found to be strongly linked to the sample intrinsic brightness.

(vi) The best-fit HOD models suggest that these LRGs reside in the massive dark matter haloes, $10^{13} - 10^{14} h^{-1} M_{\odot}$, and are typically central galaxies in their dark matter halo hosts, with the satellite fraction no more than 10 per cent.

(vii) The clustering evolution at intermediate scales ($1 < r < 20\ h^{-1}$ Mpc) is remarkably slow and may be approximately explained by a long-lived model or even a no–evolution model. The long-lived model may be in line with the observed passive evolution of the LRG luminosity function, consistent with a constant comoving LRG space density in this redshift range. This latter conclusion would also apply in the case that the no–evolution (comoving) model were found to fit better but in this case the observations may require a significantly higher bias.

(viii) Using the Lacey and Cole (1993) framework, our $M_{\rm DMH}(z)$ measurements are well fitted by the model where halo mass is grown via merging of progenitors with masses of $\approx 1.4 \times 10^{13}\ h^{-1}\, M_{\odot}$ and $\approx 2.3 \times 10^{13}\ h^{-1}\, M_{\odot}$ from $z = 1$, for haloes that typically host $\ell \geq 2L^*$ and $\geq 3L^*$ galaxies, respectively. We found that these dark matter haloes have tripled their masses over the last half of cosmic time (although see the caveat given at the end of §2.5.1) whereas it has been claimed that the LRG stellar masses have grown by less than 50 per cent (Cool et al., 2008).

(ix) At small scales ($r < 1\ h^{-1}$ Mpc) the clustering evolution appears slightly faster at fixed luminosity and the clustering increases towards lower redshift, consistent with a virialised clustering model. Since our virialised model assumes a constant comoving LRG space density, a combination of this stable clustering model at small scales and the long–lived model at intermediate scales could be consistent with the idea that merging of LRGs may not change the LRG space density significantly out to $z \approx 0.7$.

(x) However, the evolution based on HOD and the ΛCDM halo merging framework requires that $\sim 2 - 3$ per cent/Gyr of the LRGs merge with each other in order

to explain the small-scale clustering evolution, consistent with the results of White et al. (2007) and Wake et al. (2008).

(xi) In our AAΩ-LRG result we find a BAO peak at a level consistent with the best estimate of $\xi(s)$ obtained by Eisenstein et al (2005). But, given the small size of our statistical errors, these results deviate significantly, $\approx 4\sigma$, from the standard ΛCDM prediction because of an apparent large-scale clustering excess.

(xii) The excess clustering signal generally persists after a series of systematic tests we performed. However, a few of these tests did change the feature somewhat, suggesting that it could still be caused by some unknown systematic effects.

(xiii) If the ΛCDM model were correct then we would have to conclude that this excess was caused by systematics at the level of $\Delta w \approx 0.001 - 0.0015$ in the photometric AAΩ-LRG sample.

(xiv) Otherwise, the excess signal in our $w(\theta)$ relative to the standard ΛCDM model appears to be in good agreement with the C_ℓ power excess at low ℓ observed by other authors who used photo–z LRG samples at $z \approx 0.5$.

(xv) If real, the large-scale clustering excess may be interpreted as an evidence for a non-standard cosmological model, e.g. primordial non-Gaussianity or general relativistic effects. However, more, independent, data is required to check the reality of this clustering excess.

(xvi) Further improvement could be achieved with smaller photo–z error, probably via Neural Network route but a sample of a few thousands $z \approx 0.7$ LRGs would be needed in order to obtained the required photo–z accuracy, given the already narrow redshift distribution of our sample in this analysis.

(xvii) The photo–z accuracy needed to robustly detect the acoustic peak in the angular correlation function of the LRGs at $z \approx 0.7$ is $\sigma_z \approx 0.03$ which may be the best the angular correlation functions can do. This limit should be achievable with the future wide-field imaging survey such as the Pan-STARRs 3π survey.

Chapter 3

The Integrated Sachs-Wolfe Effect

3.1 Introduction

Many observations now suggest that we live in a spatially flat, dark energy dominated Universe (e.g. Perlmutter et al., 1999; Cole et al., 2005; Tegmark et al., 2006; Riess et al., 2007; Dunkley et al., 2009). In such a cosmology, positive correlation between the CMB and large-scale-structure (LSS) is expected due to the decaying gravitational potential (Sachs and Wolfe 1967). The deviation of the CMB temperature in the vicinity of LSS is caused by the non-vanishing difference in the energy gained and lost by the CMB photons as they traverse a region of over– or under–density. By integrating across all the potential wells along the line of sight from the surface of last scattering, the primordial fluctuations in the CMB are modified by this effect. This secondary anisotropy of the CMB is called the Integrated Sachs–Wolfe (ISW) effect and sometimes known as the late-time ISW effect to distinguish it from the 'early-time' Sachs–Wolfe effect. For a spatially flat Universe, a detection of the Integrated Sachs-Wolfe (ISW) effect would provide direct dynamical evidence of the accelerating expansion unlike the geometrical measurement inferred from standard candles such as the SNIa.

The SNIa results coupled with the CMB evidence that the Universe is nearly flat, suggests there exists an exotic form of energy with negative pressure. The exact nature of this so–called dark energy is not yet known but it already entails many serious problems. Foremost amongst them are the fine-tuning problem and the cosmic coincidence problem (e.g. Carroll, 2001; Peebles and Ratra, 2003).

The ISW signal in the CMB–galaxy cross–correlation is very small, generally less than one μK, and very difficult to detect. Previous ISW detections generally have less than 3σ statistical significance. These include the studies of Fosalba et al. (2003), Padmanabhan et al. (2005) and Cabré et al. (2006) who used SDSS galaxies in both photo-z and

magnitude limited samples and the WMAP3 dataset. Other authors have used X-ray sources (Boughn and Crittenden, 2004) and NVSS radio sources (Nolta et al., 2004). Of these, it seems that up to now the most significant detection of the ISW effect comes from the NVSS radio sources at 2.3σ. Other authors (e.g. Giannantonio et al. 2008 and Ho et al. 2008) have made compilations of the other results and claimed up to 4σ ISW detections in terms of the overall significance. The only other claims of ISW detections at high significance are the methods that reduced the galaxy samples to focus only on regions of high or low underdensity. In particular, Granett et al. (2008) cross-correlated the positions of ≈ 100 superclusters and voids in the MegaZ–LRG (Collister et al., 2007) sample and McEwen et al. (2007) employed a similar wavelets method using radio sources from NVSS.

Here we shall search for the ISW effect by using samples of Luminous Red Galaxies (LRGs) from the SDSS DR5 dataset. LRGs are the most luminous stellar systems in the Universe, residing in the most massive dark matter haloes. Having formed most of their stars much earlier and over short period of time, the objects appear red with reasonably uniform spectral energy distributions therefore these galaxy samples can be selected homogeneously and observed out to greater distance (or lookback time). Moreover, being massive means that the LRGs are also a highly biased tracer of the LSS (e.g. Ross et al. 2007, Wake et al. 2008). The selection techniques for $z < 0.6$ LRG samples have been well established in the literature. Many LSS studies have been carried out using these LRG samples including the claimed detections of the ISW effect (e.g. Cabré et al. 2006). The recent spectroscopic survey by Ross et al. (2008b) has shown that it is possible to extend the selection technique and hence the LRG sample out to $z \approx 1$. Applying this tested algorithm to the entire SDSS imaging significantly increases the effective volume and makes these LRGs ideal probes of large-scale structure.

Our main goal is to detect the ISW signal in the CMB by cross-correlating WMAP5 map with the new $\bar{z} \approx 0.7$ LRG sample and to test the detection of the ISW effect caused by the LRGs at lower redshift ($\bar{z} \approx 0.35, 0.55$) as claimed by a number of authors (e.g. Padmanabhan et al. 2005, Cabré et al. 2006). These studies used the LRG candidates extracted from the SDSS DR3 or DR4 whilst we are using DR5, ≈ 50 per cent and 20 per cent increase in the area coverage, respectively. The larger sky coverage should provide a statistical advantage over the previous studies. Our new higher redshift LRG sample should also provide a chance to constrain the evolution if such an effect is indeed detected. Moreover, a recent study by Douspis et al. (2008) suggests that the ISW signal-to-noise

can be optimised if the large-scale tracer probes out to a median redshift of 0.8 but there is no further improvement after a redshift of unity. The claim appears to be supported by the cross-correlation analysis of Giannantonio et al. (2008) in which the signal-to-noise of the ISW detection from the 2 Micron All Sky Survey (2MASS; Jarrett et al. 2000) is $\approx$ 4–6 times smaller than from the NRAO VLA Sky Survey (NVSS; Condon et al. 1998) where $\bar{z} \approx 0.1$ and 0.8 respectively, despite the fact that the two surveys have similar sky coverage and sky density ($N_{\rm NVSS} \approx 2N_{\rm 2MASS}$). If this is true then our higher redshift LRG should be more sensitive to the ISW signal and will provide even higher significance of detection than previous studies using the LRGs which currently reach $\approx 2\sigma$ significance at best. The new sample therefore presents a fresh opportunity to test one of the most crucial manifestations of the accelerating expansion, obtaining independent confirmation of the geometrical inference of the SNIa result if detected and a challenge to the current standard picture of the Universe otherwise.

The layout of this chapter is as follows. We present the data in §3.2. We then outline the theoretical prediction and cross-correlation technique employed in this study in §3.3 and §3.4, respectively. The results and a range of analyses performed to ensure their robustness are given in §3.5 and §3.6. The additional sky rotation tests performed on our dataset and selections of previously claimed ISW detections are reported in §3.7. We then present the discussion and conclusion of our studies in §3.8 and §3.9. Throughout this study (unless otherwise stated), we assume a standard ΛCDM cosmology with $\Omega_\Lambda = 0.73$, $\Omega_{\rm m} = 0.27$, $f_{\rm baryon} = 0.167$, $\sigma_8 = 0.8$ and $H_0 = 100h$ km s^{-1} Mpc^{-1} ($h = 0.7$ where necessary).

3.2 Data

3.2.1 CMB Temperature Map-*WMAP*5

The CMB temperature maps used here are taken from the *WMAP* five-year data release (Hinshaw et al., 2009). The data products are publicly available[1] in Hierarchical Equal Area isoLatitude Pixelisation (HEALPix, Górski et al. 2005) format. Although the *WMAP* observes in five frequency bands, we choose to use only the three highest-frequency bands, namely, *W* at 94 GHz, *V* at 61 GHz and *Q* at 41 GHz as the CMB anisotropy in these ranges are less susceptible to a contamination from the foreground anisotropy (i.e. synchrotron and free-free emission) than the lower frequency counterparts.

[1] http://lambda.gsfc.nasa.gov/

This enable us to test for any wavelength dependence in the CMB-galaxy cross-correlation where one expects the ISW signal to be achromatic. The possible SZ contamination can also be checked against multi-frequency analyses which will also benefit from using the data with highest possible resolution. We therefore concentrate our analysis mainly on the W band due to its relatively high resolution compared to the other bands, 12.′6 FWHM compared to 19.′8 for V and 29.′4 for Q band. Despite the fact that the V band has lower noise than the W band (hence often the band of choice for this type of analysis), we do not observe any major difference in either the cross-correlation results or their statistical errors (see Fig. 3.2). We also use the Internal Linear Combination (ILC, Gold et al. 2009) to further check our results, although it should be noted that, according to the *WMAP* team, there could be a significant structure in the bias correction map at scales smaller than $\approx 10^\circ$ (Limon et al., 2008).

We shall use the temperature maps at a resolution of $N_{\rm side}$=512 (res=9) which for the whole sky, contains 3 145 728 pixels each with an area of $\approx 49\,\mathrm{arcmin}^2$. The foreground-contaminated regions of the sky, mainly in Galactic Plane and Magellanic Clouds including extragalactic point sources, are excluded using a combination of 'Extended temperature analysis mask' (KQ75, Gold et al. 2009) and 'Point source catalogue mask' (Wright et al., 2009). After applying the masks, we are left with 2 239 993 pixels ($\approx$ 70 per cent). The maps contain thermodynamic temperatures with the dipole contribution subtracted from the data by the *WMAP* team (Hinshaw et al., 2009).

3.2.2 Luminous Red Galaxies

The Luminous Red Galaxy (LRG) photometric samples are extracted from the SDSS DR5 (Adelman-McCarthy et al., 2007) imaging data based on three LRG spectroscopic redshift surveys whose median redshifts are $\approx 0.35, 0.55$ and 0.7 (Eisenstein et al., 2001; Cannon et al., 2006; Ross et al., 2008b). In essence, these surveys utilised a crude but effective determination of photometric redshift (photo-z), owing to the strong 4000 Å break of a typical E/S0 galaxy spectral energy distribution (SED). As the break is redshifted through the SDSS $g, r, i,$ and z bandpasses, its colour-colour track exhibits a distinctive turning point at various redshifts for different colour pairs. Moreover, their uniform SEDs ensure that they have an extremely tight locus in the colour space. This allows the potential LRGs in the desired redshift ranges to be selected uniformly using their locations on the colour-colour plane coupled with the luminosity threshold set by the appropriate magnitude limit.

These simple methods have been proven to be highly effective in selecting the intrinsically luminous early-type galaxies in the targeted redshift ranges as demonstrated by the SDSS–LRG, 2SLAQ and AAT–AAΩ redshift surveys (Eisenstein et al., 2001; Cannon et al., 2006; Ross et al., 2008b). Although the LRG photo-z in these redshift ranges can be estimated quite accurately (Padmanabhan et al., 2007; Collister et al., 2007), we decided to base our study on the colour–magnitude cuts because a well defined photo-z error distribution is needed for the deconvolution to recover the real redshift distribution and could bias the analyses of the results. The colour-magnitude cut techniques used in the above spectroscopic surveys, applied to the entire SDSS DR5 dataset (only Northern Galactic Cap), results in ≈ 1.5 million LRG candidates and the redshift distribution of the survey is assumed for the corresponding photometric sample. The LRG samples used in this chapter are the same as that used in Chapter 2 and the outlines of their selection algorithms are given in §2.2.

3.3 Theoretical prediction

The secondary CMB anisotropy caused by the time-varying gravitational potential, Φ, is known as the Integrated Sachs-Wolfe (ISW) effect. As the CMB photons traverse such regions, the temperature perturbation associated with the time dependent potential is given by

$$\delta_T^{\rm ISW}(\hat{\mathbf{n}}) \equiv \frac{\Delta_T^{\rm ISW}(\hat{\mathbf{n}})}{T_0} = -2\int_0^{z_{LS}} dz\ \frac{1}{c^2}\frac{\partial\Phi}{\partial z}(\hat{\mathbf{n}}, z) \tag{3.1}$$

where Φ is the Newtonian gravitational potential at redshift z, $\hat{\mathbf{n}}$ is a unit vector along a line of sight, $T_0 = 2.725\,\mathrm{K}$ is the CMB temperature at present time and $z_{LS} \approx 1089$ is the redshift at the surface of last scattering.

The gravitational potential, Φ, is related to the matter density fluctuation via Poisson's equation (Eq. 7.14, Peebles 1980);

$$\nabla^2\Phi(\hat{\mathbf{n}}, z) = 4\pi G a^2 \rho_{\rm m}(z)\,\delta(\hat{\mathbf{n}}, z) \tag{3.2}$$

where a is the scale factor normalised to unity at redshift zero. By recalling that $\rho_{\rm crit}(0) = 3H_0^2/8\pi G$ and $\Omega_{\rm m} = \rho_{\rm m}(0)/\rho_{\rm crit}(0)$, the Fourier transform of the gravitational potential is

$$\Phi(\mathbf{k}, z) = -\frac{3}{2}\Omega_{\rm m}\left(\frac{H_0}{k}\right)^2 \frac{\delta(\mathbf{k}, z)}{a}. \tag{3.3}$$

Unfortunately, the ISW contribution to the CMB primary anisotropy is less than 10 per cent for $\ell \gtrsim 10$ and to make matters worse, the total anisotropy signal is dominated by cosmic variance at smaller ℓ (i.e. larger angle) where most of the ISW signal is expected to be (e.g. Hu and Scranton, 2004). To isolate the ISW signal one must cross-correlate the temperature fluctuation with a tracer of gravitational potential projected on the sky (Crittenden and Turok, 1996). For this purpose, one can use the simple 2-point statistics to compute the angular cross–correlation of the temperature and galaxy fluctuation maps in real space,

$$w_{gT}(\theta) = \langle \delta_g(\hat{\mathbf{n}}_\mathbf{1})\, \Delta_T(\hat{\mathbf{n}}_\mathbf{2}) \rangle \tag{3.4}$$

where $\hat{\mathbf{n}}_\mathbf{1} \cdot \hat{\mathbf{n}}_\mathbf{2} = \cos\theta$. To calculate the theoretical expectation for the real space cross–correlation, we start by computing the angular cross–power spectrum of the galaxy over-density and ISW temperature perturbation fields;

$$C_{gT}^{\rm ISW}(\ell) \equiv \langle \delta_{g,\ell m}\, \Delta^*_{T,\ell' m'} \rangle. \tag{3.5}$$

Firstly, we need to expand the galaxy density fields, $\delta_g(\hat{\mathbf{n}}, z)$, in spherical harmonics and Fourier transform them. For a galaxy survey with a selection function $\phi_g(z)$ and linear bias $b_g(z)$, this is

$$\begin{aligned} \delta_{g,\ell m} \;\; = \;\; i^\ell \int \frac{d^3k}{(2\pi)^3} \int dz\, 4\pi j_\ell(k\chi)\, Y^*_{\ell m}(\hat{\mathbf{k}}) \\ \times\, b_g(z)\, \phi_g(z)\, \delta(\mathbf{k}, z) \end{aligned} \tag{3.6}$$

where $j_\ell(y)$ is the spherical Bessel function of the first kind of rank ℓ, $Y_{\ell m}(\hat{\mathbf{k}})$ is the spherical harmonic function and χ is a comoving distance which is an implicit function of z through the relation $d\chi = c/H(z)\, dz$. In obtaining Eq. 3.6, we use the orthonormality of $Y_{\ell m}$ in their expansion of a plane wave (e.g. Scharf et al. 1992);

$$\exp(-i\mathbf{k}\cdot\hat{\mathbf{n}}\chi) = 4\pi \sum_{\ell m} i^\ell\, j_\ell(k\chi)\, Y_{\ell m}(\hat{\mathbf{n}})\, Y^*_{\ell m}(\hat{\mathbf{k}}) \tag{3.7}$$

Similarly, for the ISW temperature fluctuation, by putting together Eq. 3.1, 3.3 and 3.7, this is

$$\Delta^{\rm ISW}_{T,\ell m} = i^\ell \int \frac{d^3k}{(2\pi)^3} \int dz\, 4\pi j_\ell(k\chi(z))\, Y^*_{\ell m}(\hat{\mathbf{k}}) \times 3\Omega_{\rm m} T_0 \left(\frac{H_0}{kc}\right)^2 \frac{\partial}{\partial z}\left[\frac{\delta(\mathbf{k},z)}{a(z)}\right] \quad (3.8)$$

For a flat–sky approximation (Limber, 1953), following Afshordi et al. (2004) and realising that in linear perturbation theory $\delta(\mathbf{k},z) = D(z)\,\delta(\mathbf{k},0)$ and

$$\langle \delta(\mathbf{k_1})\,\delta(\mathbf{k_2})\rangle = (2\pi)^3\,\delta_{\rm Dirac}(\mathbf{k_1}-\mathbf{k_2})\,P(k)\,, \quad (3.9)$$

from Eq. 3.5, 3.6 and 3.8 , $C^{\rm ISW}_{gT}(\ell)$ can be simplified to

$$C^{\rm ISW}_{gT}(\ell) = \frac{4}{(2\ell+1)^2}\int dz\, P(k)\, W_{\rm ISW}(z)\, W_g(z). \quad (3.10)$$

$W_{\rm ISW}(z)$ and $W_g(z)$ are the ISW and galaxy window functions defined as

$$W_{\rm ISW}(z) \equiv 3\Omega_{\rm m} T_0 \left(\frac{H_0}{c}\right)^2 \frac{d}{dz}\left[\frac{D(z)}{a(z)}\right] \quad (3.11)$$

and

$$W_g(z) \equiv b_g(z)\,\phi_g(z)\,D(z) \quad (3.12)$$

where $k \approx (\ell+1/2)/\chi(z)$, $D(z)$ is the linear growth factor given by the fitting formula of Carroll et al. (1992) and $P(k)$ is the linear power spectrum at redshift zero. The survey selection function is given by

$$\phi_g(z) \equiv \frac{\chi^2 n_c(\chi)}{\int d\chi\, \chi^2 n_c(\chi)} = n(z)\frac{H(z)}{c} \quad (3.13)$$

where $n_c(\chi)$ is the comoving number density and $n(z)$ is the normalised redshift distribution, $N(z)$, of the galaxies in the survey. Finally, $w^{\rm ISW}_{gT}(\theta)$ is related to the cross–power spectrum via the expansion in Legendre polynomials;

$$w^{\rm ISW}_{gT}(\theta) = \sum_{\ell=2}^{\infty} \frac{2\ell+1}{4\pi}\, P_\ell(\cos\theta)\, C^{\rm ISW}_{gT}(\ell). \quad (3.14)$$

We set the monopole ($\ell = 0$) and dipole ($\ell = 1$) contribution to zero, as it is done in the *WMAP* maps (§3.2.1). The contributions of the monopole and dipole are significant and overpredict $w^{\rm ISW}_{gT}$ by ≈10 per cent (Cabré et al., 2006). The summation in Eq. 3.14 converges earlier than $\ell \approx 500$ but we set our upper limit to $\ell = 1000$ which provides

sufficiently stable models without sacrificing too much computing time. The linear power spectrum is computed using

$$P(k) = A\ k^{n_s}\ T^2(k) \tag{3.15}$$

where n_s is the scalar spectral index and A is the normalisation factor with the value set by σ_8. We use the transfer function, $T(k)$, fitting formula of Eisenstein and Hu (1998). Our fiducial models assume a ΛCDM Universe with $\Omega_\Lambda = 0.73,\ \Omega_{\rm m} = 0.27,\ f_{\rm baryon} = 0.167,\ \sigma_8 = 0.8,\ h = 0.7$ and $n_s = 0.95$. Note that, for a flat Universe with $\Omega_{\rm m} = 1$, the linear growth factor is equal to the scale factor, a, at all redshifts and $W_{\rm ISW}(z)$ vanishes, hence in this case we expect no correlation between large-scale-structure and the CMB.

3.4 Cross-correlation technique

Firstly, each galaxy sample is pixelised into equal area pixels on the sphere using the HEALPix (Górski et al., 2005) format, following the standard resolution and ordering scheme of the publicly-available *WMAP*5 temperature map (i.e. nested, res=9). The most conservative temperature mask, extended temperature analysis (KQ75), plus point source catalogue mask are then applied to the temperature maps (§3.2.1) and the pixelised galaxy distributions, discarding approximately 30 per cent of the entire sky. Additionally, in order to estimate fairly the galaxy background density and a robust cross–correlation result, the DR5 coverage mask including quality holes are applied to the data. We only restrict the data to the most contiguous region of the NGC and therefore exclude the SDSS stripes 39, 42 and 43 in the DR5 coverage mask. After applying 'KQ75 ∪ point source ∪ DR5' mask, 516,507 out of 3,145,728 pixels (all sky) are admitted for the cross–correlation analysis.

The galaxy number overdensity, $\delta_g(\hat{\mathbf{n}})$, is then calculated from the galaxy distribution maps and assigned to each pixel;

$$\delta_g(\hat{\mathbf{n}}) = \frac{n_g(\hat{\mathbf{n}}) - \overline{n}_g}{\overline{n}_g} \tag{3.16}$$

where n_g and $\overline{n}_g$ are the number of galaxies and its average for the sample of interest. Fig. 3.1 shows the W-band temperature fluctuation map and δ_g map for SDSS, 2SLAQ and AAΩ LRG, smoothed with Gaussian beam of 1° Full Width at Half Maximum (FWHM).

The two–point cross–correlation function at angular separation θ is computed using

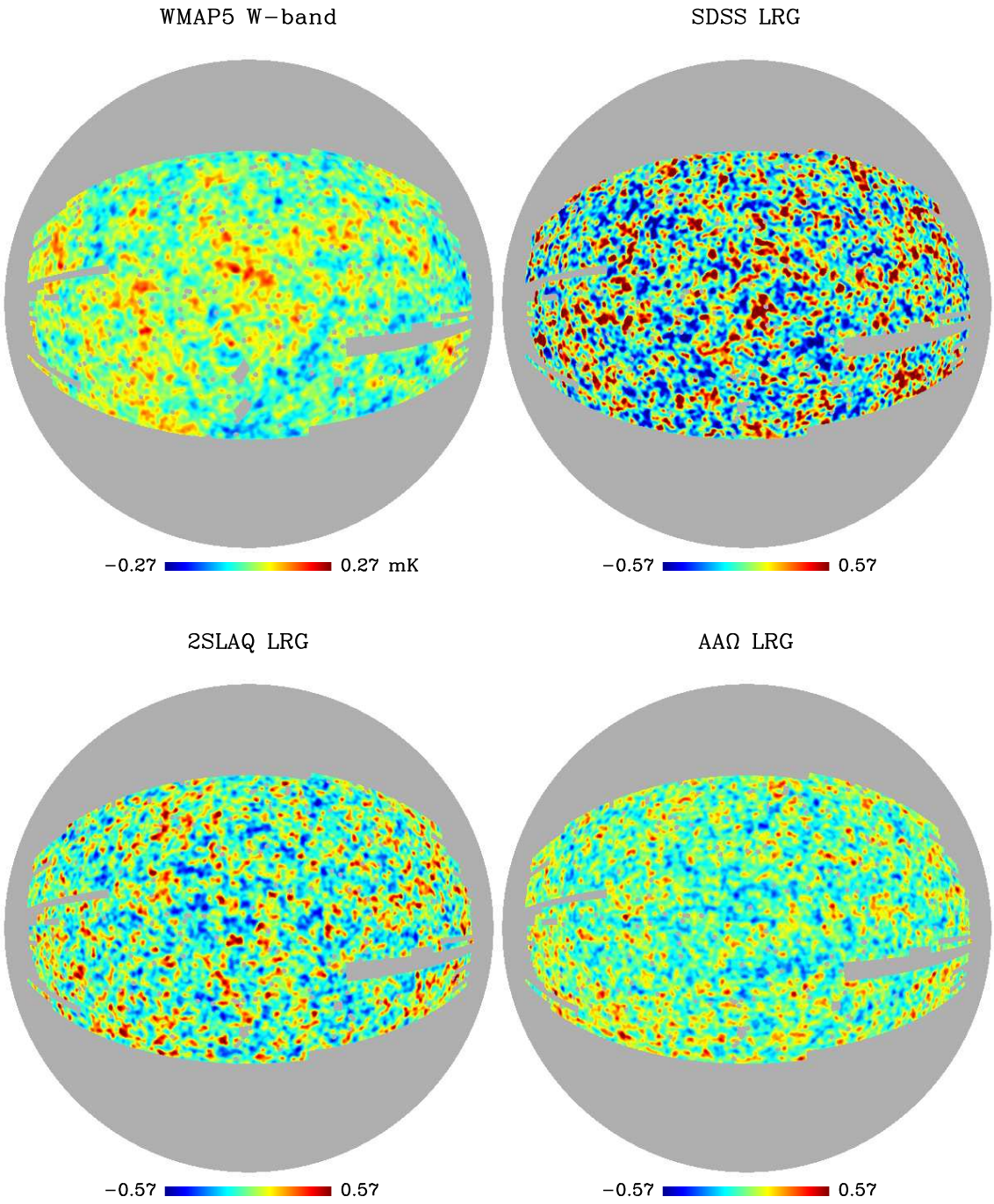

Figure 3.1: The 1° smoothed map of W-band data and galaxy number overdensity for SDSS, 2SLAQ and AAΩ LRG (Ubercal) after applying KQ75 and SDSS-DR5 mask.

$$w_{gT}(\theta) = \frac{\sum_{ij} f_i \delta_g(\hat{\mathbf{n}}_\mathbf{i})\, f_j \Delta_T(\hat{\mathbf{n}}_\mathbf{j})}{\sum_{ij} f_i\, f_j} \tag{3.17}$$

where f_i is the fraction of pixel i within the unmasked region, $\hat{\mathbf{n}}_\mathbf{i}\cdot\hat{\mathbf{n}}_\mathbf{j} = \cos\theta$ and Δ_T is the CMB temperature anisotropy measured by *WMAP*5 with the monopole and dipole contribution subtracted off. However, as we use relatively fine resolution pixels and weighting by the unmasked fraction does not alter our measurement, Eq. 3.17 is simply $w_{gT}(\theta) = \langle \delta_g(\hat{\mathbf{n}}_\mathbf{1})\, \Delta_T(\hat{\mathbf{n}}_\mathbf{2})\rangle$.

It is a well known fact that bins in the correlation function are correlated because the same points (or pixels in this case) can appear in many different pairs which are included in different bins, especially at large scales. To correctly estimate the statistical significance of the results, one needs to consider the full covariance matrix, $\mathbf{C}_{ij}$. Here, we construct the full covariance matrices using *jackknife* resampling. In order to obtain a sufficiently stable covariance matrix, the jackknife subsamples of approximately twice the number of angular bins being considered are needed. For the number of angular bins considered in this study, we split the masked temperature/overdensity map into 24 subfields with approximately equal area. The 24 jackknife subsamples are constructed from these fields, each one leaving out a different subfield. The $w_{gT}(\theta)$ are computed for each jackknife subsample and the covariance matrix is

$$\begin{aligned}\mathbf{C}_{ij} \;=\; & \frac{N_J - 1}{N_J} \sum_{m=1}^{N_J} [(w_{gT,m}(\theta_i) - \overline{w_{gT}}(\theta_i)) \\ & \times (w_{gT,m}(\theta_j) - \overline{w_{gT}}(\theta_j))]\end{aligned} \tag{3.18}$$

where $N_J = 24$ in this case, $w_{gT,m}(\theta_i)$ and $\overline{w_{gT}}(\theta_i)$ are the cross–correlation measured from the mth jackknife subsample and the average of all the subsamples in the ith bin, respectively. Note that the difference between $\overline{w_{gT}}(\theta)$ and $w_{gT}(\theta)$ estimated using the whole sample is negligible. The reason for multiplying $N_J - 1$ is because the jackknife subsamples are not independent. The statistical uncertainty for each individual angular bin is contained in the diagonal elements of the covariance matrix.

3.5 Results and Analysis

3.5.1 LRG–*WMAP*5

The cross–correlation results of the LRG distributions with the *WMAP*5 temperature maps using the three highest-frequency data plus the ILC are shown in Fig. 3.2. The

errors are 1σ statistical errors estimated from jackknife re-sampling of 24 subfields as described in §3.4. Generally, the results using different *WMAP* bands are in good agreement (within the 1σ error) for all three LRG samples. The achromatic results indicate that the contamination from effects such as dust, synchrotron and free-free emission which are frequency-dependent in nature are minimal or at least sub-dominant compared to our statistical uncertainties. This also applies to a lesser extent to the thermal Sunyaev–Zeldovich (Sunyaev and Zeldovich, 1980) effect, although for the bands shown, the difference in the SZ and CMB spectral slopes is only ≈30 per cent. However, we shall see in §3.7 that there is still a strong suggestion that other systematic effects may still be contaminating the SDSS and 2SLAQ results.

We first consider our new and higher redshift sample of 800 000 AAΩ LRGs. This sample shows virtually no positive correlation with the CMB data. If anything, the data show a slight anti-correlation out to large scales, possibly to $\theta \lesssim 1^\circ$ ($\approx 30h^{-1}$Mpc at the median redshift of the sample), although the signal to noise is still low. This weak anti-correlation is observed in all *WMAP*5 frequency bands under study here (the most right column of Fig. 3.2) with the exception of the Q band which only shows zero correlation at best with a possible zero-point shift towards very large scales. As for the SDSS and 2SLAQ results the cross–correlation with the ILC map gives a systematically lower amplitude (more negative in AAΩ case) than other bands. Given the relatively large scales of the null result in the AAΩ–*WMAP*5 CCF and the amplitude of the expected ISW signal (see Fig. 3.3), it would seem extremely unlikely that the positive correlation of the ISW effect could be cancelled out by the negative contribution from the thermal SZ effect. If this result is real and not due to some systematic effects, the implications for the view that the Universal expansion is accelerating, could be profound.

In the case of the SDSS and 2SLAQ LRG samples, our results are similar to those of the previous authors who have analysed similar datasets. We observe marginally significant positive correlations in the Q, V and W bands where the measured $w_{gT}(\theta)$'s are similar in terms of their amplitudes and angular extents for each sample although the signal is weaker in the SDSS sample. The ILC results are slightly lower than the other bands in both samples but otherwise still within 1σ error. Our SDSS results can be compared to the lowest redshift–bin sample of Scranton et al. (2003) who used the LRGs extracted from the SDSS DR2 following Eisenstein et al. (2001) but with a much fainter magnitude limit, $i < 21$, and divided their samples into redshift slices using photo–z. The results are similar in terms of amplitude but our errors are slightly smaller due to our larger area

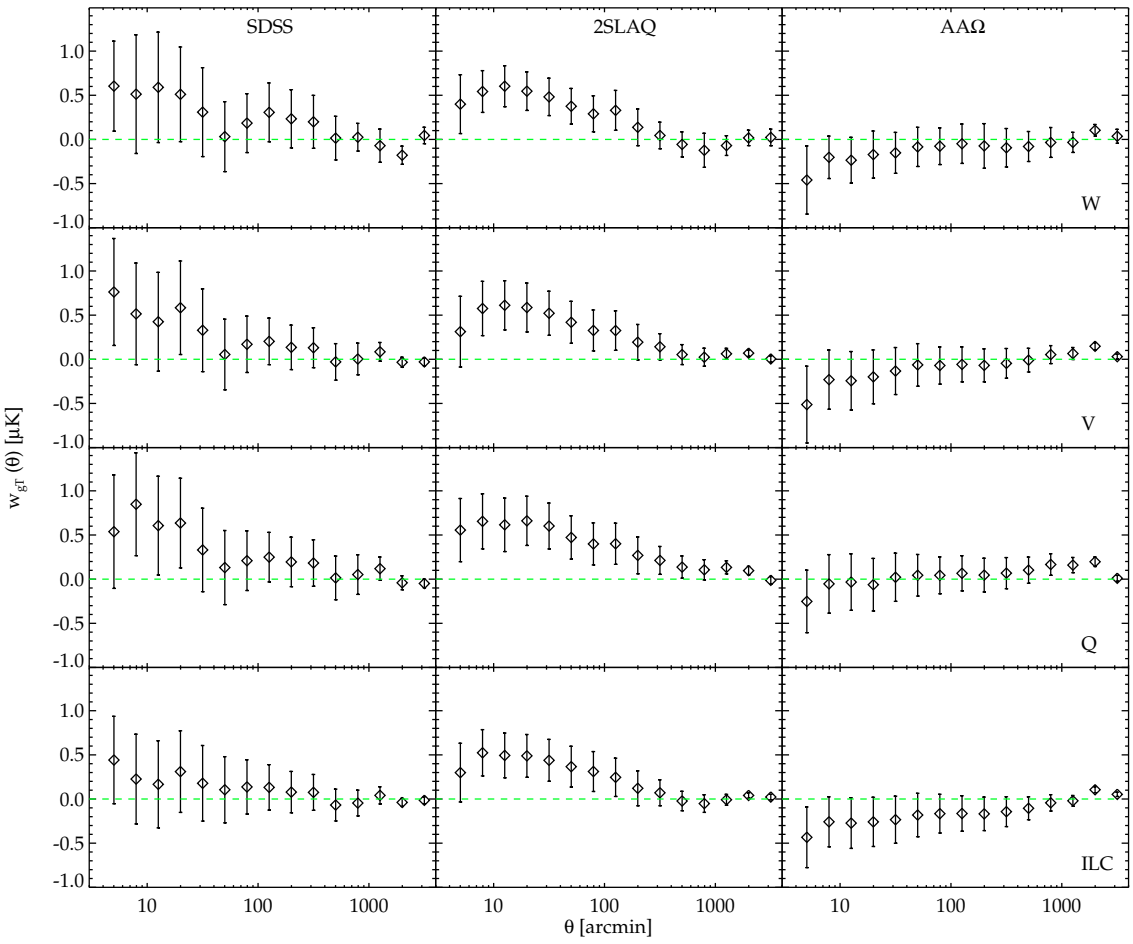

Figure 3.2: The cross-correlation results of *WMAP*5 W, V and Q band including the ILC map (top to bottom) with the SDSS, 2SLAQ and AAΩ LRG (left to right).

coverage (≈7600 deg^2 as opposed to ≈3400 deg^2) although their object numbers are ≈7 times higher than ours owing to the broader $N(z)$ and fainter flux cut.

The 2SLAQ results are comparable to the 'SDSS LRG' results of Giannantonio et al. (2008). These authors used the MegaZ-LRG photo-z catalogue of Collister et al. (2007), covering the redshift range 0.4–0.7 with a colour-magnitude selection similar to our 2SLAQ sample but a slightly fainter flux limit, $i_{\rm deV} < 20$ as opposed to 19.8. In the LRG panel of their Fig. 4, we see that their result has similar amplitude and errors (jackknife) to our 2SLAQ result. Although their Monte Carlo methods give somewhat larger errors than the jackknife estimations, the statistical significance estimated using errors drawn from both methods are very similar, 2.2–2.5σ for their LRG catalogue. Padmanabhan et al. (2005) has also performed the analysis with a similar LRG sample but using the angular cross–power spectrum, C_ℓ, making a direct comparison to our results difficult. The sample these authors used is somewhat similar to the Eisenstein et al. (2001) selection but with the flux cut as faint as 2SLAQ in 'CutII', resulting in a redshift distribution similar to our SDSS and 2SLAQ LRG samples combined, although they limited the redshift of the sample to $0.2 < z < 0.6$ using their template-fitting photo-z. The positive correlation is detected at 2.5σ, similar to Giannantonio et al. (2008) although the sample they used only covers half as much sky. We conclude that our analyses are broadly reproducing previous results in these $0.25 < z < 0.6$ LRG redshift ranges, both in terms of their amplitude and statistical significance.

3.5.2 Comparison to Models

Fig. 3.3 shows the comparison of our results to the theoretical expectation as described in §3.3. The galaxy selection functions used in construction of these models are given by the normalised $N(z)$ of the sample as shown in Fig. 2.1 (see also §2.2). The galaxy bias in the model is estimated from the angular autocorrelation function, $w_g(\theta, \bar{z})$, of each LRG sample relative to the underlying dark matter clustering, $b_g^2(\bar{z}) = \xi_g(r, \bar{z})/\xi_{\rm m}(r, \bar{z})$, where we assume the linear scale-independent bias and measure its value at large scales (≈10 h^{-1}Mpc). The matter $\xi(r, \bar{z})$ is estimated for the same fiducial cosmology as described in §3.3 and then projected onto the sky using the corresponding $n_g(z)$. This gives an unbiased prediction which can be compared to the measured $w_g(\theta, \bar{z})$ and allows $b_g(\bar{z})$ to be extracted from their relative amplitudes. Note that we assume non-evolving bias and denote the bias estimated from each sample as the bias at the corresponding average redshift which is reasonable, given the narrow redshift ranges of our samples. The galaxy

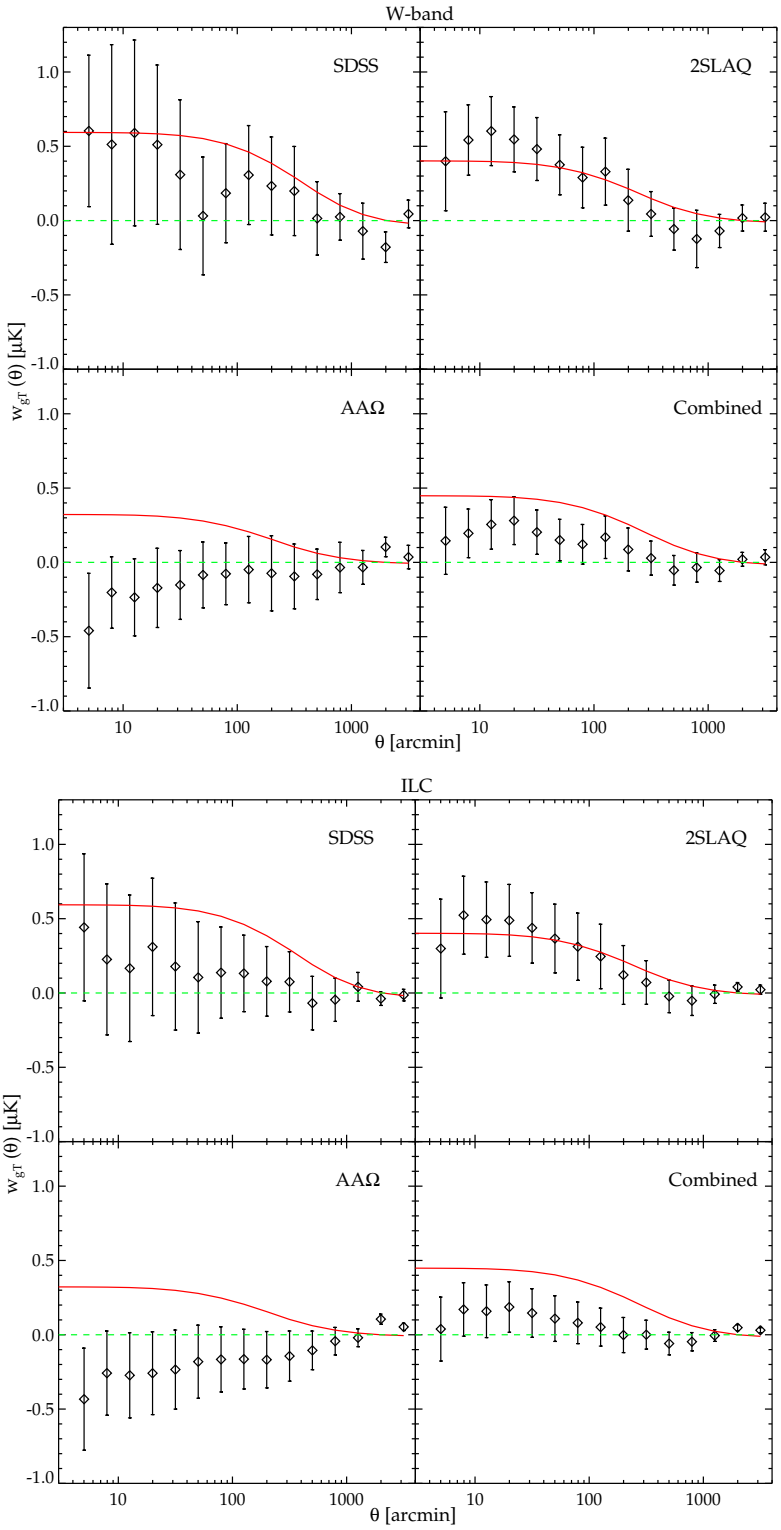

Figure 3.3: The LRG–*WMAP5* cross-correlation results using W-band and ILC map compared to the theoretical predictions (red solid lines), assuming the standard ΛCDM and the galaxy linear bias (b_g) of 2.10, 1.99, 2.2 and 2.1 for SDSS, 2SLAQ, AAΩ-LRG and the combined sample respectively. The stellar contamination correction for each sample has been applied to the corresponding model. In the 'Combined' panels, the cross–correlation results of the quadrature–error weighted mean of the three LRG samples are compared to the average model predictions.

bias measured in this way can also be viewed as an effective value for each sample. The models shown in Fig. 3.3 use $b_g(\bar{z})$ of 2.10 ± 0.04, 1.99 ± 0.02 and 2.20 ± 0.02 for the SDSS, 2SLAQ and AAΩsamples, respectively. These values are taken from Sawangwit et al. (2011a) and are compatible with the values measured by other authors, e.g. Tegmark et al. (2006), Padmanabhan et al. (2007) whose $b_g(0.35) = 1.9 \pm 0.07$ and $b_g(0.55) = 1.85 \pm 0.05$ as compared to our SDSS and 2SLAQ LRG, respectively. The b_g value of Tegmark et al. (2006) was measured from a sample of $z \approx 0.35$ LRGs similar to what we call SDSS LRG sample here but without the bright limit cut (see §2.2.1) hence allows under–luminous objects and main galaxies into their sample. And as a result we expect their bias to be somewhat lower than ours.

As emphasised earlier, the AAΩ LRG sample shows no positive correlation with the *WMAP*5 data and perhaps even a slight negative correlation. We then combined the W-band data between 12′–120′, and found the amplitude of the CCF and its jackknife error (1σ) is -0.07 ± 0.2 μK. This is consistent with the null hypothesis (only $\approx 0.4\sigma$ deviation) and rejects the ISW signal expected in the standard models at $\approx 1.9\sigma$ or at 5 per cent significance after the stellar contamination has been taken into account in the predicted signal (see §3.6.3). Performing a similar statistical analysis on the cross–correlation results using the ILC map gives a slightly higher significance of rejecting the standard model ISW hypothesis (2.2σ, see Table 3.1).

Additionally, to test that the zero correlation in the AAΩ results is not due to its faint limit making the sample incomplete, we have cut the faint limit of the sample back in steps of 0.25 mag to 20.0 (see §3.6.2 and Sawangwit et al. 2011a). The amplitude of the CCF between 12′–120′ for $i < 20.25$ (denoted by AAΩ* in Table 3.1) is -0.1 ± 0.2 for W-band data and -0.2 ± 0.21 for the ILC map. The ISW model prediction is then re-computed taking into account the corresponding $n(z)$ and linear bias, including the correction for stellar contamination at the same level as the main AAΩ sample. The significance of rejection of the standard model for the $i < 20.25$ AAΩ sample is slightly higher than that of the main AAΩ sample, at 2.2σ and 2.5σ for W-band and ILC map, respectively.

The measured w_{gT} for the SDSS LRG agrees reasonably well with the theoretical expectation at angles $\lesssim 30'$ although not at high statistical significance. However, the same cannot be said for the angle beyond this scale and up to $\approx 600'$ where the cross–correlation appears to be less than the expected signal although still not at high significance. One may be inclined to conjecture that this could be due to the negative contribution coming

Table 3.1: The significance tests of the cross–correlation results using the *WMAP* W-band data and ILC maps. The measurements are tested against the expected ISW prediction in the standard ΛCDM model and null result hypothesis. Column 5 gives the amplitudes and 1σ jackknife errors of the data binning between $12'$–$120'$. Column 6 gives the significance of the deviation of the value in column 5 relative to ISW/null signal hypothesis.

Sample		$\bar{z}$	Number	$b_g(\bar{z})$	$w_{gT}(12' - 120')$ μK	Deviation significance (ISW,null)
W-band:	SDSS	0.35	106,699	2.10 ± 0.04	0.25 ± 0.33	$(1.0\sigma, 0.8\sigma)$
	2SLAQ	0.55	655,775	1.99 ± 0.02	0.34 ± 0.21	$(0.2\sigma, 1.6\sigma)$
	AAΩ	0.68	800,346	2.20 ± 0.02	-0.07 ± 0.20	$(1.9\sigma, 0.4\sigma)$
	AAΩ*	0.67	375,056	2.37 ± 0.03	-0.10 ± 0.20	$(2.2\sigma, 0.5\sigma)$
	Combined	0.60	1,562,820	2.10 ± 0.01	0.15 ± 0.17	$(1.0\sigma, 0.9\sigma)$
	Weighted mean	–	–	–	0.14 ± 0.14	$(1.3\sigma, 1.0\sigma)$
ILC map:	SDSS	0.35	106,699	2.10 ± 0.04	0.19 ± 0.33	$(1.2\sigma, 0.6\sigma)$
	2SLAQ	0.55	655,775	1.99 ± 0.02	0.27 ± 0.22	$(0.5\sigma, 1.2\sigma)$
	AAΩ	0.68	800,346	2.20 ± 0.02	-0.18 ± 0.22	$(2.2\sigma, 0.8\sigma)$
	AAΩ*	0.67	375,056	2.37 ± 0.03	-0.20 ± 0.21	$(2.5\sigma, 1.0\sigma)$
	Combined	0.60	1,562,820	2.10 ± 0.01	0.07 ± 0.17	$(1.4\sigma, 0.4\sigma)$
	Weighted mean	–	–	–	0.07 ± 0.13	$(2.0\sigma, 0.5\sigma)$

from the thermal SZ effect, but at this redshift $100'$ corresponds to $\approx 20\ h^{-1}$Mpc which would be too large a scale to be caused by hot gas in galaxy clusters. Although the clusters do cluster among themselves, the contribution to any extended SZ effect is likely to be small (Myers et al., 2004). Besides, there is no physical reason why SZ effect should affect only the highest redshift sample. The most likely explanation for this appears to be a statistical fluctuation which means that our SDSS LRG measurement rejects neither the ISW expectation nor the zero correlation at more than $\approx 1\sigma$ significance level. If we bin the data in the angular range $12'$–$120'$ into a single bin, the correlation amplitude and its jackknife error (1σ) is $0.25 \pm 0.33\ \mu$K which deviates from the null result hypothesis by only 0.8σ and from the standard model by 1.0σ. For the 2SLAQ case, as in other studies, the positive cross-correlation signal agrees very well with the expected ISW signal in the standard cosmology in terms of its amplitude and angular extent. Nevertheless, the 2SLAQ sample's rejection of the null result is still only at the 1.2-1.6σ significance level (see Table 3.1).

3.5.3 The Combined LRG sample

We shall now consider the cross–correlation of the combined LRG sample with the CMB data. In our first method of combining the three LRG samples we shall treat these as three independent surveys and then test this assumption by presenting the cross-correlation result for the combined 1.5 million LRG sample, complete with its own direct jackknife error analysis, to check that they agree.

First, the three CCF's of the SDSS, 2SLAQ and AAΩ samples are combined by weighting inversely in quadrature according to the statistical errors of each sample[2] (see bottom right panels of Fig. 3.3 and also Fig. 3.4). The model (red solid line in Fig. 3.3) is estimated by taking an average of the ISW models of the three LRG samples. We find that the rejection significance is 1.3σ for the standard ISW model and 1.0σ for the null result in the W band. In the ILC band the significance of the rejection of the ISW model rises to 2.0σ and the significance of rejection of the null result reduces to 0.5σ. Table 3.1 gives the summary of all the significance tests performed. We conclude that while the ISW standard model is still consistent with the CCF result from the three combined, weighted LRG samples it is now more consistent with the null result due to the inclusion of the AAΩ data.

[2]This is similar to combining χ^2 from the independent samples, although we do not take any possible correlation between samples into account here (see e.g. §3.5.4).

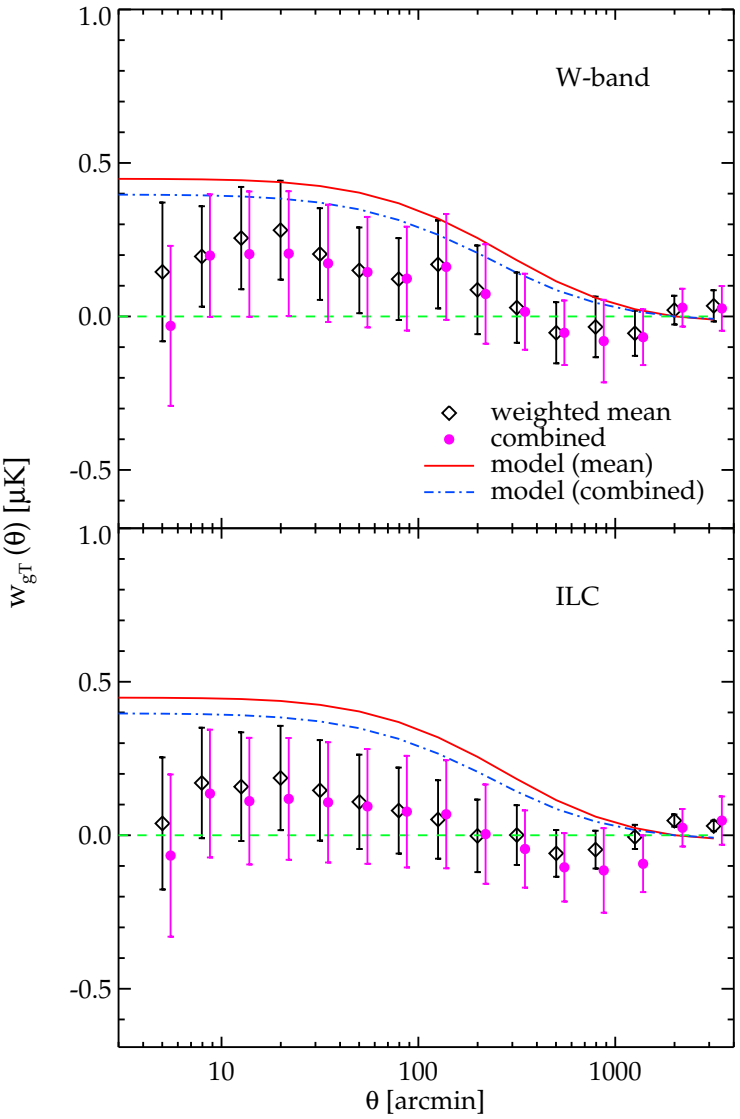

Figure 3.4: (top) The W-band cross–correlation results of the combined sample (solid circles) compared to the quadrature–error weighted mean of the three LRG sample (diamonds). Also shown are the standard model predictions by taking a weighted mean (solid line) of the models of three LRG samples and for the combined sample (dot-dash line). (bottom) Same as above but for the ILC map rather than W-band data

Second, for comparison, we also present the results of cross-correlating the combined LRG sample with the WMAP5 data i.e. we now treat the combined sample of ≈ 1.5 million LRGs as a single sample for cross-correlating with, in turn, the WMAP5 W and ILC CMB data. A full jackknife error analysis was carried out in the same way as for the individual samples. We expect the results to be similar to the weighted combination of the three samples' CCF's as presented above. Fig. 3.4 shows the comparison between these results. The models for the combined samples are computed following the procedure described in §3.3 assuming the linear galaxy bias (given in Table 3.1) estimated from the angular autocorrelation function and $N(z)$ of 1.5 million LRGs. Table 3.1 again shows the significances of rejection of the standard model and the null results. We see that the observational results in both cases are very similar. For both bands, the significances are given in Table 3.1. The results are again very similar to those where the weighted mean was adopted. The cross-correlation results are again as consistent with the zero correlation as they are with the standard ISW model for the W band. The ILC band again more significantly rejects the ISW model than the null result.

Clearly the preference for the null result over the standard model prediction depends on the accuracy of the new AAΩ result. We test the robustness of the AAΩ result in §3.6.

3.5.4 χ^2 fits

For completeness, we also quantified the goodness-of-fit of our measurements to the expected ISW signal or null result hypothesis by calculating the *chi-square*, χ^2, which uses the normal size bin as shown in Fig. 3.3 and takes into account the possible correlation of the bins through the use of the covariance matrix (§3.4). The χ^2 is given by

$$\chi^2 = \sum_{i,j} \mathbf{C}_{ij}^{-1} [w_{gT}(\theta_i) - w_{gT}^{\rm ISW}(\theta_i)] \cdot [w_{gT}(\theta_j) - w_{gT}^{\rm ISW}(\theta_j)] \tag{3.19}$$

where $\mathbf{C}_{ij}^{-1}$ is the inverse of covariance matrix, $w_{gT}(\theta_i)$ is the measured angular cross–correlation and $w_{gT}^{\rm ISW}$ is the theoretical expectation assuming the standard ΛCDM cosmology (see Fig. 3.3) which can be replaced by zero when testing the zero correlation hypothesis. Using the galaxy linear bias, b_g, and $N(z)$ for each sample as as mentioned in §3.5.2, the χ^2 tests were performed for the angular bins between $12'$–$120'$, inclusively. The lower limit is set approximately to the best WMAP5 resolution in the W band ($\approx 12'$).

The significances obtained from the χ^2 method generally confirmed the results using the $12'$–$120'$ bin, especially those of the main LRG samples. For example, assuming

standard model parameters, the SDSS-W band results give χ^2=19.4 for the predicted ISW signal and 17.7 for the zero correlation hypothesis. For the 2SLAQ results, using the standard model gives $\chi^2 = 13.2$ and relative to the null result gives $\chi^2 = 11.5$. These χ^2 were computed for 6 degrees-of-freedom (d.o.f), i.e. 6 angular bins were used in computing the χ^2. Using the χ^2 distribution, the SDSS results deviate from the ISW model and null result at 4 and 7 per cent statistical significance, respectively. The 2SLAQ results agree with the ISW model with the reduced chi-square, χ^2/d.o.f., of order of unity and reject the zero correlation hypothesis at 1.5σ significance. The AAΩ results gave $\chi^2 = 11.7$ and $\chi^2 = 4.4$ for the ISW model and null correlation respectively, corresponding to the chances of agreement of 7 per cent and 62 per cent. These all agree reasonably well with the large-bin significances presented in Table 3.1. However, similar χ^2 significance tests for the combined sample and some ILC individual samples did not perform very consistently, occasionally giving pathological results and poor agreement with the $12'$–$120'$ bin and this is why we have only quoted the simpler, single large-bin significances in Table 3.1.

3.6 Robustness tests

Given that the AAΩ LRGs comprise a new sample, there is no previous measurement that can be directly compared to our own. We now present the result of tests we have done in order to check the robustness of our new result.

3.6.1 Random realisations and simulated CMB Maps

Here we generate 100 random realisations for each of the samples. Each realisation has the same number density as the sample it tries to mimic. Note that these random realisations are not clustered. The results are shown in Fig. 3.5. The jack-knife errors that we use are seen to be much larger than the standard deviation of the random catalogues (inner green shaded region). This is expected because the random catalogues are not clustered unlike the LRGs. The means of these random realisations are consistent with zero and show no sign of bias except perhaps at the smallest scales of the SDSS sample.

We have also made simulated CMB temperature anisotropy maps and cross-correlated these with the three LRG samples. A simulated CMB map is generated as a realisation of random Gaussian fields on a sphere with the fluctuation characterised by *WMAP*5 best-fit power spectrum. The simulated maps are also convolved with a Gaussian beam with FWHM similar to the *WMAP* W-band, i.e. $12\farcm6$. The cross–correlation results are

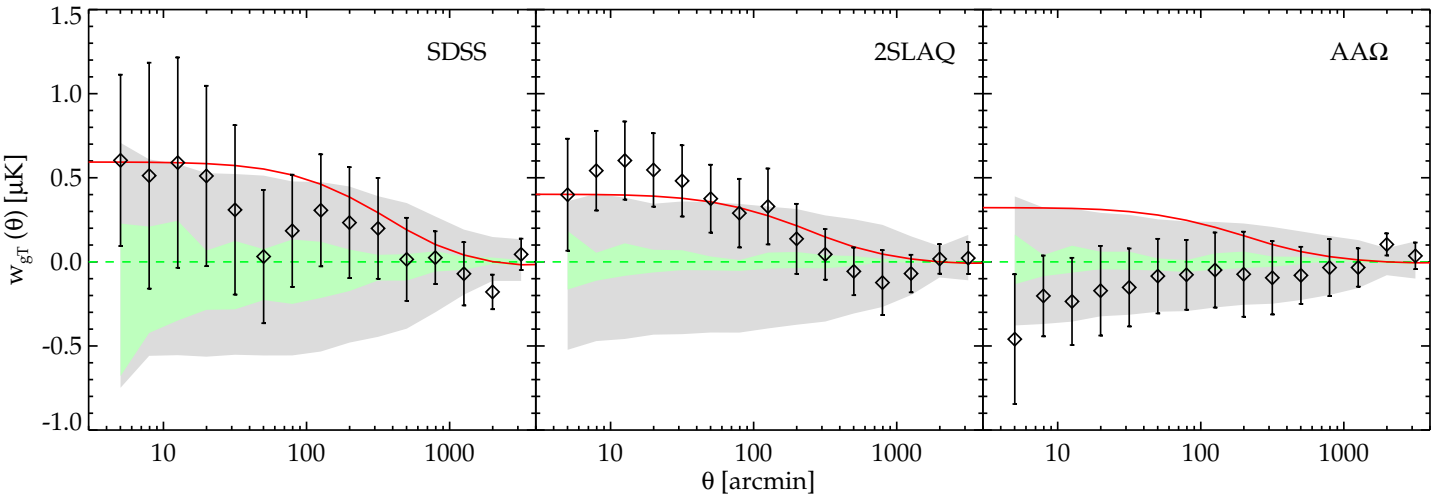

Figure 3.5: The cross–correlation results (diamonds) of three LRG samples and their jackknife errors (1σ) compared to the results of using 100 random realisations of each LRG sample (inner green shaded region) and 100 simulated CMB maps (outer grey shaded region). The shaded area signify a standard deviation in the measurement of 100 realisation for each case. Note that the means of these random realisations are consistent with zero as can be seen from their symmetry about the zero line. The solid line is again the theoretical prediction of the ISW signal in standard ΛCDM model.

shown in Fig. 3.5. The standard deviation of 100 CMB random realisations (outer grey shaded region) are roughly consistent with our jackknife estimates especially at small and intermediate scales but somewhat larger at large scales.

3.6.2 Photometry test

Next, we look to see if the AAΩ cross-correlation measurement is robust by comparing the result from the SDSS 'ubercalibration' of Padmanabhan et al. (2008) with that from the standard SDSS calibration. Fig. 3.6 shows that the results are stable to whichever calibration we used. We further looked for systematic effects in the original photometry by weighting SDSS stripes according to their overall number density. The physical motivation for this arises from the SDSS observing strategy and the fact that a slightly different calibration for different nights could affect the source density as a function of the SDSS stripe, given our faint limit. We observe a hint of these variations although not at a high level and use these to correct the source densities in each stripe as mentioned. However, such variations seem to be weaker when using the ubercalibration as opposed to the standard one. The result of weighting according to the stripe number density is shown in Fig. 3.6 and again the result appears robust when this filter is applied to the original data.

Although we work at a relatively high galactic latitude, it is possible that in some regions of the sky, high galactic dust obscuration could result in lower numbers of photometrically detected objects. Furthermore, that same dust obscuration patch could be a source of contamination in the CMB data in the sense that the temperature in that particular region could be systematically raised by the dust emission and hence results in a false anti-correlation. To test this, we exclude the region where the extinction is greater than 0.1 mag in the i-band which discards ≈ 15 per cent of the data. We observe no difference to our main results, even when a more aggressive limit, $i_{\rm extinction} < 0.08$ (23 per cent discard), is applied (see Fig. 3.6). Note that when similar tests are performed using extinction in the SDSS r-band instead, we again obtain results which are consistent with those presented in §3.5 for all three LRG samples.

We then cut back the i-band limit of the AAΩ sample in 0.25 mag steps from $i = 20.5$ to $i = 20.0$ while keeping the other conditions the same. These results are compared with the result at $i < 20.5$ in Fig. 3.7. Again the results appear robust. We have also made tests of the single epoch SDSS photometry using deeper Stripe 82 (Abazajian et al., 2009) and the William Herschel Deep Field (WHDF, Metcalfe et al. 2001) data. Both

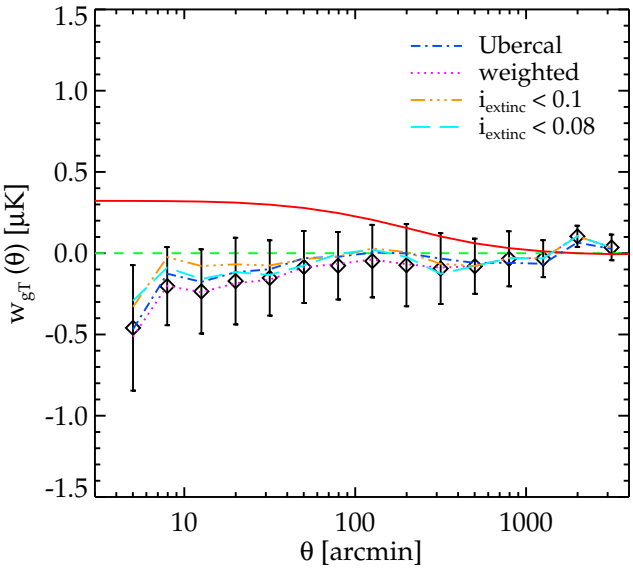

Figure 3.6: The cross-correlation of the AAΩ LRG to W-band data using the original SDSS photometry (diamond) compared to the measurements using 'ubercalibration' (dot-dash line), the stripe weighted (dotted line) and when the data is restricted to the region where galactic extinction in i-band less than 0.1 (dot-dot-dot-dash line) and 0.08 (long dashed line) magnitude.

these comparisons showed that the SDSS photometry in r, i and z bands showed good agreement with the deeper data until the errors showed a significant increase beyond the limits $r = 22.0$, $i = 21.0$ and $z = 20.2$.

3.6.3 Star–galaxy separation

We noted in §3.2 that the stellar contamination in our AAΩ-LRG sample could be as high as 16 per cent. Care should therefore be taken when analysing this dataset. We obtained this contamination fraction using the information learned from the AAΩ-LRG spectroscopic survey (Ross et al., 2008b), by imposing a star–galaxy separation in the z-band similar to the method applied in the SDSS- and 2SLAQ-LRG redshift surveys using the i-band. Our optimised star–galaxy separation procedure selects objects with $z_{\rm psf} - z_{\rm model} > 0.53 + 0.53(19.0 - z_{\rm model})$ which only loses genuine LRGs at a sub-percent level and leaves ≈16 per cent stellar contamination in our sample, as quoted earlier.

The effect of stellar contamination distributed at random in the sample is simply a dilution of the over/under density hence reducing the autocorrelation amplitude of the sample by $(1-f)^2$ and the cross–correlation by a factor of $(1-f)$ where f is the fraction of

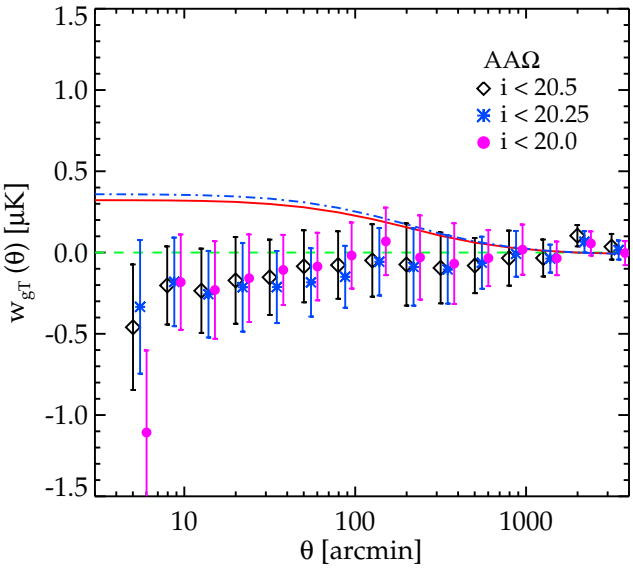

Figure 3.7: The cross-correlation of the AAΩ LRG to W-band data compared to the measurements using the same colour–colour selection sample but with brighter faint–limit cut, $i_{\rm deV} < 20.25$ and $i_{\rm deV} < 20.0$. Only the theoretical expectation of the full (solid line) and $i_{\rm deV} < 20.25$ (dash-dot line) sample are shown. The data points are shifted slightly for displaying purposes.

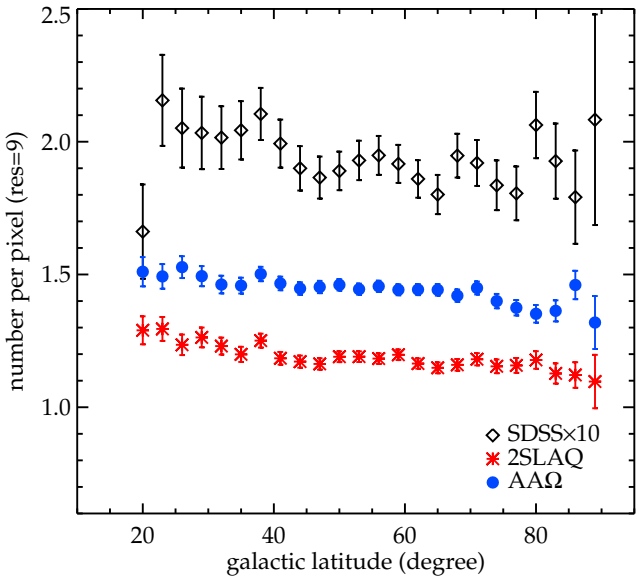

Figure 3.8: The object numbers per pixel as a function of galactic latitude, b. Recall that we use equal area (≈ 49 arcmin^2) pixels with res=9 resolution scheme (HEALPix, Górski et al., 2005). The SDSS number has been multiplied by 10 to extend the plot range.

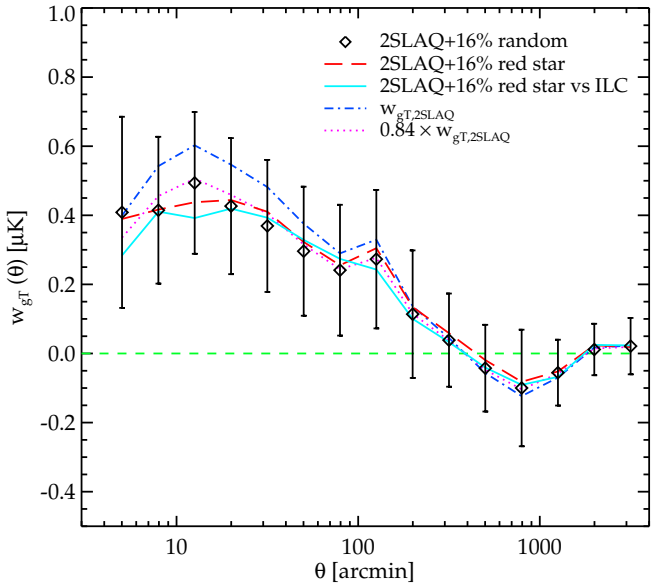

Figure 3.9: The cross–correlation of the W-band data and the 2SLAQ LRG when a sample of random realisation of ≈16 per cent is added to the LRG catalogue (diamonds). The results using original 2SLAQ sample and when multiplied by $1 - f_s$ are shown as the dot-dashed and dotted lines, respectively. The long-dashed line shows the result when the 16 per cent added contaminants are replaced by red stars. The result of cross–correlating the ILC map with the 16 per cent–red star contaminated 2SLAQ sample is also shown (solid line).

the contamination. This is true if the contamination is distributed uniformly at random in the sample. However, if there is some spatially dependent variation of the number density, a further systematic effect could arise through this process. To test this, we first check to see if there is a trend of the number density as a function of galactic latitude as one might expect for stellar contamination. Although a slight such trend is observed, it is at no more than the levels observed in the SDSS and 2SLAQ samples (see Fig. 3.8) whose stellar contamination fractions are approximately 1 and 5 per cent, respectively. Next we restrict the data to the high galactic latitude regions, namely $b > 40°, 50°$ and $60°$. The results are in good agreement with our main results for all three LRG samples up to $b > 60°$ where the cross–correlations become noisy due to the 75 per cent reduction in the sample sizes.

To simulate the effect of the stellar contamination on the LRG–CMB cross–correlation, we have introduced a set of random realisations into the 2SLAQ sample. The result is presented (diamonds) in Fig. 3.9 along with the cross–correlation of the original 2SLAQ

sample (dot-dashed line) and the result of reducing its amplitude by a factor of $(1 - 0.16)$ (dotted line). Furthermore we would like to check for any effects that may arise from possible large scale clustering of the stars. This is done by adding a sample of red stars to the 2SLAQ LRG sample at the 16 per cent level. The stars are selected with similar colour–magnitude criteria to that of the AAΩ LRGs and should mimic the angular distribution and properties of the stellar contaminants seen in the sample. The result is shown in Fig. 3.9 (long-dashed line). This test should also reveal any possible effects on the w_{gT}'s due to (if any) correlation between these stars and the CMB. We found the 16 per cent–red star contaminated 2SLAQ result to be consistent with the dilution of randomly distributed contaminants case. The result is also consistent with the cross–correlation with the foreground reduced ILC map (solid line), further confirming that our result is not affected by any star–CMB cross–correlation. Note that the significance test presented in Table 3.1 has already taken into account such an effect by multiplying the ISW model by a factor of $(1 - 0.16)$. The significance of the AAΩ sample's rejection of the standard model ISW prediction is therefore robust against the stellar contamination discussed here.

We next attempt to reduce the stellar contamination fraction by imposing a more aggressive star–galaxy separation cut which result in nearly halving the number of genuine AAΩ LRGs. The cut is a combination of the fitted 'de Vaucouleurs' radius as a function of $z_{\rm deV}$ magnitude and the correlation between the 'de Vaucouleurs' and fiber magnitudes in z-band. This reduces the contamination to ≈9 per cent. Fig. 3.10 (top panel) shows the cross–correlation of this sample with the W-band data which is in good agreement with our main result.

The contamination fractions of these samples are verified by their angular autocorrelation functions, $w_{gg}(\theta)$. The corrected $w_{gg}(\theta)$ is shown in bottom panel of Fig. 3.10. This is again in good agreement with the 16 per cent contaminated sample and consistent within $\approx 1\sigma$ of the Ross et al. (2008b) power–law fit to the semi–projected correlation function, $w_p(\sigma)$. Note that we only expect the agreement in the range $r \approx$1–15 h^{-1} Mpc where a single power-law is a good fit to the data. The measured w_{gg}'s are also consistent with the results when restricting galactic latitude to greater than 40°, 50° and 60°. We believe the slight discrepancy with the $w_p(\sigma)$ is due to the noisy measurement from the small number of spectroscopically confirmed LRGs used in Ross et al. (2008b) and not caused by the under–estimation of the contamination level as demonstrated by our two independent approaches for star–galaxy separation.

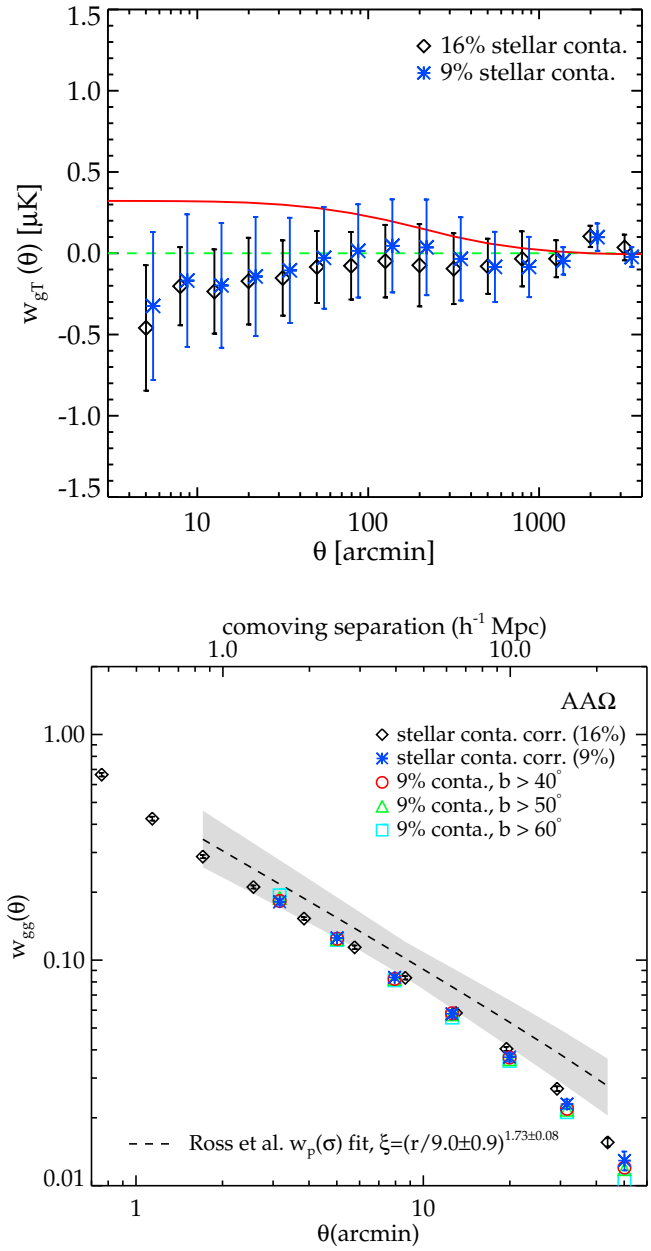

Figure 3.10: (top) The AAΩ LRG–WMAP5 cross–correlation of the 9 per cent stellar contaminated sample (asterisks) compared to the main AAΩ sample used in our study (diamonds). (bottom) The corrected autocorrelation functions of the 9 per cent– and 16 per cent–contaminated samples (asterisks and diamonds). These are compared to the results of limiting the 9 per cent–contaminated sample to the regions with galactic latitude higher than $> 40°$, $50°$ and $60°$. The dashed-line and shaded region is the $w_{gg}(\theta)$ and 1σ error inferred from the $w_p(\sigma)$ measured from ≈ 400 spectroscopically confirmed AAΩ LRGs (Ross et al., 2008b).

Even if the contamination fraction is under-estimated, the effect of an increased (uniform) stellar contamination would be to increase the ISW model amplitude when the bias value from the LRG autocorrelation is corrected upwards to obtain the true bias value. This upwards shift in the ISW model would then be exactly cancelled by the downwards correction to account for the dilution of the cross-correlation signal due to stellar contamination.

We conclude that despite the faint magnitude limit, and moderate level of stellar contamination ($\approx$ 16 per cent) our ISW results for the AAΩ LRGs seem robust to the tests we have made and the SDSS data seem accurate enough to support this ISW analysis. Up to this point, we have therefore found no explanation in terms of a systematic effect for the low AAΩ–*WMAP*5 cross–correlation result. Next, we shall perform a similar analysis on some of the large-scale tracers whose ISW effect has been previously claimed in order to test our methodology and look for other possible systematics in these samples.

3.6.4 SDSS galaxy–*WMAP*5

We next cross–correlate galaxies extracted from SDSS DR5 using r-band magnitude limits. The objects are photometrically classified as galaxies by the SDSS reduction pipeline. We subsample the galaxies in three magnitude ranges, namely, $18 < r < 19$, $19 < r < 20$ and $20 < r < 21$, where all the magnitudes are galactic extinction corrected model magnitudes. The subsamples contain approximately 2, 6 and 16 millions objects, respectively. This is the same as Cabré et al. (2006, C06 hereafter) but covering $\approx$ 20 per cent more area and we use *WMAP*5 rather than *WMAP*3. A similar r-band selected galaxy sample was also used by Giannantonio et al. (2008, G08 hereafter) although these authors use 'ubercalibration' photometry rather than the original one and limit the sample photo-z to redshift between 0.1–0.9. The ISW effect has been claimed to be detected in these samples at moderate significance level by both C06 and G08 although their results do not agree with the former having twice as much positive cross–correlation between the CMB and the r-band selected galaxy sample. As a result C06 need to fit their result with higher Ω_Λ, for a galaxy bias $b = 1.0$.

For the cross-correlation analysis, we proceed in the same manner as with the LRG samples. To compute the ISW model, we use the $n(z)$ distributions following Dodelson et al. (2002). The average redshifts inferred from the $n(z)$ are estimated to be approximately 0.17, 0.24 and 0.33. We then follow our procedure for the LRGs and obtain the galaxy linear bias from the measured amplitude of the galaxy 2-point autocorrelation

function for each subsample. We obtain the values $b_g = 1.2, 1.1$ and 1.2 for the sample with r-band magnitude limit of 18–19, 19–20 and 20–21, respectively, in agreement with the measurements of C06 and G08 whose $b_g \approx$1–1.2. The cross–correlation measurements and the theoretical models are presented in Fig. 3.11.

We marginally detected the correlation between the CMB data and all the r-band selected subsamples. We shall now compare the $20 < r < 21$ result in Fig. 3.11 to Fig. 2 (top) of C06. Our result is lower by a factor of ≈ 2 but very close to the re-analysis of the SDSS r-band data of G08 who also found a factor of two discrepancy with C06. After their discussions, the two groups found that the discrepancy is due to an extra quality–cut imposed on the data by C06, namely, r-band magnitude error less than 0.2 mag. We regard the factor of two rise in the amplitude of the cross-correlation after this small change in the magnitude error limit simply as symptomatic of the statistical fragility of the result. We conclude that our re-analyses of these data agree well with the standard ΛCDM predictions although the significance of rejection of the null result is still only $\approx$1–2σ.

3.6.5 NVSS-*WMAP*5 cross–correlation

To test our methodology further, we performed a cross–correlation analysis of *WMAP*5 with radio sources from the NRAO VLA Sky Survey (NVSS; Condon et al. 1998) which has been previously used by various groups for ISW studies. The NVSS sample comprises about 1.8 million radio sources detected to a flux limit of $\approx$ 2.5mJy at 1.4GHz. The NVSS covers the entire sky higher than -40° declination ($\approx$80 per cent of the sky). Interestingly, the previous study of Boughn and Crittenden (2002) found no correlation of these sources with the Cosmic Background Explorer (*COBE*) CMB map but a later study by Nolta et al. (2004) found a positive correlation with the first-year *WMAP* data which they claimed to be the evidence for $\Omega_\Lambda > 0$ at 95 per cent confidence, assuming a flat CDM cosmology. The re-analysis of the NVSS–CMB correlation by G08 also confirmed Nolta et al. (2004) results at approximately the 3σ significance level.

For the cross–correlation analysis we restrict the data to the declination, $\delta \geq -37^\circ$ where the survey is the most complete. We then applied the masking and pixelisation procedure described in §3.4 but for this sample we shall use lower resolution (res=6 as opposed to res=9) HEALPix Górski et al. (2005) scheme to reduce the computing time because of the much larger sky coverage of the NVSS. We checked that the measurements using different resolutions do give the same results in terms of amplitudes and statistical

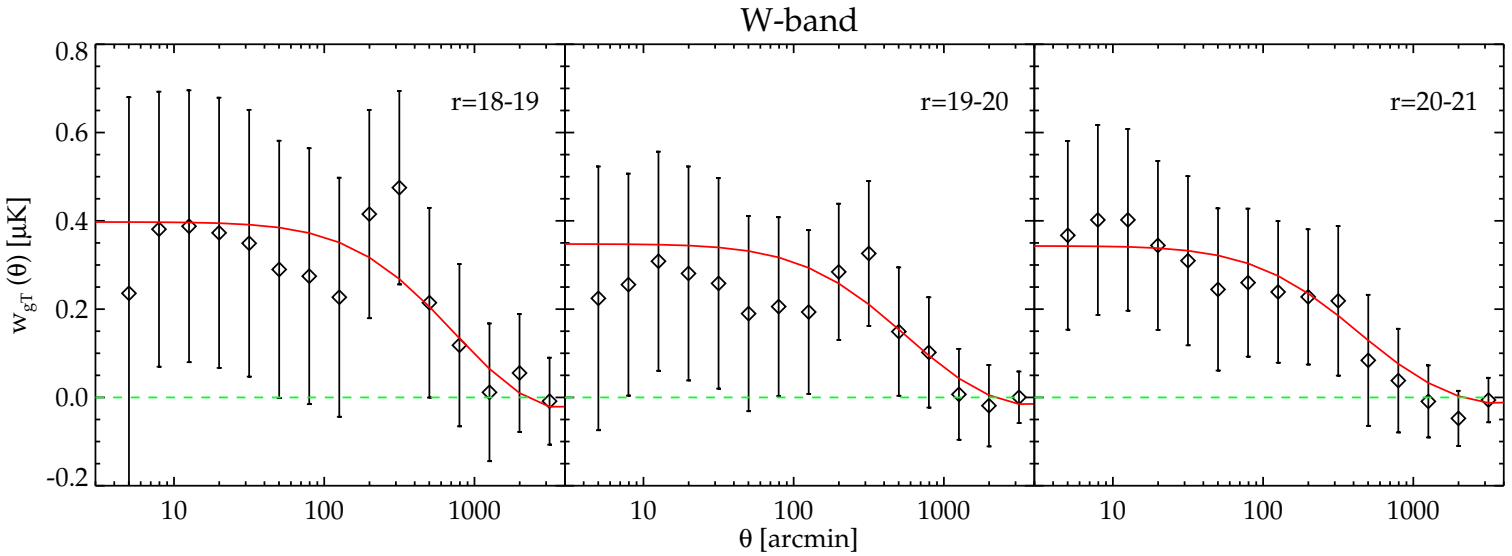

Figure 3.11: The cross–correlation of W-band data with the r-band selected galaxies. The sample magnitude ranges are as indicated in the plots. The ISW model prediction is shown for each sample, assuming Dodelson et al. (2002) $n(z)$ with the measured bias of 1.2, 1.1 and 1.2 for $18 < r < 19$, $19 < r < 20$ and $20 < r < 21$ sample, respectively.

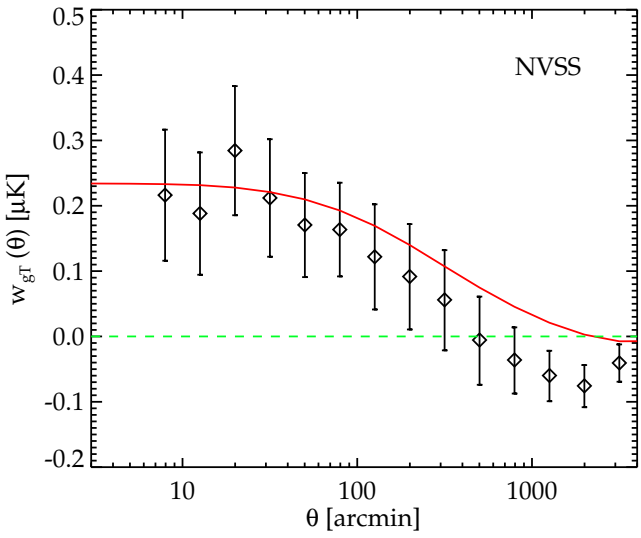

Figure 3.12: The cross-correlation of the NVSS sources to the W-band data. The ISW prediction (red solid line), assumes linear bias of 1.5 (Boughn and Crittenden, 2002; Giannantonio et al., 2008) and $n(z)$ derived from Dunlop and Peacock (1990) radio source luminosity function (mean-z model 1).

uncertainties (§3.6). The higher resolution (res=9) result shall be discussed in this section but for the purpose of the systematics test in §3.7, we shall present the results using res=6.

Boughn and Crittenden (2002) noticed a number density trend with the declination which affected their autocorrelation measurement. Following Nolta et al. (2004), we applied a correction for this by splitting the sample into $\sin\delta$ strips of width ≈ 0.1 and scaling the galaxy numbers in pixels belonging to a particular strip by the ratio of global mean to the strip mean. The cross–correlation procedure is then carried out as outlined in §3.4 but the statistical uncertainties and covariance matrix are now estimated from approximately 20 equal–area jackknifes rather than 24. The result using W-band data along with the standard model ISW prediction (red solid line) is presented in Fig. 3.12.

The ISW predictions for the NVSS sources are computed using the number–redshift distribution, $n(z)$, derived from the radio source luminosity function (mean-z model 1) of Dunlop and Peacock (1990). The median redshift estimated from such $n(z)$ is ≈ 0.8 with a tail extending out to $z \approx 3$. We assume the source bias, b, of 1.5 as measured by a number of authors (e.g. Boughn and Crittenden, 2002; Giannantonio et al., 2008).

Fig. 3.12 shows that we find a marginally positive correlation similar to the prediction of the standard model at scales smaller than $\approx 5^\circ$ at $\approx 2\sigma$ significance. Our result can

be directly compared with that of G08 who, like us, cross–correlate the source number fluctuations to $\Delta_{\rm T}$ as opposed to the source number per pixel approach of Nolta et al. (2004). Similarly, G08 observed a good agreement between their measurement and the standard ΛCDM model which also starts to breakdown at $\approx 5^{\circ}$. We take this agreement as a further indication of the robustness of our cross–correlation methodology and analyses. In the next section, we shall further test the NVSS–*WMAP*5 result for contamination by systematic effects.

3.7 CMB Sky rotation test

Here we shall perform an additional test for systematics, similar to that used by Myers et al. (2004) and Bielby and Shanks (2007) for testing their detection of the SZ effect, particularly in checking the reality of a large scale temperature decrement around galaxy groups and clusters. We follow these authors and rotate the *WMAP* maps around the galactic pole in the clockwise direction, each time adding 40° to galactic ℓ. There is an area very close to the pole where there is less movement from the rotation, but given that we use a 40° shift the effect of this slight non-independence is small. We have checked that if we cut out the circumpolar region down to galactic latitude $b = 75^{\circ}$ our results are unaffected.

The CMB masks (KQ75 plus point source) are rotated with the temperature maps to ensure that the contaminated regions are excluded from both galaxy and temperature fluctuation maps. The SDSS DR5 mask is then applied to the data in the case of LRG and r-band selected samples. The cross–correlation is performed using the W-band data following the procedure described in §3.4. We use the cross–correlation results between $12' < \theta < 120'$ where the difference between the ISW and null result is at its maximum as in §3.5. The cross–correlations are then performed at eight 40° intervals.

3.7.1 LRGs

The cross-correlation measurements are presented in Fig. 3.13 (top panel). The errors shown are jackknife errors (1σ) and as expected they are similar at all rotation angles which makes the data points straightforward to compare. For the SDSS sample at z=0.35, there is a higher positive point at rotation angle 40 degrees. For the 2SLAQ sample at z=0.55 the points at rotation angles 160 and 240 degrees are more negative than the zero degree point is positive. There is no reason to expect anything other than a null result at

any rotation angle other than zero. Therefore, based on this rotation test the significances are now reduced to the $\approx 12-25$ per cent level, suggesting that systematics as well as statistical errors may be affecting the data.

3.7.2 SDSS galaxies

We also applied the same test to the ISW results using three SDSS r-band selected galaxy samples of $18 < r < 19$, $19 < r < 20$ and $20 < r < 21$. The results are shown in Fig. 3.13 (middle). Again we see that there are rotation angles that show more significant non-zero detections than at the zero degree rotation angle. We see that at 40° rotation angle, the results are very negative in all three samples. At the rotation angle of 200°, the results are more positive than the zero degree rotation, again in all three samples. As for the LRG samples, this means that the significance is reduced to a marginal ≈ 10 per cent level and the results suggest that systematic effects as well as statistical errors may be contributing to the apparent ISW detection at zero degrees rotation angle.

3.7.3 NVSS radio sources

We then applied the same test to the NVSS–*WMAP*5 cross–correlation result. (see Fig. 3.13, bottom). This time the point at rotation angle 280 degrees is more positive than the point at zero degrees. As with other samples, the jackknife errors on all the points are similar so this comparison is fair. Again we conclude that systematic effects may be contributing to the apparent ISW detection which explains the reduction in statistical significance to > 10 per cent from the rotation test.

3.8 Discussion

Given the consistency of the AAΩ and the combined LRG results with the zero correlation, we now discuss whether there is any contradiction between our conclusions and those of other authors. In particular, we discuss the results of G08 who claim a 4.5σ ISW detection from the combined analyses of several large-scale tracers. These tracers include some of the LRG samples. They also include NVSS radio sources. The most significant detection in their Table 1 is from the NVSS at 3.3σ. Their LRG analysis gives 2.2σ for a sample roughly equivalent to our 2SLAQ LRG sample. These compare to 1.6σ for our 2SLAQ samples. For the NVSS we find a 1.8σ result. Their SDSS galaxy sample gives 2.2σ equivalent to our combined SDSS r–band limited sample which gives $\approx 1.3\sigma$

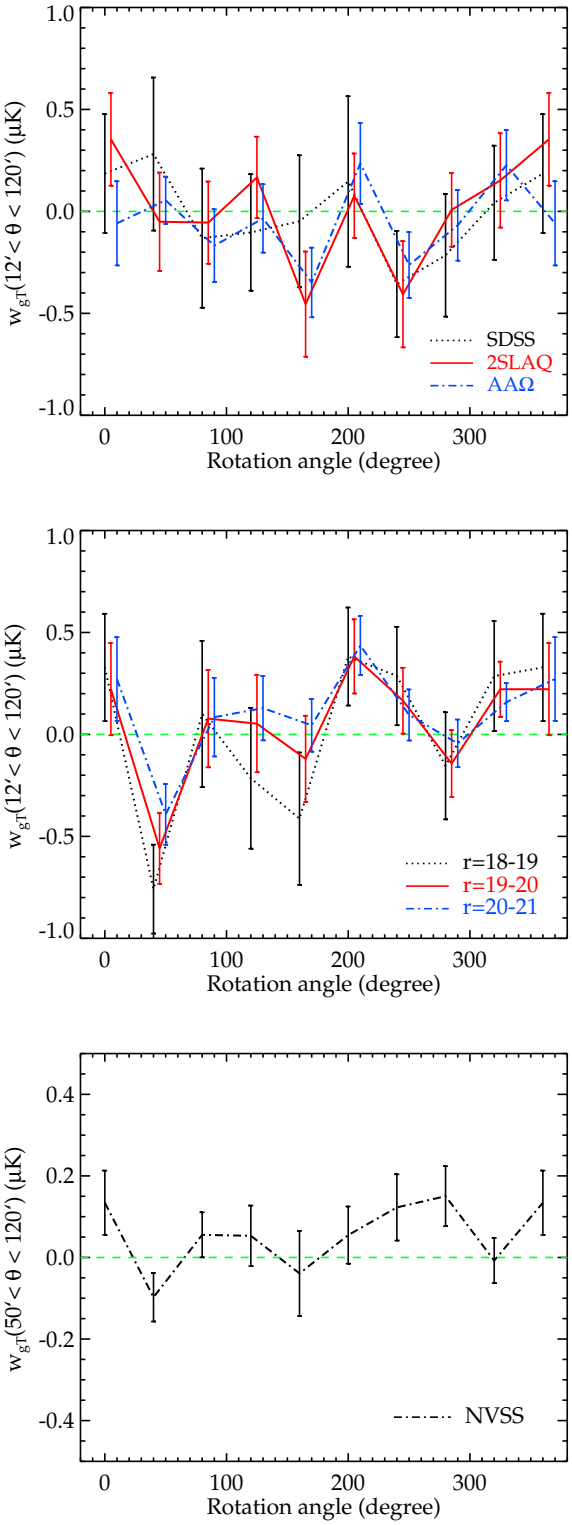

Figure 3.13: The cross-correlation of the three LRG samples (top), r-band selected galaxies (middle) and the NVSS sources (bottom) to the rotated W-band data in our rotation test (see text for more details). Note that for the top two plots, the points have been shifted slightly in the x-axis for clarity.

significance. Thus our significances appear lower than those of G08, particularly for NVSS. This discrepancy increases when we consider the rotation test. In the rotation test of the NVSS sample, 1 out of 8 points has higher amplitude than zero rotation measurement which is only $\approx 1.5\sigma$ significance. For the 2SLAQ case, this gives 1–2 out of 8 points which is equivalent to 1.2–1.5σ significance. The SDSS galaxy gives 2 higher (or lower) points in 8 or $\approx 1.2\sigma$.

The two methods G08 used to assess the significance of their results also show differences. Their Table 1 assumes the hypothesis of the standard ΛCDM model to obtain a maximum likelihood amplitude, A, and an associated error from their data. This error is different from the error that can be inferred from the χ^2 statistic in their Table 2 which tests the null result hypothesis. For example, their LRG result is 0.4σ significant from Table 2 whereas it is 2.2σ significant from Table 1. Their SDSS galaxy sample rejects the null result hypothesis at 1.3σ significance from the χ^2 statistic, again lower than their Table 1 at 2.2σ. Also the NVSS only reject the null result at 1.3σ rather than 3.3σ. We assume that these differences may be due partly to different null hypotheses (see Francis and Peacock, 2010, for a detailed discussion of the effect) and partly due to different methodologies. Certainly, the levels of significance in their Table 2 are lower and more in line with what our rotation tests show, i.e. 1–2 higher (or lower) points in 8 or 1.2–1.5σ. It remains to be seen for the other samples in their Table 1 and 2, if the same pattern applies with the maximum likelihood significances in Table 1 being higher than the χ^2 significances in Table 2. We conclude that the rejection of the null result by their χ^2 test may be more consistent with what we have found than the results in their Table 1. Indeed their χ^2 summed from all surveys is 67 on 74 degrees of freedom which is hardly a significant rejection of the null result and can be compared to our overall rejection of the null result of 0.5 to 1σ in our Table 2. Therefore as long as we refer to the χ^2 test of G08, there seems to be no inconsistency with our estimate of the significance of the low rejection of the null result.

3.9 Summary and Conclusion

We have performed a cross–correlation analysis between the *WMAP*5 CMB data and various large-scale structure tracers including our new high redshift AAΩ-LRG survey. The summarised conclusions of our findings are as follows:

(i) We have found a null ISW result for $z \approx 0.7$ AAΩ–LRG sample. The standard

model is rejected at $\approx 2.2\sigma$ significance by this dataset.

(ii) We have confirmed the marginal correlations between *WMAP*5 CMB temperature fluctuations and SDSS LRGs at z=0.35 and 2SLAQ LRGs at z=0.55.

(iii) The null result in the AAΩ–LRG sample at large scales is unlikely to be caused by the negative contribution of the SZ effect, given its angular extent and the expected amplitude of ISW signal.

(iv) We have made a range of tests on the AAΩ cross-correlation measurement which confirms its robustness. These include moving the magnitude limits up to 0.5mag brighter, removing areas of sky with significant dust absorption, using an estimate of the cross-correlation that takes out any possible systematic effects due to SDSS stripes and comparing the standard and uber-calibrations of the SDSS photometry. We have also checked the effects of stellar contamination in our samples. All these tests produce results consistent with our original measurements.

(v) We have also reproduced the cross-correlation results of most previous authors using our techniques. In particular we have reproduced the marginally positive correlations seen using SDSS magnitude limited samples of galaxies and NVSS radio sources.

(vi) However, rotation tests indicate that accidental alignment or some unknown systematics can give rise to a correlation signal comparable to and in many cases even larger than the ISW signal itself. This suggests that the previous positive detections may still be subject to unknown systematic effects.

(vii) Combining the new $\bar{z} \approx 0.7$ LRG survey with the lower redshift LRG samples, the overall cross–correlation result is now as consistent with a null detection as it is with the standard ΛCDM model for both W-band and ILC data. For the ILC map, the significance of rejecting the standard model is $\approx 2\sigma$ whereas the result is only 0.5σ away from the zero correlation hypothesis.

(viii) Given the results of the rotation test on the SDSS and 2SLAQ LRG samples, the support these give to the standard ISW model in the combined sample may have even less statistical weight than indicated above.

(ix) There is a possibility that the absence of the ISW correlation in the high redshift dataset is due to evolution of the dark energy equation of state. However, we regard it as unlikely that evolution could take place over the short redshift interval between

the 2SLAQ and AAΩ datasets. It is more plausible that the differences between the redshift bins are purely statistical, particularly given the rotation test results. We note that the individual positive detections that we have discussed are only marginally statistically significant and the combined ILC dataset is more consistent with zero than with the standard model prediction.

(x) If the ISW effect was generally absent then the impact on cosmology would be large because this would be strong evidence against an accelerating Universe. This would therefore argue against a significant role for a cosmological constant or dark energy in the Universe. Moreover, the absence of ISW would also argue against any modified gravity model which produced acceleration. The model which would be heavily favoured would be an Einstein-de Sitter model with $\Omega_{\rm m} = 1$. However, if such a model had a critical density of exotic, CDM particles then there might be a contradiction with the high baryon densities in rich galaxy clusters such as Coma. This rich cluster 'baryon catastrophe' has previously argued against a high CDM density because starting from $\Omega_b/\Omega_{\rm m} \approx 0.03$, it was difficult to understand in a hierarchical model how to produce a $5\times$ bigger baryon fraction in rich galaxy clusters (White et al., 1993).

(xi) It is therefore important to repeat the LRG measurements made here, now in the Southern sky. One opportunity to do this will arise from the new ESO imaging surveys in the South which are about to start, the VST ATLAS and the VISTA Hemisphere Survey. If the results we have found here are repeated then there could be significant consequences for cosmology.

Chapter 4

Beam profile sensitivity of WMAP CMB power spectrum

4.1 Introduction

The *Wilkinson Microwave Anisotropy Probe* (*WMAP*; Bennett et al., 2003a) has produced some of the best support for the standard ΛCDM cosmological model. By measuring the first two acoustic peaks in the Cosmic Microwave Background (CMB) temperature power spectrum it has shown that the Universe is spatially flat with $(\Omega_{\rm m},\, \Omega_\Lambda) = (0.26,\, 0.74)$ and $H_0 = 72\ {\rm km\,s^{-1}\,Mpc^{-1}}$ (Hinshaw et al., 2009; Spergel et al., 2007). The precision of the fit is impressive and rules out many competing simple models such as the low H_0, $\Omega_{\rm baryon} = 1$ model of Shanks (1985, 2005, 2007).

Of course, statistically precise measurements can also contain systematic errors which have to be guarded against. Such systematics include Galactic foregrounds which at the least cause mode coupling due to the incomplete sky (e.g. Hinshaw et al., 2003b; Chon et al., 2004). There are also potentially more subtle systematics that arise from cosmological foregrounds. For example, Myers et al. (2004) and Bielby and Shanks (2007) have detected the SZ effect in the *WMAP* data by cross-correlating the CMB with rich cluster positions. Shanks (2007) has also discussed the effect of foreground lensing, prompted by quasi-stellar object (QSO) lensing results (Myers et al., 2003, 2005; Mountrichas and Shanks, 2007). But SZ is unlikely to make a strong contribution to the first acoustic peak (Huffenberger et al., 2004). Also lensing requires a high anti-bias between galaxies and the mass distribution to have a significant effect at the first peak which needs to be reconciled with measures of bias from galaxy clustering dynamics (e.g. Ratcliffe et al., 1998b; Hawkins et al., 2003).

However, there are also many potential systematics involved with the *WMAP* instru-

ment, although the *WMAP* team have taken care that the effects of such systematics are minimised. One major potential systematic concerns the question of the *WMAP* radio telescope beam profile. We shall see that even at the wavenumber $\ell \approx 220$ of the first acoustic peak, the *WMAP* CMB power spectrum has significant dependence on the beam profile even in the highest resolution 94 GHz *W*-band. Here the W-band resolution quoted by the *WMAP* team is 12.′6 FWHM which is roughly equivalent to $\ell \approx 1800$. It is also noted that the beam is not Gaussian. Now the *WMAP* team have extensive papers devoted to the important question of measuring the beam (Page et al., 2003b; Jarosik et al., 2007; Hill et al., 2009). The standard method is to use *WMAP* observations of a bright source such as the planet Jupiter to measure the beam profiles.

The layout of this chapter is as follows. The data used in this study are described in §4.2. We then re-derive in §4.3 the beam convolved CMB power spectrum from the *WMAP* data to show directly the effect of the beam. The new estimates of the *WMAP* beam profiles using *WMAP*5 point sources and other tests including the robustness of our method are presented in §4.4. In §4.5 we then make fits to the radio source beam profiles and use these to debeam the *WMAP*5 data and explore the range of power spectra that results. Our discussion and conclusions are then presented in §4.6.

4.2 Data

4.2.1 *WMAP* temperature maps

Here we use the five-year *WMAP* datasets which are available from the LAMBDA CMB website. The maps from the individual detectors in 5 frequency bands, *K*, *Ka*, *Q*, *V* and *W* are supplied. The FWHM of the 94-GHz *W* beam is 12.′6 compared to 19.′8 at *V* (61 GHz), 29.′4 at *Q* (41 GHz), 37.′2 at *Ka* (33 GHz) and 49.′2 at *K* (23 GHz). There are 10 differencing assemblies (DAs), namely *K*1, *Ka*1, *Q*1, *Q*2, *V*1, *V*2, *W*1, *W*2, *W*3 and *W*4. The different DA maps can be cross-correlated to obtain power spectra free of uncorrelated detector noise bias (Hinshaw et al., 2003b). The Jupiter beam profiles for each DA and the corresponding transfer functions are also given. The maps are in HEALPix (Górski et al., 2005) format with $N_{\rm side} = 512$ and $N_{\rm side} = 1024$. These give equal area pixels of dimension $\approx 7'$ and $\approx 3'$, respectively.

Table 4.1: Summary of the *WMAP* sources listed as point sources in the Greenbank and PMN 5-GHz catalogues.

Band	≥1.1 Jy	< 1.1 Jy	Total ($> 2\sigma$)
Q	182	165	347
V	164	153	317
W	97	84	181

4.2.2 *WMAP* point source catalogue

We use the radio sources drawn from the *WMAP*5 point source catalogue (Wright et al., 2009). These sources have to be detected to $> 5\sigma$ in at least one *WMAP* band and their flux density is reported if they are detected at $> 2\sigma$ in any of the other four *WMAP* bands. This gives a list of 390 sources to a limit of ≈0.5 Jy in each band. The source positions are accurate to $\sim 4'$ (Wright et al., 2009). 365 out of 390 sources are pre-detected at 4.85 GHz in the Greenbank (GB6) northern sky survey (Gregory et al., 1996) and the Parkes-MIT-NRAO (PMN) surveys (Griffith and Wright, 1993). Here, we only use *WMAP*5 sources with 4.85 GHz counterparts and exclude sources (12 out of 365) that were found to be resolved at $\approx 4\farcm6$ FWHM resolution of GB6 and PMN. Table 4.1 shows the number of these sources in each band, also split into those brighter or fainter than 1.1 Jy.

From the optical identifications of Trushkin (2003) of the 208 *WMAP* first-year sources the survey contains 77 per cent QSOs or BL Lac with the remainder being radio galaxies/AGN. This is as expected given the dominance of flat-spectrum compact sources at the high *WMAP* frequencies.

4.2.3 NVSS radio sources

The NRAO VLA Sky Survey (NVSS) covers ≈82 per cent of the celestial sphere, including all the sky north of $\delta > -40°$, at a frequency of 1.4 GHz (Condon et al., 1998) and $45''$ FWHM beam. It contains 1.8×10^6 sources with a sky density of $\approx 44\,\mathrm{deg}^{-2}$ to a flux limit of ≈ 2.5 mJy. The uncertainties in the source positions vary from $< 1''$ for $S > 15$ mJy point sources to $7''$ for the faintest detectable sources, $S = 2.3$ mJy. Here we used samples limited to peak flux density > 1.0 Jy and $\delta > -37°$ which gives 1082 sources outside *WMAP*5 'point source catalogue mask' (Wright et al., 2009, see also Fig. 4.1).

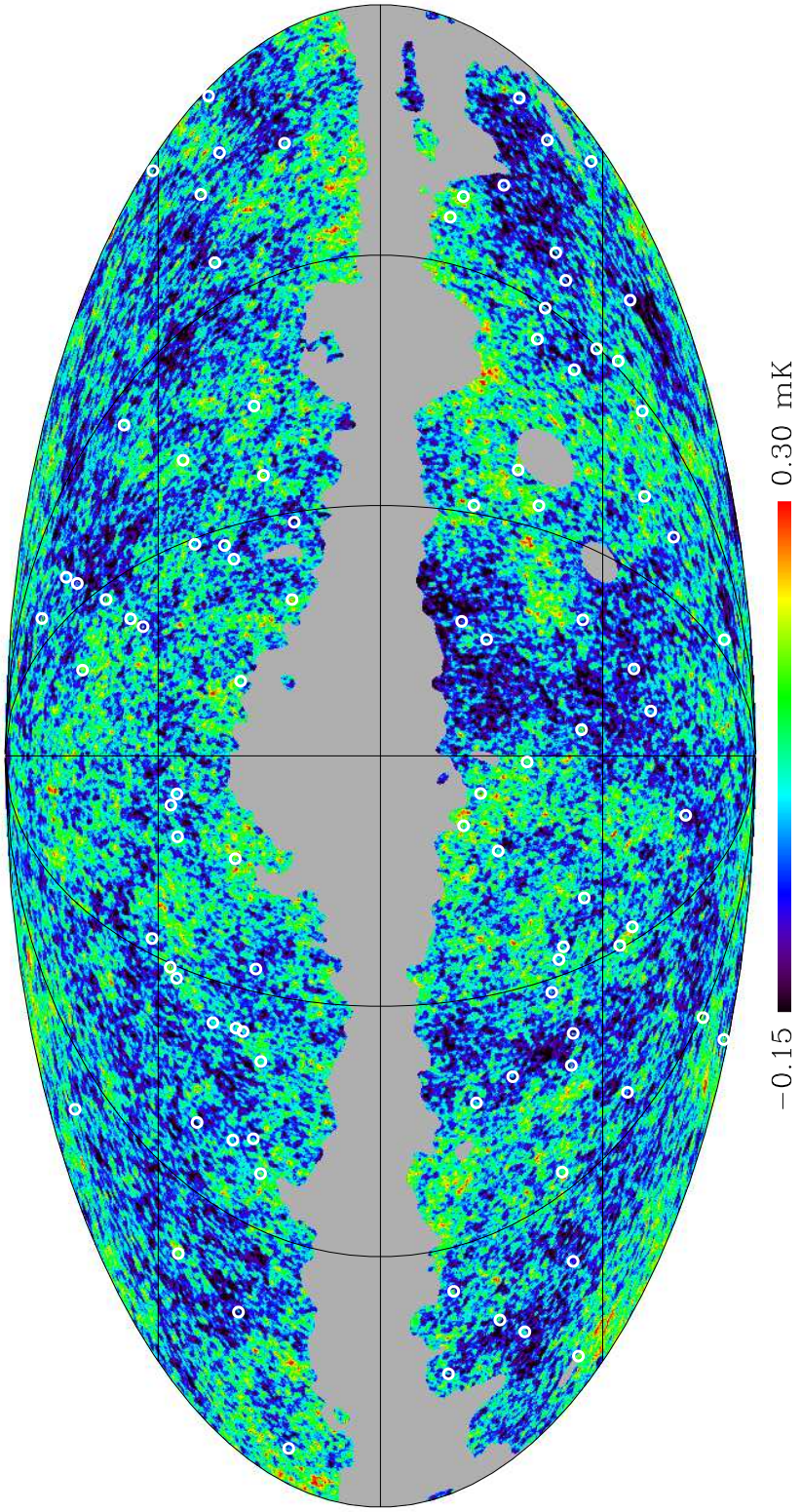

Figure 4.1: *WMAP*5 *W*-band temperature map overlaid by the positions (open circles) of $S_W > 1.1$ Jy point sources used in the analysis. The temperature map has been smoothed with a 12′.6 FWHM Gaussian kernel. The grey region represents the *WMAP*5 'point source catalogue mask' (Wright et al., 2009).

These low frequency selected sources are more likely to be extended than those selected at higher *WMAP* frequencies. However, with the 45″ FWHM beam their substructure can be resolved into multiple components by NVSS. Overzier et al. (2003) (see also Blake and Wall, 2002) made an auto-correlation analysis of the source positions which showed evidence of multiple components to separation $\theta \approx 6'$ for the 0.5 Jy limited sample. This suggests that even here the effect of multiple-component sources is likely to be small even in the highest resolution *W*-band beam. Furthermore, Blake and Wall (2002) showed that only ≈7 per cent of the $S > 50$ mJy sources were resolved into multiple components by NVSS and the size distribution of $\theta > 2'$ sources is a steep power-law, $f(\theta) \propto \theta^{-2.4}$. However as a precautionary measure, we shall also exclude any source that has neighbouring source(s) within 1°. This leaves 933 $S > 1.0$ Jy sources for the *WMAP* beam analysis.

4.2.4 Ground-based 90-95GHz Radio Sources

We shall compare *WMAP* *W*-band fluxes with ground-based radio source fluxes from the Australia Telescope Compact Array (ATCA; Sadler et al., 2008) and the IRAM 30-m radio telescope (Steppe et al., 1988). The ATCA survey was made at 95 GHZ and the IRAM survey at 90 GHz. The ATCA survey was based on sources selected from the Australia Telescope 20 GHz survey. Of the 130 sources observed, 17 were detected at more than 2σ by *WMAP*5. The IRAM survey observed 294 sources at 90 and 230 GHz, targeting sources which are brighter than 1 Jy at 5 GHz. Here 66 sources were detected at more than 2σ by *WMAP*5. At these high frequencies the sources are mainly QSOs, BL Lacs or blazars. Many of the sources in the ATCA and IRAM surveys are variable and so where this is an issue we shall use the average source fluxes in our comparison with the *WMAP* fluxes.

4.3 Deriving the beam convolved C_ℓ

We now analyse the *WMAP* data to make an initial estimate of the power spectrum and to highlight the effect of the finite beam width using the *WMAP* highest resolution (band) data. To reduce the effect of correlated detector noise which would result from an auto-correlation of an individual CMB map, we make a cross-correlation of the maps from different DA's (Hinshaw et al., 2003b). Here, we use the five-year *W*1 and *W*2 temperature maps with the HEALPix resolution 9.

We derive the cross-power spectra by using *PolSpice* code (Chon et al., 2004) which is a generalisation of *SpICE* (Spatially Inhomogeneous Correlation Estimator; Szapudi, Prunet, and Colombi, 2001) to include the analysis of CMB polarization. The code calculates a pixel space two-point correlation function via a fast spherical harmonics decomposition, which is then transformed to give an estimate of the power spectrum. Note that the algorithms employed by the code is mathematically equivalent to a 'pseudo-C_ℓ' estimator (for a review of different power-spectrum estimators see Efstathiou, 2004). The default *WMAP*5 'temperature analysis mask' (KQ85; Nolta et al., 2009; Gold et al., 2009) is used to exclude the foreground-contaminated regions of the sky. The cut-sky corrected angular power spectrum, C'_ℓ, is then obtained directly from *PolSpice*. Hereafter, we shall call an angular power spectrum after a cut-sky and pixel transfer function (see Eq. 4.2) correction a 'beam convolved C_ℓ'.

In Fig. 4.2, we immediately see that the beam convolved C_ℓ (green line) is not only drastically smoothed at the position of the second and third peaks but there is also a significant effect at the position of the first peak at $\ell \approx 220$ in that the amplitude of the standard ΛCDM result (blue line) is ≈ 70 per cent higher. The reason for this is seen in Fig. 4.3(f) where the beam profile from the Jupiter observations using the *W*1 detector are shown. It can be seen that the beam is not Gaussian and has a θ^{-3} power-law tail out to $> 1^\circ$. Hill et al. (2009) give the relation between the beam transfer function, b_ℓ, and the normalised symmetrised beam profile, $b^S(\theta)$, as,

$$b_\ell = 2\pi \int b^S(\theta) P_\ell(\cos\theta) d\cos\theta / \Omega_B, \tag{4.1}$$

where Ω_B is the main-beam solid angle and $P_\ell(x)$ is Legendre polynomial of order ℓ.

The debeamed cross-power spectrum measured from DA i and j is then determined from the measured C'_ℓ by

$$C_\ell = C'_\ell / b^i_\ell b^j_\ell p^2_\ell, \tag{4.2}$$

where p_ℓ is the pixel transfer function supplied with the HEALPix package. For $N_{\rm side} = 512$, the pixel window function lowers the measured C'_ℓ by ≈ 1 and 10 per cent at $\ell \approx 200$ and 500, respectively.

If we use Eq. 4.2 with the Jupiter beam transfer function from the *WMAP* team, we find that we get back to the usual ΛCDM model (green and orange lines in Fig. 4.13). The black line shows the C_ℓ measured from a full-sky CMB simulation (*WMAP*5 best-fit ΛCDM model) after smoothing by a Gaussian beam, using *synfast* (Górski et al., 2005).

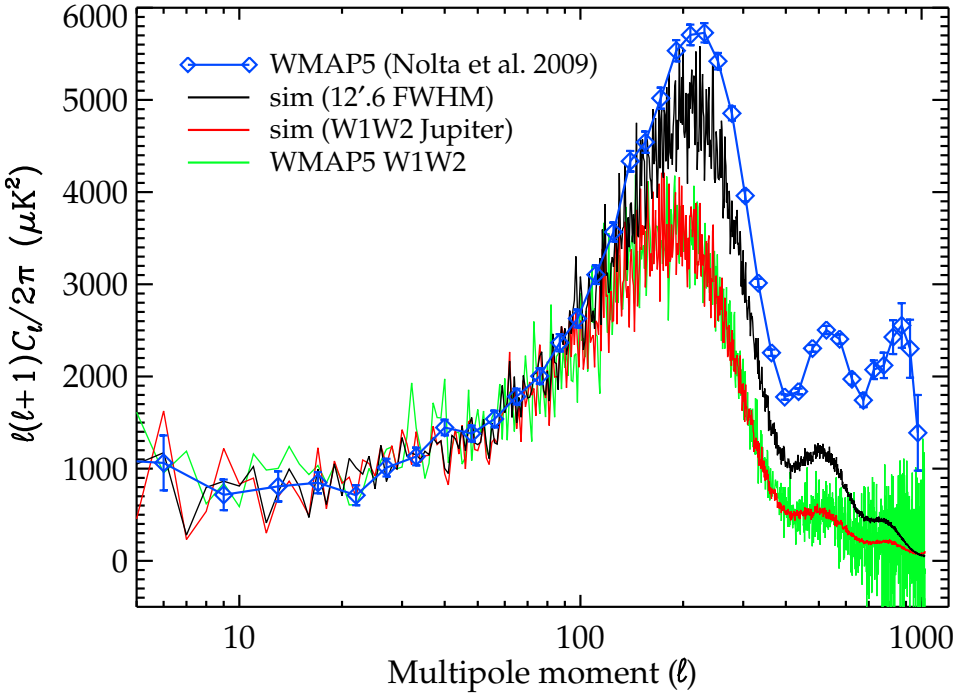

Figure 4.2: The beam convolved C_ℓ measured from cross-correlating $W1$ and $W2$ maps (green line) compared to the standard debeamed *WMAP* result (blue line) as presented by Nolta et al. (2009). Also shown are C_ℓ measurements of a full-sky CMB simulation (*WMAP*5 best-fit ΛCDM model) smoothed with a 12.′6 FWHM Gaussian beam (black line), and a similar simulation now smoothed with the $W1$ and $W2$ Jupiter beams (red line). Although the beam convolved C_ℓ (green) and the Jupiter beam-smoothed standard simulation C_ℓ (red) agree, the difference between these and the Nolta et al. result (blue) shows the large effect of debeaming even at the scale of the first acoustic peak.

The red line shows the effect of the similar simulation now smoothed with $W1$ and $W2$ Jupiter beam profiles (Hill et al., 2009). The latter shows excellent agreement with our beam convolved C_ℓ measured from the real $W1$ and $W2$ maps. The $W1$-$W2$ cross-C_ℓ is noisier than the simulation due to radiometer noise in the data. The effect of the Jupiter beam compared to the Gaussian beam is thus very significant in decreasing the height of the first peak. We also see that when the Jupiter beam is used, the ΛCDM model does give an accurate fit to the beam-convolved C_ℓ. Thus when we use the same parameters as the *WMAP* team, we reproduce the *WMAP* result.

4.4 Testing the *WMAP* beam profile

4.4.1 Beam profiles via *WMAP* point sources

We then estimated a beam from the radio sources by making a stacking analysis of *WMAP*5 temperature maps around radio source positions. Extended foreground emission regions are excluded from the temperature maps using the 'point source catalogue mask' (Wright et al., 2009, see Fig. 4.1). We calculated the average ΔT (per 49 arcmin^2 pixel) in annuli as a function of angular distance, θ, between radio source position and the pixel centre. In the first instance we show the raw cross-correlation function for the Q, V and W bands in Fig. 4.3(a)-(c), split into bright ($\geq$ 1.1 Jy) and faint ($<$ 1.1 Jy) *WMAP*5 source subsamples. The errors on the radio source profiles are *jackknife* errors. These are estimated from six approximately-equal-area subfields,

$$\sigma^2_{\rm JK}(\theta) = \frac{N_J - 1}{N_J} \times \sum_{i'=1}^{N_J} [\Delta T_{i'}(\theta) - \overline{\Delta T}(\theta)]^2 \tag{4.3}$$

where $N_J = 6$, and $\Delta T_{i'}$ is the stacked temperature measured from all except the ith subfield. The multiplication by a factor $N_J - 1$ reflects the fact that the six re-sampling fields are not entirely independent.

We see that the fainter source profiles appear to agree with the brighter source profiles at scales of $\theta \approx 30'$ but have significantly lower peak values. This is most clearly shown in the un-renormalised profiles shown for the bright and faint Q, V, W band sources in Fig. 4.3(a)-(c). Although noise may be an issue for the faintest sources, this suggests that there may possibly be some form of non-linearity in the *WMAP* beam. We also note that the raw profiles from both bright and faint sources show a positive offset at the 0.01-0.02 mK level. The offset shows an increasing trend from $1^\circ - 5^\circ$. The main uncertainty in

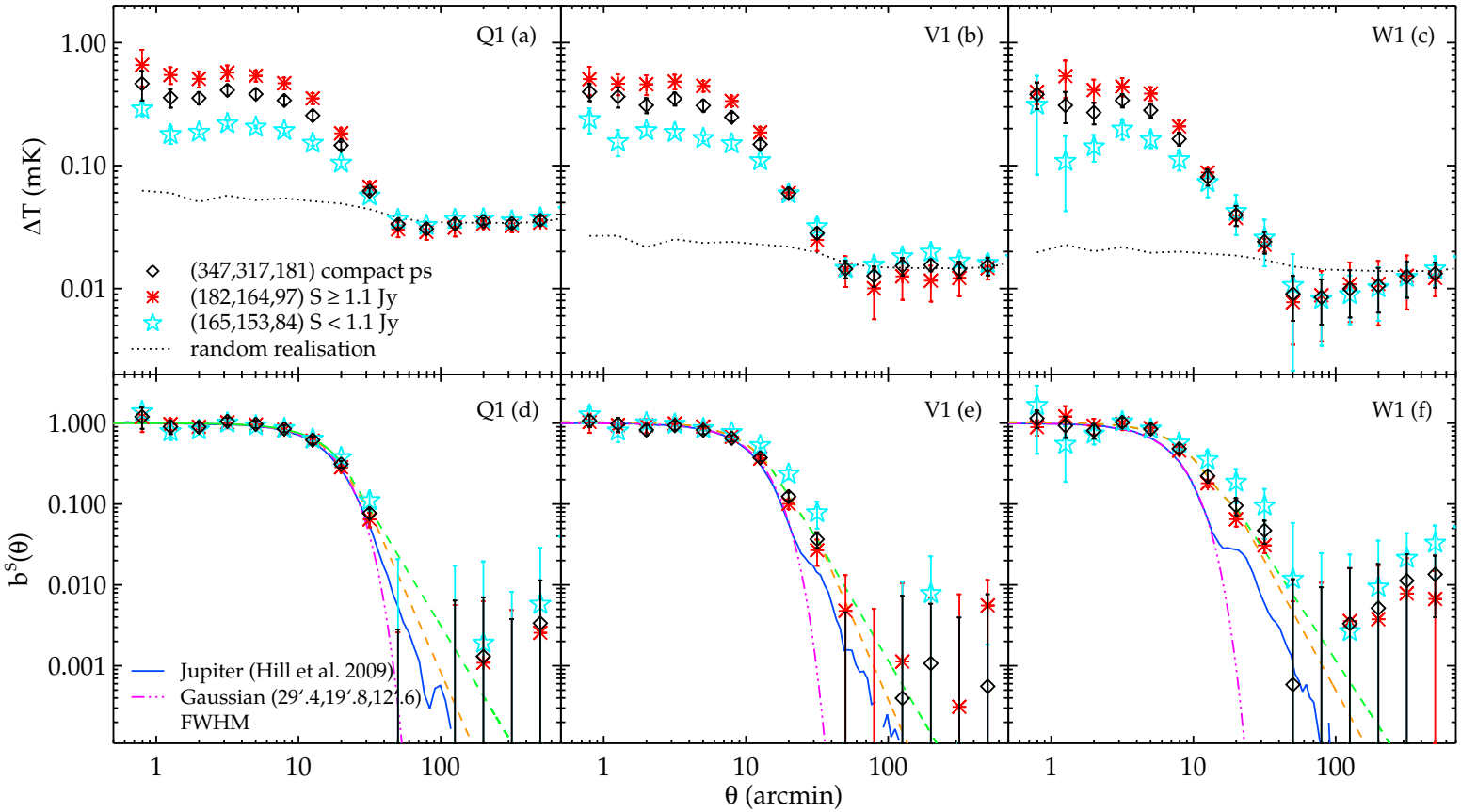

Figure 4.3: (a-c) The raw radio source beam profiles for the *WMAP* sources compared to the beam profiles from Jupiter (blue solid lines) and random realisations (dotted lines) for $Q1$, $V1$ and $W1$. (d-f) The zero-offset subtracted (see text) and normalised beam profiles for $Q1$, $V1$ and $W1$. The radio source profiles for all compact *WMAP* sources are shown as diamonds. Profiles derived from *WMAP* sources with flux brighter (fainter) than 1.1 Jy are shown as asterisks (stars). A Gaussian is shown as a magenta dot-dashed line and empirical fits to the radio source profiles are shown as orange and green dashed lines.

estimating *WMAP* beam profiles from these data is in subtracting this offset at scales $> 1^\circ$.

Since *WMAP* has significant sidelobes stretching to $\approx 90^\circ$ (Barnes et al., 2003), there was a possibility that the offsets are also part of the beam. However, when we distributed points at random in the masked region and used these as our centres for our stacking analysis we also found a similar offset [dotted lines in Fig. 4.3(a)-(c)]. This makes it look like the offset is not associated with the existence of sources and hence not associated with the *WMAP* beam. Our Monte Carlo simulations (see §4.4.2) shows that these offsets are caused by the CMB fluctuations. We therefore employed a 'photometry' approach for the stacking analysis where we have subtracted the *WMAP* flux in an annulus at $1^\circ < \theta < 2^\circ$ for the *W* band and proportionately bigger annuli in the *V* and *Q* bands. Using sky annuli close to the sources will clearly improve background subtraction in the presence of local background fluctuations.

The resulting *WMAP* radio source beam profiles for *Q*, *V* and *W* bands are shown in Fig. 4.3(d)-(f). The profiles have been renormalised (≈ 10 per cent statistical uncertainties in the normalising factors) to fit the peak in the *WMAP* Jupiter beam profile at $\theta < 4'$. For each band we also compare the profiles to a Gaussian beam with the FWHM as indicated in the plot. We see that on average the profiles from the radio sources are broader than the Jupiter profile in the *W*, *V* and *Q* bands. In the lower frequency, lower resolution *K* and *Ka* bands the radio source profiles fit the Jupiter beam better, indeed almost perfectly (not shown here). Clearly, given the size of the errors there is little information from the radio sources on the beam profile at $\theta > 30'$. Fig. 4.3 again shows the *WMAP* radio sources divided into faint and bright sources, split at 1.1 Jy. In the *W* and *V* bands particularly we again note that the fainter sources appear to be wider than the brighter sources. We also find similar results for *W*2, *W*3, *W*4, *V*2 and *Q*2 but choose not to include them here for clarity. These deviations from the *WMAP* Jupiter beam are puzzling and we now check to see if they could be caused by systematics.

We first checked the effect of pixelisation on the sources by using the smallest HEALPix pixels with $N_{\rm side} = 1024$ (i.e. dimension $\sim 3'$). There were no differences seen in the results. Furthermore, the convolution with $N_{\rm side} = 512$ pixel window function (magenta dot-dashed lines in Fig. 4.5) is also too narrow to explain the discrepancy between the Jupiter beam of the *WMAP* team and our measurements.

Many of the *WMAP* sources show flux variability from year to year (Wright et al., 2009). To test that this does not affect our beam measurements, we exclude sources which

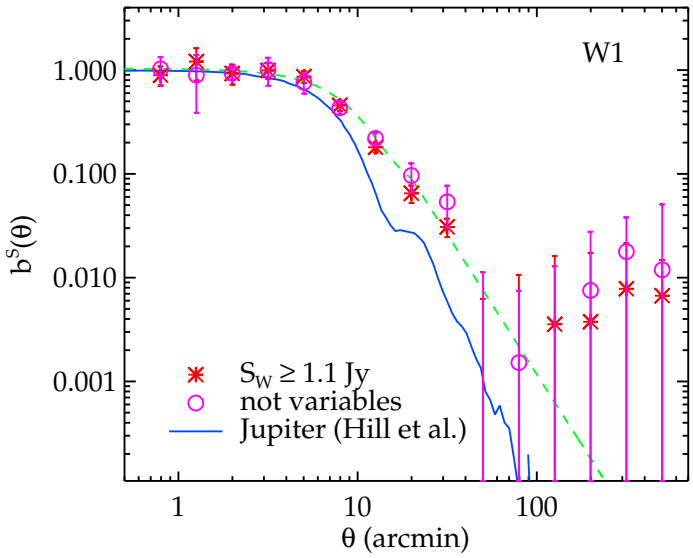

Figure 4.4: The W1 beam profile measured using the $S_W \geq 1.1$ Jy point sources which are not flagged as variable source (magenta circles), comparing to the main result (red asterisks) as shown in Fig. 4.3(f)

have been found to be variable. These sources are flagged with 'v' and 'V' in Table 1 of Wright et al. (2009). For the $S \geq 1.1$ Jy samples the number of objects remain after the variable source exclusion are 29, 60 and 72 for W, V and Q-band, respectively. The resulting beam profiles are consistent with the results derived earlier. Fig. 4.4 shows the $W1$ beam profile measured using the non-flagged subsample. Our beam measurement appears to be unaffected by the fact that majority of these bright sources are variable. However, the variability of the sources' fluxes may contribute to larger statistical errors of the beam measurements.

Next, we check the likely contribution of radio source clustering to the beam profiles, using the clustering analysis of the NVSS radio survey by Overzier et al. (2003). At $S \geq 200$ mJy where the sky density of NVSS sources is $n \approx 0.6$ deg^{-2},

$$w(\theta) = 3 \times 10^{-5}\theta^{-3.4} + 6.6 \times 10^{-3}\theta^{-0.8}. \tag{4.4}$$

This is a 2-power-law form which changes slope at $\theta \approx 0.1°$. At smaller scales, double-lobed radio sources split into two components dominate while at larger scales source-source clustering dominates. We estimate the contribution of sources by first calculating the excess number of sources in an annulus of area ΔA at radius θ from an average source, $N_{ex}(\theta) = w(\theta)n\Delta A$. The excess flux/temperature per unit area in the profile in

the annulus is then given by $\Delta T_{ex} = N_{ex} \times \bar{f}/\Delta A$ where $\bar{f}$ is the average source flux. For a Gaussian point source of central intensity/temperature per unit area, T_0, and width, σ, the flux is $2\pi\sigma^2 T_0$. Therefore in this case,

$$\Delta T_{ex}(\theta) = w(\theta) 2\pi n \sigma^2 T_0. \tag{4.5}$$

Substituting in the above values for n and W at $\theta = 0.5^\circ$ with $\sigma = 5\farcm4$ as for the W band we find $\Delta T_{ex} \approx 3 \times 10^{-4} T_0$ which is a negligible contribution in explaining the excess in Fig. 4.3f at this scale, if T_0 is taken to be the central profile value. Taking the parameters for 100 mJy from Overzier et al. (2003) makes the effect even smaller. These results are also likely to be upper limits for the *WMAP* sources which only have a density of $n \approx 0.01$ deg^{-2} and an average 95 GHz flux of 500 mJy. Note also that there is no object in the W-band point-source list which lies within a degree of the other sources in the same list. We conclude that radio source clustering is not likely to be an issue for our radio source beam profiles.

Wright et al. (2009) noted that the faint *WMAP*5 sources show a selection effect and flux density bias arising from possible coincidence with CMB peaks, i.e. Eddington bias. Therefore one might suspect that their positions and widths could also be affected by CMB fluctuations as well. To check that such a bias does not affect our beam profile measurements, we use a combination of (a) purpose-made simulations and (b) radio sources pre-selected at frequencies far from the *WMAP* bands.

4.4.2 Monte Carlo simulations

We made 100 Monte Carlo simulations to check our method and the robustness of the results. We followed the procedures described by Wright et al. (2009) (see also Chen and Wright, 2009). For each set of simulation, 10^6 point sources are generated with a power-law distribution, $N(> S) \propto S^{-1.7}$, at *WMAP* Q-band (Bennett et al., 2003c; Chen and Wright, 2009). Their spectral indices, α, are drawn from a Gaussian distribution with a mean -0.09 and standard deviation 0.176 as characterised by *WMAP*5 point source catalogue (Wright et al., 2009). The flux density for each object is scaled to the centre of the other four bands using the relation $S_\nu \propto \nu^\alpha$. The source positions are then randomly distributed on the sky and each source is assigned to a pixel in a HEALPix res=11 map.

For a source with flux density S_ν, the peak antenna temperature difference is given by

$$\begin{aligned} \Delta T_{\rm a} &= S_\nu \left(\Omega \frac{\partial B_\nu}{\partial T}\bigg|_{T_0} \right)^{-1} \frac{x^2 e^x}{(e^x-1)^2} \\ &= \Delta T_{\rm t} \frac{x^2 e^x}{(e^x-1)^2}\,, \end{aligned} \tag{4.6}$$

where B_ν is the Planck function, $\Omega = 2.5 \times 10^{-7}$ sr is a solid angle of res=11 pixel, $x = h\nu/kT_0$, h is the Planck constant, k is the Boltzmann constant, $T_0 = 2.725$ K is the CMB temperature (Mather et al., 1999) and ν is the frequency which we use the values given in Table 1 of Hinshaw et al. (2009). Eq. 4.6 gives $\Delta T_{\rm a} \propto \nu^\beta$ where $\beta = \alpha - 2$, following the notation convention (see e.g. Bennett et al., 2003b; Hinshaw et al., 2009). The publicly available *WMAP* maps (§4.2) are given in thermodynamic temperature, $\Delta T_{\rm t}$ (Limon et al., 2008). For a direct comparison with our results, we thus use $\Delta T_{\rm t}$ and not $\Delta T_{\rm a}$ in the simulations.

Five temperature maps, one for each band, are then smoothed with the corresponding *WMAP* beam transfer function (Hill et al., 2009) before being downgraded to res=9. The simulated CMB temperature map (smoothed with an appropriate beam transfer function) constructed from *WMAP*5 best-fit C_ℓ and pixel noise are then added to the source temperature maps. The pixel noise is modelled as a Gaussian distribution with zero mean and standard deviation $\sigma = \sigma_0/\sqrt{N_{\rm obs}}$, where $N_{\rm obs}$ is the number of observations in each pixel and σ_0 is given for each DA and frequency band (Limon et al., 2008). Before we proceed further, we check our stacking technique as described in §4.4.1 by applying it to the simulated $Q1$, $V1$ and $W1$ maps using the known source positions. The results for sources with $S_{Q,V,W} > 1$ Jy and $0.3 < S_{Q,V,W} < 1$ Jy are shown in Fig. 4.5. The figure shows that the beam profiles can be accurately recovered using both bright and faint sources once the pixelisation effect has been taken into consideration (magenta dot-dashed lines).

Next, we applied the five-band detection technique following procedures utilised by *WMAP* team (Bennett et al., 2003c; Hinshaw et al., 2007, 2009). Firstly, the temperature maps are weighted by the number of observations in each pixel, $N_{\rm obs}^{1/2} T$. The weighted map is then filtered in the harmonic space by (e.g. Tegmark and de Oliveira-Costa, 1998; Refregier et al., 2000)

$$W_\ell = b_\ell / (b_\ell^2 C_\ell^{\rm CMB} + C_\ell^{\rm noise}), \tag{4.7}$$

where $C_\ell^{\rm CMB}$ is the CMB power spectrum and $C_\ell^{\rm noise}$ is the noise power, and b_ℓ is the beam transfer function (Hill et al., 2009). The filter is designed to suppress fluctuations

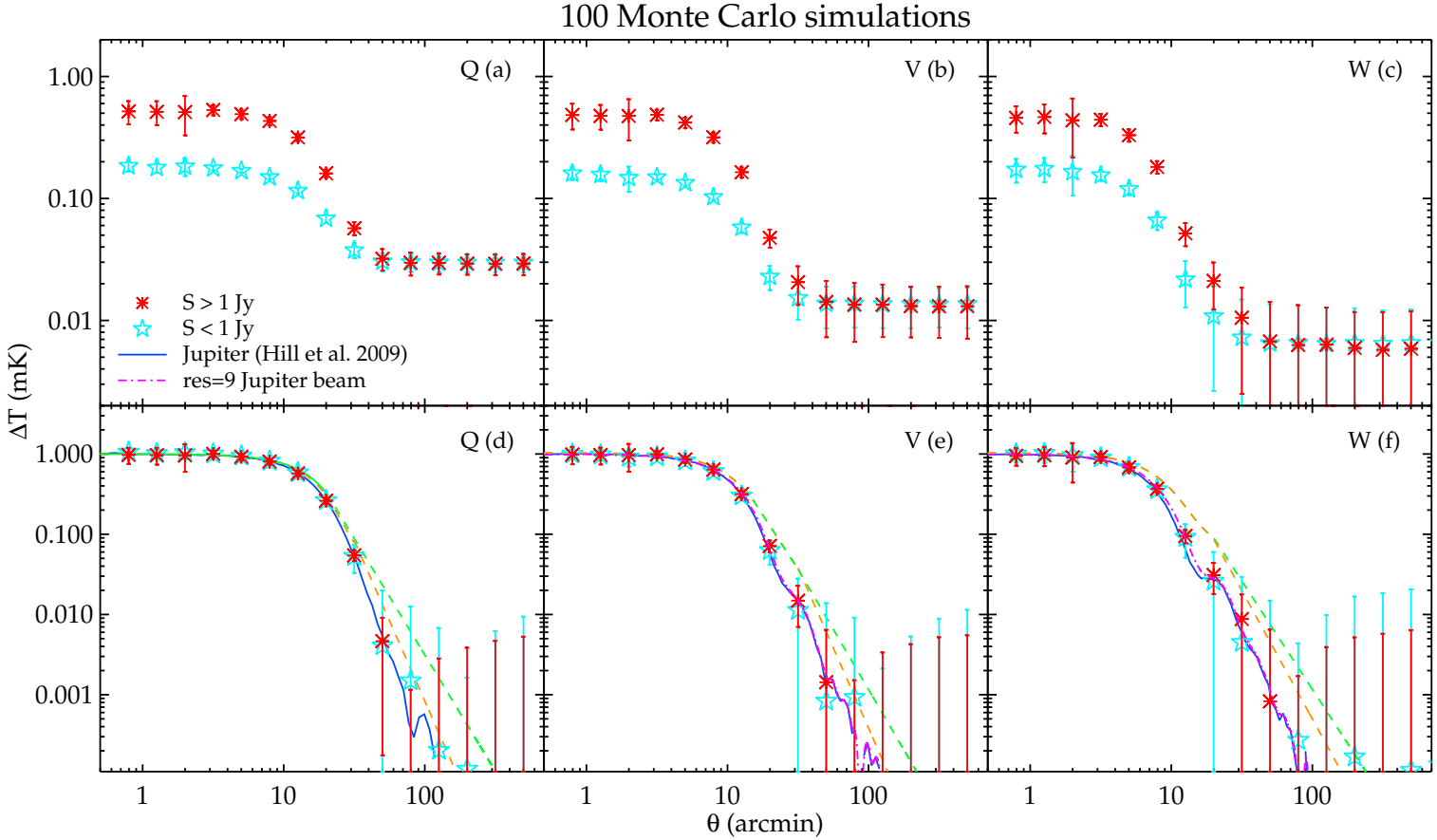

Figure 4.5: The simulated beam profiles using radio point sources. The results for bright and faint sources are shown as asterisks and stars, respectively. The error bars are 1σ rms of 100 simulations. The raw measurements before background subtraction and normalisation, akin to the top row of Fig. 4.3 are shown in panel a), b) and c). The effect of finite pixel size on the profile measurement is shown by the magenta dot-dashed lines. The green and orange dashed lines are the empirical fits to the real point source measurement as shown in Fig. 4.3

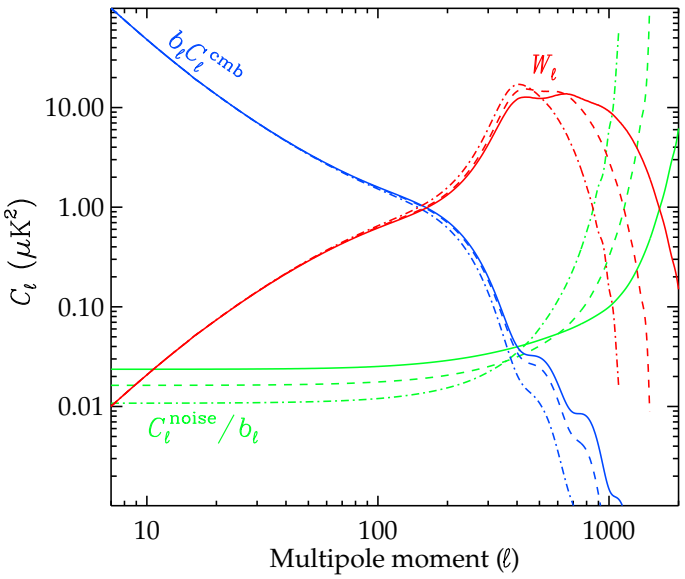

Figure 4.6: The filtering functions W_ℓ used to detect point sources in Q, V and W-band temperature maps (red dot-dashed, dashed and solid lines, respectively). The blue and green lines show contributions from the CMB and noise fluctuations, following the same line symbols as W_ℓ.

due to the CMB at large scales and pixel noise at scales smaller than the beam width. The filtering function, W_ℓ, for Q, V and W bands are shown in Fig. 4.6 as red dot-dashed, dashed and solid lines, respectively. We used the *WMAP*5 best-fit C_ℓ for $C_\ell^{\rm CMB}$ (blue lines). The $C_\ell^{\rm noise}$ (green lines) are determined from pixel noise maps constructed using σ_0 and five-year $N_{\rm obs}$ for each band as described above. Note that the derived noise power is consistent with the analytic formula given in Tegmark and Efstathiou (1996) where $C_\ell^{\rm noise} = \Omega_{\rm pix}\sigma_0^2 / < N_{\rm obs} >$.

We then search the filtered maps for peaks which are $> 5\sigma$. Peaks detected in any band are fitted to a Gaussian profile plus a planar baseline in the unfiltered maps for all other bands. The recovered source positions are set to the best-fit Gaussian centres in W-band. The best-fit Gaussian amplitude is converted to antenna temperature, using the relation given in Eq. 4.6, and then to a flux density using conversion factors, $\Gamma_{ff}(\nu)$, given in Table 4 of Hill et al. (2009). Note that the $\Gamma(\nu)$ factor can also be determined using Eq. 4.6 but with the pixel solid angle replaced by that of the beam (e.g. Page et al., 2003b). In any given band, we only use sources that are $> 2\sigma$ and the fitted source width smaller than 2x the beam width, following the *WMAP* team. The number of detected sources is 352 ± 30 using 100 realisations, consistent with *WMAP*5 point source analyses

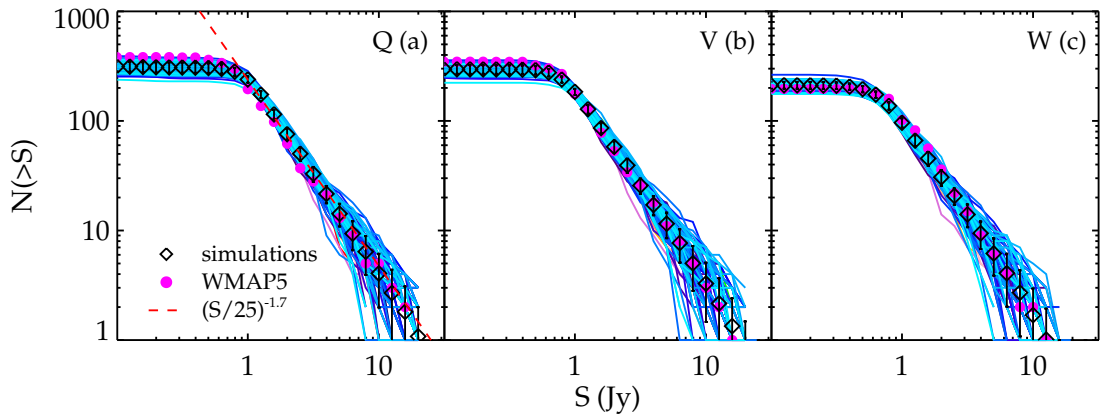

Figure 4.7: The integral counts, $N(>S)$, of the detected sources in Q (a), V (b) and W (c) bands from 100 simulations (coloured solid lines). On average, the recovered $N(>S)$ are in good agreement with the *WMAP*5 point source catalogue (magenta circles) and the input power-law distribution in Q-band (red dashed line) for $S > 1$ Jy.

by Wright et al. (2009) and Chen and Wright (2009). Fig. 4.7 shows that on average the integral source counts, $N(>S)$, detected in our simulations (diamonds with error bars) are in good agreement with *WMAP*5 (magenta circles). Our simulations also recover the input power-law $N(>S)$ distribution (red dashed line in Fig. 4.7a) down to the expected *WMAP*5 limit, $S \approx 1$ Jy, remarkably well.

For each simulation we applied our beam profile analysis outlined in §4.4.1. The average beam profiles derived from 100 simulations are plotted in Fig. 4.8 where the error bar represents their standard deviation in each angular bin. We found that even profiles as narrow as the W-band Jupiter profile can be retrieved remarkably well out to $30'$. The flux dependence of measured profiles were small with only a hint of possible Eddington bias in the faintest bin. The estimated uncertainties using these Monte Carlo simulations are consistent with our Jackknife error estimation presented in §4.4.1. Note that the Monte Carlo error converges after ≈60-70 simulations. The Monte Carlo simulations we performed here suggests that our method for recovering beam profile by stacking temperature maps around point sources is robust and the Jackknife error estimation is reliable.

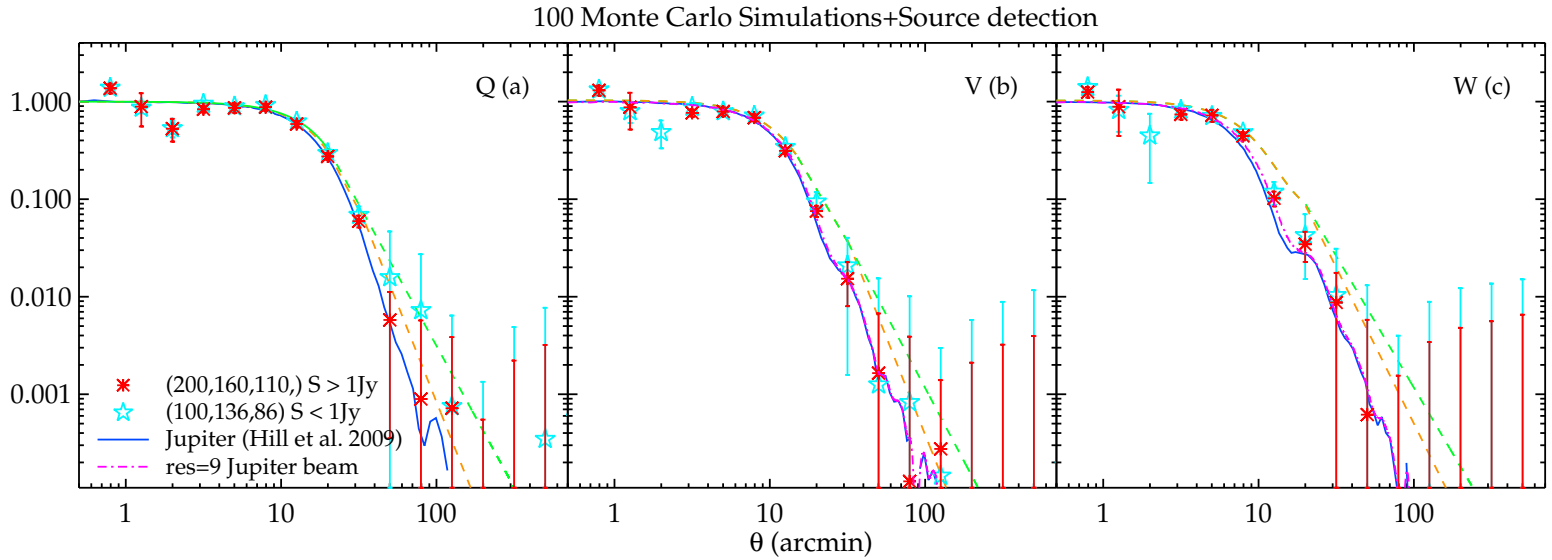

Figure 4.8: Same as Fig. 4.5, but now the stacking analysis are centred on the sources which are detected in the simulations following *WMAP* team's five-band detection method. The error bar is a standard deviation of the 100 simulations. The number indicated in the plots are the recovered source numbers averaging over 100 simulations.

4.4.3 NVSS radio sources

Point source catalogues made at significantly lower frequencies than the *WMAP* bands are unlikely to be affected by Eddington bias, if identification is done independently of the *WMAP*5 point source catalogue. For example, point source selected at 1.4 GHz will have antenna temperature $\approx$ 4500x higher than a source with similar flux density selected at *W*-band ($\approx$ 94 GHz), i.e. $T_{\rm a} \propto \Omega_{\rm beam}^{-1}\nu^{-2}$, whereas the rms antenna temperature due to the CMB fluctuations stays roughly the same between the two frequency bands (e.g. Bennett et al., 2003c). The NVSS beam width is $\approx$ 15x (§4.2.3) smaller than the *WMAP* highest resolution band, *W*, thus the factor quoted above is likely to be at least another factor of $\approx$ 200x bigger. Therefore we now stack *WMAP*5 temperature data centred around the positions of the 1082 $S_{1.4} > 1$ Jy NVSS point sources (§4.2.3). Fig. 4.9 shows the resulting *Q*1, *V*1 and *W*1 profiles. We see that they are consistent with those measured using *WMAP*5 total/bright sources presented in §4.4.1. However, the profiles do not appear to be wider or at least not as wide as the *WMAP*5 faintest subsample given that the average flux (at *WMAP* bands) of the NVSS sample is $\approx$ 3x lower. Although one might be inclined to suggest that the beam measured using the *WMAP* faintest bin is affected by Eddington bias, the faint data are rather noisy and this conclusion is not supported by the simulation results found in the last section.

In §4.4.1, *WMAP*5 sources used in the analysis had to be pre-detected in the GB6 or PMN 5-GHz surveys which already reduces somewhat the effect of Eddington bias. We now check the robustness of this result by imposing a more conservative matching threshold to a GB6 or PMN source from $< 11'$ (Wright et al., 2009) to $< 4'$ (i.e. $\approx$1/2 pixel size at res=9). This removed $\approx$ 100, 90 and 40 '$> 2\sigma$' sources (mostly faint) in *Q*, *V* and *W*-band, respectively. The resulting beam profiles are plotted in Fig. 4.9 and are in good agreement with the main results presented in §4.4.1.

As we noted in §4.2.3 that many of the NVSS sources are resolved into multiple components (Blake and Wall, 2002). Although this is unlikely to cause the widening of the beam beyond $\theta \gtrsim 6'$ and certainly not via the source clustering (see §4.4.1 and below). Here, as a precautionary measure, we shall test the beam profile measured using the NVSS by excluding any source that has neighbouring source(s) within 1°. This extra condition reduces the number of $S_{1.4} > 1.0$ Jy sources outside the *WMAP*5 'point source catalogue' mask to 933. The resulting beam profiles are shown in the Fig. 4.10(d)-(f). We see that the beam profiles are in good agreement with the previous results shown in

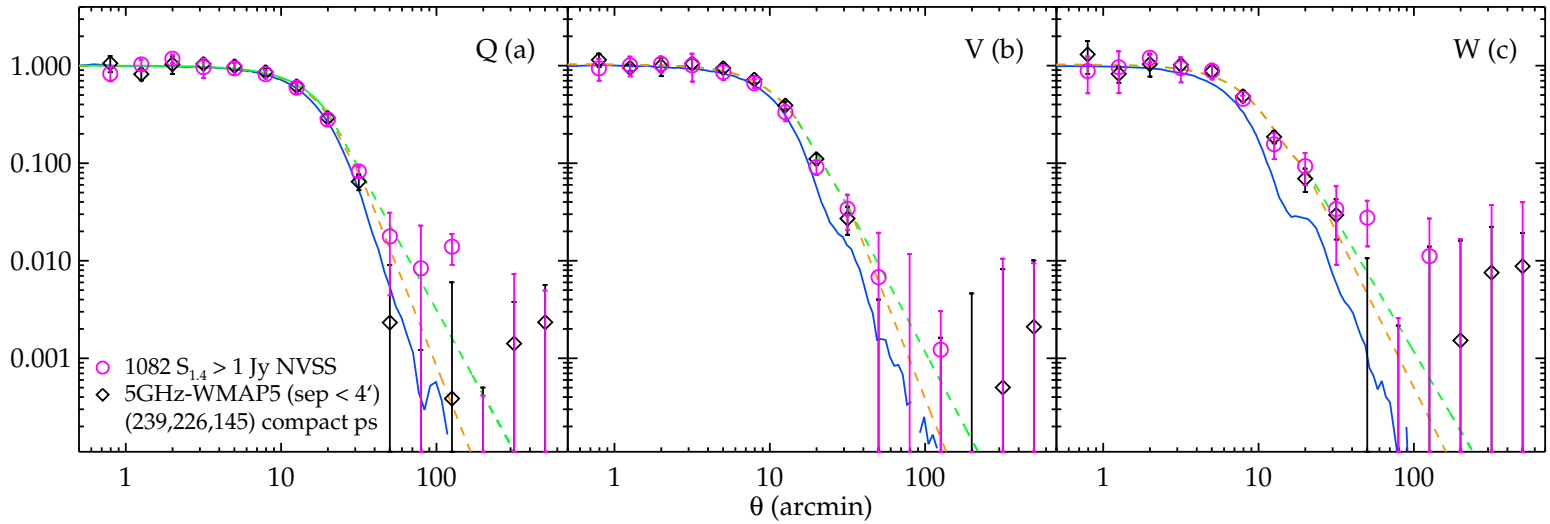

Figure 4.9: The beam profiles measured using 1082 NVSS 1.4GHz sources with $S > 1$ Jy (open circles). Also shown are results from using only *WMAP*5 point sources that has GB6/PMN 5GHz counterpart within $4'$ (diamonds). These are compared to *WMAP* team's (Jupiter) beam profiles (blue solid lines) and our empirical fits (green and orange dashed lines).

Fig. 4.9.

Although we argued above that sources (i.e. their identifications and positions) selected at NVSS frequency are robust against the CMB fluctuations compared to *WMAP* bands, our beam analysis is still carried out using *WMAP* temperature maps. As we noted above that the average flux of the $S_{1.4} > 1$ Jy NVSS sources in the *WMAP* bands is $\approx$ 3x lower than that of the *WMAP*5 faintest sample used in §4.4.1. Therefore it is important to check whether the *WMAP* beam profiles can be recovered robustly using these NVSS sources.

For this purpose, we created 100 Monte Carlo simulations similar to that described in §4.4.2 but without the five-band detection procedure since these sources are pre-detected by NVSS with high position accuracy (§4.2.3). The 933 NVSS source positions are used and fluxes at 1.4 GHz are extrapolated to *WMAP* Q, V and W bands assuming mean spectral index, α, of -0.45 in order to mimic the observed average flux density in these bands. The temperature maps are smoothed with the corresponding *WMAP* (Jupiter) beam profiles. The simulated CMB fluctuations and radiometer noise are then added to the source temperature maps. For each *WMAP* band, we applied our beam profile analysis to each of the 100 simulated maps. The results are shown in Fig. 4.10(a)-(c). The plot shows that with these NVSS radio sources the *WMAP* beam profiles can be robustly recovered out to $30'$ and are not affected by the source clustering consistent with our semi-empirical calculation presented in §4.4.1. We then take the standard deviation of the 100 simulated results in each angular bin as the 1σ error. The ratio of the Monte Carlo error to the Jackknife error is shown as the dotted line in Fig. 4.10(a)-(c). The Monte Carlo and Jackknife errors are in good agreement except at scales $< 10'$ where Jackknife errors are somewhat over-estimated in Q and V bands.

We conclude that in the W and V bands and probably the Q band, the average radio source profile is wider than the Jupiter beam and the fainter sources tentatively show a wider profile than the brighter sources. For $W1$ and $S > 1.1$ Jy sources, the beam profile measured in §4.4.1 rejects that of Jupiter with 4.0, 3.0 and 3.5σ significance for $\theta = 12\farcm6, 20'$ and $31\farcm6$. These become 4.4, 3.2 and 2.8σ when Monte Carlo errors are used instead. Note that the pixelisation has been taken into account when estimating these significances. The results using NVSS sources further support that the *WMAP* beam is wider than the Jupiter beam as found by using *WMAP*'s own point source catalogue. The 1.4-GHz selection frequency of NVSS is far from 94 GHz and any widening therefore cannot be due to any selection bias at 94 GHz from the Eddington effect.

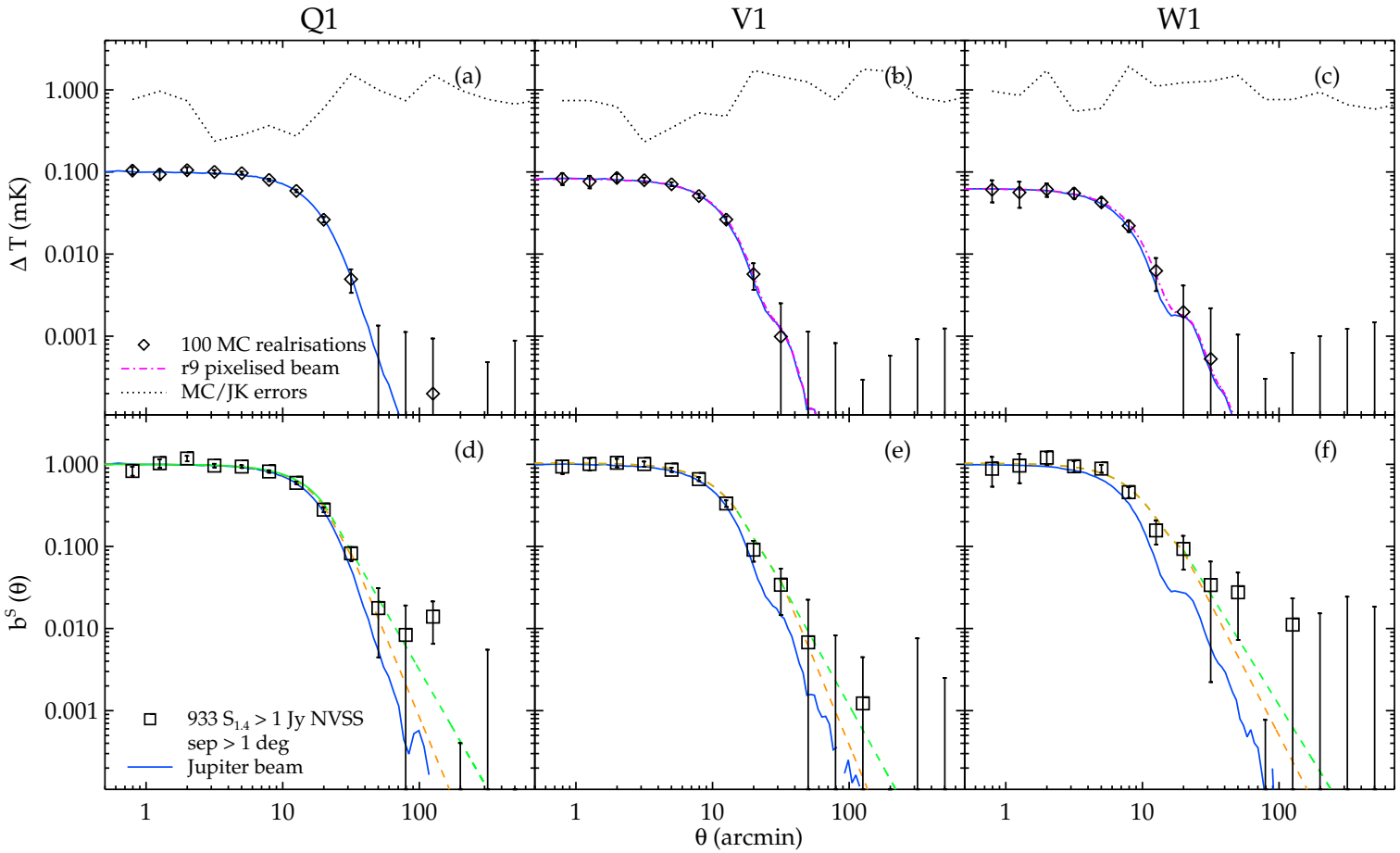

Figure 4.10: (a-c) The *WMAP* beam profiles measured from 100 Monte Carlo simulation using $S_{1.4} > 1$ Jy NVSS sources, where the ratios between Monte Carlo and Jackknife errors are also shown (dotted lines). (d-f) The *WMAP* beam profiles measured with 933 NVSS sources without any neighbouring source within 1°. These are compared to *WMAP* team's (Jupiter) beam profiles (blue solid lines) and our empirical fits (green and orange dashed lines).

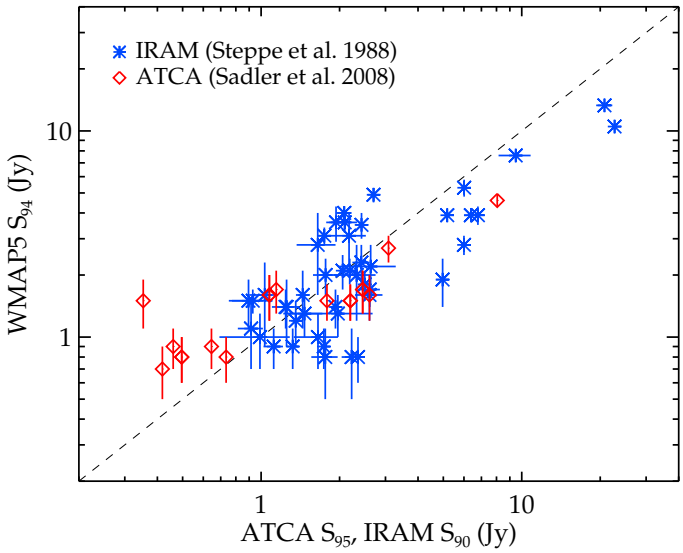

Figure 4.11: The comparison of the ATCA (diamonds) and IRAM (asterisks) source flux densities with the *WMAP* *W*-band data.

4.4.4 Comparison of *WMAP* and ground-based source fluxes

We now make a check of the *WMAP*5 *W* band fluxes as presented by Wright et al. (2009) in their Table 1. We checked these against the ATCA and IRAM source flux densities. The comparison in Fig. 4.11 shows that for both surveys, the brighter sources with fluxes > 3 Jy are about a factor of 1.5 fainter in the *WMAP* source list than in the ATCA or IRAM lists whereas Wright et al. (2009) claimed that for fluxes > 2 Jy the assumed Gaussian profile used in the fit caused the under-estimation of the recovered flux by only 10 per cent. The *WMAP* fluxes at $S < 1$ Jy are over-estimated due to Eddington bias (Wright et al., 2009; Chen and Wright, 2009). The agreement between the ATCA and IRAM fluxes appears better than for *WMAP*, if we use *WMAP* as an intermediary between these two surveys. The under-estimation of the flux cannot be explained by variability because this would results in a scattering around 1:1 relationship rather than a clear trend seen at the bright end of the plot. If the scale error is due to *WMAP*, then this might confirm the idea that there is a non-linearity in the *WMAP* flux scale. It could mean that the narrower *WMAP* beam at brighter fluxes is missing a significant amount of flux in the tail of the beam profile. There is also evidence that *WMAP* *W*-band fluxes of the bright sources are significantly under-estimated compared to the *Planck* Early Release Compact Source Catalogue (Ade et al., 2011) at 100 GHz (Whitbourn, Shanks & Sawangwit, in prep.).

4.4.5 Evidence for extended *W*-band beam from *WMAP* SZ effect?

Further evidence that the width of *W* band beam profile has been underestimated may come from results on the SZ effect. Previously, Myers et al. (2004) found what looked like an extended SZ effect in the *WMAP*1 data by cross-correlating Abell cluster and APM cluster positions with *WMAP* data. Then Bielby and Shanks (2007) compared the *WMAP*3 SZ decrements with X-ray data to show that while nearby rich clusters such as Coma are correctly predicted, at higher redshifts the clusters show less SZ effect than predicted. Indeed, for a sample of 38 higher redshift clusters of Bonamente et al. (2006), the predicted, stacked SZ decrement was rejected at 5.5σ. Bielby and Shanks (2007) used a Gaussian profile at *W* and at *Ka*. We therefore first used the Jupiter profile in both these bands and noticed little reduction of the predicted SZ decrement in both bands. Then we used our point source beam at the *W*-band to predict the SZ decrement. Given that the Gaussian width equivalent of the point source beam is now $\approx 8'$ rather than $\approx 5.4'$, this means that there will be a $8/5.4 = 1.5\times$ lower central normalisation for the wider beam. The discrepancy with the convolved SZ model is now reduced to $\approx 3.7\sigma$. However, taking into account that the X-ray models only apply out to $\approx 2'$ Bielby and Shanks (2007) found that the significance then dropped to 2.5σ. Given another 50 per cent reduction caused by the beam reduces the significance to 1.7σ. We conclude that the SZ fits support the evidence from the radio sources that the *W*-band beam profile has been significantly underestimated. The *Ka* band significance of this result is unaffected but always was lower because of the wider beam profile at this frequency. These results would help to explain the increased difficulty in getting *WMAP* SZ detections at higher redshift as being due to the increased domination of a wider than expected beam.

4.5 Impact on the debeamed C_ℓ

Finally, we use the information from our radio source beam profiles to judge what the effect might be on the debeamed *WMAP* C_ℓ. Unfortunately we will have to extrapolate our radio source fits in the regime beyond $\sim 1^\circ$ out to 5° because of the large errors on the radio source beam profile in this range. We first make an extrapolation where we fit the small-scale beam profile points and then extrapolate continuing with the power-law as shown by the green dashed lines in Fig. 4.3(d)-(f). We also made a more conservative extrapolation where we again fit the small-scale data but then extrapolate continuing parallel to the Jupiter beam profiles at large scales [orange dashed lines in Fig. 4.3(d)-

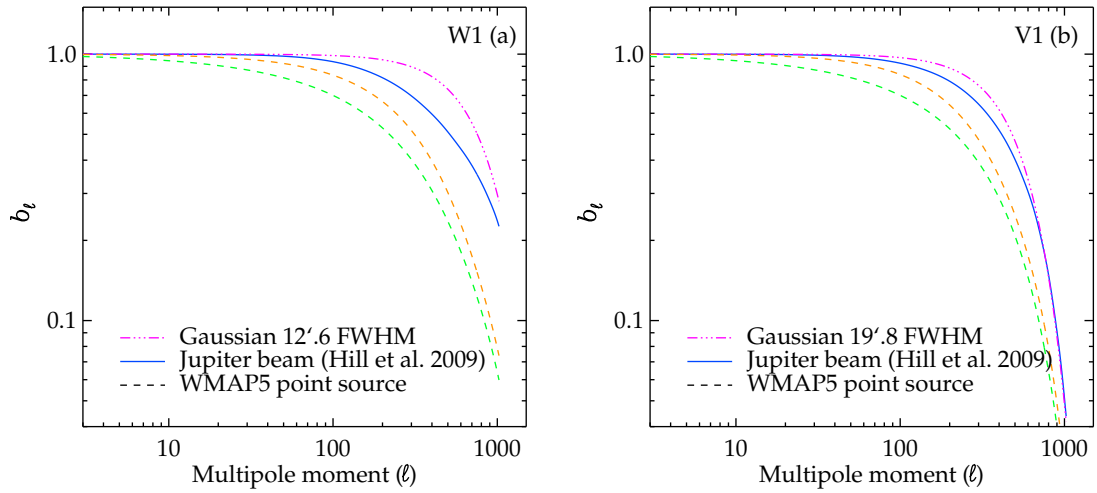

Figure 4.12: The *W*1 (a) and *V*1 (b) beam transfer functions, b_ℓ, derived from *WMAP*5 radio point source profiles (orange and green dashed lines), comparing to *WMAP* team's official b_ℓ (blue solid lines) and those derived from Gaussian profiles with 12.′6 and 19.′8 FWHM. The colour of the point-source b_ℓ corresponds to that of the $b^S(\theta)$ which it was derived from [Fig. 4.3(e) and (f)].

(f)]. The beam transfer functions, b_ℓ, required in debeaming of the power spectra are calculated from the radio source beam profiles using Eq. 4.1. The derived beam profiles presented in §4.4.1 are in fact smoothed by the pixelisation effect, as already mentioned above. Therefore one needs to correct for such an effect although this is expected to be small, given the beam width and pixel resolution relevant here. The correction is relatively trivial in the harmonic space, since the pixel transfer function is readily available from HEALPix package. The unsmoothed beam transfer function is just a division of the derived b_ℓ by the pixel window function. The resulting b_ℓ for *W*1 and *V*1 are shown in Fig. 4.12(a) and (b), respectively.

The beam convolved cross-power spectra for *V*1-*V*2 and *W*1-*W*2 are derived following the procedure outlined in §4.3. The debeamed C_ℓ are calculated using Eq. 4.2, assuming *WMAP*5 Jupiter beam transfer function (Hill et al., 2009) and the radio-source beam transfer functions derived above. The binned, debeamed cross-power spectra are shown in Fig. 4.13. We followed the *WMAP* binning scheme and for each ℓ bin we plot the mean value of the debeamed TT power spectrum, i.e. $\ell(\ell+1)/2\pi \times C_\ell$, in that bin. The error bars shown in the plot are estimated from the dispersion of the data in that bin. These are only given as a guide and not meant to replace the errors derived from the

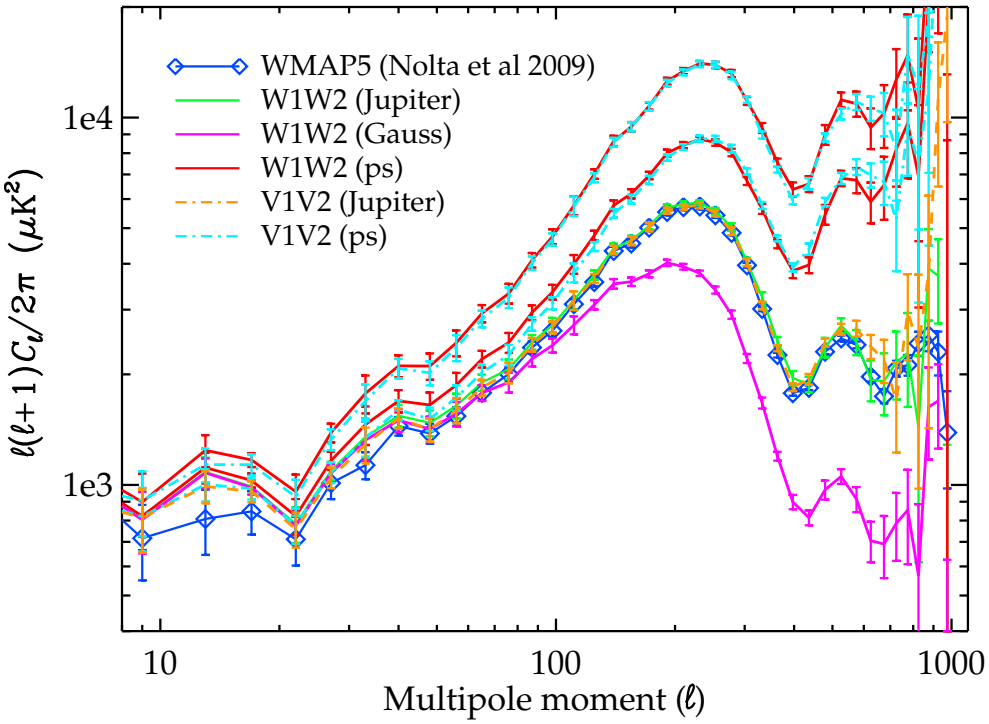

Figure 4.13: The debeamed CMB power spectra. The blue diamonds show the *WMAP* team's result. The cross-C_ℓ for the $W1$ and $W2$ ($V1$ and $V2$) maps and debeaming with the Jupiter beam profile is shown as the green (orange) line. The same result but now debeamed using the 12.′6 FWHM Gaussian is shown as the magenta line, significantly different from the result using the Jupiter beam profile to debeam. The same results but now using the profiles from the compact radio sources are shown as the red and cyan lines for W and V band, respectively. The differences in the two sets of debeamed W and V spectra are due to the difference in extrapolations of the radio source beam profiles beyond $\theta = 30'$ (see Fig. 4.3e and 4.3f.)

diagonal elements of the covariance matrix. For $\ell \gtrsim 40$, the Jupiter debeamed cross-power spectra (green and orange lines) are in good agreement with the *WMAP*5 official results (Nolta et al., 2009) up to $\ell \approx 500$ where the noise starts to dominate. On the other hand, below $\ell \approx 30$ our results appear to be different from the *WMAP*5 official results. This is, perhaps, not surprising, given that we use *PolSpice* code (Szapudi et al., 2001; Chon et al., 2004) which employs a 'pseudo-C_ℓ' based estimator (Peebles and Hauser, 1974; Hivon et al., 2002) whereas the *WMAP* team used a hybrid estimator (Efstathiou, 2004). The *WMAP* hybrid method utilised a maximum-likelihood estimate (Tegmark, 1997; Bond, Jaffe, and Knox, 1998; Wandelt, Larson, and Lakshminarayanan, 2004) at low ℓ and a pseudo-C_ℓ based estimate at high ℓ, making a transition at $\ell = 32$ (Hinshaw et al., 2007; Nolta et al., 2009). Another possible reason is that the *WMAP* five-year low-ℓ power spectrum analysis (Dunkley et al., 2009) used the Internal Linear Combination (ILC) map (Gold et al., 2009) as the input temperature map thus minimising the residual foreground contamination.

The range of the radio-source debeamed C_ℓ is shown by the two red lines and two cyan lines (for W and V bands) in Fig. 4.13. The most conservative beam model yields ≈ 50 per cent higher than the Jupiter debeamed C_ℓ at the scale of the first peak. But the most extreme model is now a factor of 2-3 higher even at $\ell = 220$ than the standard model power spectrum. We note that it has been possible to derive consistent C_ℓ's between the V, W (and Q) bands, although we accept that this is due to the freedom we have in extrapolating our radio source beam profiles beyond $\theta \approx 30'$. It seems that if the radio sources are indicating a wider beam profile, then the systematic uncertainty in the beam at the largest scales will dominate the error budget of the C_ℓ even at the scale of the first acoustic peak. These larger errors would then allow a wider range of cosmological models to be fitted, including models where the first peak lies at ℓ as high as 330 (Sawangwit and Shanks, 2010b).

4.6 Discussion and conclusions

Clearly it is important to understand why the radio source profiles are so wide in the Q, V and W bands. If there is a correlation between beam width and source flux then it will be wrong to use Jupiter profile to debeam the CMB power spectra because in the W band, for example, the ≈1-Jy radio sources are much closer to the $\approx$ 0.5-Jy rms flux of the CMB fluctuations than the 1200-Jy flux of Jupiter.

In estimating the new beam profiles, we have excluded radio sources that were observed to be extended by higher resolution surveys at 5 GHz, GB6 and PMN. We have also showed that the extended profiles are not caused by radio-source clustering or the flux variability. Furthermore, our Monte Carlo simulations with a realistic point source detection algorithm same as that used by *WMAP* team showed that the *WMAP* beam profiles can be robustly recovered out to $30'$ using our stacking analysis of both *WMAP*'s own source and NVSS catalogues. We also argued that the smaller than expected SZ decrements from *WMAP* observations of rich clusters (Myers et al., 2004; Bielby and Shanks, 2007) may also be explained by a wider than expected *WMAP* beam at *W*-band.

The non-linearity shown by the *WMAP* source fluxes compared to independently measured ATCA/IRAM fluxes (also *Planck* fluxes, Whitbourn, Shanks & Sawangwit, in prep.) is powerful supporting evidence of non-linearity in the *WMAP* data calibration. In considering possible causes of *WMAP* non-linearity, we first note that detector saturation is unlikely to be the problem since this would lead to the brighter sources having a wider profile than the fainter sources, which is not observed. However, Jupiter, being a moving source, has to be dealt with in a different way to the radio sources and the CMB fluctuations in the maps. This means that if there was a problem in the *WMAP* analysis, it would be necessary to check any filtering that is done to the maps. A filter with a non-linear effect would be needed to explain our radio-source results.

One possible source of error is the radiometer gain model but this appears to be well calibrated using the CMB dipole. But it is clear that in modelling the gain there is the opportunity to apply a non-linear filter to the data. In their Section 4, Hinshaw et al. (2009) state that a main goal of the *WMAP* data processing is to fit the calibration and sky signal simultaneously. They note that since the data model is non-linear and the number of parameters is large, the general problem is intractable. They therefore proceed iteratively but it might be speculated whether there could be any issues with this iteration. Their Eq. 2 has $d_i = g_i(\Delta T_{vi} - \Delta T_{ai}) + b_i$, where d_i is the difference recorded between the two radiometer channels, g_i is the radiometer gain and b_i is a baseline that has to be fitted. ΔT_{vi} and ΔT_{ai} are the true temperature differences from the dipole and the CMB fluctuations respectively. It is conceivable that badly fitting baselines and/or gains might lead to non-linearities with the radio source profiles. For example, if the gain is non-linear and its dependence on the temperature is such that

$$\widetilde{g} \propto \Delta T^{-\alpha} \tag{4.8}$$

The wrongly assumed gain linearity would lead to wider source profiles and underestimated fluxes at bright end,

$$\widetilde{b}^S(\theta) \propto b^S(\theta)^{1-\alpha} \tag{4.9}$$

and

$$\widetilde{S}_\nu \propto S_\nu^{1-\alpha} \tag{4.10}$$

The preliminary results suggest that the above equations may be a good fit to the data (Whitbourn, Shanks & Sawangwit, in prep.)

However, Hinshaw et al. (2009) argue that the fits for g_i and b_i are generally correct based on checks with simulations that include known systematic effects. The input maps for the simulations are accurately recovered. This is reassuring but it may still be the case that other unknown systematics may be affecting these iterative fits. There appear to be no further empirical checks that have been made on the linearity of the resulting maps. It might be wondered whether if the calibration uncertainties are actually relatively small, could they be ignored for some part of the map production to see how robust the fully fitted results are? Otherwise, we do not understand the reason for the difference between the Jupiter and radio source beam profiles.

We conclude the following.

(i) The *WMAP* power spectrum is heavily dependent on the beam profile. Indeed even the first acoustic peak at $\ell \approx 220$ is very dependent on the form of the profile at $1^\circ - 2^\circ$ where the profile is only ≈ 0.1 per cent of its peak value.

(ii) The radio point sources detected by *WMAP* in the Q, V and W bands generally show a broader beam profile than the Jupiter beam used by the *WMAP* team. For example, using $S_W \geq 1.1$ Jy sources, our $W1$ beam profile rejects the Jupiter beam with $\gtrsim 99.5$ per cent confidence.

(iii) There may be tentative evidence for a flux-dependent effect within the *WMAP* data in that fainter radio sources appear to have broader profiles than brighter sources, although the faint data are noisy.

(iv) Non-linearity in the *WMAP* flux scale may also be indicated by comparisons of *WMAP* radio source fluxes with ATCA and IRAM fluxes which show 50 per cent reduced flux from *WMAP*.

(v) Further arguments against possible systematics such as Eddington bias affecting our results come from simulation checks and NVSS sources selected at frequency where CMB fluctuations are sub-dominant.

(vi) The systematic errors on the *WMAP* C_ℓ due to the beam may be much larger than previously expected and in turn, this means that the systematic error on the best fit cosmological model may also be larger. It will be interesting to see if a revised estimate of the *WMAP* beam profile then allows a simpler cosmological model to be fitted than ΛCDM.

Chapter 5

WMAP scan pattern and on-sky beam maps

5.1 Introduction

In Chapter 4, we assumed that the beams are axially symmetric when estimating the CMB angular power spectrum (C_ℓ). However this is generally not the case for the *WMAP* (Page et al., 2003a,b) and many CMB experiments, e.g. SPT (Lueker et al., 2010), ARCHEOPS (Macías-Pérez et al., 2007), BOOMERANG (Masi et al., 2006), MAXIMA (Rabii et al., 2006) and the *Planck* mission (Maffei et al., 2010). An asymmetric beam coupled with a survey's complex scanning pattern can also result in an effective beam being a function of its position on the sky. This makes inferring the true CMB angular power spectrum, $C_\ell^{\rm sky}$, from the estimated $C_\ell^{\rm est}$ very complicated. In the past, many CMB analyses have neglected this difficulty by assuming the azimuthally-symmetrised beam in the C_ℓ estimations (e.g. Wu et al., 2001). However, there are also many studies (e.g. Wandelt and Górski, 2001; Souradeep and Ratra, 2001; Mitra et al., 2004, 2011) which attempt to model the effect of more realistic beams on the C_ℓ estimations. The symmetric-beam assumption will generally bias the estimates of the temperature C_ℓ at high ℓ, corresponding roughly to scales smaller than the beam width. Another important effect is the introduction of statistical anisotropies into the observed CMB temperature and polarisation (Shimon et al., 2008), thus mimicking anisotropic effects such as gravitational lensing (Hanson, Lewis, and Challinor, 2010).

Our adopted azimuthally-symmetrised beam approach is the same as that employed by *WMAP* team in their map-making, beam transfer function and angular power spectrum estimates (Page et al., 2003b; Hinshaw et al., 2003b; Jarosik et al., 2007; Hinshaw et al., 2007; Hill et al., 2009; Nolta et al., 2009). *WMAP*'s scan strategy helps to alleviate the effect of the beam asymmetry somewhat by observing each sky pixel over a wide range of azimuth angles. However, as we shall see later that this is not the case at low

Ecliptic latitudes where the scanning is sparse and mostly in the orthogonal direction of the Ecliptic plane. In the *WMAP* three-year temperature analysis, Hinshaw et al. (2007) estimated the bias induced by the residual beam asymmetry and found that the *Q*-band cross-power spectrum requires the largest correction (≈ 6.3 per cent at $\ell = 600$) due to its most elliptical beam of the three highest frequency bands used in the C_ℓ analysis. The *V*- and *W*-band, however, only require $\lesssim 1$ per cent corrections at $\ell < 1000$, i.e. significantly smaller than the instrument noise for these ℓ ranges. Consequently, the corrections for *V*- and *W*-band are neglected and the *Q*-band data were excluded from the final three-year (and later) power spectrum. For a more sensitive CMB experiment such as the ongoing ESA *Planck* mission (The *Planck* Collaboration, 2006) which has a less symmetrising scan strategy (Tauber et al., 2010) than *WMAP*, the beam asymmetry is expected to be a major source of systematic errors. And many efforts have now been devoted to the studying of its effect on the *Planck* results (e.g. Ashdown et al., 2009; Huffenberger et al., 2010; Mitra et al., 2011).

Recently, Liu et al. (2010) claimed that there exists a timing offset between the satellite pointing and the differential temperature data in the 'Time Ordered Data' (TOD) which has been missed by the *WMAP* team's data analysis pipeline. The offset of 25.6 ms has been explicitly shown to be present between the starting time of the 'Meta Data Table' and 'Science Data Table' using a computer script provided by Roukema (2010a). Such an error, if it exists, would induce an artificial quadrupole signal arising from incorrect Doppler-dipole subtraction due to the satellite pointing offsets as demonstrated by Liu et al. (2010) and Moss et al. (2011). The former found that most of the detected *WMAP* quadrupole signal can be explained by this systematic error although the latter disputed that it only produced a third of the claimed signal. Moss et al. (2011) further demonstrated that the coincidental alignment of the induced and primordial quadrupole fields is due to an unfortunate coupling of the *WMAP* scan pattern and the dipole field and suggested that this should not be the case for the *Planck* mission.

Besides the induced quadrupole signal, Moss et al. (2011) (see also Roukema, 2010a) noted that given the *WMAP* scanning strategy, the satellite pointing error will also affect the observation of point sources. At low Ecliptic latitudes, the scan pattern is mostly orthogonal to the Ecliptic plane while near the pole it is much more isotropic. The pointing error would mean that a point source near the Ecliptic plane will appear elongated in the Ecliptic North-South direction whereas a point source near the pole will remain circularly symmetric. Moss et al. (2011) suggested that by stacking sources in Ecliptic latitude

bin, the timing residual can be constrained. Here, we investigate the possibility of using the real point source data and numerical simulations to test the timing offset claimed in the literature. We will also check if such an effect can explain the wider than expected *WMAP* beam profile as observed in Chapter 4 (see also Sawangwit and Shanks, 2010a). We shall also use the algorithm for deriving the on-sky beam maps developed during this study to check if the azimuthally-symmetrised beam profile observed near the Ecliptic plane, i.e. as in the analysis of Jupiter beam profile, can be applied everywhere else on the sky.

The layout of this chapter is as follows. We first outline the key ingredients for modelling the on-sky beam maps in §5.2. The algorithm for generating the on-sky beam maps are then used to investigate the effect of possible *WMAP* timing offset on the point source profile and the beam ellipticity, including its detectability by stacking radio point sources in §5.3. The summary and conclusions are then presented in §5.4.

5.2 Modelling the on-sky beam maps

5.2.1 *WMAP* scanning strategy

The *WMAP* observatory was launched on June 30, 2001 and has been collecting science data from a Lissajous orbit around the Sun-Earth L2 Lagrange point since August 10, 2001 (see Bennett et al., 2003a, for the mission review and summary of the instrument design). The *WMAP* is a differential experiment which means that it measures the temperature by taking a difference measurement between two points in the sky through a series of scanning arcs by two feed horns (called A- and B-side) at a fixed separation on the sky, $\approx 141^\circ$ where the exact values differ slightly for different 'Differencing Assemblies' (DAs). The experiment used the CMB dipole field[1] and its modulation due to *WMAP*'s motion as a continuous calibration source. Since the separation of the two feed horns is large, the probe always see a substantial CMB dipole modulation which is crucial for a stable calibration of the data.

To achieve its goal of reconstructing the full sky temperature map with minimum systematics and maximising polarisation sensitivity and beam symmetry, *WMAP* employs a compound motion which allows it to scan each sky pixel through as many azimuth angles and on many different time scales as possible (Bennett et al., 2003a, and reference therein).

[1] which was precisely measured by the *Cosmic Background Explorer* (*COBE*; Kogut et al., 1993; Lineweaver et al., 1996)

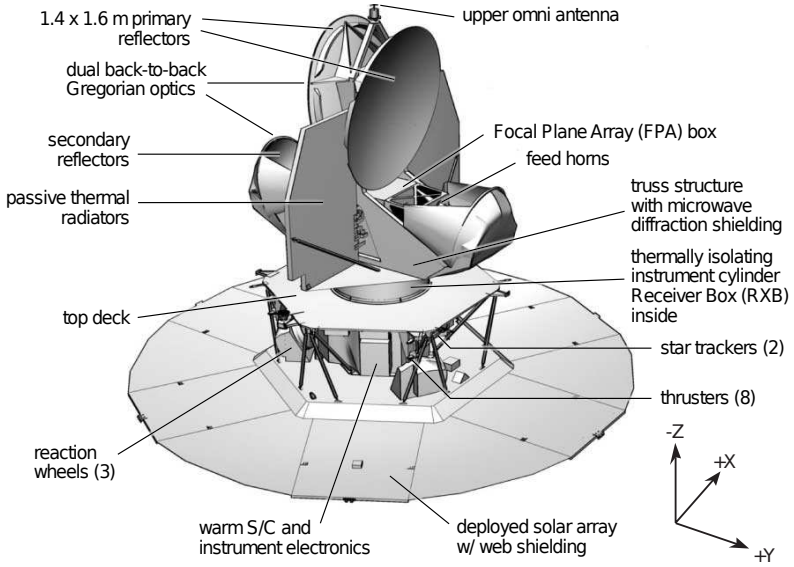

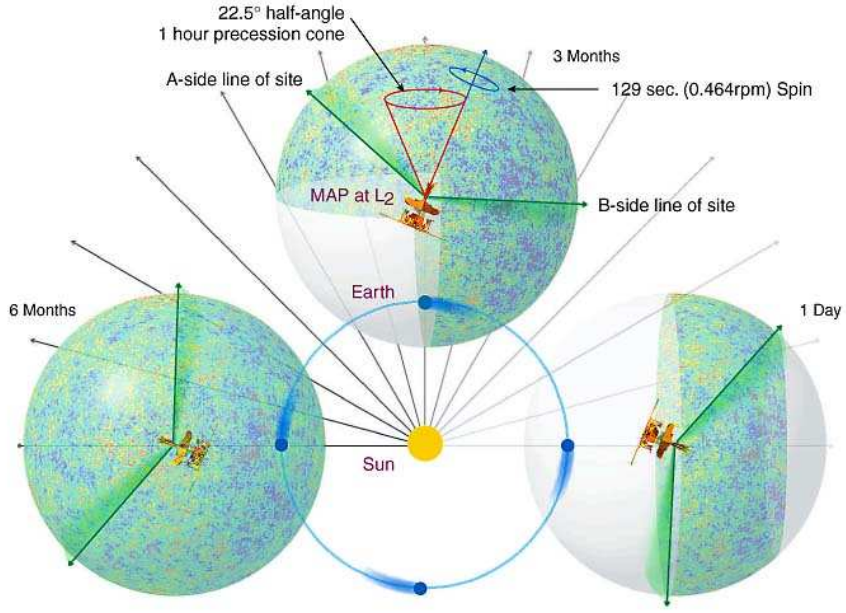

Figure 5.1: (top) Overview of the *WMAP* observatory, showing its major components and the spacecraft (S/C) coordinate. Figure credit: Bennett et al. (2003a). (bottom) The *WMAP*'s compound motion in its 'observing mode', showing spin and precession rates including its orientation relative to the Sun-Earth system. This is an illustrative guide only and not to scale. Picture adapted from the NASA *WMAP* mission website (`http://map.gsfc.nasa.gov/mission/observatory_scan.html`).

The two feed horns spin around the satellite symmetry axis (-Z axis in Fig. 5.1) at 0.464 rpm (±0.13 per cent). Simultaneously, the spin axis precesses around the Sun-*WMAP* line (in the anti-Sun direction) at an angle $\vartheta_{\rm P} = 22\overset{\circ}{.}5$ ($\pm 0\overset{\circ}{.}023$) with a period of one hour (±3.6 per cent). For a pictorial representation of the *WMAP* scan strategy see the bottom panel of Fig. 5.1. This fast spin strategy combined with reasonably fast precession means that the requirements mentioned above can be met. The full sky can be covered every six months while maintaining the reasonable azimuth coverage, i.e. $\sim$ 30 per cent near the Ecliptic plane and increases to $\sim$ 70 per cent at $|\beta| \approx 50^\circ$ (the cusps seen in Fig. 5.2) and 100 per cent at the Ecliptic pole. The reason for these different azimuthal coverages is due to the *WMAP* scan pattern where it is mostly confined to the North-south direction closer to the Ecliptic plane and become more isotropic as it approaches the pole.

We model the *WMAP* scanning strategy and use the parameters given above to construct a set of rotating coordinates and their corresponding rotation matrices which in turn can be used to transform any vector in the satellite coordinate to Ecliptic coordinate, and vice versa. The time-dependent rotation matrix (see Appendix B) is used to determine the *WMAP* pointing of any DA horn (either A- or B-side) at any given time by applying it to the line-of-sight (LOS) unit vector of that particular horn. The LOS vectors for all the 20 DAs, 10 for each side, are given in the satellite coordinates and can be extracted from the LOS Table of the TOD (Limon et al., 2008).

Fig. 5.2(top) shows the scan model (orange solid line) for W1A (A-side beam boresight of the W1 DA) predicted for the first hour of *WMAP* observing mode, using only the first few quaternions (attitude data) extracted from the TOD to triangulate its starting point. The model is compared to the real *WMAP* scan pattern (white dashed line) of the same DA and side. The *WMAP* pointing data are determined from the TOD using *WMAP* software[2]. The number of observations ($N_{\rm obs}$) per pixel per year for W1 map which are constructed from the scan model (pointing data) is also shown in top (bottom) panel of Fig. 5.2. The model was run for 365 days to simulate a stream of TOD which is then processed with the map-making procedure explained in §5.2.3. In the bottom panel of Fig. 5.2, the regions where data were rejected due to one of the outer planets (Mars through Neptune) is within 7° of either A or B-side beam (Bennett et al., 2003b) are clearly visible in the Ecliptic plane. The data which are flagged with Jupiter passages within a few to several degrees (exact values depend on the frequency band) of the beam centre are kept for the *WMAP* beam analyses (Page et al., 2003b, see also §5.2.2). Another

[2] `http://lambda.gsfc.nasa.gov/product/map/current/m_sw.cfm`

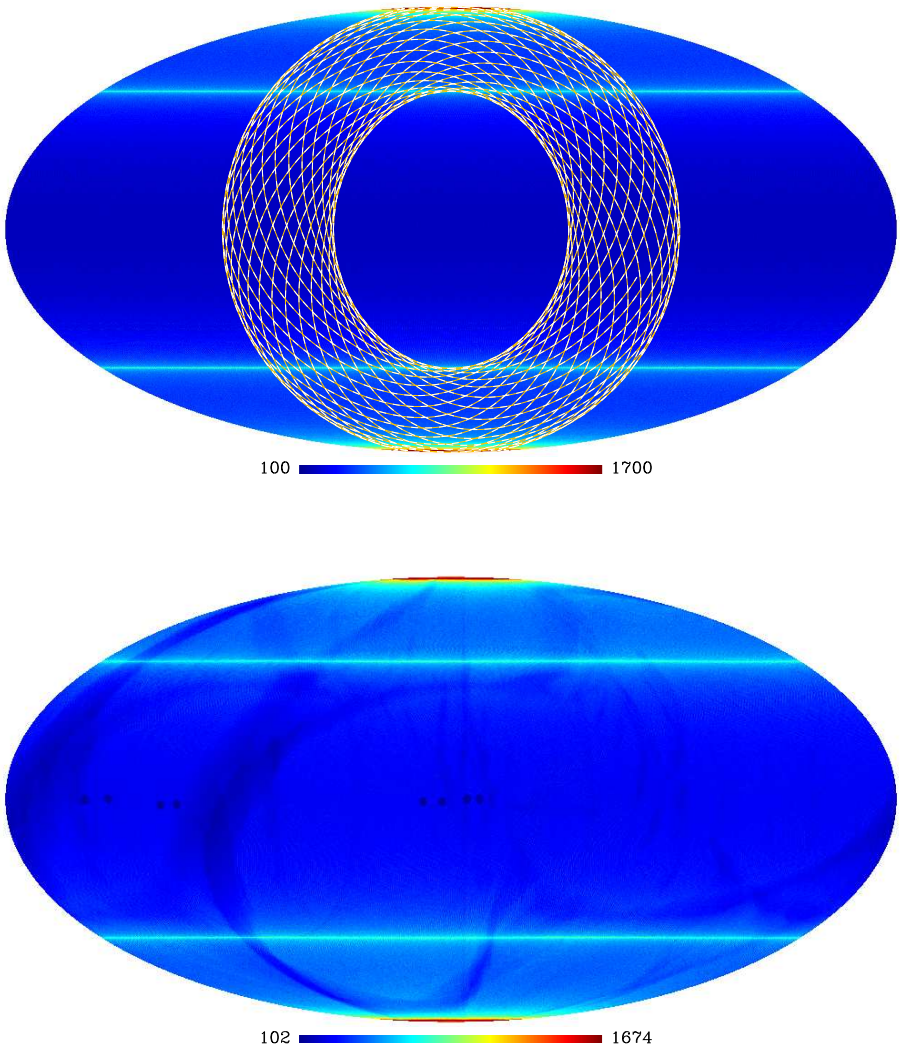

Figure 5.2: Number of observation per pixel per year for $W1$ in Ecliptic coordinates. (Top) The predicted $N_{\rm obs}$ map using the scanning model (§5.2.1). The map is overlaid by the first hour of the scan pattern (orange line), comparing to the *WMAP* in-flight attitude data from TOD (white dashed line). The first few quaternions from *WMAP* TOD were used to triangulate the starting point of the satellite spin axis and the beam boresight. (Bottom) The first-year *WMAP* $N_{\rm obs}$ map. The regions where data were rejected due to one of the outer planets (Mars through Neptune) is within 7° of either A or B-side beam are clearly visible in the Ecliptic plane.

notable feature is the cusps in the $N_{\rm obs}$ at $|\beta| \approx 50^\circ$, corresponding to $|\vartheta_{\rm P} - 141^\circ/2|$ the angular distance between precessing spin-axis and the antenna pointing. The good agreement between our model and the real scan pattern including the general feature seen in the $N_{\rm obs}$ maps demonstrate that the assumed scanning model should be adequate for our purpose here.

5.2.2 *WMAP* beam response

The *WMAP* telescope focal plane makes an angle of 19.°5 with the spin (spacecraft symmetry) axis (see Page et al., 2003a, for the probe's optical design and characterisation). The feed horns for the A- and B-side are located back-to-back to facilitate the 141° angular separation on the sky to achieve *WMAP* observing goal as highlighted in §5.2.1. Each side consists of 10 DAs, namely *K*1, *Ka*1, *Q*1, *Q*2, *V*1, *V*2, *W*1, *W*2, *W*3 and *W*4. Their main beams are situated on the focal plane around the optic axis.

The in-flight beam response is determined from the repeated observations of Jupiter over the course of the experiment. Jupiter is observed by *WMAP* twice a year, each time lasting for ≈ 45 days. The data are taken in normal 'observing mode' when Jupiter passes within ≈ 7°, 5°, 5°, 4° and 3.°5 of either the A- or B-side beam centre for *K*, *Ka*, *Q*, *V* and *W* bands, respectively. Here, we consider the five-year data release[3] which includes the beam maps analysis of 10 Jupiter observing seasons; Oct/Nov 2001, Feb/Mar 2002, Nov/Dec 2002, Mar/Apr 2003, Dec 2003/Jan 2004, Apr/May 2004, Jan/Feb 2005, May/Jun 2005, Feb/Mar 2006 and Jun/Jul 2006 (Hill et al., 2009). We shall only focus on the *W*-band, especially *W*1 DA, beam response which is found to be significantly wider than expected using stacking analysis of point sources' profiles (see Chapter 4 and Sawangwit and Shanks, 2010a).

The beam maps are constructed from the hybridisation of Jupiter data with a beam model which allows the low signal-to-noise beam pedestal to be better constrained. In other words, the beam model substitutes the Jupiter data in the low signal region set by the hybridisation threshold of 3, 4, 6, 8 and 11 dBi for *K*, *Ka*, *Q*, *V* and *W* bands, respectively (Hill et al., 2009). The beam map, $B(\hat{\mathbf{n}})$, is related to the observed Jupiter temperature maps by (Page et al., 2003b)

$$T(\theta, \phi) = T_{\rm J}^{\rm m}\, \Omega_B\, B(\theta, \phi), \tag{5.1}$$

[3]Available at `http://lambda.gsfc.nasa.gov/product/map/dr3/m_products.cfm`

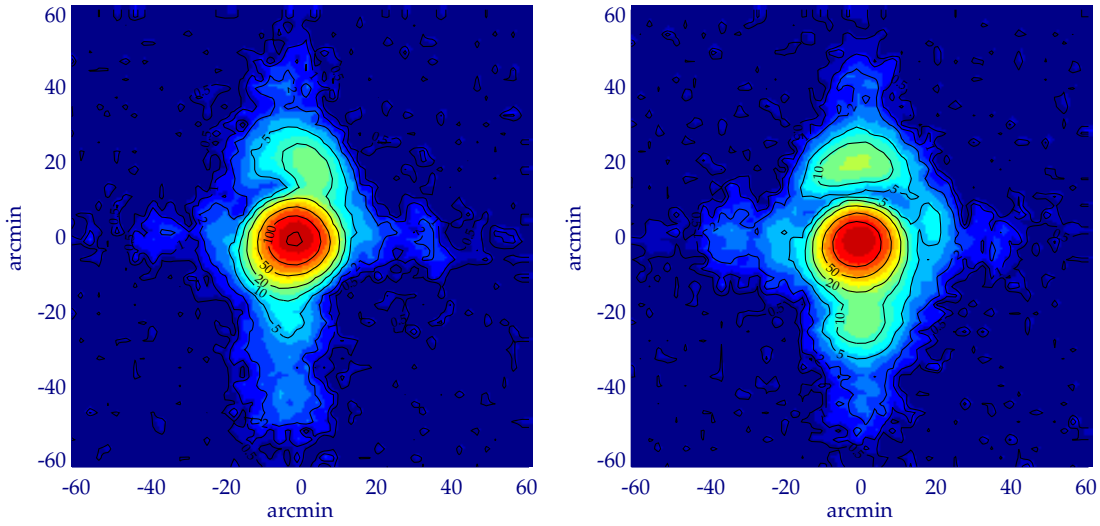

Figure 5.3: The *WMAP* Jupiter beam maps (Hill et al., 2009) for W1A (left) and W1B (right) used in conjunction with the scan strategy to model the on-sky beam maps.

where $T_{\rm J}^{\rm m}$ is the amplitude observed by *WMAP* and Ω_B is the main-beam solid angle. The five-year Jupiter (antenna) temperature maps, background subtracted and aberration corrected, for W1A and W1B are shown in the left and right panels of Fig. 5.3, respectively. The maps are pixelised into $2\farcm4 \times 2\farcm4$ bins and have undergone the hybridisation. Note that the probe scanning direction is parallel to the x-axis of the plotted beam map (Limon et al., 2008).

From Fig. 5.3, it is immediately obvious that the beams are not axially symmetric as expected (Page et al., 2003a). The beams appear slightly non-circular within $\approx 12\farcm6$ FWHM of the beam centre. This arises from the fact that the beam centre is not on the primary focus although not too far off compared to the lower-frequency DAs whose beam asymmetries are more severe as a result (Page et al., 2003a). Other notable features can be seen at ≈ -10 to -20 dB level. These are caused by the distortion of the primary mirror upon cooling (Page et al., 2003a,b). Note that the beam profiles we studied in the last Chapter is the azimuthally-symmetrised beam response, $b^S(\theta)$, of a combination of A- and B-side maps. Therefore any asymmetry is averaged out and should not directly affect our previous results. However, it may give rise to an echo ring at 140° around a bright source (see §5.3).

The hybrid beam maps are used for the purpose of estimating the hybridised symmetrised beam profiles, $B^S(\theta)$. The azimuthally-symmetrised beam response is calculated by averaging the temperature within an annulus centred on the beam centroid with a ra-

dius θ. The normalised (at $\theta = 0$) symmetrised beam profile, $b^S(\theta)$, is defined such that

$$b^S(\theta) = \Omega_B B^S(\theta), \quad \Omega_B = 2\pi \int b^S(\theta) \sin\theta \, d\theta. \tag{5.2}$$

For the five-year beam analysis, the *W*-band main-beam solid angle was evaluated out to the 'transition radius' of 3°.5 (Hill et al., 2009, Table 3). The effective $b^S(\theta)$ for each DA is then determined by combining the A- and B-side profiles, $b^{S,\mathrm{A}}$ and $b^{S,\mathrm{B}}$, (Page et al., 2003b; Hinshaw et al., 2003a);

$$b^S(\theta) = \frac{\Omega^S}{2} \left[\frac{b^{S,\mathrm{A}}}{(1+x_{\mathrm{im}})\Omega_B^{\mathrm{A}}} + \frac{b^{S,\mathrm{B}}}{(1-x_{\mathrm{im}})\Omega_B^{\mathrm{B}}} \right], \tag{5.3}$$

where $x_{\mathrm{im}} \approx 0.01$ accounting for the transmission imbalance between A- and B-side (Jarosik et al., 2003), Ω^S is the effective beam solid angle, Ω_B^{A} and Ω_B^{B} are the main-beam solid angles for sides A and B.

5.2.3 Map-making process

The *WMAP* experiment reconstructs the temperature map, $\boldsymbol{T}(\hat{\mathbf{n}})$, by scanning the sky with two antennas (called A- and B-side). In fact, the probe recorded raw differential signals, i.e. uncalibrated Time-Ordered Data (TOD), as it scans the sky;

$$\boldsymbol{d}_{\mathrm{raw}}(t) = \boldsymbol{g}(t) \left[\boldsymbol{d}(t) + \boldsymbol{\varepsilon}(t) \right] + \boldsymbol{b}(t), \tag{5.4}$$

where $\boldsymbol{g}(t)$, $\boldsymbol{b}(t)$ and $\boldsymbol{\varepsilon}(t)$ are instrument gain (responsivity), baseline and noise as a function of time, respectively (Hinshaw et al., 2003a, and references therein). Once the raw TOD are calibrated (using the Dipole modulation), the differential temperature data can be written in the form

$$\boldsymbol{d}(t) = (1+x_{\mathrm{im}})\, \boldsymbol{T}(\hat{\mathbf{n}}_{\mathrm{A}}) - (1-x_{\mathrm{im}})\, \boldsymbol{T}(\hat{\mathbf{n}}_{\mathrm{B}}), \tag{5.5}$$

where $\hat{\mathbf{n}}_{\mathrm{A}}$ and $\hat{\mathbf{n}}_{\mathrm{B}}$ are unit vectors denote the A- and B-side pointing on the sky at a given time t. The terms $(1+x_{\mathrm{im}})$ and $(1-x_{\mathrm{im}})$ account for the input transmission imbalance between the A and B sides (Jarosik et al., 2003). In practice, each antenna observes the sky through a beam $B(\theta, \phi)$, thus Eq. 5.5 becomes

$$\boldsymbol{d}(t) = \int d\Omega\, \boldsymbol{T}(\hat{\mathbf{n}}) \Big[(1+x_{\mathrm{im}})\, B_{\mathrm{A}}\big(\mathbf{R}(t)\cdot\hat{\mathbf{n}}\big) - (1-x_{\mathrm{im}})\, B_{\mathrm{B}}\big(\mathbf{R}(t)\cdot\hat{\mathbf{n}}\big) \Big], \tag{5.6}$$

where $\mathbf{R}(t)$ is the rotation matrix constructed from *WMAP* scan pattern (§5.2.1) and is used to transform a sky coordinate[4] into the spacecraft (S/C) and then the beam map coordinates. For the purpose of sky map reconstruction, this is written simply as

$$\boldsymbol{d}(t) = (1 + x_{\rm im})\,\widetilde{\boldsymbol{T}}(p_{\rm A}) - (1 - x_{\rm im})\,\widetilde{\boldsymbol{T}}(p_{\rm B}), \tag{5.7}$$

where $\widetilde{\boldsymbol{T}}(p)$ is the beam-smoothed sky map at the pth pixel observed either by A- or B-side antenna. The sky map has now been discretised into $N_{\rm pix}$ elements which introduces further smearing to the map. However, such a smearing effect can be easily corrected if the pixel window function is known. The pixelisation scheme employed by the *WMAP* team (and also in this work) is the 'Hierarchical Equal Area isoLatitude Pixelisation' of a sphere (HEALPix; Górski et al., 2005).

Now, the calibrated TOD can be written in terms of a mapping matrix $\mathbf{M}$ and the beam-smoothed sky map;

$$\boldsymbol{d} = \mathbf{M}\widetilde{\boldsymbol{T}} \tag{5.8}$$

The mapping matrix has $N_t \times N_{\rm pix}$ elements, with each row contains only two non-zero elements in the columns correspond to the A- and B-side antennas pointing;

$$\mathbf{M}_{t,*} = [\ldots, (1 + x_{\rm im}), \ldots, -(1 - x_{\rm im}), \ldots] \tag{5.9}$$

Note that we have deliberately ignored the instrument noise, $\boldsymbol{\varepsilon}(t)$, in Eq. (5.5)-(5.8). Including noise would affect the statistic and not the general feature of the beams we attempt to measure here. However, in §5.3.2 where the statistic of the noise is required, we shall assume white noise because for most radiometers the noise covariance matrix, $\left\langle \boldsymbol{\varepsilon}\boldsymbol{\varepsilon}^T \right\rangle$, is reasonably diagonal. Even if this is not the case, any residual off-diagonal terms are likely to affect pixels at the beam separation angle, i.e. 141°, (Hinshaw et al., 2003a) therefore such an effect is not expected to be an issue for our study here. In the standard *WMAP* map-making pipeline, the effect of correlated noise in the TOD which would result in striping in the final sky map is reduced by an application of a pre-whitening filter on the calibrated TOD (e.g. Hinshaw et al., 2003a).

Following the *WMAP* team's map-making routine, we determine the sky map solution from the differential time-ordered data using a maximum likelihood estimate;

[4]Here, we choose Ecliptic coordinate with longitude λ and latitude β.

$$\begin{aligned} \widetilde{\boldsymbol{T}} &= \mathbf{D}^{-1} \cdot \widetilde{\boldsymbol{T}}_0 \\ &= \left(\mathbf{M}^T\mathbf{M}\right)^{-1} \cdot \left(\mathbf{M}^T\boldsymbol{d}\right) \end{aligned} \tag{5.10}$$

To solve for the sky map using the above equation, one needs to invert the $N_{\rm pix} \times N_{\rm pix}$ matrix $\mathbf{D}$. For the *WMAP* resolution, there are more than one million sky pixels and such an evaluation becomes computationally prohibitive. To work around this, the iterative approach was introduced by Wright et al. (1996). Because $\mathbf{M}^T\mathbf{M}$ is diagonally dominant, its inverse can be approximated[5] as (Hinshaw et al., 2003a)

$$\widetilde{\mathbf{D}}^{-1}_{i,j} \approx \frac{1}{N_{\rm obs}(p_i)}\,\delta_{ij} \tag{5.11}$$

The iterative solution to the above equation is then given by

$$\widetilde{\boldsymbol{T}}_{n+1} = \left(\widetilde{\mathbf{D}}^{-1}\mathbf{M}^T\right)\boldsymbol{d} + \left(\mathbf{I} - \widetilde{\mathbf{D}}^{-1}\mathbf{D}\right)\widetilde{\boldsymbol{T}}_n, \tag{5.12}$$

where $\mathbf{I}$ is an identity matrix and the initial guess of the sky map is $\widetilde{\boldsymbol{T}}_0 = \mathbf{M}^T\boldsymbol{d}$ (Eq. 5.10). For a single beam experiment, the second term on the RHS is zero and the sky map solution for a given pixel is simply an average of all the observations belong to that pixel. In the *WMAP* case (and any differential experiments), the second term serves as a correction for the approximation made in Eq. 5.11 by using the sky map from previous iteration. The number of observations per pixel is defined as the total number of times a particular pixel has been observed by either A or B side. The map solutions usually converge after ≈ 50 iterations as demonstrated by *WMAP* flight-like simulations (Hinshaw et al., 2003a).

5.3 The on-sky beam maps and the effect of timing offset

Here, we investigate the on-sky beam response in a noiseless temperature map by incorporating all the ingredients outlined in §5.2. We put four mock point-sources which have the same brightness temperature as Jupiter on a CMB-free sky. The sources are placed at different Ecliptic latitudes, β, to check for any latitude dependence of the beams which may result from the beam asymmetry coupled with the complex scanning pattern. The scan model was run for 365 days with the W1A and W1B Jupiter beam maps (Fig. 5.3).

[5]The approximation is in fact exact for a single beam experiment such as the *Planck* mission.

We use the same time step (integration time) as the real *W*-band data, i.e. 51.2 ms. The sky map is then constructed from the time-ordered differential data resulting from the 'one-year' mapping simulation. The map-making process described in the last section is employed with 50 iterations.

The resulting $N_{\rm obs}$ map is shown in Fig. 5.2, comparing to *WMAP* one-year data for *W*1 DA map. The beam maps for the point sources at different β are shown in the left panels of Figs. 5.4 and 5.5. For low Ecliptic latitudes $\beta = 0^\circ - 30^\circ$, the substructures seen in the Jupiter beam maps (Fig. 5.3) at ≈ -10 dB level (at $\theta \approx 20'$ from the beam boresight) are still clearly visible in the point-source beam response. The feature is aligned with the Ecliptic east-west direction on the sky due to its cross-scan orientation in the beam rest-frame and the scan pattern at low Ecliptic latitudes being nearly orthogonal to the plane. The scan strategy did very little in symmetrising the beam at these latitude ranges. As a result, outside the central 12.′6 FWHM, the beam appear rather elongated in the direction parallel to the Ecliptic plane. The situation is improved somewhat by the time we get to $\beta = 60^\circ$ and the beam appears to be completely symmetric at the pole as expected.

Another important effect, is the 'echoes' of the bright sources into rings at $\theta \approx 141^\circ$ around the sources. This is caused by the source being observed with a different orientation each time and the measured differential signal changes due to the beam asymmetry. A similar effect can also be seen if the symmetric beam is assumed but then a timing offset is introduced which effectively elongates the beam profile in the scan direction (Moss et al., 2011). In the *WMAP* pipeline, this is dealt with by incorporating a bright Galactic source mask which only allows the iterative map-making to update the pixel where the source is observed but not the paired pixel (e.g. Hinshaw et al., 2003a). Despite this effort, there are a couple of studies which detected the existence of cold rings around hot pixels in the five-year maps (Liu and Li, 2009; Aurich et al., 2010). It is possible that the observed cold rings are caused by the beam asymmetry coupled with the scan strategy and the bright sources which are left unmasked. We leave this study for future work and only focus on the source beam response here.

5.3.1 Symmetrised beam profile

Next, we deliberately introduce a timing offset between the antennas pointing and the recorded differential signal in the time-ordered data. The objective is to investigate the effect of a possible *WMAP* timing error claimed in the literature (Liu et al., 2010, 2011;

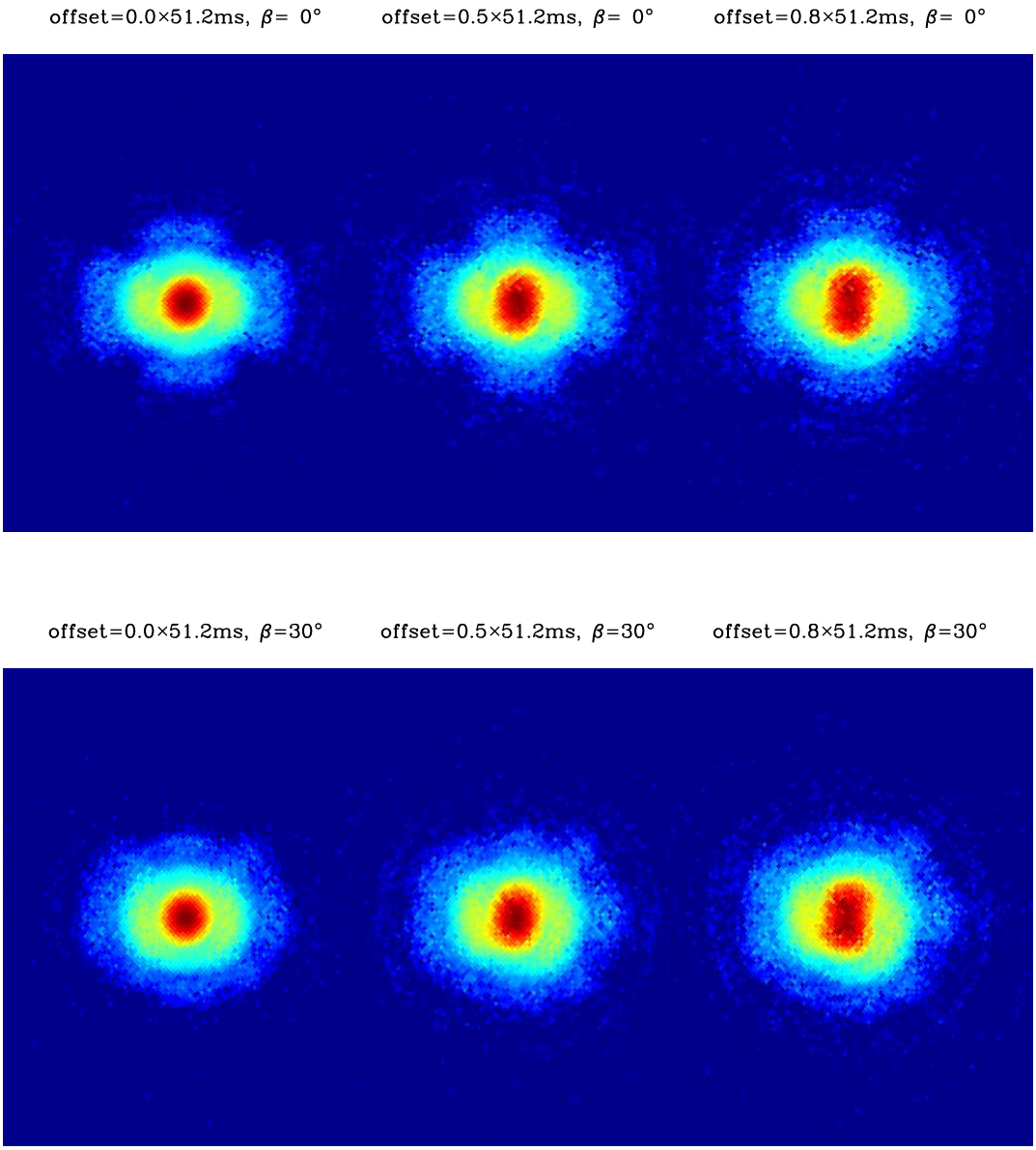

Figure 5.4: The on-sky beam maps as a function of Ecliptic latitude, β, and timing offset. The beam maps are constructed by applying the map-making process (§5.2.3) on simulated time-ordered data resulting from 365 days of scanning with Jupiter beam maps (Fig. 5.3). The y-axis is aligned to the Ecliptic north-south direction. Top to Bottom; $\beta = 0°$ and 30°. Left to Right; Offset= 0.0×, 0.5× and 0.8 × 51.2 ms. The scale of the colour range is similar to Fig. 5.3

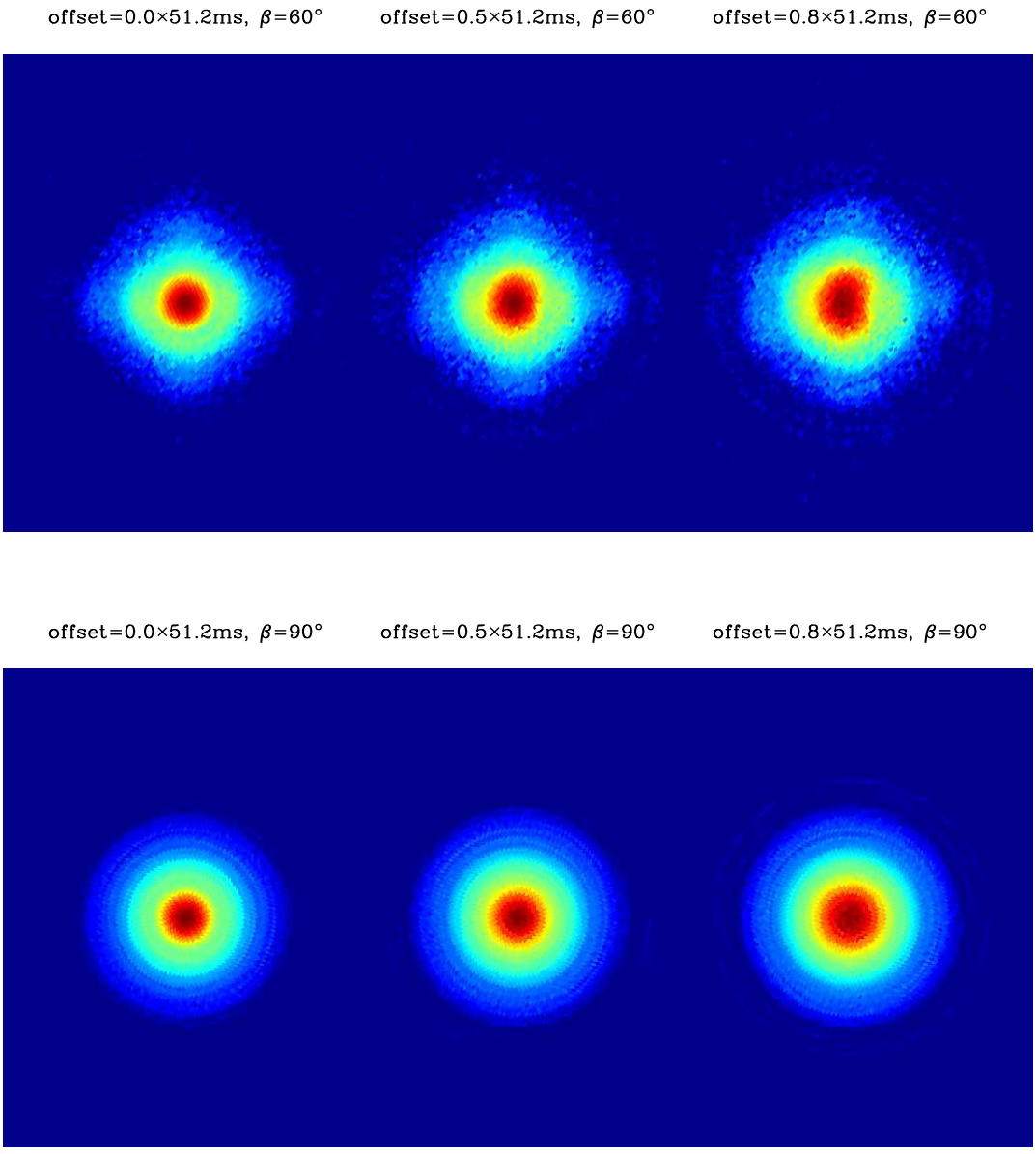

Figure 5.5: Same as Fig. 5.4. Top to Bottom; $\beta = 60°$ and $90°$. Left to Right; Offset= $0.0\times$, $0.5\times$ and 0.8×51.2 ms.

Roukema, 2010a,b) on the point-source beam profiles. In Chapter 4 (see also Sawangwit and Shanks, 2010a), we found that by stacking radio point-source the recovered beam profile for *W*-band is significantly wider than *WMAP* five-year beam profile from Jupiter map analysis. The reasons why the measured radio source profile may be more appropriate than the Jupiter profile if non-linearity in the calibration does exist (as indicated by *WMAP* source fluxes comparison with the ground-base) has also been discussed in Chapter 4. Here, we shall check whether the smearing due to the timing error could be the cause of the wider beam profile.

We generate a stream of simulated time-ordered data of a noiseless map with mock point sources (see above). The map-making is then applied to the TOD which contain an induced timing offset between the pointing and differential data. The claimed timing offset is 25.6 ms which has also been shown to be present in the time-stamp of the *WMAP* TOD 'Meta Data Table' and 'Science Data Table' (Roukema, 2010a). Here, we parametrise the timing offset as a fraction of the *W*-band integration time, i.e. $\Delta t = 0.5 \times 51.2$ ms. However, note that timing offsets of similar amplitudes are also claimed to exist in the *Q*- and *V*-band data (Liu et al., 2010, 2011) which have integration time of 102.4 and 76.8, respectively. Therefore, this timing offset is not to be confused with how one might choose to interpolate the pointing within the integration time although it is conceivable that such an error could have originated from it.

The resulting beam maps as a function of Ecliptic latitude and timing offset are plotted in Figs. 5.4 and 5.5. Within $\approx 12\farcm6$ FWHM of the beam centre, the map become elongated in the Ecliptic north-south direction for $\beta \approx 0^\circ - 30^\circ$ because the scan pattern is mostly orthogonal to the Ecliptic plane. Outside $\theta \approx 12\farcm6$ where the beam asymmetry is caused by the -10 dB substructure, the timing offset appears to improve the symmetry of the beam somewhat. For timing offset $\Delta t = 0.8 \times 51.2$ ms which corresponds to angular separation of $2.784\,(\mathrm{deg\,s^{-1}}) \cdot \big(0.8 \times 51.2\,(\mathrm{ms})\big) \cdot \sin(70\fdg5) = 6\farcm7$ which is bigger than the *W*-band beam width $\approx 12\farcm6/\sqrt{8\,\ln 2}$, we see in the right panels of Fig. 5.4 that the point sources start to appear as double peaks. For a point source at high Ecliptic latitude the beam map remains circularly symmetric as expected, although we note some strange 'squeezed' shape for the source at $\beta \approx 60^\circ$ when the timing offset is induced into the TOD.

We then estimate the symmetrised beam profiles from the beam maps. Here, the on-sky beam maps are used rather than independently combining the A- and B-side beams (Eq. 5.3, see also Page et al., 2003b). The normalised symmetrised beam profiles as a func-

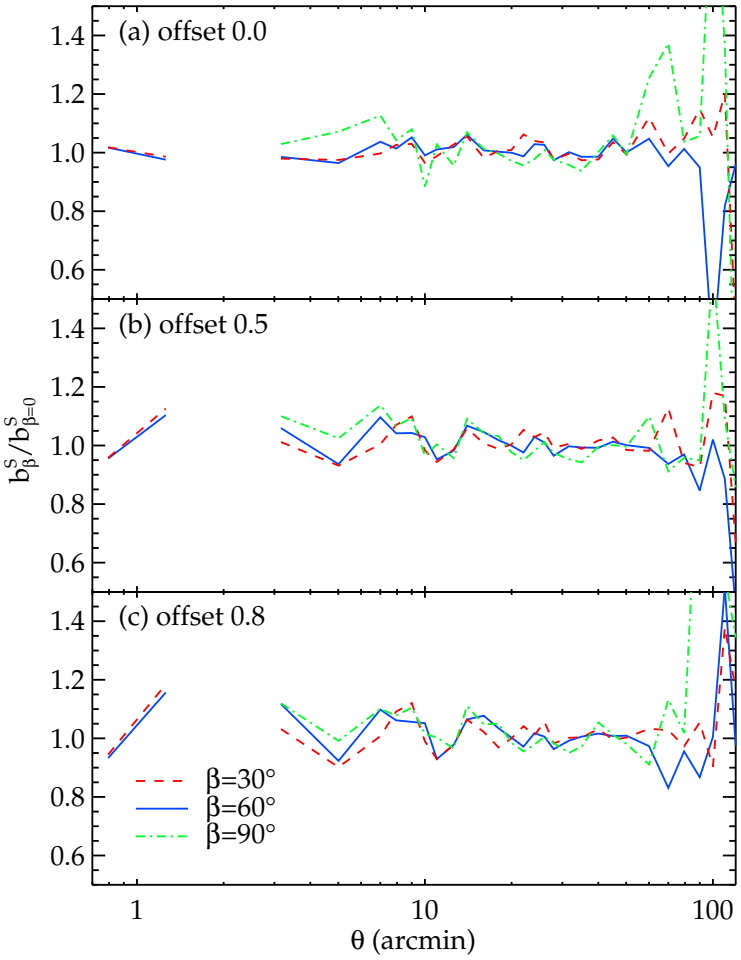

Figure 5.6: The symmetrised beam profile at Ecliptic latitude β divided by the profile at $\beta = 0°$ for different timing offsets. The gaps are due to no data contained in the bin at $\simeq 2'$ for the $\beta = 0°$ source.

tion of timing offset are plotted in Fig. 5.7 but first we check whether the symmetrised profiles show any indication of latitude dependence. Fig. 5.6 show the ratio of the symmetrised beam profile of a point source at $\beta = 30°$, $60°$ and $90°$ to that at $\beta = 0°$. The symmetrised profiles at different latitudes are in good agreement with each others even though the beam maps near Ecliptic plane are markedly different from those closer to the pole. Therefore, the assumption that the symmetrised beam profile is independent of the sky position appears to hold to a certain degree as demonstrated by this test. Even with the induced timing offsets, the assumption still appear to be a good approximation.

Fig. 5.7 show the symmetrised beam profiles for different timing offsets, comparing to the five-year *WMAP* 's official beam profile (Hill et al., 2009). The beam profile for

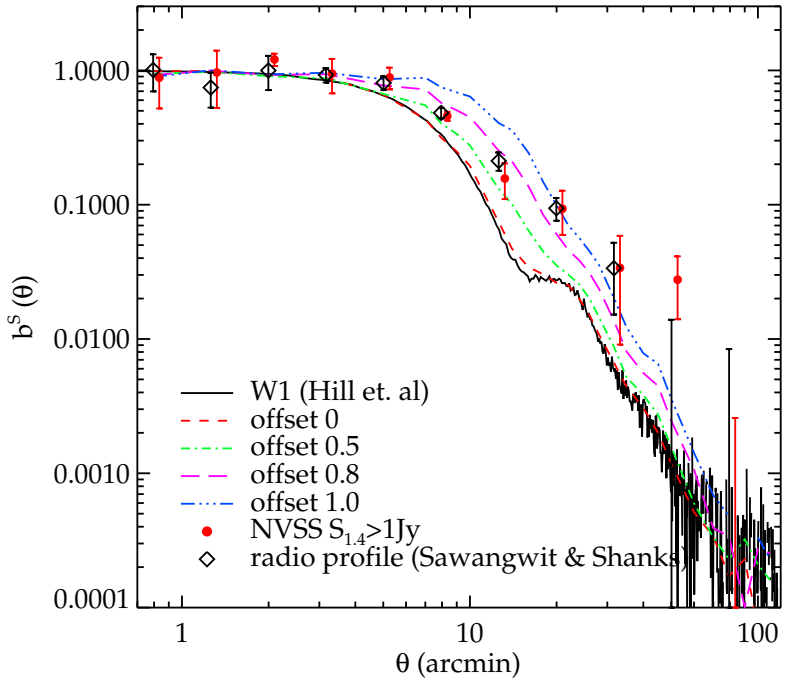

Figure 5.7: The normalised symmetrised *W*1 beam profiles determined from a noiseless map constructed from a flight-like scan pattern and Jupiter beam map. The beam profiles measured from stacking radio point sources (Chapter 4, see also Sawangwit and Shanks, 2010a) in the *WMAP*5 (diamonds) and 1.4-GHz NVSS catalogues (red solid circles) are also shown for comparison. The zero-offset beam profile is slightly wider than the five-year Jupiter beam profile (black solid line; Hill et al., 2009) is due to the pixelisation effect (as expected).

the nominal timing offset $\Delta t = 0.5 \times 51.2$ ms as claimed by Liu et al. (2010) is wider than the zero offset as expected. However, it fails to produce a profile as wide as the observed *WMAP*5 (diamonds) and NVSS (red solid circles) source profiles at $\theta \gtrsim 20'$. For $\Delta t = 0.8 \times 51.2$ ms, the beam profile are generally in better agreement with the data. Upon closer inspection, however, the profile is somewhat broader at $\theta \approx 10'$ while still slightly narrower than the data at $\theta > 20'$. As noted above that $\Delta t = 0.8 \times 51.2$ ms timing offset corresponds to $\Delta\theta = 6\farcm7$ which is larger than the *W*-band beam width $\approx 12\farcm6/\sqrt{8\ln 2}$ and in the beam map this can seen as double peaks. Here, the profile displays a slight dip at small θ as one may expect. If the offset is increased to 1.0×51.2 ms, the profile dip at small θ becomes more apparent and the resulting profile at $\theta \approx 8' - 20'$ now becomes too wide for the data.

If the timing offset in the *WMAP* TOD which is left uncorrected in the map-making process is the cause of the observed point source profile being wider than the Jupiter beam profile, the test we carried out in this section would require timing offset of $\Delta t \approx 0.8\times51.2$ ms. This is somewhat larger than the value claimed by Liu et al. (2010, 2011). We shall return to discuss this in §5.4.

5.3.2 Beam ellipticity

As we can see in Figs. 5.4 and 5.5 that the induced timing offset in the map-making process affect the ellipticity of the beam map which is confined mostly within the central $12\farcm6$ FWHM of the beam. The effect of the timing offset on the beam shape is also latitude dependent. Here, we attempt to exploit the full 2D information of the beam maps unlike in §5.3.1 where we average the beam map over its 2π azimuth angle. In other words, we shall measure the ellipticity of the beam within $\approx \theta_{\rm FWHM}$ as a function of Ecliptic latitude and use this to constrain the size of a possible timing offset if it indeed does exist.

Method

We use the *WMAP*5 point source catalogue Wright et al. (2009) and stacking the temperature maps around these sources. The selection criteria of the sources, e.g. fluxes, mask and 5-GHz cross-identification plus non-extended flag, are the same as that used in §5.3.1. In an attempt to maximise signal-to-noise, here we shall use *WMAP* seven-year temperature maps rather than the five-year maps. And we use the highest resolution *WMAP* map available, res=10, which has pixel dimension of $\approx 3\farcm5$. Note that the symmetrised beam profiles derived from *WMAP*7 temperature maps are consistent with the results presented

in Chapter 4 (see also Fig. 5.7). The sources are divided into three Ecliptic latitude bins with a width $\Delta \sin\beta$=1/3 to help keeping similar number of objects in each bin. Because of the directionality of the problem, the temperature map around each point source is re-orientated so that the Ecliptic north-south direction is aligned in the same direction before stacking. The re-orientated maps are put into a new xy coordinate gridded with $3\farcm4 \times 3\farcm4$ pixel size. The mean map, $T(x, y)$, is determined by averaging all the maps surrounding point sources in each latitude bin. The mean for each pixel is weighted by the number of observations in that pixel.

The beam ellipticity we measure is defined such that

$$\bar{\varepsilon} \equiv 1 - \frac{\sigma_b}{\sigma_a}, \tag{5.13}$$

where σ_a and σ_b are the semi-major and semi-minor axis lengths of an elliptical profile. We apply algorithms to extract the shape parameters similar to those used for source extraction in optical astronomy (e.g. SExtractor; Bertin and Arnouts, 1996, and references therein). The σ_a and σ_b are given by

$$\sigma_a^2 = \frac{\langle x^2\rangle + \langle y^2\rangle}{2} + \sqrt{\frac{\left(\langle x^2\rangle + \langle y^2\rangle\right)^2}{4} + \langle xy\rangle}, \tag{5.14}$$

and

$$\sigma_b^2 = \frac{\langle x^2\rangle + \langle y^2\rangle}{2} - \sqrt{\frac{\left(\langle x^2\rangle + \langle y^2\rangle\right)^2}{4} + \langle xy\rangle}, \tag{5.15}$$

where $\langle x^2\rangle$, $\langle y^2\rangle$, $\langle xy\rangle$ are the second-order moments and are calculated from

$$\langle x^2\rangle = \frac{\sum\limits_i T_i\, x_i^2}{\sum\limits_i T_i} - \langle x\rangle^2, \quad \langle y^2\rangle = \frac{\sum\limits_i T_i\, y_i^2}{\sum\limits_i T_i} - \langle y\rangle^2, \quad \langle xy\rangle = \frac{\sum\limits_i T_i\, x_i y_i}{\sum\limits_i T_i} - \langle x\rangle\langle y\rangle, \tag{5.16}$$

where $\langle x\rangle$ and $\langle y\rangle$ are the first-order moments given by

$$\langle x\rangle = \frac{\sum\limits_i T_i\, x_i}{\sum\limits_i T_i}, \quad \langle y\rangle = \frac{\sum\limits_i T_i\, y_i}{\sum\limits_i T_i} \tag{5.17}$$

The first moments can also be thought of as the beam map barycentre. In our calculation of the stacked maps, this always gives a value within half a pixel of the stack centre (see Fig. 5.8), i.e. the fitted source positions. To check our method, we first apply it to the high signal-to-noise Jupiter beam map (Fig 5.3). Because the observed on-sky beam

is a combination of A- and B-side beam maps, we therefore measure the beam ellipticity of the average map after correcting for the transmission imbalance similar to Eq. 5.3. The measured beam ellipticity of the *combined* A- and B-side maps is $\bar{\varepsilon} = 0.049$ if all the sums in Eqs. 5.16 and 5.17 are calculated using all the pixels within a radius of $12'$ of the beam centre. Increasing and decreasing the sum radius to $15'$ and $10'$ result in the measured ellipticities of 0.046 and 0.041, respectively. The recovered semi-major and semi-minor axis lengths are approximately $5'$.

Mitra et al. (2004) measured the eccentricity, e, of the first-year W1A Jupiter beam map to be around 0.35-0.4. The author used a couple of elliptical Gaussian fitting routines, AIPS and IRAF, and obtained consistent measurements from both software. Now, the the ellipticity is related to the eccentricity via

$$e = \sqrt{1 - \left(\frac{\sigma_b}{\sigma_a}\right)^2}, \quad \bar{\varepsilon} = 1 - \sqrt{1 - e^2} \tag{5.18}$$

This corresponds to $\bar{\varepsilon} \approx 0.063 - 0.083$ and is in good agreement with our W1A measurement of $\bar{\varepsilon} = 0.079$ using the method above. However, as their results (Fig. 9) indicate that while the measurements are quite stable at the similar semi-major axis lengths recovered by our method, measurements made at larger distances are affected by the substructure at $\approx 20'$. This would systematically increase the measured beam ellipticity and therefore bias our measurement which is intended only for the central $\theta \lesssim \theta_{\rm FWHM}$ part of the beam maps. However, as noted above that outside $\theta_{\rm FWHM}$, the timing offset acts to reduce the beam ellipticity we seek to measure. We therefore apply our beam ellipticity measurement only out to $\theta \approx 10'$.

Results and Monte Carlo simulations

We create Monte Carlo simulations to help with interpreting the beam ellipticity measurements as well as to obtain estimates of the statistical uncertainties on the measurements. The point source temperature maps are created from a power-law $N(> S)$ distribution (see Chapter 4). But instead of smoothing the map with a symmetric beam, here, we use the Jupiter beam maps and the scan model (see §5.2) to simulate *WMAP* TOD. The sky map is then re-constructed from the TOD. Note that the CMB fluctuations are not included at the scanning stage but is added after the sky map is recovered to help reduce computing time. The white noise is then added to the temperature maps. This is the same as what we called radiometer/pixel noise in Chapter 4. The noise map is con-

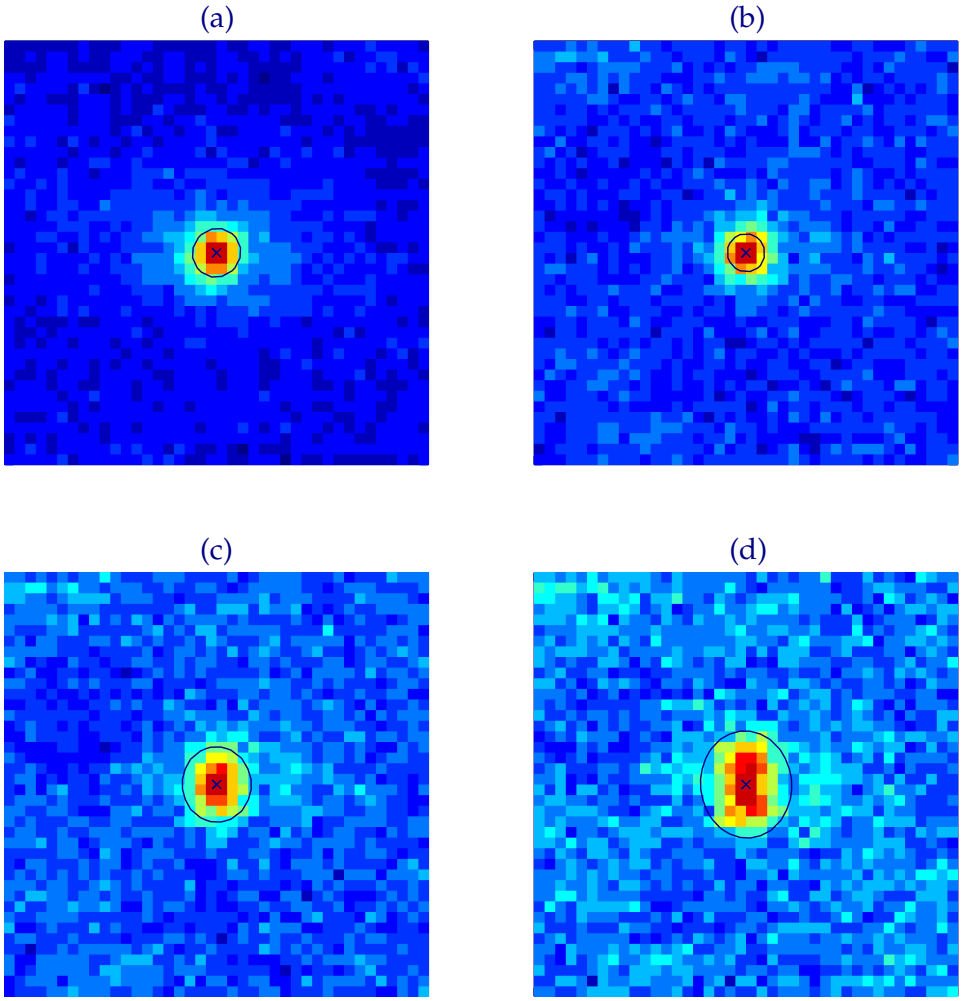

Figure 5.8: The stacked temperature maps around point sources in the real data and simulations in the lowest β bin; (a) *WMAP*5 point sources, (b) simulation with zero offset, (c) simulation with 0.5×51.2 ms offset and (d) simulation with 0.8×51.2 ms offset. The crosses indicate the first moments for each stacked map. Each map is overlaid by an ellipse constructed from its shape parameters derived from the second moments.

structed from the seven-year $N_{\rm obs}$ map and the σ_0 value (noise per pixel per observation) taken from Limon et al. (2008). We then apply the point source detection as outlined in Chapter 4. For each induced timing offset, we generate 50 Monte Carlo realisations.

The beam ellipticity analysis described above is then applied to each simulation. Fig. 5.8(b)-(d) show examples of the stacked map (for the lowest β bin) from one of the Monte Carlo realisation with different induced timing offsets. The stacked temperature map around *WMAP*5 point sources is also given in panel (a) of Fig. 5.8 for comparison. The averages and the standard deviations determined from sets of 50 simulations are

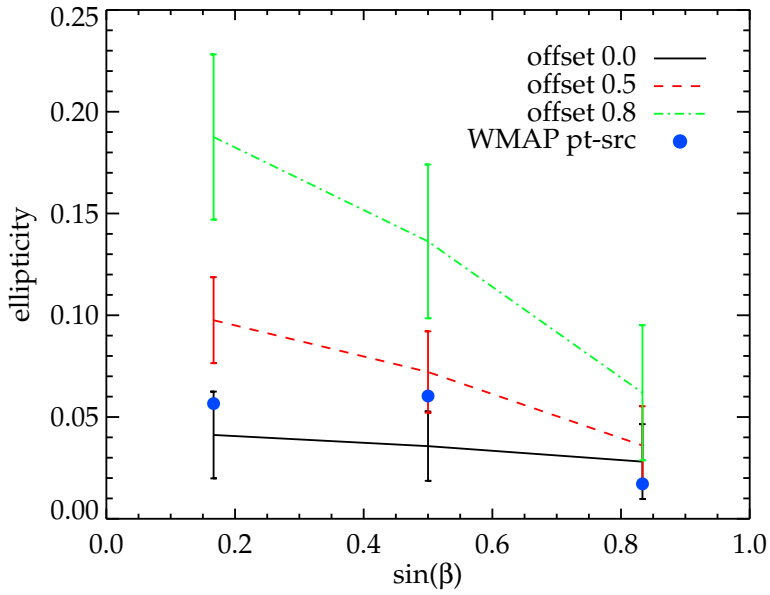

Figure 5.9: The beam ellipticity measurements as a function of Ecliptic latitude and timing offset. For each timing offset, the expected values are determined from 50 Monte Carlo simulations. The beam ellipticity measured from stacking *WMAP*5 point sources in Ecliptic latitude bins are shown as the blue solid circles.

plotted as the coloured lines and their error bars in Fig. 5.9. The simulation results show a decreasing trend of the beam ellipticity as a function of Ecliptic latitude as expected. As a result, the measurements in the lowest β bin have the most discriminating power in terms of constraining the size of timing offset. For $\Delta t = 0.8 \times 51.2$ ms, the statistical errors increase because of the rise in the uncertainty in the recovered positions of the point sources. The ellipticity measured in the lowest β bin and zero-offset is consistent with the rest-frame beam map, $\bar{\varepsilon} \approx 0.04 - 0.05$, presented above as expected.

The beam ellipticities measured from stacking *WMAP*5 point sources are consistent within 1σ statistical uncertainty ($\chi^2 = 2.96$ over 3 d.o.f) of the zero timing offset. However, the $\Delta t = 0.5 \times 51.2$ ms results from the simulations indicate that, using only the lowest β bin, it can be *marginally* ruled out at 1.9σ significance level. Using all three bins, $\chi^2 = 5.07$ and the probability of acceptance $P(< \chi^2) = 0.17$. But as we see in the last section that its symmetrised beam profile is not wide enough to explain the point source measurements. For $\Delta t = 0.8 \times 51.2$ ms case which is preferred by the symmetrised beam profile test, the beam ellipticity is too large for the measured value with $\chi^2 = 16.3$ over 3 d.o.f and can be ruled out at 99.9 per cent significance level.

5.4 Discussion and conclusions

We have used both the symmetrised profiles and the full 2D information of the beam maps measured from stacking the radio point sources to investigate the effect of a possible timing offset in the *WMAP* time-ordered data. The analyses we performed are in the contexts of testing if the wider beam profiles we measured in Chapter 4 can be explained by the presence of a timing offset which may be left uncorrected in the map-making process. The claimed timing offset $\Delta t = 0.5 \times 51.2$ ms (Liu et al., 2010, 2011; Roukema, 2010b) would widen the observed beam profile but as our simulation which incorporates *WMAP* scan strategy and the realistic Jupiter beam map shows that the resulting symmetrised beam profile is still not wide enough. If we then assume that the timing offset is real and look for a size of Δt required to explain the point source profile, our measurements indicate that the timing offset of $\Delta t = 0.8 \times 51.2$ ms would be needed, still not too far off from the claimed value in the literature.

The notable feature observed in the on-sky beam maps with the induced timing offset is the elongation of the point source temperature map along the scanning direction. Although the *WMAP* scan strategy is designed to observe a sky pixel from all azimuth angles, the scan pattern and its direction are rather sparse and confined mostly in the orthogonal direction of the Ecliptic plane at low Ecliptic latitudes (§5.2). This couples with a timing offset means that the elongation effect is expected to be most severe at low β and should be observable by stacking the temperature maps around point sources at low β. We exploited this and performed an analysis which shows that the data are consistent with a zero-offset case, although 25.6 ms timing offset cannot be ruled out at high significance level using our measurements. However, the preferred timing offset, $\Delta t = 0.8 \times 51.2$ ms, suggested by the symmetrised beam profile test, is ruled out at 99.9 per cent significance level.

Our results support the finding of Roukema (2010a) who despite pointing out the existence of an offset in the starting time of the meta data and science data tables in the time-ordered data has found that the timing adopted by the *WMAP* team (zero timing offset as used here) is preferred at 4.6σ significance, comparing to the 25.6 ms timing offset. The author indirectly measured the image sharpness of the sky maps using percentiles of the pixels temperature above certain threshold. Therefore, it seems that the timing offset may be ruled out, at least in the map-making process. Liu et al. (2011) and Roukema (2010b) have independently confirmed that there may in fact be a timing error in the

calibration process which could have been caused by the starting time offset mentioned above. However, it is difficult to imagine how any timing error in the calibration process could effect a point source spatially and act to widen its profile.

Although it is possible that if any pointing error (which is not associated with timing offset nor scan direction) does exist, this may act to blur out any elongation expected to result from the timing offset. Such an error would have to be of similar size to that considered here. However, according to Hinshaw et al. (2009) *WMAP* team expects only $\approx 1'$ temperature-dependent pointing offset between the probe's star tracker and the beam boresight. This is not big enough to cause the smearing of the possible beam elongation observed here or indeed to widen the point source profile at the level seen in the data. Therefore, we conclude that the recently claimed timing offset in the TOD is not the cause of the observed wider than expected beam profile presented in Chapter 4.

Chapter 6 | *Conclusions*

6.1 Summary of the main results

In this thesis, we confronted the current standard cosmological paradigm with observations regraded as the main pillars of modern cosmology, namely the large-scale structure and the cosmic microwave background including their cross-correlation. In Chapter 1, we reviewed the theoretical framework, assumptions and observational evidence which contribute to the rise of the ΛCDM model and highlighted its successes and problems. The need to continually checking the model was also emphasised.

In Chapter 2, we measured the angular correlation functions of LRGs at three average redshifts and used them to study the clustering evolution. The shape of the angular correlation functions in the linear regime is consistent with a 'high-peaks' bias model and linear theory within the ΛCDM framework. The departure from the conventional power-law can be described by the Halo Occupation Distribution framework where a strong effect is expected in a more luminous ($L > L_*$) and high-z galaxy sample (Watson et al., 2011). Using the estimated linear bias factors in conjunction with the dark matter halo bias (Sheth et al., 2001; Tinker et al., 2005) and halo merger formalism (Lacey and Cole, 1993), the haloes which typically host $\approx 2L_* - 3L_*$ LRG at $z \lesssim 0.7$ can be regarded as the descendants of haloes with mass $\sim 1 \times 10^{13}\ h^{-1}\, M_\odot$ at $z = 1$. In the CDM model, the rapid growth of these haloes and therefore of the LRG are expected. This is very different to the long-lived or no-evolution model which may be suggested by the slow evolution observed in the LRG luminosity function (e.g. Wake et al., 2006; Brown et al., 2007). However, in order to explain the small-scale clustering evolution, the LRGs must be allowed to merge at $\sim 2 - 3$ per cent per Gyr. These also have to be 'dry' mergers to explain the little stellar masses growth observed in the LRGs since $z = 1$.

We then searched for the BAO peak in the LRG angular correlation function. Our result shows good agreement with the SDSS LRG result of Eisenstein et al. (2005) but we find an apparent excess clustering signal beyond the BAO scale. Angular power spectrum analyses of similar LRG samples also detect a similar apparent large-scale clustering

excess but more data is required to check for this feature in independent galaxy datasets. Certainly, if the ΛCDM model were correct then we would have to conclude that this excess was caused by systematics at the level of $\Delta w \approx 0.001 - 0.0015$ in the photometric AAOmega-LRG sample. We then investigated a possible improvement in detecting a BAO peak in $w(\theta)$ of photometric LRG samples at $z \sim 1$ where we argued that for photo-z error of $\approx 0.03 - 0.05$ (expected in upcoming photometric surveys) photo-z+$w(\theta)$ may provide a competitive route to the BAO detection, provided that systematic errors can be kept under control.

In Chapter 3, we cross-correlated various LSS tracers with the CMB temperature maps from five-year observations of the *WMAP* satellite to look for the ISW effect. We found that the new LRG sample at $z \approx 0.7$ shows very little positive evidence for the ISW effect. Indeed, the cross-correlation is negative out to $\approx 1^\circ$. The standard ΛCDM model is rejected at $\approx 2.2\sigma$ significance by the new LRG data. We then analysed the previous samples at $z \approx 0.35$ and $z \approx 0.55$. As found by other authors, these results appear consistent with the standard ISW model, although many of these results appear to require higher Ω_Λ than other observations and the statistical significance remains marginal. Taking the $z \approx 0.35$ and $z \approx 0.55$ LRG results in combination with the new $z \approx 0.7$ sample, the overall result is now more consistent with a null detection than with the standard ΛCDM model prediction.

We then performed a new test on the robustness of the LRG ISW detections at $z \approx 0.35$ and $z \approx 0.55$. We made 8 rotations through 360° of the CMB maps with respect to the LRG samples around the galactic pole. We find that in both cases there are stronger effects at angles other than zero. This implies that the $z \approx 0.35$ and $z \approx 0.55$ ISW detections may still be subject to systematic errors which combined with the known sizeable statistical errors may leave the $z \approx 0.35$ and $z \approx 0.55$ ISW detections looking unreliable. We have further made the rotation test on several other samples where ISW detections have been claimed and find that they also show peaks when rotated. We conclude that in the samples we have tested the ISW effect may be absent and we argue that this result may not be in contradiction with previous results.

In Chapter 4, we made an independent estimation of the CMB temperature angular power spectrum using the publicly available *WMAP* data and C_ℓ computation code. We showed how sensitive the WMAP power spectra are to the form of the instrumental beam. Even though the beam core width corresponds to wavenumber $l \approx 1800$, the form of the beam still significantly affects the WMAP results even at $l \approx 200$ which is the scale of

the first acoustic peak. The difference between the beam convolved C_l and the final C_l is $\approx 70\%$ at the scale of the first peak, rising to $\approx 400\%$ at the scale of the second.

New estimates of the Q, $V$and W-band beam profiles are then presented, based on a stacking analysis of the *WMAP*5 radio source catalogue and temperature maps where we demonstrate its robustness through Monte Carlo simulations. The radio sources show a significantly $(3-4\sigma)$ broader beam profile on scales of $10' - 30'$ than that found by the *WMAP* team whose beam analysis is based on measurements of Jupiter. Beyond these scales the beam profiles from the radio sources are too noisy to give useful information. Furthermore, we find tentative evidence for a non-linear relation between *WMAP* and ATCA/IRAM 95 GHz source fluxes. We discuss whether the wide beam profiles could be caused either by radio source extension or clustering and find that neither explanation is likely. The reasons for the difference between the radio source and the Jupiter beam profiles are therefore still unclear. If the radio source profiles were then used to define the WMAP beam, there could be a significant change in the amplitude and position of even the first acoustic peak. It is therefore important to identify the reasons for the differences between these two beam profile estimates.

In Chapter 5, we developed a method to construct the on-sky beam maps for a differential CMB experiment such as *WMAP*. As a demonstration the *WMAP* scan strategy and the realistic beam maps as measured by the *WMAP* team were used to produce the on-sky beam map for the $W1$ DA. We showed that the azimuthally symmetrised beam profiles are independent of the Ecliptic latitude even though the 2D maps appear very different. We then used this to investigate the timing offset in the *WMAP* time-ordered data recently claimed in the literature. The claimed timing offset of $\Delta t = 0.5 \times 51.2$ ms cannot produced the radio source beam profile as wide as that observed in Chapter 4 and $\Delta t = 0.8 \times 51.2$ ms may better describe our results. However, using the full 2D information of the beam maps via the beam ellipticity, the offset $\Delta t = 0.8 \times 51.2$ ms can be ruled out at 99.9 per cent significance level while $\Delta t = 0.5 \times 51.2$ ms is only marginally ruled out. We argued that the timing offset cannot explain the wider than expected beam profile observed in the stacking of radio sources we performed in Chapter 4. The marginally rejection of the timing offset $\Delta t = 0.5 \times 51.2$ ms in the map-making process is also consistent with Roukema (2010a). Although the author found a much higher significance of rejection by indirectly measuring the sharpness of the temperature maps.

6.2 Final Conclusions and Future Prospects

The accelerated expansion and the inferred presence of dark energy is no doubt the most enigmatic discovery of modern cosmology. Our current cosmological, flat ΛCDM, model, though apparently supported by plethora of observations, is based on two pieces of undiscovered physics which are believed to contribute 95 per cent of the energy density of the Universe. So far none of the proposed dark energy models is completely successful and convincing enough (Sahni, 2004; Shanks, 2005). Many dark energy experiments are now being designed with a common goal to achieve an unprecedented level of precision measurement on the equation of state w, employing variety of techniques and cosmological probes such as weak lensing, BAO, cluster abundance and SNIa (see e.g. Dark Energy Task Force report, Albrecht et al. 2006, for a review on strengths, weaknesses and constraining power of each method). However, the converging of astronomy community to measure dark energy ever more precisely is not without its criticism (White, 2007). More importantly, the attention should also be paid to testing our gravity theory and not just the equation of state as demonstrated by the redshift-space distortion study of Guzzo et al. (2008).

The lack of direct detection of dark matter particles and satisfactory explanation for cosmological constant problems means that one should remain sceptical. This thesis has confronted the standard cosmological model using a few of the tools usually employed in modern cosmology. We particularly found that the shape of LRG angular correlation function at large scales is consistent with the ΛCDM prediction in the 'high-peaks' bias and linear theory frameworks. At the largest scales, we found an excess clustering which might be evidence for some new physics or non-Gaussianity beyond the standard inflationary ΛCDM model if confirmed in independent datasets. Although a systematic effect is also a possibility based on the tests we performed. If this is the case then our attempt to search for the BAO peak in the angular correlation function may be prohibited by the level of systematic effects. LRG surveys form the ideal BAO route to study dark energy at $z \lesssim 1$ owing to their high bias and intrinsically luminous nature. Their homogeneous SEDs also provides a further argument for using LRGs in the photo-z BAO study in ongoing and upcoming photometric surveys such as Pan-STARRs, DES, VST ATLAS and LSST. In fact, the ongoing SDSS-III's Baryon Oscillation Spectroscopic Survey (BOSS; Eisenstein et al. 2011) is targeting $z \approx 0.55$ LRG's as one of their LSS tracers to measure the BAO distance scale and dark energy equation-of-state at great precision.

An LRG sample also provides a good LSS tracer for detecting the ISW effect by cross-correlating it with the CMB. Our new photometric LRG sample at $\bar{z} \approx 0.7$ showed zero correlation with the *WMAP*5 maps despite the fact this is the redshift where the ISW signal is expected to be maximised. We further showed that the previous detections of the ISW effect may not be as significant as previously claimed. The absence of the ISW effect would be evidence against any model that produced accelerated expansion. In a spatially flat Universe, this would therefore argue against a significant role of a cosmological constant or dark energy in the Universe and that the matter density is equal to the critical density. It is therefore important to repeat similar LRG measurements in the southern sky and with a larger sky coverage. The surveys mentioned above will also provide new opportunities to do just that.

On the CMB front, the much anticipated *Planck* mission will soon shed light on some of the controversial issues raised in the literature and this thesis regarding the *WMAP* results. This also includes the possible induced quadrupole component due to the unfortunate coupling of the dipole with the *WMAP* scan strategy (Liu et al., 2010, 2011; Roukema, 2010b; Moss et al., 2011). In fact, the *Planck* Early Release Compact Source Catalog is now being used to check (Whitbourn, Shanks & Sawangwit, in prep.) the possible non-linearity in the *WMAP* radio source fluxes found here as well as the *WMAP* SZ anomaly found by Myers et al. (2004) and Bielby and Shanks (2007). Although it is true that the *WMAP* results agree remarkably well with ground-based and balloon-borne CMB experiments, the aforementioned issues still demand explanations. All these issues aside, the *Planck* mission with its much improved sensitivity and impressive frequency coverage will provide a valuable source of information for cosmology and astrophysics. The cosmological parameters will no doubt be measured with even greater precision. It will also provide further informations regarding the inflationary models of the early Universe.

Finally, the Square Kilometre Array (SKA) will provide a great opportunity to bridge the observation gap between the reionisation ($z \sim 6$) and recombination ($z \sim 1000$) epochs by making a map of neutral hydrogen via the HI 21-cm emission line. The tomography of redshifted 21-cm emission line will revolutionise our understanding of the Universe at this pivotal epoch when galaxy formation started. The quest for a better picture of our Cosmos is set to remain lively and exciting for, at least, decades to come.

Appendix A

LRG angular correlation functions and their covariance matrices

Here, we tabulate the angular correlation functions (Table A.1) measured from the three photometric LRG samples studied in Chapter 2. The full covariance matrices in the form of correlation coefficients are shown in Fig. A.1.

Table A.1: The measured angular correlation functions for the SDSS, 2SLAQ and AAΩ-LRG and their 1σ JK errors.

$\theta(')$	SDSS	2SLAQ	AAΩ
0.100	26.78 ± 2.37	9.85 ± 0.39	6.27 ± 0.24
0.150	15.96 ± 1.47	7.40 ± 0.14	4.65 ± 0.10
0.225	11.09 ± 0.56	4.54 ± 0.085	2.95 ± 0.057
0.337	6.10 ± 0.33	2.95 ± 0.050	1.86 ± 0.033
0.506	3.93 ± 0.19	1.83 ± 0.026	1.11 ± 0.016
0.759	2.04 ± 0.090	1.09 ± 0.020	0.65 ± 0.014
1.139	1.55 ± 0.061	0.68 ± 0.011	0.419 ± 0.0095
1.708	1.00 ± 0.038	0.416 ± 0.0057	0.282 ± 0.0059
2.562	0.56 ± 0.025	0.285 ± 0.0061	0.213 ± 0.0036
3.844	0.31 ± 0.019	0.199 ± 0.0038	0.151 ± 0.0023
5.766	0.22 ± 0.012	0.152 ± 0.0026	0.112 ± 0.0020
8.649	0.171 ± 0.0081	0.113 ± 0.0019	0.083 ± 0.0013
12.97	0.118 ± 0.0053	0.078 ± 0.0018	0.057 ± 0.0011

Continued on next page

Table A.1 – continued from previous page

$\theta(')$	SDSS	2SLAQ	AAΩ
19.46	0.091 ± 0.0055	0.055 ± 0.0012	0.0405 ± 0.00077
29.19	0.060 ± 0.0041	0.038 ± 0.0011	0.0264 ± 0.00062
43.78	0.038 ± 0.0031	0.0226 ± 0.0009	0.0157 ± 0.00060
60.00	0.028 ± 0.0023	0.0144 ± 0.0008	0.0093 ± 0.00053
80.00	0.018 ± 0.0020	0.0086 ± 0.00076	0.0056 ± 0.00051
100.0	0.014 ± 0.0019	0.0054 ± 0.00067	0.0040 ± 0.00045
120.0	0.011 ± 0.0017	0.0034 ± 0.00060	0.0039 ± 0.00036
140.0	0.0071 ± 0.0018	0.0024 ± 0.00061	0.0035 ± 0.00027
160.0	0.0063 ± 0.0014	0.0019 ± 0.00064	0.0029 ± 0.00032
180.0	0.0045 ± 0.0013	0.0021 ± 0.00065	0.0024 ± 0.00039
200.0	0.0026 ± 0.0014	0.0020 ± 0.00060	0.0020 ± 0.00039
220.0	0.0020 ± 0.0014	0.0022 ± 0.00062	0.0011 ± 0.00035
240.0	0.0014 ± 0.0013	0.0019 ± 0.00058	0.0014 ± 0.00039
260.0	0.0014 ± 0.0015	0.0015 ± 0.00045	0.0015 ± 0.00040
280.0	0.0017 ± 0.0011	0.0013 ± 0.00044	0.0018 ± 0.00032
300.0	0.0020 ± 0.00077	0.0013 ± 0.00045	0.0021 ± 0.00038
320.0	0.0016 ± 0.00091	0.0015 ± 0.00045	0.0021 ± 0.00043
340.0	0.0032 ± 0.0010	0.0013 ± 0.00053	0.0019 ± 0.00048
360.0	0.0025 ± 0.0010	0.0011 ± 0.00047	0.0016 ± 0.00048
380.0	0.0023 ± 0.0011	0.0012 ± 0.00045	0.0016 ± 0.00045
400.0	0.0025 ± 0.0010	0.0010 ± 0.00045	0.0013 ± 0.00041
420.0	0.0017 ± 0.0011	0.00054 ± 0.00045	0.0007 ± 0.00041
440.0	0.0020 ± 0.0012	0.00064 ± 0.00042	0.0006 ± 0.00038
460.0	0.0003 ± 0.0012	0.00017 ± 0.00045	0.0008 ± 0.00038
480.0	0.0006 ± 0.0014	0.00002 ± 0.00047	0.0005 ± 0.00039
500.0	-0.0001 ± 0.0012	0.00018 ± 0.00051	0.0005 ± 0.00044

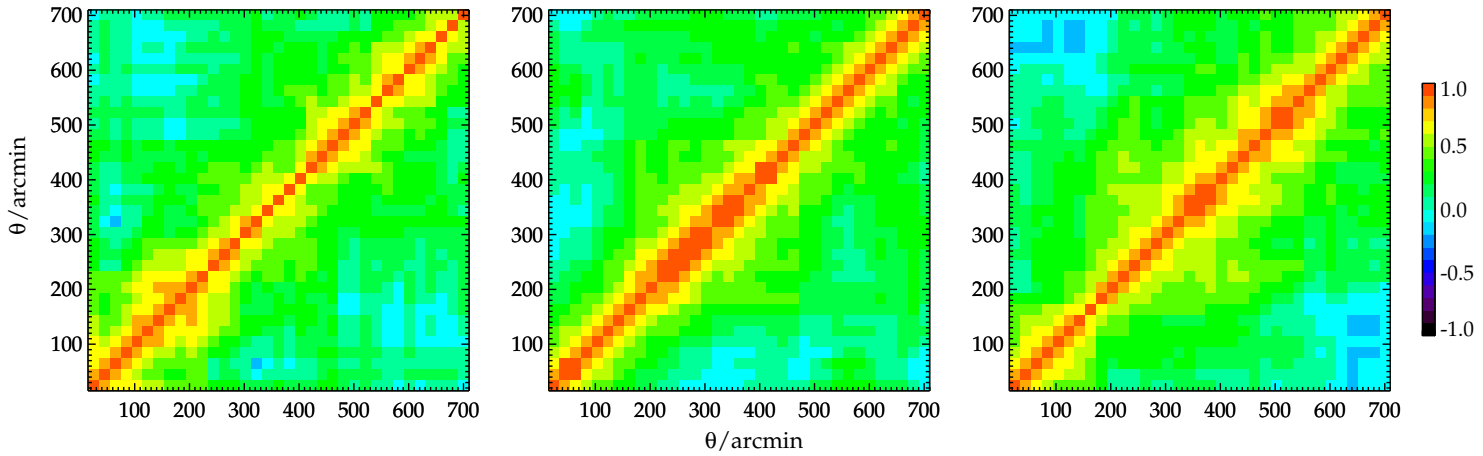

Figure A.1: The correlation coefficients, $\mathbf{r}_{ij}$, out to very large angular separations. These are derived from the covariance matrices (Eq. 2.13) via 96 jackknife re-sampling fields. Three panels show $\mathbf{r}_{ij}$ for SDSS, 2SLAQ and AAΩ -LRG samples from left to right.

Appendix B

Constructing WMAP line-of-sight rotation matrix

The *WMAP* beam line-of-sight (LOS) for each side (A and B) of a 'Differencing Assembly' (DA) is given in the spacecraft (SC) coordinates[1]. The beam pointing on the sky as a function of time can be determined by incorporating the survey scan strategy (Chapter 5, Fig. 6.1) with the LOS unit vector ($\hat{\mathbf{n}}_{\rm SC}$). Here, we construct a time-dependent rotation matrix, $\mathbf{R}(t)$, for the purpose of transforming the beam LOS given in the SC coordinates into the sky (Ecliptic) coordinates.

The coordinate transformation is done in the following four steps.

(I) The probe spins around its axis of symmetry (-Z axis in Fig. 6.1) which is pointing in the anti-Sun direction. A new coordinate (x', y', z') is constructed from the SC coordinate (x, y, z) so that the $z'-$axis is aligned with the $-z$ direction, $\hat{\mathbf{n}}' = \mathbf{R}_1 \hat{\mathbf{n}}_{\rm SC}$;

$$\begin{pmatrix} n'_x \\ n'_y \\ n'_z \end{pmatrix} = \begin{pmatrix} -1 & 0 & 0 \\ 0 & 1 & 0 \\ 0 & 0 & -1 \end{pmatrix} \begin{pmatrix} n_x \\ n_y \\ n_z \end{pmatrix} \tag{B.1}$$

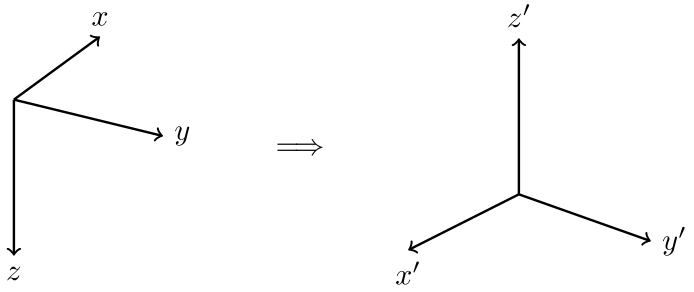

Figure B.1: Step 1 in the coordinate transformations.

[1]See e.g. Table 7 of Hinshaw et al. (2003a), and the full precision unit vectors are available in the released time-ordered data (Limon et al., 2008)

(II) The (x', y', z') coordinate spins around its z'-axis with a spin rate $\dot{\psi}$. In a new stationery coordinate (x'', y'', z''), $\hat{\mathbf{n}}'' = \mathbf{R}_2(t)\hat{\mathbf{n}}'$;

$$\begin{pmatrix} n''_x \\ n''_y \\ n''_z \end{pmatrix} = \begin{pmatrix} \cos\psi(t) & -\sin\psi(t) & 0 \\ \sin\psi(t) & \cos\psi(t) & 0 \\ 0 & 0 & 1 \end{pmatrix} \begin{pmatrix} n'_x \\ n'_y \\ n'_z \end{pmatrix}, \tag{B.2}$$

where $\psi(t) = \dot{\psi}t + \psi_0$, $\dot{\psi} = 2.784\ \mathrm{deg\,s^{-1}}$ and ψ_0 is the initial value to be determined.

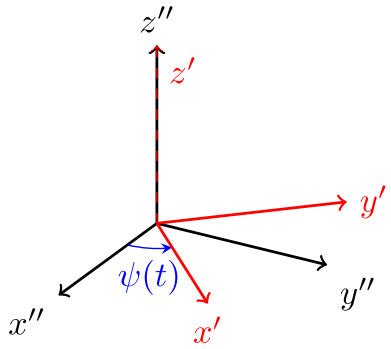

Figure B.2: Step 2 in the coordinate transformations.

(III) The spin axis precesses around the anti-Sun direction (z'''-axis) at an angle $\vartheta_{\mathrm{P}} = 22.^{\circ}5$ and precession rate $\dot{\phi}$. In (x''', y''', z''') coordinate, the LOS unit vector is given by $\hat{\mathbf{n}}''' = \mathbf{R}_3(t)\hat{\mathbf{n}}''$;

$$\begin{pmatrix} n'''_x \\ n'''_y \\ n'''_z \end{pmatrix} = \begin{pmatrix} \cos\vartheta_{\mathrm{P}}\cos\phi(t) & -\sin\phi(t) & \sin\vartheta_{\mathrm{P}}\cos\phi(t) \\ \cos\vartheta_{\mathrm{P}}\sin\phi(t) & \cos\phi(t) & \sin\vartheta_{\mathrm{P}}\sin\phi(t) \\ -\sin\vartheta_{\mathrm{P}} & 0 & \cos\vartheta_{\mathrm{P}} \end{pmatrix} \begin{pmatrix} n''_x \\ n''_y \\ n''_z \end{pmatrix}, \tag{B.3}$$

where $\phi(t) = \dot{\phi}t + \phi_0$, $\dot{\phi} = -0.1\ \mathrm{deg\,s^{-1}}$ and ϕ_0 is the initial value to be determined.

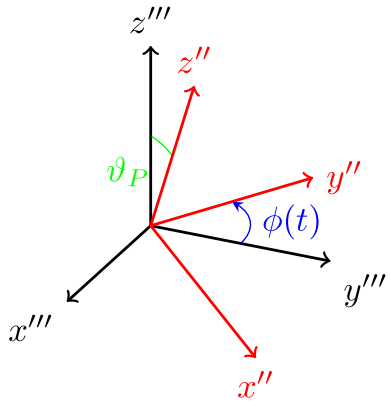

Figure B.3: Step 3 in the coordinate transformations.

(IV) Finally, the (x''', y''', z''') coordinate can be transformed into the Ecliptic coordinate (EC), here denoted by (X, Y, Z). The precession axis (z''') is rotated onto the Ecliptic plane (XY plane). Any possible misalignment with the plane is parametrised by an angle β_0, to be determined later. The (x''', y''', z''') coordinate rotates around the Z-axis (pointing in the North Ecliptic pole direction) as the *WMAP* (and Earth) orbits around the Sun at an orbiting speed $\dot{\lambda}$. Here, we assume $\dot{\lambda}$ is approximately constant along the entire orbit. In the EC coordinate, the LOS unit vector becomes $\hat{\mathbf{n}}_{\rm EC} = \mathbf{R}_4(t)\hat{\mathbf{n}}'''$;

$$\begin{pmatrix} n_X \\ n_Y \\ n_Z \end{pmatrix} = \begin{pmatrix} -\sin\beta_0\cos\lambda(t) & \sin\lambda(t) & \cos\beta_0\cos\lambda(t) \\ -\sin\beta_0\sin\lambda(t) & -\cos\lambda(t) & \cos\beta_0\sin\lambda(t) \\ \cos\beta_0 & 0 & \sin\beta_0 \end{pmatrix} \begin{pmatrix} n'''_x \\ n'''_y \\ n'''_z \end{pmatrix}, \tag{B.4}$$

where $\lambda(t) = \dot{\lambda}t + \lambda_0$ and λ_0 is the initial value to be determined. The orbiting speed is calculated for a circular orbit at $a = 1.01$ AU, i.e. period=1.015 yr. Using *WMAP* Quaternions in a triangulation, the β_0 is determined to be very close to zero, $\approx -0.^{\circ}04$. The similar technique can also be used to determine the scan starting point, ψ_0, ϕ_0 and λ_0, using Quaternions available in the *WMAP* TOD.

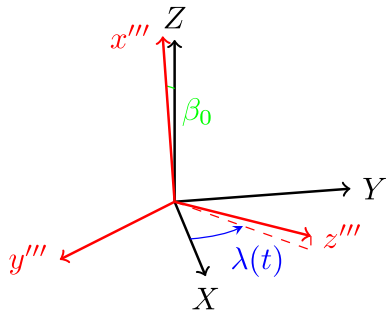

Figure B.4: Step 4 in the coordinate transformations.

The *WMAP* beam boresight on the sky at any given time can be determined for either A- or B-side of any DA using its LOS unit vector extracted from the LOS table of the released time-ordered data, $\hat{\mathbf{n}}_{\rm EC} = \mathbf{R}(t)\hat{\mathbf{n}}_{\rm SC}$. Putting all the steps outlined above together,

$$\hat{\mathbf{n}}_{\rm EC} = \mathbf{R}_4(t)\mathbf{R}_3(t)\mathbf{R}_2(t)\mathbf{R}_1\hat{\mathbf{n}}_{\rm SC}, \tag{B.5}$$

i.e. $\mathbf{R}(t) = \mathbf{R}_4(t)\mathbf{R}_3(t)\mathbf{R}_2(t)\mathbf{R}_1$. For the reverse transformation, $\hat{\mathbf{n}}_{\rm SC} = \mathbf{R}^{-1}\hat{\mathbf{n}}_{\rm EC} = \mathbf{R}^T\hat{\mathbf{n}}_{\rm EC}$, where the last equality applies because rotation matrix is orthogonal.

Bibliography

K. N. Abazajian et al. The Seventh Data Release of the Sloan Digital Sky Survey. *ApJS*, 182:543–558, June 2009.

F. B. Abdalla, M. Banerji, O. Lahav, and V. Rashkov. A Comparison of Six Photometric Redshift Methods Applied to 1.5 Million Luminous Red Galaxies. *arXiv:0812.3831*, Dec 2008.

P. A. R. Ade, N. Aghanim, M. Arnaud, M. Ashdown, J. Aumont, C. Baccigalupi, A. Balbi, A. J. Banday, R. B. Barreiro, and et al. Planck Early Results: The Early Release Compact Source Catalog. *arXiv:1101.2041*, Jan 2011.

J. K. Adelman-McCarthy et al. The Fourth Data Release of the Sloan Digital Sky Survey. *ApJS*, 162:38–48, Jan 2006.

J. K. Adelman-McCarthy et al. The Fifth Data Release of the Sloan Digital Sky Survey. *ApJS*, May 2007.

N. Afshordi, Y.-S. Loh, and M. A. Strauss. Cross-correlation of the cosmic microwave background with the 2MASS galaxy survey: Signatures of dark energy, hot gas, and point sources. *Phys. Rev. D*, 69(8):083524–+, Apr 2004.

A. Albrecht, G. Bernstein, R. Cahn, W. L. Freedman, J. Hewitt, W. Hu, J. Huth, M. Kamionkowski, E. W. Kolb, L. Knox, J. C. Mather, S. Staggs, and N. B. Suntzeff. Report of the Dark Energy Task Force. *arXiv:0609591*, Sept 2006.

R. A. Alpher and R. Herman. Evolution of the Universe. *Nature*, 162:774–775, Nov 1948.

R. E. Angulo, C. M. Baugh, C. S. Frenk, and C. G. Lacey. The detectability of baryonic acoustic oscillations in future galaxy surveys. *MNRAS*, 383:755–776, Jan 2008.

E. Aprile et al. First Dark Matter Results from the XENON100 Experiment. *Physical Review Letters*, 105(13):131302–+, Sept 2010.

M. A. J. Ashdown et al. Making maps from Planck LFI 30 GHz data with asymmetric beams and cooler noise. *A&A*, 493:753–783, Jan 2009.

R. Aurich, S. Lustig, and F. Steiner. Hot pixel contamination in the CMB correlation function? *Classical and Quantum Gravity*, 27(9):095009–+, May 2010.

M. Banerji, F. B. Abdalla, O. Lahav, and H. Lin. Photometric redshifts for the Dark Energy Survey and VISTA and implications for large-scale structure. *MNRAS*, 386: 1219–1233, May 2008.

C. Barnes et al. First-Year Wilkinson Microwave Anisotropy Probe (WMAP) Observations: Galactic Signal Contamination from Sidelobe Pickup. *ApJS*, 148:51–62, Sept 2003.

C. M. Baugh. A primer on hierarchical galaxy formation: the semi-analytical approach. *Reports on Progress in Physics*, 69:3101–3156, Dec 2006.

C. M. Baugh and G. Efstathiou. The Three-Dimensional Power Spectrum Measured from the APM Galaxy Survey - Part One - Use of the Angular Correlation Function. *MNRAS*, 265:145–+, Nov 1993.

C. L. Bennett et al. Preliminary separation of galactic and cosmic microwave emission for the COBE Differential Microwave Radiometer. *ApJ*, 396:L7–L12, Sept 1992.

C. L. Bennett et al. The Microwave Anisotropy Probe Mission. *ApJ*, 583:1–23, Jan 2003a.

C. L. Bennett et al. First-Year Wilkinson Microwave Anisotropy Probe (WMAP) Observations: Preliminary Maps and Basic Results. *ApJS*, 148:1–27, Sept 2003b.

C. L. Bennett et al. First-Year Wilkinson Microwave Anisotropy Probe (WMAP) Observations: Foreground Emission. *ApJS*, 148:97–117, Sept 2003c.

C. L. Bennett, A. J. Banday, K. M. Gorski, G. Hinshaw, P. Jackson, P. Keegstra, A. Kogut, G. F. Smoot, D. T. Wilkinson, and E. L. Wright. Four-Year COBE DMR Cosmic Microwave Background Observations: Maps and Basic Results. *ApJ*, 464:L1+, June 1996.

A. J. Benson, R. G. Bower, C. S. Frenk, C. G. Lacey, C. M. Baugh, and S. Cole. What Shapes the Luminosity Function of Galaxies? *ApJ*, 599:38–49, Dec 2003.

A. J. Benson, C. S. Frenk, C. M. Baugh, S. Cole, and C. G. Lacey. The clustering evolution of the galaxy distribution. *MNRAS*, 327:1041–1056, Nov 2001.

A. A. Berlind and D. H. Weinberg. The Halo Occupation Distribution: Toward an Empirical Determination of the Relation between Galaxies and Mass. *ApJ*, 575:587–616, Aug 2002.

E. Bertin and S. Arnouts. SExtractor: Software for source extraction. *A&AS*, 117: 393–404, June 1996.

R. M. Bielby et al. The VLT LBG Redshift Survey - I. Clustering and dynamics of ≈1000 galaxies at z≈ 3. *MNRAS*, 414:2–27, June 2011.

R. M. Bielby and T. Shanks. Anomalous SZ contribution to three-year WMAP data. *MNRAS*, 382:1196–1202, Dec 2007.

C. Blake, A. Collister, S. Bridle, and O. Lahav. Cosmological baryonic and matter densities from 600000 SDSS luminous red galaxies with photometric redshifts. *MNRAS*, 374:1527–1548, Feb 2007.

C. Blake, A. Collister, and O. Lahav. Halo-model signatures from 380000 Sloan Digital Sky Survey luminous red galaxies with photometric redshifts. *MNRAS*, 385:1257–1269, Apr 2008.

C. Blake and K. Glazebrook. Probing Dark Energy Using Baryonic Oscillations in the Galaxy Power Spectrum as a Cosmological Ruler. *ApJ*, 594:665–673, Sept 2003.

C. Blake and J. Wall. Quantifying angular clustering in wide-area radio surveys. *MNRAS*, 337:993–1003, Dec 2002.

M. R. Blanton et al. The Luminosity Function of Galaxies in SDSS Commissioning Data. *AJ*, 121:2358–2380, May 2001.

G. R. Blumenthal, H. Pagels, and J. R. Primack. Galaxy formation by dissipationless particles heavier than neutrinos. *Nature*, 299:37–+, Sept 1982.

N. W. Boggess et al. The COBE mission - Its design and performance two years after launch. *ApJ*, 397:420–429, Oct 1992.

M. Bonamente et al. Determination of the Cosmic Distance Scale from Sunyaev-Zel'dovich Effect and Chandra X-Ray Measurements of High-Redshift Galaxy Clusters. *ApJ*, 647: 25–54, Aug 2006.

J. R. Bond, A. H. Jaffe, and L. Knox. Estimating the power spectrum of the cosmic microwave background. *Phys. Rev. D*, 57:2117–2137, Feb 1998.

H. Bondi and T. Gold. The Steady-State Theory of the Expanding Universe. *MNRAS*, 108:252–+, 1948.

S. Boughn and R. Crittenden. A correlation between the cosmic microwave background and large-scale structure in the Universe. *Nature*, 427:45–47, Jan 2004.

S. P. Boughn and R. G. Crittenden. Cross Correlation of the Cosmic Microwave Background with Radio Sources: Constraints on an Accelerating Universe. *Physical Review Letters*, 88(2):021302–+, Jan 2002.

R. G. Bower, A. J. Benson, R. Malbon, J. C. Helly, C. S. Frenk, C. M. Baugh, S. Cole, and C. G. Lacey. Breaking the hierarchy of galaxy formation. *MNRAS*, 370:645–655, Aug 2006.

M. J. I. Brown, A. Dey, B. T. Jannuzi, K. Brand, A. J. Benson, M. Brodwin, D. J. Croton, and P. R. Eisenhardt. The Evolving Luminosity Function of Red Galaxies. *ApJ*, 654: 858–877, Jan 2007.

M. J. I. Brown, Z. Zheng, M. White, A. Dey, B. T. Jannuzi, A. J. Benson, K. Brand, M. Brodwin, and D. J. Croton. Red Galaxy Growth and the Halo Occupation Distribution. *ApJ*, 682:937–963, Aug 2008.

G. Bruzual and S. Charlot. Stellar population synthesis at the resolution of 2003. *MNRAS*, 344:1000–1028, Oct 2003.

J. S. Bullock, T. S. Kolatt, Y. Sigad, R. S. Somerville, A. V. Kravtsov, A. A. Klypin, J. R. Primack, and A. Dekel. Profiles of dark haloes: evolution, scatter and environment. *MNRAS*, 321:559–575, March 2001.

A. Cabré, E. Gaztañaga, M. Manera, P. Fosalba, and F. Castander. Cross-correlation of Wilkinson Microwave Anisotropy Probe third-year data and the Sloan Digital Sky Survey DR4 galaxy survey: new evidence for dark energy. *MNRAS*, 372:L23–L27, Oct 2006.

Y.-C. Cai, R. E. Angulo, C. M. Baugh, S. Cole, C. S. Frenk, and A. Jenkins. Mock galaxy redshift catalogues from simulations: implications for Pan-STARRS1. *MNRAS*, 395: 1185–1203, May 2009.

R. R. Caldwell, R. Dave, and P. J. Steinhardt. Cosmological Imprint of an Energy Component with General Equation of State. *Physical Review Letters*, 80:1582–1585, Feb 1998.

R. Cannon et al. The 2dF-SDSS LRG and QSO (2SLAQ) Luminous Red Galaxy Survey. *MNRAS*, 372:425–442, Oct 2006.

S. M. Carroll. The Cosmological Constant. *Living Reviews in Relativity*, 4:1–+, Feb 2001.

S. M. Carroll, V. Duvvuri, M. Trodden, and M. S. Turner. Is cosmic speed-up due to new gravitational physics? *Phys. Rev. D*, 70(4):043528–+, Aug 2004.

S. M. Carroll, W. H. Press, and E. L. Turner. The cosmological constant. *ARA&A*, 30: 499–542, 1992.

K. C. Chambers. Pan-STARRS Telescope #1 Status and Science Mission. In *Bulletin of the American Astronomical Society*, volume 41 of *Bulletin of the American Astronomical Society*, pages 270–+, Jan 2009.

X. Chen and E. L. Wright. Extragalactic Point Source Search in Five-Year WMAP 41, 61, and 94 Ghz Maps. *ApJ*, 694:222–234, March 2009.

G. Chon, A. Challinor, S. Prunet, E. Hivon, and I. Szapudi. Fast estimation of polarization power spectra using correlation functions. *MNRAS*, 350:914–926, May 2004.

S. Cole et al. The 2dF Galaxy Redshift Survey: power-spectrum analysis of the final data set and cosmological implications. *MNRAS*, 362:505–534, Sept 2005.

P. Coles and F. Lucchin. *Cosmology: The Origin and Evolution of Cosmic Structure, Second Edition*. John Wiley, July 2002. ISBN 9780471489092.

M. Colless et al. The 2dF Galaxy Redshift Survey: spectra and redshifts. *MNRAS*, 328: 1039–1063, Dec 2001.

A. Collister et al. MegaZ-LRG: a photometric redshift catalogue of one million SDSS luminous red galaxies. *MNRAS*, 375:68–76, Feb 2007.

J. J. Condon, W. D. Cotton, E. W. Greisen, Q. F. Yin, R. A. Perley, G. B. Taylor, and J. J. Broderick. The NRAO VLA Sky Survey. *AJ*, 115:1693–1716, May 1998.

R. J. Cool, D. J. Eisenstein, X. Fan, M. Fukugita, L. Jiang, C. Maraston, A. Meiksin, D. P. Schneider, and D. A. Wake. Luminosity Function Constraints on the Evolution of Massive Red Galaxies since z ˜ 0.9. *ApJ*, 682:919–936, Aug 2008.

A. Cooray and R. Sheth. Halo models of large scale structure. *Phys. Rep.*, 372:1–129, Dec 2002.

E. J. Copeland, M. Sami, and S. Tsujikawa. Dynamics of Dark Energy. *International Journal of Modern Physics D*, 15:1753–1935, 2006.

C. J. Copi, D. N. Schramm, and M. S. Turner. Big-Bang Nucleosynthesis and the Baryon Density of the Universe. *Science*, 267:192–199, Jan 1995.

L. L. Cowie, A. Songaila, E. M. Hu, and J. G. Cohen. New Insight on Galaxy Formation and Evolution From Keck Spectroscopy of the Hawaii Deep Fields. *AJ*, 112:839–+, Sept 1996.

R. G. Crittenden and N. Turok. Looking for a Cosmological Constant with the Rees-Sciama Effect. *Physical Review Letters*, 76:575–578, Jan 1996.

S. M. Croom et al. The 2dF-SDSS LRG and QSO Survey: the spectroscopic QSO catalogue. *MNRAS*, 392:19–44, Jan 2009.

S. M. Croom, B. J. Boyle, T. Shanks, R. J. Smith, L. Miller, P. J. Outram, N. S. Loaring, F. Hoyle, and J. da Ângela. The 2dF QSO Redshift Survey - XIV. Structure and evolution from the two-point correlation function. *MNRAS*, 356:415–438, Jan 2005.

S. M. Croom and T. Shanks. Statistical lensing of faint QSOs by galaxy clusters. *MNRAS*, 307:L17–L21, Aug 1999.

J. da Ângela, T. Shanks, S. M. Croom, P. Weilbacher, R. J. Brunner, W. J. Couch, L. Miller, A. D. Myers, R. C. Nichol, K. A. Pimbblet, R. de Propris, G. T. Richards, N. P. Ross, D. P. Schneider, and D. Wake. The 2dF-SDSS LRG and QSO survey: QSO clustering and the L-z degeneracy. *MNRAS*, 383:565–580, Jan 2008.

M. Davis, G. Efstathiou, C. S. Frenk, and S. D. M. White. The evolution of large-scale structure in a universe dominated by cold dark matter. *ApJ*, 292:371–394, May 1985.

P. de Bernardis et al. A flat Universe from high-resolution maps of the cosmic microwave background radiation. *Nature*, 404:955–959, Apr 2000.

G. De Lucia, V. Springel, S. D. M. White, D. Croton, and G. Kauffmann. The formation history of elliptical galaxies. *MNRAS*, 366:499–509, Feb 2006.

R. H. Dicke, P. J. E. Peebles, P. G. Roll, and D. T. Wilkinson. Cosmic Black-Body Radiation. *ApJ*, 142:414–419, July 1965.

S. Dodelson et al. The Three-dimensional Power Spectrum from Angular Clustering of Galaxies in Early Sloan Digital Sky Survey Data. *ApJ*, 572:140–156, June 2002.

M. Douspis, P. G. Castro, C. Caprini, and N. Aghanim. Optimising large galaxy surveys for ISW detection. *A&A*, 485:395–401, July 2008.

M. J. Drinkwater et al. The WiggleZ Dark Energy Survey: survey design and first data release. *MNRAS*, 401:1429–1452, Jan 2010.

J. Dunkley et al. Five-Year Wilkinson Microwave Anisotropy Probe Observations: Likelihoods and Parameters from the WMAP Data. *ApJS*, 180:306–329, Feb 2009.

J. S. Dunlop and J. A. Peacock. The Redshift Cut-Off in the Luminosity Function of Radio Galaxies and Quasars. *MNRAS*, 247:19–+, Nov 1990.

G. Dvali, G. Gabadadze, and M. Porrati. 4D gravity on a brane in 5D Minkowski space. *Physics Letters B*, 485:208–214, July 2000.

G. Efstathiou. An anthropic argument for a cosmological constant. *MNRAS*, 274:L73–L76, June 1995.

G. Efstathiou. Myths and truths concerning estimation of power spectra: the case for a hybrid estimator. *MNRAS*, 349:603–626, Apr 2004.

G. Efstathiou, N. Kaiser, W. Saunders, A. Lawrence, M. Rowan-Robinson, R. S. Ellis, and C. S. Frenk. Largescale Clustering of IRAS Galaxies. *MNRAS*, 247:10P–+, Nov 1990a.

G. Efstathiou, W. J. Sutherland, and S. J. Maddox. The cosmological constant and cold dark matter. *Nature*, 348:705–707, Dec 1990b.

A. Einstein. Kosmologische Betrachtungen zur allgemeinen Relativitätstheorie (Cosmological Considerations in the General Theory of Relativity). *Sitzungsberichte der Königlich Preußischen Akademie der Wissenschaften (Berlin), Seite 142-152.*, pages 142–152, 1917.

D. J. Eisenstein et al. Spectroscopic Target Selection for the Sloan Digital Sky Survey: The Luminous Red Galaxy Sample. *AJ*, 122:2267–2280, Nov 2001.

D. J. Eisenstein et al. Detection of the Baryon Acoustic Peak in the Large-Scale Correlation Function of SDSS Luminous Red Galaxies. *ApJ*, 633:560–574, Nov 2005.

D. J. Eisenstein et al. SDSS-III: Massive Spectroscopic Surveys of the Distant Universe, the Milky Way Galaxy, and Extra-Solar Planetary Systems. *arXiv:1101.1529*, Jan 2011.

D. J. Eisenstein and W. Hu. Baryonic Features in the Matter Transfer Function. *ApJ*, 496:605–+, March 1998.

B. D. Fields and S. Sarkar. in K. Nakamura et al. Review of Particle Physics. *Journal of Physics G: Nuclear and Particle Physics*, 37(7A):075021, 2010. URL `http://pdg.lbl.gov`.

A. V. Filippenko. Evidence from Type Ia Supernovae for an Accelerating Universe and Dark Energy. *Measuring and Modeling the Universe*, pages 270–+, 2004.

D. J. Fixsen, E. S. Cheng, J. M. Gales, J. C. Mather, R. A. Shafer, and E. L. Wright. The Cosmic Microwave Background Spectrum from the Full COBE FIRAS Data Set. *ApJ*, 473:576–+, Dec 1996.

P. Fosalba, E. Gaztañaga, and F. J. Castander. Detection of the Integrated Sachs-Wolfe and Sunyaev-Zeldovich Effects from the Cosmic Microwave Background-Galaxy Correlation. *ApJ*, 597:L89–L92, Nov 2003.

C. L. Francis and J. A. Peacock. Integrated Sachs-Wolfe measurements with photometric redshift surveys: 2MASS results and future prospects. *MNRAS*, 406:2–13, July 2010.

W. L. Freedman, B. F. Madore, B. K. Gibson, L. Ferrarese, D. D. Kelson, S. Sakai, J. R. Mould, R. C. Kennicutt, Jr., H. C. Ford, J. A. Graham, J. P. Huchra, S. M. G. Hughes, G. D. Illingworth, L. M. Macri, and P. B. Stetson. Final Results from the Hubble Space Telescope Key Project to Measure the Hubble Constant. *ApJ*, 553:47–72, May 2001.

A. Friedman. Über die Krümmung des Raumes. *Zeitschrift fur Physik*, 10:377–386, Dec 1922.

J. N. Fry. The Evolution of Bias. *ApJ*, 461:L65+, Apr 1996.

M. Fukugita, T. Ichikawa, J. E. Gunn, M. Doi, K. Shimasaku, and D. P. Schneider. The Sloan Digital Sky Survey Photometric System. *AJ*, 111:1748–+, Apr 1996.

G. Gamow. Expanding Universe and the Origin of Elements. *Physical Review*, 70:572–573, Oct 1946.

T. Giannantonio, R. Scranton, R. G. Crittenden, R. C. Nichol, S. P. Boughn, A. D. Myers, and G. T. Richards. Combined analysis of the integrated Sachs-Wolfe effect and cosmological implications. *Phys. Rev. D*, 77(12):123520–+, June 2008.

M. D. Gladders and H. K. C. Yee. A New Method For Galaxy Cluster Detection. I. The Algorithm. *AJ*, 120:2148–2162, Oct 2000.

K. Glazebrook et al. The WiggleZ Project: AAOmega and Dark Energy. In N. Metcalfe and T. Shanks, editors, *Cosmic Frontiers*, volume 379 of *Astronomical Society of the Pacific Conference Series*, pages 72–+, Dec 2007.

B. Gold et al. Five-Year Wilkinson Microwave Anisotropy Probe Observations: Galactic Foreground Emission. *ApJS*, 180:265–282, Feb 2009.

B. Gold et al. Seven-year Wilkinson Microwave Anisotropy Probe (WMAP) Observations: Galactic Foreground Emission. *ApJS*, 192:15–+, Feb 2011.

K. M. Górski, E. Hivon, A. J. Banday, B. D. Wandelt, F. K. Hansen, M. Reinecke, and M. Bartelmann. HEALPix: A Framework for High-Resolution Discretization and Fast Analysis of Data Distributed on the Sphere. *ApJ*, 622:759–771, Apr 2005.

B. R. Granett, M. C. Neyrinck, and I. Szapudi. An Imprint of Superstructures on the Microwave Background due to the Integrated Sachs-Wolfe Effect. *ApJ*, 683:L99–L102, Aug 2008.

P. C. Gregory et al. The GB6 Catalog of Radio Sources. *ApJS*, 103:427–+, Apr 1996.

M. R. Griffith and A. E. Wright. The Parkes-MIT-NRAO (PMN) surveys. I - The 4850 MHz surveys and data reduction. *AJ*, 105:1666–1679, May 1993.

E. J. Groth and P. J. E. Peebles. Statistical analysis of catalogs of extragalactic objects. VII - Two- and three-point correlation functions for the high-resolution Shane-Wirtanen catalog of galaxies. *ApJ*, 217:385–405, Oct 1977.

A. C. C. Guimarães, A. D. Myers, and T. Shanks. QSO lensing magnification associated with galaxy groups. *MNRAS*, 362:657–665, Sept 2005.

A. H. Guth. Inflationary universe: A possible solution to the horizon and flatness problems. *Phys. Rev. D*, 23:347–356, Jan 1981.

L. Guzzo et al. A test of the nature of cosmic acceleration using galaxy redshift distortions. *Nature*, 451:541–544, Jan 2008.

A. J. S. Hamilton. Toward Better Ways to Measure the Galaxy Correlation Function. *ApJ*, 417:19–+, Nov 1993.

A. J. S. Hamilton. Towards optimal measurement of power spectra - II. A basis of positive, compact, statistically orthogonal kernels. *MNRAS*, 289:295–304, Aug 1997.

A. J. S. Hamilton, P. Kumar, E. Lu, and A. Matthews. Reconstructing the primordial spectrum of fluctuations of the universe from the observed nonlinear clustering of galaxies. *ApJ*, 374:L1–L4, June 1991.

S. Hanany et al. MAXIMA-1: A Measurement of the Cosmic Microwave Background Anisotropy on Angular Scales of $10' - 5°$. *ApJ*, 545:L5–L9, Dec 2000.

D. Hanson, A. Lewis, and A. Challinor. Asymmetric beams and CMB statistical anisotropy. *Phys. Rev. D*, 81(10):103003–+, May 2010.

E. Hawkins et al. The 2dF Galaxy Redshift Survey: correlation functions, peculiar velocities and the matter density of the Universe. *MNRAS*, 346:78–96, Nov 2003.

R. S. Hill et al. Five-Year Wilkinson Microwave Anisotropy Probe Observations: Beam Maps and Window Functions. *ApJS*, 180:246–264, Feb 2009.

G. Hinshaw et al. First-Year Wilkinson Microwave Anisotropy Probe (WMAP) Observations: Data Processing Methods and Systematic Error Limits. *ApJS*, 148:63–95, Sept 2003a.

G. Hinshaw et al. First-Year Wilkinson Microwave Anisotropy Probe (WMAP) Observations: The Angular Power Spectrum. *ApJS*, 148:135–159, Sept 2003b.

G. Hinshaw et al. Three-Year Wilkinson Microwave Anisotropy Probe (WMAP) Observations: Temperature Analysis. *ApJS*, 170:288–334, June 2007.

G. Hinshaw et al. Five-Year Wilkinson Microwave Anisotropy Probe Observations: Data Processing, Sky Maps, and Basic Results. *ApJS*, 180:225–245, Feb 2009.

E. Hivon, K. M. Górski, C. B. Netterfield, B. P. Crill, S. Prunet, and F. Hansen. MASTER of the Cosmic Microwave Background Anisotropy Power Spectrum: A Fast Method for Statistical Analysis of Large and Complex Cosmic Microwave Background Data Sets. *ApJ*, 567:2–17, March 2002.

S. Ho, C. Hirata, N. Padmanabhan, U. Seljak, and N. Bahcall. Correlation of CMB with large-scale structure. I. Integrated Sachs-Wolfe tomography and cosmological implications. *Phys. Rev. D*, 78(4):043519–+, Aug 2008.

F. Hoyle. A New Model for the Expanding Universe. *MNRAS*, 108:372–+, 1948.

W. Hu and S. Dodelson. Cosmic Microwave Background Anisotropies. *ARA&A*, 40: 171–216, 2002.

W. Hu and R. Scranton. Measuring dark energy clustering with CMB-galaxy correlations. *Phys. Rev. D*, 70(12):123002–+, Dec 2004.

E. Hubble. A Relation between Distance and Radial Velocity among Extra-Galactic Nebulae. *Proceedings of the National Academy of Science*, 15:168–173, March 1929.

K. M. Huffenberger, B. P. Crill, A. E. Lange, K. M. Górski, and C. R. Lawrence. Measuring Planck beams with planets. *A&A*, 510:A58+, Feb 2010.

K. M. Huffenberger, U. Seljak, and A. Makarov. Sunyaev-Zeldovich effect in WMAP and its effect on cosmological parameters. *Phys. Rev. D*, 70(6):063002–+, Sept 2004.

Z. Ivezic et al. LSST: from Science Drivers to Reference Design and Anticipated Data Products. *arXiv:0805.2366*, May 2008.

A. H. Jaffe et al. Cosmology from MAXIMA-1, BOOMERANG, and COBE DMR Cosmic Microwave Background Observations. *Physical Review Letters*, 86:3475–3479, Apr 2001.

N. Jarosik et al. Three-Year Wilkinson Microwave Anisotropy Probe (WMAP) Observations: Beam Profiles, Data Processing, Radiometer Characterization, and Systematic Error Limits. *ApJS*, 170:263–287, June 2007.

N. Jarosik et al. Seven-year Wilkinson Microwave Anisotropy Probe (WMAP) Observations: Sky Maps, Systematic Errors, and Basic Results. *ApJS*, 192:14–+, Feb 2011.

N. Jarosik, C. Barnes, C. L. Bennett, M. Halpern, G. Hinshaw, A. Kogut, M. Limon, S. S. Meyer, L. Page, D. N. Spergel, G. S. Tucker, J. L. Weiland, E. Wollack, and E. L. Wright. First-Year Wilkinson Microwave Anisotropy Probe (WMAP) Observations: On-Orbit Radiometer Characterization. *ApJS*, 148:29–37, Sept 2003.

T. H. Jarrett, T. Chester, R. Cutri, S. Schneider, M. Skrutskie, and J. P. Huchra. 2MASS Extended Source Catalog: Overview and Algorithms. *AJ*, 119:2498–2531, May 2000.

N. Kaiser. Clustering in real space and in redshift space. *MNRAS*, 227:1–21, July 1987.

E. A. Kazin, M. R. Blanton, R. Scoccimarro, C. K. McBride, A. A. Berlind, N. A. Bahcall, J. Brinkmann, P. Czarapata, J. A. Frieman, S. M. Kent, D. P. Schneider, and A. S. Szalay. The Baryonic Acoustic Feature and Large-Scale Clustering in the Sloan Digital Sky Survey Luminous Red Galaxy Sample. *ApJ*, 710:1444–1461, Feb 2010.

A. Klypin, A. V. Kravtsov, O. Valenzuela, and F. Prada. Where Are the Missing Galactic Satellites? *ApJ*, 522:82–92, Sept 1999.

T. Kodama et al. Down-sizing in galaxy formation at z˜ 1 in the Subaru/XMM-Newton Deep Survey (SXDS). *MNRAS*, 350:1005–1014, May 2004.

A. Kogut et al. Dipole Anisotropy in the COBE Differential Microwave Radiometers First-Year Sky Maps. *ApJ*, 419:1–+, Dec 1993.

E. W. Kolb, S. Matarrese, and A. Riotto. On cosmic acceleration without dark energy. *New Journal of Physics*, 8:322–+, Dec 2006.

E. Komatsu et al. Five-Year Wilkinson Microwave Anisotropy Probe Observations: Cosmological Interpretation. *ApJS*, 180:330–376, Feb 2009.

E. Komatsu et al. Seven-year Wilkinson Microwave Anisotropy Probe (WMAP) Observations: Cosmological Interpretation. *ApJS*, 192:18–+, Feb 2011.

A. V. Kravtsov, A. A. Berlind, R. H. Wechsler, A. A. Klypin, S. Gottlöber, B. Allgood, and J. R. Primack. The Dark Side of the Halo Occupation Distribution. *ApJ*, 609: 35–49, July 2004.

C. Lacey and S. Cole. Merger rates in hierarchical models of galaxy formation. *MNRAS*, 262:627–649, June 1993.

O. Lahav and Y. Suto. Measuring our Universe from Galaxy Redshift Surveys. *Living Reviews in Relativity*, 7:8–+, July 2004.

S. D. Landy and A. S. Szalay. Bias and variance of angular correlation functions. *ApJ*, 412:64–71, July 1993.

D. Larson et al. Seven-year Wilkinson Microwave Anisotropy Probe (WMAP) Observations: Power Spectra and WMAP-derived Parameters. *ApJS*, 192:16–+, Feb 2011.

A. Lawrence et al. The UKIRT Infrared Deep Sky Survey (UKIDSS). *MNRAS*, 379: 1599–1617, Aug 2007.

G. Lemaître. Un Univers homogène de masse constante et de rayon croissant rendant compte de la vitesse radiale des nébuleuses extra-galactiques. *Annales de la Societe Scietifique de Bruxelles*, 47:49–59, 1927.

G. Lemaître. The Beginning of the World from the Point of View of Quantum Theory. *Nature*, 127:706–+, May 1931.

Antony Lewis, Anthony Challinor, and Anthony Lasenby. Efficient computation of CMB anisotropies in closed FRW models. *Astrophys. J.*, 538:473–476, 2000.

D. N. Limber. The Analysis of Counts of the Extragalactic Nebulae in Terms of a Fluctuating Density Field. *ApJ*, 117:134–+, Jan 1953.

M. Limon, E. Wollack, M. R. Greason, C. L. Bennett, M. Halpern, G. Hinshaw, N. Jarosik, A. Kogut, S. S. Meyer, L. Page, D. N. Spergel, G. S. Tucker, E. L. Wright, R. S. Hill, E. Komatsu, M. Nolta, N. Odegard, and J. L. Weiland. Wilkinson Microwave Anisotropy Probe (*WMAP*): Five Year Explanatory Supplement. `http://lambda.gsfc.nasa.gov/data/map/doc/MAP_supplement.pdf`, 2008.

W.-B. Lin. Remarks on the Theory of Cosmological Perturbation. *Chinese Physics Letters*, 18:1539–1542, Nov 2001.

C. H. Lineweaver, L. Tenorio, G. F. Smoot, P. Keegstra, A. J. Banday, and P. Lubin. The Dipole Observed in the COBE DMR 4 Year Data. *ApJ*, 470:38–+, Oct 1996.

H. Liu and T. Li. Systematic distortion in cosmic microwave background maps. *Science in China G: Physics and Astronomy*, 52:804–808, May 2009.

H. Liu, S.-L. Xiong, and T.-P. Li. The origin of the WMAP quadrupole. *arXiv:1003.1073*, March 2010.

H. Liu, S.-L. Xiong, and T.-P. Li. Diagnosing timing error in WMAP data. *MNRAS*, 413:L96–L100, May 2011.

M. Lovell, V. Eke, C. Frenk et al. The Haloes of Bright Satellite Galaxies in a Warm Dark Matter Universe. *arXiv:1104.2929*, Apr 2011.

L. B. Lucy. An iterative technique for the rectification of observed distributions. *AJ*, 79: 745–+, June 1974.

M. Lueker et al. Measurements of Secondary Cosmic Microwave Background Anisotropies with the South Pole Telescope. *ApJ*, 719:1045–1066, Aug 2010.

R. Lupton, J. E. Gunn, Z. Ivezić, G. R. Knapp, and S. Kent. The SDSS Imaging Pipelines. In F. R. Harnden, Jr., F. A. Primini, and H. E. Payne, editors, *Astronomical Data Analysis Software and Systems X*, volume 238 of *Astronomical Society of the Pacific Conference Series*, pages 269–+, 2001.

R. Maartens. Is the Universe homogeneous? *arXiv:1104.1300*, Apr 2011.

J. F. Macías-Pérez et al. Archeops in-flight performance, data processing, and map making. *A&A*, 467:1313–1344, June 2007.

S. J. Maddox, G. Efstathiou, W. J. Sutherland, and J. Loveday. Galaxy correlations on large scales. *MNRAS*, 242:43P–47P, Jan 1990.

B. Maffei et al. Planck pre-launch status: HFI beam expectations from the optical optimisation of the focal plane. *A&A*, 520:A12+, Sept 2010.

N. F. Martin, J. T. A. de Jong, and H.-W. Rix. A Comprehensive Maximum Likelihood Analysis of the Structural Properties of Faint Milky Way Satellites. *ApJ*, 684:1075–1092, Sept 2008.

V. J. Martínez, P. Arnalte-Mur, E. Saar, P. de la Cruz, M. J. Pons-Bordería, S. Paredes, A. Fernández-Soto, and E. Tempel. Reliability of the Detection of the Baryon Acoustic Peak. *ApJ*, 696:L93–L97, May 2009.

V. J. Martínez and E. Saar. *Statistics of the Galaxy Distribution*. Statistics of the Galaxy Distribution, Published by Chapman & Hall/CRC, Boca Raton, ISBN: 1584880848, 2002.

S. Masi et al. Instrument, method, brightness, and polarization maps from the 2003 flight of BOOMERanG. *A&A*, 458:687–716, Nov 2006.

J. C. Mather et al. Measurement of the cosmic microwave background spectrum by the COBE FIRAS instrument. *ApJ*, 420:439–444, Jan 1994.

J. C. Mather, D. J. Fixsen, R. A. Shafer, C. Mosier, and D. T. Wilkinson. Calibrator Design for the COBE Far-Infrared Absolute Spectrophotometer (FIRAS). *ApJ*, 512: 511–520, Feb 1999.

P. D. Mauskopf et al. Measurement of a Peak in the Cosmic Microwave Background Power Spectrum from the North American Test Flight of Boomerang. *ApJ*, 536:L59–L62, June 2000.

P. McDonald and D. J. Eisenstein. Dark energy and curvature from a future baryonic acoustic oscillation survey using the Lyman-α forest. *Phys. Rev. D*, 76(6):063009–+, Sept 2007.

J. D. McEwen, P. Vielva, M. P. Hobson, E. Martínez-González, and A. N. Lasenby. Detection of the integrated Sachs-Wolfe effect and corresponding dark energy constraints made with directional spherical wavelets. *MNRAS*, 376:1211–1226, Apr 2007.

A. Meiksin, M. White, and J. A. Peacock. Baryonic signatures in large-scale structure. *MNRAS*, 304:851–864, Apr 1999.

L. Mersini-Houghton and F. C. Adams. Limitations of anthropic predictions for the cosmological constant Λ: cosmic heat death of anthropic observers. *Classical and Quantum Gravity*, 25(16):165002–+, Aug 2008.

N. Metcalfe, T. Shanks, A. Campos, H. J. McCracken, and R. Fong. Galaxy number counts - V. Ultradeep counts: the Herschel and Hubble Deep Fields. *MNRAS*, 323: 795–830, May 2001.

S. Mitra, G. Rocha, K. M. Górski, K. M. Huffenberger, H. K. Eriksen, M. A. J. Ashdown, and C. R. Lawrence. Fast Pixel Space Convolution for Cosmic Microwave Background Surveys with Asymmetric Beams and Complex Scan Strategies: FEBeCoP. *ApJS*, 193: 5–+, March 2011.

S. Mitra, A. S. Sengupta, and T. Souradeep. CMB power spectrum estimation using noncircular beams. *Phys. Rev. D*, 70(10):103002–+, Nov 2004.

H. J. Mo and S. D. M. White. An analytic model for the spatial clustering of dark matter haloes. *MNRAS*, 282:347–361, Sept 1996.

A. W. Moore, A. J. Connolly, C. Genovese, A. Gray, L. Grone, N. I. Kanidoris, R. C. Nichol, J. Schneider, A. S. Szalay, I. Szapudi, and L. Wasserman. Fast Algorithms and Efficient Statistics: N-Point Correlation Functions. In A. J. Banday, S. Zaroubi, and M. Bartelmann, editors, *Mining the Sky*, pages 71–+, 2001.

B. Moore, S. Ghigna, F. Governato, G. Lake, T. Quinn, J. Stadel, and P. Tozzi. Dark Matter Substructure within Galactic Halos. *ApJ*, 524:L19–L22, Oct 1999a.

B. Moore, T. Quinn, F. Governato, J. Stadel, and G. Lake. Cold collapse and the core catastrophe. *MNRAS*, 310:1147–1152, Dec 1999b.

A. Moss, D. Scott, and K. Sigurdson. Induced CMB quadrupole from pointing offsets. *JCAP*, 1:1–+, Jan 2011.

G. Mountrichas and T. Shanks. QSO lensing magnification: a comparison of 2QZ and Sloan Digital Sky Survey results. *MNRAS*, 380:113–125, Sept 2007.

A. D. Myers, P. J. Outram, T. Shanks, B. J. Boyle, S. M. Croom, N. S. Loaring, L. Miller, and R. J. Smith. The 2dF QSO Redshift Survey - X. Lensing of background QSOs by galaxy groups. *MNRAS*, 342:467–482, June 2003.

A. D. Myers, P. J. Outram, T. Shanks, B. J. Boyle, S. M. Croom, N. S. Loaring, L. Miller, and R. J. Smith. On statistical lensing and the anticorrelation between 2dF QSOs and foreground galaxies. *MNRAS*, 359:741–754, May 2005.

A. D. Myers, T. Shanks, P. J. Outram, W. J. Frith, and A. W. Wolfendale. Evidence for an extended Sunyaev-Zel'dovich effect in WMAP data. *MNRAS*, 347:L67–L72, Feb 2004.

J. F. Navarro, C. S. Frenk, and S. D. M. White. A Universal Density Profile from Hierarchical Clustering. *ApJ*, 490:493–+, Dec 1997.

J. G. Nollenberg and L. L. R. Williams. Galaxy-Quasar Correlations between APM Galaxies and Hamburg-ESO QSOs. *ApJ*, 634:793–805, Nov 2005.

M. R. Nolta et al. Five-Year Wilkinson Microwave Anisotropy Probe Observations: Angular Power Spectra. *ApJS*, 180:296–305, Feb 2009.

M. R. Nolta, E. L. Wright, L. Page, C. L. Bennett, M. Halpern, G. Hinshaw, N. Jarosik, A. Kogut, M. Limon, S. S. Meyer, D. N. Spergel, G. S. Tucker, and E. Wollack. First Year Wilkinson Microwave Anisotropy Probe Observations: Dark Energy Induced Correlation with Radio Sources. *ApJ*, 608:10–15, June 2004.

P. Norberg et al. The 2dF Galaxy Redshift Survey: the b_J-band galaxy luminosity function and survey selection function. *MNRAS*, 336:907–931, Nov 2002a.

P. Norberg et al. The 2dF Galaxy Redshift Survey: the dependence of galaxy clustering on luminosity and spectral type. *MNRAS*, 332:827–838, June 2002b.

R. A. Overzier, H. J. A. Röttgering, R. B. Rengelink, and R. J. Wilman. The spatial clustering of radio sources in NVSS and FIRST; implications for galaxy clustering evolution. *A&A*, 405:53–72, July 2003.

N. Padmanabhan et al. The clustering of luminous red galaxies in the Sloan Digital Sky Survey imaging data. *MNRAS*, 378:852–872, July 2007.

N. Padmanabhan et al. An Improved Photometric Calibration of the Sloan Digital Sky Survey Imaging Data. *ApJ*, 674:1217–1233, Feb 2008.

N. Padmanabhan, C. M. Hirata, U. Seljak, D. J. Schlegel, J. Brinkmann, and D. P. Schneider. Correlating the CMB with luminous red galaxies: The integrated Sachs-Wolfe effect. *Phys. Rev. D*, 72(4):043525–+, Aug 2005.

L. Page et al. The Optical Design and Characterization of the Microwave Anisotropy Probe. *ApJ*, 585:566–586, March 2003a.

L. Page et al. First-Year Wilkinson Microwave Anisotropy Probe (WMAP) Observations: Beam Profiles and Window Functions. *ApJS*, 148:39–50, Sept 2003b.

D. Parkinson, C. Blake, M. Kunz, B. A. Bassett, R. C. Nichol, and K. Glazebrook. Optimizing baryon acoustic oscillation surveys - I. Testing the concordance ΛCDM cosmology. *MNRAS*, 377:185–197, May 2007.

J. A. Peacock. Testing anthropic predictions for Λ and the cosmic microwave background temperature. *MNRAS*, 379:1067–1074, Aug 2007.

J. A. Peacock and S. J. Dodds. Non-linear evolution of cosmological power spectra. *MNRAS*, 280:L19–L26, June 1996.

J. A. Peacock and R. E. Smith. Halo occupation numbers and galaxy bias. *MNRAS*, 318: 1144–1156, Nov 2000.

P. J. Peebles and B. Ratra. The cosmological constant and dark energy. *Reviews of Modern Physics*, 75:559–606, Apr 2003.

P. J. E. Peebles. Recombination of the Primeval Plasma. *ApJ*, 153:1–+, July 1968.

P. J. E. Peebles. The Nature of the Distribution of Galaxies. *A&A*, 32:197–+, May 1974.

P. J. E. Peebles. *The large-scale structure of the universe*. Princeton University Press, 1980.

P. J. E. Peebles. Large-scale background temperature and mass fluctuations due to scale-invariant primeval perturbations. *ApJ*, 263:L1–L5, Dec 1982.

P. J. E. Peebles. Tests of cosmological models constrained by inflation. *ApJ*, 284:439–444, Sept 1984.

P. J. E. Peebles and M. G. Hauser. Statistical Analysis of Catalogs of Extragalactic Objects. III. The Shane-Wirtanen and Zwicky Catalogs. *ApJS*, 28:19–+, Nov 1974.

P. J. E. Peebles and J. T. Yu. Primeval Adiabatic Perturbation in an Expanding Universe. *ApJ*, 162:815–+, Dec 1970.

A. A. Penzias and R. W. Wilson. A Measurement of Excess Antenna Temperature at 4080 Mc/s. *ApJ*, 142:419–421, July 1965.

W. J. Percival, S. Cole, D. J. Eisenstein, R. C. Nichol, J. A. Peacock, A. C. Pope, and A. S. Szalay. Measuring the Baryon Acoustic Oscillation scale using the Sloan Digital Sky Survey and 2dF Galaxy Redshift Survey. *MNRAS*, 381:1053–1066, Nov 2007.

W. J. Percival, B. A. Reid, D. J. Eisenstein et al. Baryon acoustic oscillations in the Sloan Digital Sky Survey Data Release 7 galaxy sample. *MNRAS*, 401:2148–2168, Feb 2010.

S. Perlmutter et al. Measurements of Omega and Lambda from 42 High-Redshift Supernovae. *ApJ*, 517:565–586, June 1999.

V. Petrosian. Surface brightness and evolution of galaxies. *ApJ*, 209:L1–L5, Oct 1976.

S. Phillipps, R. Fong, R. S. E. S. M. Fall, and H. T. MacGillivray. Correlation analysis deep galaxy samples - 1. Techniques with applications to a two-colour sample. *MNRAS*, 182:673–686, March 1978.

S. Phleps, J. A. Peacock, K. Meisenheimer, and C. Wolf. Galaxy clustering from COMBO-17: the halo occupation distribution at <z> = 0.6. *A&A*, 457:145–155, Oct 2006.

W. H. Press and P. Schechter. Formation of Galaxies and Clusters of Galaxies by Self-Similar Gravitational Condensation. *ApJ*, 187:425–438, Feb 1974.

B. Rabii et al. MAXIMA: A balloon-borne cosmic microwave background anisotropy experiment. *Review of Scientific Instruments*, 77(7):071101–+, July 2006.

A. Ratcliffe, T. Shanks, Q. A. Parker, and R. Fong. The Durham/UKST Galaxy Redshift Survey - III. Large-scale structure via the two-point correlation function. *MNRAS*, 296: 173–190, May 1998a.

A. Ratcliffe, T. Shanks, Q. A. Parker, and R. Fong. The Durham/UKST Galaxy Redshift Survey - IV. Redshift-space distortions in the two-point correlation function. *MNRAS*, 296:191–205, May 1998b.

A. Refregier, D. N. Spergel, and T. Herbig. Extragalactic Foregrounds of the Cosmic Microwave Background: Prospects for the MAP Mission. *ApJ*, 531:31–41, March 2000.

A. G. Riess et al. Observational Evidence from Supernovae for an Accelerating Universe and a Cosmological Constant. *AJ*, 116:1009–1038, Sept 1998.

A. G. Riess et al. New Hubble Space Telescope Discoveries of Type Ia Supernovae at z = 1: Narrowing Constraints on the Early Behavior of Dark Energy. *ApJ*, 659:98–121, Apr 2007.

A. G. Riess, L. Macri, S. Casertano, H. Lampeitl, H. C. Ferguson, A. V. Filippenko, S. W. Jha, W. Li, and R. Chornock. A 3% Solution: Determination of the Hubble Constant with the Hubble Space Telescope and Wide Field Camera 3. *ApJ*, 730:119–+, Apr 2011.

H. P. Robertson. Kinematics and World-Structure. *ApJ*, 82:284–+, Nov 1935.

N. Roche and S. A. Eales. The angular correlation function and hierarchical moments of ∼70000 faint galaxies to R=23.5. *MNRAS*, 307:703–721, Aug 1999.

A. J Ross et al. Ameliorating Systematic Uncertainties in the Angular Clustering of Galaxies: A Study using SDSS-III. *arXiv:1105.2320*, May 2011.

A. J. Ross and R. J. Brunner. Halo-model analysis of the clustering of photometrically selected galaxies from SDSS. *MNRAS*, 399:878–887, Oct 2009.

A. J. Ross, R. J. Brunner, and A. D. Myers. Normalization of the Matter Power Spectrum via Higher Order Angular Correlations of Luminous Red Galaxies. *ApJ*, 682:737–744, Aug 2008a.

N. P. Ross et al. The 2dF-SDSS LRG and QSO Survey: the LRG 2-point correlation function and redshift-space distortions. *MNRAS*, 381:573–588, Oct 2007.

N. P. Ross, T. Shanks, R. D. Cannon, D. A. Wake, R. G. Sharp, S. M. Croom, and J. A. Peacock. Luminous red galaxy clustering at z $\sim=$ 0.7 - first results using AAOmega. *MNRAS*, 387:1323–1334, July 2008b.

B. F. Roukema. On the suspected timing error in Wilkinson microwave anisotropy probe map-making. *A&A*, 518:A34+, July 2010a.

B. F. Roukema. On the suspected timing-offset-induced calibration error in the Wilkinson microwave anisotropy probe time-ordered data. *arXiv:1007.5307*, July 2010b.

R. K. Sachs and A. M. Wolfe. Perturbations of a Cosmological Model and Angular Variations of the Microwave Background. *ApJ*, 147:73–+, Jan 1967.

E. M. Sadler et al. The extragalactic radio-source population at 95GHz. *MNRAS*, 385: 1656–1672, Apr 2008.

V. Sahni. Dark Matter and Dark Energy. In E. Papantonopoulos, editor, *Lecture Notes in Physics, Berlin Springer Verlag*, volume 653 of *Lecture Notes in Physics, Berlin Springer Verlag*, pages 141–+, 2004.

E. E. Salpeter. The Luminosity Function and Stellar Evolution. *ApJ*, 121:161–+, Jan 1955.

P. Sarkar, J. Yadav, B. Pandey, and S. Bharadwaj. The scale of homogeneity of the galaxy distribution in SDSS DR6. *MNRAS*, 399:L128–L131, Oct 2009.

U. Sawangwit and T. Shanks. Beam profile sensitivity of the WMAP CMB power spectrum. *MNRAS*, 407:L16–L20, Sept 2010a.

U. Sawangwit and T. Shanks. Lambda-CDM and the WMAP power spectrum beam profile sensitivity. *arXiv:1006.1270*, June 2010b.

U. Sawangwit, T. Shanks, F. B. Abdalla, R. D. Cannon, S. M. Croom, A. C. Edge, N. P. Ross, and D. A. Wake. Angular correlation function of 1.5 million luminous red galaxies: clustering evolution and a search for baryon acoustic oscillations. *MNRAS*, 416:3033–3056, Oct 2011a.

U. Sawangwit, T. Shanks, R. D. Cannon, S. M. Croom, N. P. Ross, and D. A. Wake. Cross-correlating WMAP5 with 1.5 million LRGs: a new test for the ISW effect. *MNRAS*, 402:2228–2244, March 2010.

U. Sawangwit, T. Shanks, S. Croom, M. J. Drinkwater, S. Fine, D. Parkinson, and N. P. Ross. Measuring BAO and non-Gaussianity via QSO clustering. *MNRAS*, in press, 2011b.

C. Scharf, Y. Hoffman, O. Lahav, and D. Lynden-Bell. Spherical harmonic analysis of IRAS galaxies - Implications for the Great Attractor and cold dark matter. *MNRAS*, 256:229–237, May 1992.

P. Schechter. An analytic expression for the luminosity function for galaxies. *ApJ*, 203: 297–306, Jan 1976.

D. J. Schlegel, D. P. Finkbeiner, and M. Davis. Maps of Dust Infrared Emission for Use in Estimation of Reddening and Cosmic Microwave Background Radiation Foregrounds. *ApJ*, 500:525–+, June 1998.

N. Scoville et al. The Cosmic Evolution Survey (COSMOS): Overview. *ApJS*, 172:1–8, Sept 2007.

R. Scranton et al. Analysis of Systematic Effects and Statistical Uncertainties in Angular Clustering of Galaxies from Early Sloan Digital Sky Survey Data. *ApJ*, 579:48–75, Nov 2002.

R. Scranton et al. Physical Evidence for Dark Energy. *arXiv:0307335*, July 2003.

R. Scranton et al. Detection of Cosmic Magnification with the Sloan Digital Sky Survey. *ApJ*, 633:589–602, Nov 2005.

S. Seager, D. D. Sasselov, and D. Scott. How Exactly Did the Universe Become Neutral? *ApJS*, 128:407–430, June 2000.

U. Seljak and M. Zaldarriaga. A Line-of-Sight Integration Approach to Cosmic Microwave Background Anisotropies. *ApJ*, 469:437–+, Oct 1996.

H.-J. Seo and D. J. Eisenstein. Probing Dark Energy with Baryonic Acoustic Oscillations from Future Large Galaxy Redshift Surveys. *ApJ*, 598:720–740, Dec 2003.

H.-J. Seo, D. J. Eisenstein, and I. Zehavi. Passive Evolution of Galaxy Clustering. *ApJ*, 681:998–1016, July 2008.

T. Shanks. Arguments for an Omega = 1, low H0 baryon dominated universe. *Vistas in Astronomy*, 28:595–609, 1985.

T. Shanks. Problems with the Current Cosmological Paradigm. In M. Colless, L. Staveley-Smith, & R. A. Stathakis, editor, *Maps of the Cosmos*, volume 216 of *IAU Symposium*, pages 398–+, Jan 2005.

T. Shanks. The effect of lensing on the large-scale cosmic microwave background anisotropy. *MNRAS*, 376:173–179, March 2007.

T. Shanks, A. J. Bean, R. S. Ellis, R. Fong, G. Efstathiou, and B. A. Peterson. The clustering of galaxies in a complete redshift survey. *ApJ*, 274:529–533, Nov 1983.

T. Shanks, B. J. Boyle, S. Croom, N. Loaring, L. Miller, and R. J. Smith. The 2dF QSO Redshift Survey. In A. Mazure, O. Le Fèvre, & V. Le Brun, editor, *Clustering at High Redshift*, volume 200 of *Astronomical Society of the Pacific Conference Series*, pages 57–+, 2000.

T. Shanks, D. H. Sutton, R. Fong, and N. Metcalfe. An Extended Galaxy Redshift Survey - Part Three - Constraints on Largescale Structure. *MNRAS*, 237:589–+, Apr 1989.

R. K. Sheth and G. Lemson. Biasing and the distribution of dark matter haloes. *MNRAS*, 304:767–792, Apr 1999.

R. K. Sheth, H. J. Mo, and G. Tormen. Ellipsoidal collapse and an improved model for the number and spatial distribution of dark matter haloes. *MNRAS*, 323:1–12, May 2001.

R. K. Sheth and G. Tormen. An excursion set model of hierarchical clustering: ellipsoidal collapse and the moving barrier. *MNRAS*, 329:61–75, Jan 2002.

M. Shimon, B. Keating, N. Ponthieu, and E. Hivon. CMB polarization systematics due to beam asymmetry: Impact on inflationary science. *Phys. Rev. D*, 77(8):083003–+, Apr 2008.

J. Silk. Cosmic Black-Body Radiation and Galaxy Formation. *ApJ*, 151:459–+, Feb 1968.

P. Simon. How accurate is Limber's equation? *A&A*, 473:711–714, Oct 2007.

F. Simpson, J. A. Peacock, and P. Simon. Locating the baryon acoustic peak. *Phys. Rev. D*, 79(6):063508–+, March 2009.

R. A. Skibba and R. K. Sheth. A halo model of galaxy colours and clustering in the Sloan Digital Sky Survey. *MNRAS*, 392:1080–1091, Jan 2009.

J. A. Smith et al. The u'g'r'i'z' Standard-Star System. *AJ*, 123:2121–2144, Apr 2002.

R. E. Smith, J. A. Peacock, A. Jenkins, S. D. M. White, C. S. Frenk, F. R. Pearce, P. A. Thomas, G. Efstathiou, and H. M. P. Couchman. Stable clustering, the halo model and non-linear cosmological power spectra. *MNRAS*, 341:1311–1332, June 2003.

G. Smoot et al. COBE Differential Microwave Radiometers - Instrument design and implementation. *ApJ*, 360:685–695, Sept 1990.

G. F. Smoot et al. Structure in the COBE differential microwave radiometer first-year maps. *ApJ*, 396:L1–L5, Sept 1992.

G. F. Smoot. The Cosmic Microwave Background Spectrum. *arXiv:9705101*, May 1997.

T. Souradeep and B. Ratra. Window Function for Noncircular Beam Cosmic Microwave Background Anisotropy Experiment. *ApJ*, 560:28–40, Oct 2001.

D. N. Spergel et al. First-Year Wilkinson Microwave Anisotropy Probe (WMAP) Observations: Determination of Cosmological Parameters. *ApJS*, 148:175–194, Sept 2003.

D. N. Spergel et al. Three-Year Wilkinson Microwave Anisotropy Probe (WMAP) Observations: Implications for Cosmology. *ApJS*, 170:377–408, June 2007.

V. Springel, J. Wang, M. Vogelsberger, A. Ludlow, A. Jenkins, A. Helmi, J. F. Navarro, C. S. Frenk, and S. D. M. White. The Aquarius Project: the subhaloes of galactic haloes. *MNRAS*, 391:1685–1711, Dec 2008.

G. D. Starkman and R. Trotta. Why Anthropic Reasoning Cannot Predict Λ. *Physical Review Letters*, 97(20):201301–+, Nov 2006.

G. Steigman. Primordial Nucleosynthesis:. Successes and Challenges. *International Journal of Modern Physics E*, 15:1–35, 2006.

H. Steppe et al. Millimeter continuum measurements of extragalactic radio sources. *A&AS*, 75:317–351, Oct 1988.

R. A. Sunyaev and I. B. Zeldovich. Microwave background radiation as a probe of the contemporary structure and history of the universe. *ARA&A*, 18:537–560, 1980.

L. Susskind. The Anthropic Landscape of String Theory. In *The Davis Meeting On Cosmic Inflation*, March 2003.

F. Sylos Labini. Inhomogeneities in the universe. *arXiv:1103.5974*, March 2011.

I. Szapudi, S. Prunet, and S. Colombi. Fast Analysis of Inhomogenous Megapixel Cosmic Microwave Background Maps. *ApJ*, 561:L11–L14, Nov 2001.

N. R. Tanvir, H. C. Ferguson, and T. Shanks. The Cepheid distance to M96 and the Hubble constant. *MNRAS*, 310:175–188, Nov 1999.

J. A. Tauber, N. Mandolesi, J.-L. Puget, T. Banos, M. Bersanelli, F. R. Bouchet, R. C. Butler, J. Charra, G. Crone, J. Dodsworth, and et al. Planck pre-launch status: The Planck mission. *A&A*, 520:A1+, Sept 2010.

M. Tegmark et al. The Three-Dimensional Power Spectrum of Galaxies from the Sloan Digital Sky Survey. *ApJ*, 606:702–740, May 2004.

M. Tegmark et al. Cosmological constraints from the SDSS luminous red galaxies. *Phys. Rev. D*, 74(12):123507–+, Dec 2006.

M. Tegmark. How to measure CMB power spectra without losing information. *Phys. Rev. D*, 55:5895–5907, May 1997.

M. Tegmark and A. de Oliveira-Costa. Removing Point Sources from Cosmic Microwave Background Maps. *ApJ*, 500:L83+, June 1998.

M. Tegmark and G. Efstathiou. A method for subtracting foregrounds from multifrequency CMB sky maps**. *MNRAS*, 281:1297–1314, Aug 1996.

M. Tegmark and M. J. Rees. Why is the Cosmic Microwave Background Fluctuation Level 10^{-5}? *ApJ*, 499:526–+, May 1998.

The *Planck* Collaboration. The Scientific Programme of Planck. *arXiv:0604069*, Apr 2006.

S. A. Thomas, F. B. Abdalla, and O. Lahav. Excess Clustering on Large Scales in the MegaZ DR7 Photometric Redshift Survey. *arXiv:1012.2272*, Dec 2010.

S. A. Thomas, F. B. Abdalla, and O. Lahav. The angular power spectra of photometric Sloan Digital Sky Survey luminous red galaxies. *MNRAS*, pages 170–+, Feb 2011.

J. L. Tinker, D. H. Weinberg, Z. Zheng, and I. Zehavi. On the Mass-to-Light Ratio of Large-Scale Structure. *ApJ*, 631:41–58, Sept 2005.

S. A. Trushkin. Radio spectra of the WMAP catalog sources. *Bull. Special Astrophys. Obs.*, 55:90–132, 2003.

L. Verde, A. F. Heavens, W. J. Percival et al. The 2dF Galaxy Redshift Survey: the bias of galaxies and the density of the Universe. *MNRAS*, 335:432–440, Sept 2002.

D. A. Wake et al. The 2df SDSS LRG and QSO survey: evolution of the luminosity function of luminous red galaxies to z = 0.6. *MNRAS*, 372:537–550, Oct 2006.

D. A. Wake et al. The 2dF-SDSS LRG and QSO Survey: evolution of the clustering of luminous red galaxies since z = 0.6. *MNRAS*, 387:1045–1062, July 2008.

A. G. Walker. On Milne's Theory of World-Structure. *Proceedings of The London Mathematical Society*, s2-42:90–127, 1936.

B. D. Wandelt and K. M. Górski. Fast convolution on the sphere. *Phys. Rev. D*, 63(12): 123002–+, June 2001.

B. D. Wandelt, D. L. Larson, and A. Lakshminarayanan. Global, exact cosmic microwave background data analysis using Gibbs sampling. *Phys. Rev. D*, 70(8):083511–+, Oct 2004.

L. L. Watkins, N. W. Evans, V. Belokurov, M. C. Smith, P. C. Hewett, D. M. Bramich, G. F. Gilmore, M. J. Irwin, S. Vidrih, Ł. Wyrzykowski, and D. B. Zucker. Substructure revealed by RRLyraes in SDSS Stripe 82. *MNRAS*, 398:1757–1770, Oct 2009.

D. F. Watson, A. A. Berlind, and A. R. Zentner. A Cosmic Coincidence: The Power-Law Galaxy Correlation Function. *accepted by ApJ, arXiv:1101.5155*, 2011.

S. Weinberg. The cosmological constant problem. *Reviews of Modern Physics*, 61:1–23, Jan 1989.

S. Weinberg. *Cosmology*. Oxford University Press, 2008.

M. White, D. Scott, J. Silk, and M. Davis. Cold dark matter resuscitated? *MNRAS*, 276: L69–L75, Oct 1995.

M. White, Z. Zheng, M. J. I. Brown, A. Dey, and B. T. Jannuzi. Evidence for Merging or Disruption of Red Galaxies from the Evolution of Their Clustering. *ApJ*, 655:L69–L72, Feb 2007.

S. D. M. White. Fundamentalist physics: why Dark Energy is bad for astronomy. *Reports on Progress in Physics*, 70:883–897, June 2007.

S. D. M. White, C. S. Frenk, M. Davis, and G. Efstathiou. Clusters, filaments, and voids in a universe dominated by cold dark matter. *ApJ*, 313:505–516, Feb 1987.

S. D. M. White, J. F. Navarro, A. E. Evrard, and C. S. Frenk. The Baryon Content of Galaxy Clusters - a Challenge to Cosmological Orthodoxy. *Nature*, 366:429–+, Dec 1993.

C. Wolf, S. Dye, M. Kleinheinrich, K. Meisenheimer, H.-W. Rix, and L. Wisotzki. Deep BVR photometry of the Chandra Deep Field South from the COMBO-17 survey. *A&A*, 377:442–449, Oct 2001.

E. L. Wright et al. Five-Year Wilkinson Microwave Anisotropy Probe Observations: Source Catalog. *ApJS*, 180:283–295, Feb 2009.

E. L. Wright, G. Hinshaw, and C. L. Bennett. Producing Megapixel Cosmic Microwave Background from Differential Radiometer Data. *ApJ*, 458:L53+, Feb 1996.

J. H. P. Wu, A. Balbi, J. Borrill, P. G. Ferreira, S. Hanany, A. H. Jaffe, A. T. Lee, S. Oh, B. Rabii, P. L. Richards, G. F. Smoot, R. Stompor, and C. D. Winant. Asymmetric Beams in Cosmic Microwave Background Anisotropy Experiments. *ApJS*, 132:1–17, Jan 2001.

K. K. S. Wu, O. Lahav, and M. J. Rees. The large-scale smoothness of the Universe. *Nature*, 397:225–230, Jan 1999.

J.-Q. Xia, M. Viel, C. Baccigalupi, G. De Zotti, S. Matarrese, and L. Verde. Primordial Non-Gaussianity and the NRAO VLA Sky Survey. *ApJ*, 717:L17–L21, July 2010.

J. Yoo, A. L. Fitzpatrick, and M. Zaldarriaga. New perspective on galaxy clustering as a cosmological probe: General relativistic effects. *Phys. Rev. D*, 80(8):083514–+, Oct 2009.

D. G. York et al. The Sloan Digital Sky Survey: Technical Summary. *AJ*, 120:1579–1587, Sept 2000.

I. Zehavi et al. Galaxy Clustering in Early Sloan Digital Sky Survey Redshift Data. *ApJ*, 571:172–190, May 2002.

I. Zehavi et al. The Intermediate-Scale Clustering of Luminous Red Galaxies. *ApJ*, 621: 22–31, March 2005a.

I. Zehavi et al. The Luminosity and Color Dependence of the Galaxy Correlation Function. *ApJ*, 630:1–27, Sept 2005b.

Y. B. Zel'Dovich, V. G. Kurt, and R. A. Syunyaev. Recombination of Hydrogen in the Hot Model of the Universe. *Soviet Journal of Experimental and Theoretical Physics*, 28:146–+, Jan 1969.

Z. Zheng, A. L. Coil, and I. Zehavi. Galaxy Evolution from Halo Occupation Distribution Modeling of DEEP2 and SDSS Galaxy Clustering. *ApJ*, 667:760–779, Oct 2007.

Z. Zheng, I. Zehavi, D. J. Eisenstein, D. H. Weinberg, and Y. P. Jing. Halo Occupation Distribution Modeling of Clustering of Luminous Red Galaxies. *ApJ*, 707:554–572, Dec 2009.

F. Zwicky. On the Masses of Nebulae and of Clusters of Nebulae. *ApJ*, 86:217–+, Oct 1937.